KAUNAS UNIVERSITY OF TECHNOLOGY

BENGISU YILMAZ

EVALUATION OF BONDING QUALITY IN AIRCRAFT STRUCTURES USING DIFFERENT NONDESTRUCTIVE TESTING METHODS

Doctoral dissertation
Technological sciences, Electrical and Electronics Engineering (T 001)

Kaunas, 2021

This doctoral dissertation was prepared at Kaunas University of Technology, Faculty of Electrical and Electronic Engineering, Prof. K. Baršauskas Ultrasound Research Institute during the period of 2017–2021. The studies were supported by *the Research Council of Lithuania and European Union Horizon 2020 Marie Sklodowska Curie Actions.*

Scientific Supervisor
Prof. Dr. Elena JASIŪNIENĖ (Kaunas University of Technology, Technological Sciences, Electrical and Electronic Engineering, T 001).

The dissertation was edited by: English language editor Dr. Armandas Rumšas (Publishing House *Technologija*), Lithuanian language editor Aurelija Gražina Rukšaitė (Publishing House *Technologija*).

Dissertation Defense Board of Electrical and Electronic Engineering Science Field:

Prof. Dr. Arūnas LUKOŠEVIČIUS (Kaunas University of Technology, Technological Sciences, Electrical and Electronic Engineering, T 001) – **chairperson**;
Prof. Dr. Chiara BISAGNI (Delft University of Technology, the Netherlands, Technological Sciences, Mechanical Engineering, T 009);
Prof. Dr. Liudas MAŽEIKA (Kaunas University of Technology, Technological Sciences, Electrical and Electronic Engineering, T 001);
Prof. Dr. Dangirutis NAVIKAS (Kaunas University of Technology, Technological Sciences, Electrical and Electronic Engineering, T 001);
Prof. Dr. Helge PFEIFFER (University of Leuven, Belgium (KU Leuven), Technological Sciences, Measurement Engineering, T 010).

The official defense of the dissertation will be held at 10 a.m. on 10 January, 2022 at the public meeting of the Dissertation Defense Board of Electrical and Electronics Engineering Science Field in the Dissertation Defense Hall at Kaunas University of Technology.

Address: Donelaičio 73-403, Kaunas LT-44249, Lithuania.
Phone (+370) 37 30 00 42; fax (+370) 37 32 41 44; email doktorantura@ktu.lt

The doctoral dissertation was sent out on 10 December, 2021.
The doctoral dissertation is available on the internet at http://ktu.edu and at the library of Kaunas University of Technology (Donelaičio 20, Kaunas LT-44239, Lithuania).

KAUNO TECHNOLOGIJOS UNIVERSITETAS

BENGISU YILMAZ

AVIACINIŲ KONSTRUKCIJŲ SUJUNGIMŲ KOKYBĖS ĮVERTINIMAS NAUDOJANT ĮVAIRIUS NEARDOMŲJŲ BANDYMŲ METODUS

Daktaro disertacija
Technologijos mokslai, elektros ir elektronikos inžinerija (T 001)

Kaunas, 2021

Disertacija rengta 2017–2021 metais Kauno technologijos universiteto Elektros ir elektronikos inžinerijos fakultete, Prof. K. Baršausko ultragarso mokslo institute. Mokslinius tyrimus rėmė *Lietuvos mokslo taryba ir Europos Sąjungos programa „Horizontas 2020“ Marie Sklodowskos Curie veiksmai*.

Mokslinis vadovas
prof. dr. Elena JASIŪNIENĖ (Kauno technologijos universitetas, technologijos mokslai, elektros ir elektronikos inžinerija, T 001).

Disertaciją redagavo: anglų kalbos redaktorius dr. Armandas Rumšas (leidykla „Technologija“), lietuvių kalbos redaktorė Aurelija Gražina Rukšaitė (leidykla „Technologija“).

Elektros ir elektronikos inžinerijos mokslo krypties disertacijos gynimo taryba:
prof. dr. Arūnas LUKOŠEVIČIUS (Kauno technologijos universitetas, technologijos mokslai, elektros ir elektronikos inžinerija, T 001) – **pirmininkas**;
prof. dr. Chiara BISAGNI (Delftų technologijos universitetas, Nyderlandai, technologijos mokslai, mechanikos inžinerija, T 009);
prof. dr. Liudas MAŽEIKA (Kauno technologijos universitetas technologijos mokslai, elektros ir elektronikos inžinerija, T 001);
prof. dr. Dangirutis NAVIKAS (Kauno technologijos universitetas, technologijos mokslai, elektros ir elektronikos inžinerija, T 001);
prof. dr. Helge PFEIFFER (Leuveno universitetas, Belgija, technologijos mokslai, matavimų inžinerija, T 010).

Disertacija bus ginama viešame Elektros ir elektronikos inžinerijos mokslo krypties disertacijos gynimo tarybos posėdyje 2022 m. sausio 10 d. 10 val. Kauno technologijos universiteto disertacijų gynimo salėje.

Adresas: K. Donelaičio g. 73–403, Kaunas LT-44249, Lietuva.
Tel. (+370) 373 00042; faks. (+370) 37 32 41 44; el. paštas doktorantura@ktu.lt

Disertacija išsiųsta 2021 m. gruodžio 10 d.
Su disertacija galima susipažinti interneto svetainėje http://ktu.edu ir Kauno technologijos universiteto bibliotekoje (K. Donelaičio g. 20, Kaunas LT-44239).

NOMENCLATURE AND ABBREVIATIONS

ACUT	Air-coupled ultrasonic testing
CFRP	Carbon fiber reinforced plastic
DB	Debonding
ECPuCT	Eddy current pulse compression thermography
FEM	Finite element method
GW	Guided waves
K-PCA	Kernel principal component analysis
MAPOD	Model assisted probability of detection
NDT	Nondestructive testing
PB	Perfect bond
PLS	Partial least square
PoD	Probability of detection
ROC	Receiver operating characteristic
SAFE	Semi-analytical finite element
SAM	Scanning acoustic microscopy
ToF	Time of flight
WB	Weak bond
WB-FC	Weak bond due to faulty curing
WB-RA	Weak bond due to release agent contamination

TABLE OF CONTENTS

INTRODUCTION

Motivation and relevance of the problem

Adhesive bonding is an effective joining technology for aircraft structures made of composites [1] and metals [2]. Adhesively bonded structures are suitable for aerospace industry with many aspects, such as a high strength-to-weight ratio, homogenous load distribution, corrosion resistance, or ability to connect complex shapes and dissimilar materials. On the contrary, mechanical fasteners such as bolts require opening holes which lead to composite fiber breakage, loss in mechanical performance, damage of structural integrity, and also significantly increases the structural weight and susceptibility to fatigue and residual stress [3].

Among aircraft parts, joints remain the most critical components – most structural failures historically started from joints. The usage of adhesive bonding for aircraft joints increased significantly in the 21st century by virtue of the rise in carbon-fiber reinforced plastic (CFRP) usage [4]. The first adhesive usage was recorded in 1945 as *Redux 775* adhesive in the liquid and powder form for *de Havilland Dove* aircraft [5]. In addition to *de Havilland Dove*, *Fokker* aircraft started to use the same adhesive to make primary structural parts in 1955. Hot cure epoxy adhesives started to be used in Boeing 727 aircraft in 1963. Also, the first Airbus aircraft, the A300, used hot cure epoxy adhesive *Cytec FM123-2* [4]. Since hot cure epoxy was first used, the usage of adhesive bonding increased to fasten secondary load structures. Specifically, Airbus A380 contains an extensive amount of adhesive bonding in several structural parts, such as elevators and flaps as seen in **Fig. 1** [4].

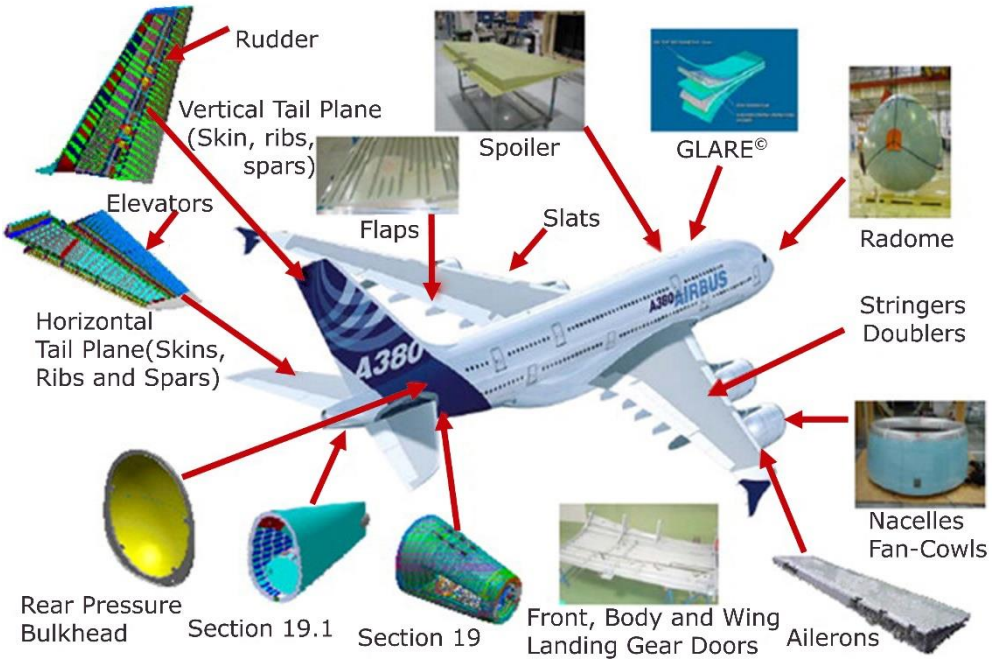

Fig. 1 Aircraft parts containing adhesive bonding in Airbus A380 [4]

Although the adhesive joint is an advantageous joining technology, the usage of bonded structures in regulated industries like aerospace is limited [6]. Several reasons restrict adhesive joint application in aircraft: the joint quality highly depends on the surface preparation, and the durability of adhesive bonding is restricted [4]. Non-destructive testing methods can determine the surface preparation quality and the adhesive durability prior to usage and during maintenance. However, in the aerospace industry, the quality assurance of adhesive joints is categorized as a 'special process' which requires reliable NDT techniques.

Adhesively bonded structures or adhesive joints can be defined as two or more structures – also known as adherends – getting bonded by a structural adhesive. The bonding quality in adhesive joints depends on multiple factors in the production phase, namely, surface preparation, wettability, environmental conditions, and the curing process. Also, in service, other defects may occur, and previously initiated defects might propagate as a result of fatigue and usage. The structural failure of adhesive joints is usually caused by such defects as debonding at the interface, porosity, moisture and contamination [7]. Prior to failure, contamination may lead to the *kissing bond* – where the adherend and the adhesive are in complete contact without any chemical bonding [8]. This interface condition makes kissing bond very challenging to detect with conventional non-destructive testing methods. Furthermore, not just the interface quality but also the integrity of the adhesive layer may decrease drastically due to contamination, moisture and pure curing [9]. This drastic decrease in the quality of adhesive bonding, also known as the *weak bond*, is hardly detectable with nondestructive testing methods. Not being able to detect weak bonds and determine the inclusions in the adhesive-adherend interface may lead to significant strength reduction as well as unexpected catastrophic failures. Hence, it is essential to have reliable non-destructive testing methods to enable the wide usage of adhesive joints.

Nondestructive evaluation of adhesive bonding is a complex task because bonding is an interfacial phenomenon which involves a very thin layer of matter, most of the time significantly lower than the wavelengths in nondestructive testing methods [10]. Up to date, several nondestructive testing methods have been used to evaluate bonding quality. Mostly, the structural integrity of bonded structures is determined by ultrasonic inspection and active thermography. The rise in the usage of advance signal processing algorithms including data fusion allow these techniques to be more efficient to visualize the internal structure as well as defect defection. This leads to the **scientific hypothesis** that a novel nondestructive evaluation methodology for adhesive bonding quality investigations can be developed based on primary experimental research, which would allow to qualitatively and quantitatively evaluate the quality of bonded structures with high reliability and to distinguish debonding and weak bonds.

Objectives and tasks

The **objective of the thesis** is to develop and evaluate the novel nondestructive evaluation methodology for bonding quality determination in adhesively bonded aircraft structures using ultrasonic, electromagnetic and thermography techniques, as

well as data fusion. In order to achieve this objective, the following tasks were foreseen:

1. To investigate the wave propagation through perfect, debonded, and weak adhesive joints, to determine the promising NDT techniques, possible post-processing algorithms, and reliability evaluation methods for numerical and experimental applications.
2. To investigate ultrasonic wave interaction, both numerically and experimentally, within adhesively bonded structures by determination of the ultrasonic parameters that are strongly correlated with the bonding quality and to detect weak bonds.
3. To determine the electromagnetic (including thermal) parameters that contain information on the bonding quality and detection of the bonding quality by using numerical and experimental investigations.
4. To compare the performance of various ultrasonic NDT techniques for debonding detection and defect sizing in adhesively bonded joints.
5. To implement data fusion of ultrasonic and eddy-current thermography NDT techniques for the improvement of bonding quality evaluation.
6. To quantitatively evaluate the reliability of various ultrasonic features for debonding and weak bond evaluation with such statistical methods as the Probability of Detection (PoD) curves.

Scientific novelty

1. The ultrasonic and electromagnetic features and parameters affecting bonding quality are determined as the ultrasonic pulse-echo amplitude and phase in the time and frequency domain, ultrasonic attenuation of the adhesive layer, the principal component of eddy-current thermography, the derivative, skewness and kurtosis of the impulse response in eddy-current pulse compression thermography.
2. The novel numerical models with different bonding quality including the weak bond have been developed with the semi-analytical finite element method (SAFE) for the ultrasonic propagation and finite element method (FEM) for eddy current thermography.
3. A novel post-processing algorithm has been developed for high-frequency ultrasonic investigations of adhesively bonded structures based on the observed time and frequency response, and the performance of the developed techniques is evaluated quantitatively.
4. A novel post-processing algorithm has been developed for eddy current pulse compression thermography of adhesively bonded structures based on kernel principal component analysis, skewness and kurtosis of impulse response. The results were quantitatively evaluated so that to determine the size, depth and conductivity (both electrical and thermal) of the contaminations within the adhesive-adherend interface.
5. The novel quantitative comparison technique to evaluate the performance of various ultrasonic NDT techniques in defect detection and defect sizing has been developed based on ultrasonic wavelength within a bonded specimen.

Additionally, data fusion applications have been innovated to improve the reliability in ultrasonic and eddy current thermography NDT for bonding quality evaluation.

6. Model assisted probability of detection curves has been calculated for weak bonds for the first time. Innovative numerical models for weak bond and debonding have been validated with experimental investigations. Feature based post-processing algorithms that were developed previously have been evaluated quantitatively with probability of detection curves.

Practical value of work

1. The proposed novel post-processing methodology with high frequency acoustic microscopy investigations and eddy current pulse-compression thermography can be used to detect debonding, to characterize inclusions at the bonding interface, and to predict weak bonds.
2. The proposed ultrasonic nondestructive testing techniques as well as eddy current thermography can be used for defect sizing and localization. While eddy current thermography and air-coupled ultrasound provide non-contact inspection advantages, immersion ultrasonic techniques with novel post-processing enable precise determination of defects, as well as the materials and sizing of inclusions.
3. The proposed data fusion applications on ultrasonic and eddy current thermography results for bonding quality evaluation can be extended for various multidimensional nondestructive evaluation as long as the response signals do not contradict each other. Also, the reported receiver operator characteristic curves can be used to determine the reliability of data fusion applications when samples with known defects are being studied.
4. The model based probability of detection curves can be utilized for any nondestructive evaluation technique that can be represented with finite element simulations to compare reliability for debonding detection, weak bond due to contamination detection, and weak bond due to faulty curing detection.

Some parts of this work were used in the reports of the international project NDTonAIR “Nondestructive testing and structural health monitoring of aircraft structures” (H2020-2016-2020-722134) – European Union’s *Horizon 2020* research and innovation program under Marie Sklodowska-Curie initial training networks.

Presented results for the defense of dissertation

1. Advanced ultrasonic NDT with a novel post-processing technique to determine the bonding quality and detect weak bonds.
2. Bonding quality evaluation with pulse-compression eddy current thermography based on kernel-principal component analysis thermal and electrical feature extraction.
3. Comparison of air-coupled, immersion, contact ultrasonic NDT techniques on the detection of debonding in metal-adhesive joints.
4. Data fusion of ultrasonic pulse-echo immersion and induction thermography nondestructive evaluations on composite-adhesive joints.

5. Reliability estimation of the developed feature-based ultrasonic NDT post-processing technique with model assisted probability of detection curves.

Approbation

The scientific results were published in 8 publications during the period of the dissertation research: half of the articles were published in international journals referred in *ISI Web of Science*, whereas the other half were accepted to reviewed international conference proceedings. Additionally, the results were disseminated in 11 international conferences held in Vilnius, Gothenburg, Glasgow, Bucharest, Turin, Bruges, Paris, Athens, and online. Based on the research results, in 2020 and 2021, a doctoral scholarship provided by the Research Council of Lithuania was received. In 2021, an international student research grant was awarded by the Committee for International Research and Education (CIRE) of the Acoustical Society of America (ASA).

Structure and content of the thesis

This thesis consists of an introduction, five chapters based on the review of the articles, conclusions, a list of references, curriculum vitae, a list of publications along with the attended conferences, and copies of scientific publications. Overall, the dissertation is composed of 212 pages, including 31 figures, 9 equations, 3 tables, 93 bibliographic references and copies of 5 publications.

1. In the first chapter, the relationship between ultrasonic parameters and adhesive bonding quality is investigated. Numerical simulations and experimental investigations for adhesive joints are reported. A novel post-processing algorithm that is able to detect weak bonds and debonding with high reliability is explained with the case study on carbon fiber composite-epoxy single lap joints.
2. In the second chapter, the relationship between electromagnetic (including thermal) parameters and adhesive bonding quality is investigated. Numerical and experimental investigations for composite-adhesive joints are reported. Debonding detection and sizing and inclusion detection that might cause weak bonds are investigated with a case study using pulse-compression induction thermography.
3. In the third chapter, extensive study and comparison of various ultrasonic NDT techniques on the evaluation of bonding quality are investigated. Several ultrasonic NDT techniques including guided waves, air-coupled ultrasonics, immersion pulse-echo, immersion through transmission and acoustic microscopy were applied on aluminum-epoxy single lap joints containing debonding defects. During metal-adhesive joint investigations, defect detection and defect sizing capabilities were evaluated while considering the ultrasonic wavelength traveling through the structures.
4. In the fourth chapter, a case study on composite-epoxy single lap joints containing artificial debonding inclusions of several sizes and materials were investigated with pulse-echo immersion ultrasonic NDT and induction thermography. In order to utilize the advantages of each technique, several data

fusion algorithms were applied. The results of experimental investigations and data fusion were evaluated quantitatively with receiver operating characteristic (ROC) curves.

5. In the fifth chapter, the reliability of ultrasonic nondestructive evaluation is discussed. The quantitative reliability of advanced ultrasonic NDT was studied in detail for high frequency acoustic microscopy investigations. The case study focused on aluminum-epoxy single lap joints with debonding, weak bond due to contamination, and weak bond due to faulty curing. Model based probability of detection curves was obtained by numerous semi-analytical finite element simulations.

Author's contribution

A1: *Advanced ultrasonic NDT for weak bond detection in composite-adhesive bonded structures* [11]: contribution from each co-author is reported at the end of the article. The first author, who is also the corresponding author, **Bengisu Yilmaz** contributed on the conceptualization of the study, data curation with experimental investigations, formal analysis of the data, funding acquisition, methodology, novel post-processing software, figure creation and interface visualization, writing the original draft as well as review and editing. The second co-author **Elena Jasiuniene** contributed to the work with project administration, supervision, validation of the results, and the review and editing of the manuscript.

A2: *Evaluation of debonding in CFRP-epoxy adhesive single-lap joints using eddy current pulse-compression thermography* [12]: third co-author **Bengisu Yilmaz** contributed to the conceptualization, data curation and experimental investigation, formal analysis, visualization of figures, writing review and editing. **Qiuji Yi** contributed to the conceptualization, data curation and experimental investigation, formal analysis with software development, methodology of eddy current thermography investigations, visualization of the results, writing the original draft as well as review and editing. **Gui Yin Tian** contributed by conceptualization of the work, methodology of eddy current thermography investigation, project administration, funding acquisition, supervision, validation of the results, writing for review and editing. **Hamed Malekmohammadi** contributed to the pulse-compression methodology, visualization of figures, writing review and editing. **Stefano Laureti** contributed with funding acquisition, pulse-compression methodology, project administration, as well as writing review and editing. **Marco Ricci** contributed with funding acquisition, pulse-compression methodology, project administration, supervision, writing review and editing. **Elena Jasiuniene** contributed to the work with funding acquisition, project administration, supervision, writing review and editing.

A3: *Air-coupled, contact and immersion ultrasonic nondestructive testing: comparison for bonding quality evaluation* [13]: contribution from each co-author is reported at the end of the publication. The first and corresponding author **Bengisu Yilmaz** contributed to conceptualization, methodology in immersion ultrasonic and acoustic microscopy, software development for numerical analysis as well as signal

processing, data acquisition and experimental investigations, visualization, writing original draft as well as review and editing. **Aadhik Asokkumar** contributed to conceptualization, methodology in air-coupled and guided ultrasonic wave, software development for numerical analysis as well as signal processing, data acquisition and experimental investigations, visualization, writing the original draft as well as review and editing. **Elena Jasiuniene** contributed to conceptualization, methodology, validation of results, supervision, writing review and editing, project administration and funding acquisition. **Rymantas Jonas Kazys** contributed to conceptualization, methodology, validation of the results, supervision, writing review and editing.

A4: *Evaluation of bonding quality with advanced NDT and data fusion* [14]: the contribution of each co-author is reported at the end of the publication. The first and corresponding author **Bengisu Yilmaz** contributed to conceptualization, ultrasonic investigation methodology, development of signal processing software and data acquisition, formal analysis of the results, ultrasonic and eddy current thermography investigations, visualization and writing the original draft. **Abdoulaye Ba** contributed to methodology and experimental investigations for eddy current thermography, software development, writing review and editing. **Elena Jasiuniene** contributed to conceptualization, methodology and validation of ultrasonic investigation results, supervision, project administration, funding acquisition, writing review and editing. **Huu-Kien Bui** contributed to methodology, investigation and validation of eddy current thermography experiments, supervision, writing review and editing. **Gerard Berthiau** contributed to methodology and validation of eddy-current thermography investigation results, supervision, project administration, funding acquisition, writing review and editing.A5: *Model assisted reliability assessment for adhesive bonding quality evaluation with advanced ultrasonic NDT* [15]: the contribution of each co-author is given at the end of the publication. The first and corresponding author **Bengisu Yilmaz** contributed to conceptualization, data curation, formal analysis, funding acquisition, investigation, methodology, software, visualization, and writing the original draft. **Damira Smagulova** contributed to investigation, methodology, software, writing review and editing. **Elena Jasiuniene** contributed to project administration, supervision, validation, writing review and editing.

Literature review on bonding quality evaluation with NDT

1. Bonding quality

Nondestructive testing of adhesive joints is a challenging task because adhesion is an interfacial phenomenon that involves a very thin layer of material which is usually smaller than the inspection wavelengths. The quality of the interfacial adhesion between the adherend and the adhesive, hereinafter called *bonding quality*, can be affected by several factors during manufacturing in the course of surface preparation, wettability, environmental conditions (temperature – pressure – humidity), and the curing process. Additionally, the bonding quality may decrease during usage due to fatigue effects. The typical defects in bonded joints as defined by Adams and Cawley are poor curing, cracks, zero-volume and air-gap disbond (debonding), porosity, and void [16]. They suggest that if the adherend's surface is contaminated by oil deposits, or loose oxide layers prior to bonding; as a result, the

bonding quality may be poor, and adhesion becomes weak. Moreover, Nagy stated that interface contamination may lead to the *kissing bond* – where the adherend and the adhesive are in complete contact when compressed; but otherwise disbonded surfaces[8]. Jiao and Rose defined the *kissing bond* as a smooth (or slip) boundary where two surfaces are separated by a thin layer of liquid [17]. Yan et al. combined these two definitions and declared the kissing bond as a bonding defect where the adhesive and the adherend are in some way coupled through an interface that shows altered normal and shear stiffness [18]. Furthermore, contaminations, moisture and pure curing may lead to a drastic decrease in adhesive integrity, i.e., the so-called *weak bond* [9]. The difference between the kissing bond and the weak bond is defined by the presence of residual tensile strength, while the *kissing bond* has no residual tensile strength, the *weak bond* has residual strength below the design thresholds [18]. Therefore, the detection of a weak bond with nondestructive testing methods is more challenging than that of the kissing bond [10].

2. Nondestructive testing (NDT) methods for adhesive bonding

Nondestructive testing of adhesively bonded structures has been studied throughout the world. NDT techniques can be categorized under two main branches: ultrasonic and electromagnetic (including thermography). Additionally, extended NDT techniques and a detailed comparison are reported.

2.1 Ultrasonic NDT methods

Ultrasonic NDT relies on the sound wave propagation inside the specimen, and the change in ultrasonic impedance is recorded when a wave scatters, reflects or is attenuated by an obstacle that can be a backwall, a defect or some interface. What regards bonding quality evaluation, ultrasonic NDT has been one of the most commonly used techniques [19].

The ultrasonic wave interaction with the adhesive bonding is a complex phenomenon where the superposition of all the possible acoustic impedance differences through bonding interfaces is of interest. Acoustic wave propagation through a multi-layered medium has been studied for straightforward problems [20] as well as irregular interfaces [21]. Brekhovskikh showed that acoustic wave propagation can be modeled by three approaches: by solving boundary equations, by means of impedances (the transmission line theory) and by considering multiple reflections which occur at each and every interface [22]. Anastasi and Roberts modeled adhesively bonded multi-layered structures with the impedance approach [23].Reflection coefficients for ultrasonic waves propagating through a plane interface with the plane wave, normal incidence and semi-infinite media assumptions is calculated as:

$$R = (Z_1 - Z_2)/(Z_1 + Z_2); \quad (1)$$

where Z_1 and Z_2 correspond to the acoustic impedances of the first and the second medium, respectively. Acoustic impedance (Z) is a product of acoustic wave velocity (v) and the density (ρ) of the medium:

$$Z = \rho\, v; \tag{2}$$

By the one-dimensional analytical model, or where the second and third dimensions have a very slight effect, acoustic wave equation can be given as:

$$\rho \frac{\partial^2 u}{\partial t^2} = V_L \frac{\partial^2 u}{\partial z^2} + V_S \frac{\partial^2 u}{\partial y^2} + \eta_L \frac{\partial^3 u}{\partial z^2 \partial t} + \eta_S \frac{\partial^3 u}{\partial y^2 \partial t} + F(t); \tag{3}$$

where ρ is the material density, V_L is the longitudional wave velocity, V_S is the shear wave velocity, η_L is the damping parameter in the z direction, η_S is the mechanical damping parameter in the y direction, and $F(t)$ is the applied force density on the structure surface.

Several ultrasonic NDT techniques are used to determine the bonding quality with a combination of different measurement parameters, such as transducers (focus, flat, single, phased array), the contact medium (immersion, air-coupled, laser stimulated), the inspection mode (pulse-echo, through transmission, pitch-catch) and the ultrasonic wave that is generated within a structure (guided waves, lamb waves, shear waves, longitudinal waves). Immersion through-transmission ultrasonic NDT is considered to be a reference technique among ultrasonic techniques; however, it requires structures to be immersed in water in addition to two-sided access [24]. The immersion pulse-echo technique allows users to inspect structures with only one-sided access; however, still requires them to be submerged in water [25]. Specifically, immersion pulse-echo ultrasonic NDT has been utilized to visualize the bonding interface [26], to detect debonding [27], to evaluate adhesive quality [28], to measure the effect of moisture and extreme humidity on a weak bond [29], to detect kissing bonds [30] and weak bonds [31], and to determine defect positions [3]. Also, scanning acoustic microscopy (SAM) in the pulse-echo mode with fast inspections, high resolution and high frequency is used to evaluate the weak bond with holography [32] and porosity identification in dissimilar joints [33]. High frequencies of acoustic microscopy cause high attenuation to be observed, and the structure size to be inspected is limited. Both immersion and SAM techniques require bulky systems, hence, *in-situ* applications are limited.

While immersion ultrasonic research provides a range of variety in terms of high frequency, air coupled ultrasonic testing offers a great advantage of contactless inspection. The air-coupled ultrasonic technique (ACUT) has been reported to calculate the interfacial stiffness of weak bonds [34] and to visualize the interface of a three-layer bonded aluminum joint [35]. Although contactless measurements of ACUT makes it a good candidate for in-situ measurements for production and maintenance, high amplitude loss in air limits the potential applications.

On the other hand, guided wave (GW) ultrasonic testing that allows large structures to be inspected in a short amount of time is a promising technique to evaluate bonding quality. Some studies worked on the debonding and delamination detection with Lamb waves and vibrometry [36,37]; others discussed the scattering of the guided waves due to the change in the interface quality [38,39]. Additionally, Lamb waves may be used to investigate the weak bond by checking the change in

amplitude response [40]. GW ultrasonics usually requires complex post-processing algorithms and is limited by the thickness of the adhesive joint.

Moreover, the nonlinearity level measured by nonlinear ultrasound is associated with the bonding quality, particularly when a weak bond is present [41,42]. Nowadays, nonlinear ultrasound is still not mature enough to be implemented in industrial applications, and the obtained results contain a high level of error. In addition to nonlinear ultrasound, laser based ultrasound has been used to evaluate the quality of adhesive joints based on reflection-transmission coefficients [43]. Laser ultrasound is specifically a highly promising technique to detect debonding in honeycomb bonded structures, however, it uses high excitation amplitudes which cause high noise and difficulty in the interpretation of results.

2.2 Electromagnetic NDT methods and thermography

In addition to ultrasonic NDT techniques, electromagnetic NDT is also widely used to determine the bonding quality. Electromagnetic NDT relies on the induced electric currents and/or magnetic fields into the structure; the electromagnetic response is monitored with a variety of sensors. Ranging from low to high frequency, electromagnetic NDT techniques can be listed as radio frequency NDT, microwave NDT, eddy current testing, infrared thermography, shearography, visual inspection, X-ray and gamma ray radiography. Among all, visual inspection is the most commonly used NDT technique. Adhesive joints are visually inspected prior to bonding in order to verify the successful surface preparation [44]. Furthermore, surface damages in bonded structures can be detected by high frequency radio frequency and microwave NDT [45,46]. While terahertz imaging is used for the interface visualization of non-conductive bonded composites [47], eddy current NDT can be used to evaluate surface and sub-surface defects in joints with conductive adherends such as carbon fiber reinforced composites [46].

Thermography is one of the most widely used NDT techniques to evaluate the bonding quality [48–50] because it is highly sensitive and responsive. On top of that, it is suitable for large areas and offers non-contact inspection. However, mostly surface and subsurface defects are detected with thermography. In order to increase the sensitivity of the inspection, structures are stimulated via several options, one of which is active thermography. Active thermography has been extensively utilized to detect fabrication defects in bonded joints [51,52], and to determine the presence of contamination in adhesive bonds [53,54]. In metallic adhesive joints, surface roughness, artificial defects and grooves are detected with lock-in active thermography [55]. The conventional light-based active thermography is highly influenced by the thermal diffusion and structural anisotropy. By this technique, the thermal energy travels from the heated surface and then back propagates to the surface to be captured by an infrared camera. For effective defect detection in higher skin depths, eddy current (induction) pulsed thermography can be used since it provides volumetric heating to the electrically conductive structure [12,56]. Even though induction thermography is preferable, the thickness of bonded structures and the dimensional complexity of the results may limit its application [57].

Induction thermography consists of electromagnetic wave excitation and thermal radiation observance with infrared thermography. The temperature distribution on the adhesive joint can be modeled by solving boundary based weak electromagnetic (Formulas 4, 5) and nodal thermal formulation (Formula 6) [58]:

$$\int_{\Omega}\left(\mathbf{curl}\left(w_e\frac{1}{[\mu]}\mathbf{curl}(\mathbf{A})\right)+jw[\sigma]w_e(\mathbf{A}+\mathbf{grad}\varphi)\right)d\Omega-\int_{\Gamma}w_e\left(n\wedge\frac{1}{[\mu]}\mathbf{curl}(A)\right)=\int_{\Omega}w_e\mathbf{J_s}d\Omega; \tag{4}$$

$$\int_{\Omega c}(jw[\sigma]\mathbf{grad}\mathrm{w_n}(A+\mathbf{grad}\varphi))\,d\Omega=0; \tag{5}$$

$$\int_{\Omega_c}\left(\rho C_P\frac{\delta\mathbf{T}}{\delta t}-div([\lambda]\mathbf{gradT})\right)w_n d\Omega=\int_{\Omega_c}Pw_n\,d\Omega; \tag{6}$$

where **A** and φ are, respectively, the magnetic vector potential and the primitive in time of the electric scalar potential, P is the electromagnetic induced power density, $\mathbf{J_s}$ is the source current density, w_e and w_n are, respectively, the denoted edge shape function and the nodal shape function, **T** is the temperature, C_P is the specific heat, ρ is the specific mass and $[\lambda]$ is the tensor of thermal conductivities. $[\lambda]$ is the thermal conductivity tensor, and $[\sigma]$ is the electrical conductivity tensor.

Similar to thermography, shearography is very responsive and can detect large areas within a short time, however, it provides an effective detection for surface and sub-surface defects and requires high stress solicitation [44]. It has been reported that shearography performs well to detect debonding and subsurface defects in aluminum-adhesive bonds [49].

X-ray radiography and X-ray computed tomography (CT) are powerful NDT techniques to investigate inner defects in bonded structures [50]. For composite-adhesive joints, X-ray CT is a challenging task, not just because it is a significantly expensive and bulky system, but also because of the high aspect ratios of structures and similar diffraction coefficients [59]. Also, X-ray CT is not a very effective method to detect zero volume defects, such as debonding.

2.3. Extended NDT methods

While the majority of previous studies relied on the usage of ultrasonic inspection techniques and active thermography, others focused on unconventional nondestructive testing techniques. Recent studies have been discussing the potential applications of electromechanical impedance NDT to inspect interface defects [60] and weak bonds caused by contaminations, moisture, and pure curing [61,62]. Additionally, laser based techniques, such as the laser shock adhesion test (LASAT) [63] and laser bond inspection (LBI) [64] had, have been reported to be promising techniques to detect weak bonds. LASAT and LBI creates a debonding defect if the adhesive joint has already had weak bonds, hence, the destructive and fatigue effects of these techniques are under question. While extended NDT methods are promising as they have potential to detect defects in adhesive joints, yet these systems are fairly expensive both in terms of purchase and maintenance.

2.4. Comparison of NDT methods

A comparison of all the above discussed NDT techniques is reported in Table 1 with the possible applications on bonding quality evaluation, as along with their advantages and limitations.

Table 1. Advantages and limitations of different NDT techniques for bonding quality evaluation.

NDT Technique	**Bonding Quality Evaluation**		
	Defect / Inclusion type	***Advantages***	***Limitation***
Immersion ultrasonic testing – through transmission	Any type [24]	Reference method, directional information	Requires two-sided inspection and immersion, bulky system
Immersion ultrasonic testing – Pulse-echo	Debonding [27]	One-sided inspection, sufficient directional information. Focusing and post-processing can increase the performance	Requires immersion. Usually bulky system. Interface quality and debonding detection is limited due to attenuation levels and joint dimensions
	Interface quality [26], adhesive quality [28]		
	Moisture & Humidity [29]		Weak bond and kissing bond detection is not sufficient without complex post-processing
	Weak bond & Kissing bond [30,31]		
Acoustic Microscope	Interface quality [33,65]	High resolution, fast inspection	High attenuation caused by high frequency. Requires immersion. Limited to the structure size. Bulky system
Air-coupled ultrasonic testing (ACUT)	Interface quality [35]	Contactless. Applicable to in-situ monitoring.	Through-transmission requires two-sided inspection. Limited due to high amplitude loss in air
	Weak bond & Kissing bond [34]		Weak and kissing bond detection is not sufficient
Guided-wave (GW) ultrasonic testing	Debonding [36,37]	Inspection of large structures in short time	Complex processing needed. Usually limited by the total joint thickness
	Interface quality [38,39]		
	Weak bond [40]		

NDT Technique	Bonding Quality Evaluation		
	Defect / Inclusion type	***Advantages***	***Limitation***
Nonlinear ultrasound	Weak bond & Kissing bond [41,42]	Potential to detect weak and kissing bond	High ultrasonic magnitudes, not mature enough, lots of errors in calculation
Laser Ultrasound	Interface quality [43]	Promising to detect debonding in honeycombs	Susceptible to damage and fatigue due to high excitation amplitude
Visual Inspection	Prior to bonding [44]	Easy, cheap, in-situ applicable	Limited to surface defect detection
Microwave & Terahertz Imaging	Interface quality [45,46], [47]	Contactless, high resolution and ability to focus	Limited to non-conductive adherend
Eddy current	Interface quality [46]	Can be non-contact, in-situ applicable, easy interpretation	Limited to conductive adherend and subsurface defects
Thermography	Interface quality [48–50]	Sensitive, responsive, contactless, suitable for in-situ monitoring	Limited to adherend thickness, effective on surface-subsurface defects
Active thermography	Fabrication defects [51,52] Contamination [53,54] Surface roughness [55]	Increased detectability compared to passive thermography	Restricted by joint dimensions and thermal conductivity
Induction thermography	Interface quality [12]	Higher skin depth due to volumetric heating	Sensitive to joint geometry, not effective with non-conductive adherends
Shearography	Debonding [49]	Sensitive, responsive, contactless fast detection	Limited to surface – subsurface defects
Radiography/CT	Internal structure / inner defects [50] [59]	Full structure visualization with computed tomography (CT). Possibility to obtain high resolution	Expensive, challenging on complex geometry ad high aspect ratio. Not sensitive to two-dimensional defects like debonding
Electromechanical Impedance	Interface quality [60]		

NDT Technique	Bonding Quality Evaluation		
	Defect / Inclusion type	***Advantages***	***Limitation***
	Weak bond [61,62]	Promising alternative weak bond detection	Expensive, new, experimental technique
Laser shock adhesion test / Laser bond inspection	Weak bond [63] [64]	High detectability of weak bond, in-situ applications	Expensive, questionable destructive level: product damaged if there is defect, fatigue effect

3. Data fusion

Although nondestructive evaluation of adhesive bonding may be performed with several different techniques, all of them have advantages and limitations. In order to overcome the limitations of the currently available techniques, it is possible to combine the information from different types of inspection by using data fusion. Data fusion was introduced to NDT by Gros *et al*., and the research into this topic has been continuing to grow [66]. Data fusion applications for concrete samples have mostly used ground penetrating radar (GPR), impact echo and ultrasonic testing as data fusion resources while deploying several data fusion algorithms such as fuzzy logic [67,68], artificial neural networks (ANN) [69], Hadamard, and the Dempster-Shafer rule of combination [70]. For composite structures, data fusion studies have focused on several different combinations of NDT techniques. For example, it has been reported that porosity detection in composites has improved with X-ray tomography and interferometer data fusion [71]. Also, damages can be monitored in composites by combination of acoustic emission, digital image correlation (DIC), and thermography data [72]. On the other hand, convolutional neural networks (CNN) can be used to improve lock-in thermography imaging [73]. Specifically, Daryabor and Safizadeh [74] studied the image fusion for ultrasonic inspection and active thermography for adhesive quality evaluation in between dissimilar joints. They compared several basic and complex fusion algorithms, namely: minimum, maximum, average, principal component analysis, wavelet transformation and pyramid.

4. Reliability analysis and probability of detection

Most of the time, data fusion improves the performance compared to a single NDT technique, however, the reliability of the NDT technique should be quantified with statistical methods. NDT reliability is described as being able to obtain accurate and consistent results with various equipment and operators, or, in other words, repeatable and reproducible nondestructive tests [75]. Usually, NDT reliability is measured with probability of detection (PoD) curves [76] which relate the probability of detecting a defect with its characteristic value [77]. There are two methods to obtain PoD curves:

- a vs. $\hat{a}$ algorithm: the signal response values for each defect size are recorded, and quantitative results are used.

- Hit/Miss algorithm: the binary response is recorded (a defect is either detected or not detected).

Each inspection is valid for the specific NDT test performed on the specific sample because the detectability of defects is affected by multiple uncontrollable factors, such as temperature, radiation, moisture, inspection set-up and condition, digital and analog noise, personnel qualifications, experience, and variance occurring in structures due to material and dimensional properties [78,79].

In practice, it is costly and time consuming to conduct experiments to obtain probability of detection curves because this strategy requires numerous samples, inspection and personnel. Yet, the need and the acceptance of PoD curves has been increasing for safety regulations. Therefore, some emerging industries, such as aerospace, are choosing simulation based reliability analysis, model assisted probability of detection (MAPOD) [80–82]. Choosing model based PoD over experimental PoD not only reduces the high cost of reliability studies with simulations, but also allows configurations that are not possible to achieve with experiments. Currently, MAPOD applications include but are not limited to eddy current inspection of fatigue cracks in engine components [83], eddy current inspection of wing lap joints [83] and titanium plates [84], induction thermography for crack detection [85], ultrasonic testing for defects in engine disk alloys [83] and in railway axles [86]. A detailed review on the trial studies that involve MAPOD has been reported by Meyer *et al*. [87]. Recently, a comparison study between experimental PoD and MAPOD for eddy current testing of surface fatigue cracks has been reported [77]. Additionally, two signal responses have been integrated with MAPOD for flaw detectability via eddy current testing [88]. Also, MAPOD is used to estimate response operating characteristic curves for magnetic field measurements [89]. A case study on flat bottom hole detection by ultrasonic NDT has been reported regarding the MAPOD implementation procedure and challenges [90]. Also, Smagulova *et al*. studied the debonding detection detectability in dissimilar joints with ultrasonic testing while using MAPOD [91].

Research methodology

This work aims to evaluate the quality of adhesively bonded aircraft structures with different nondestructive testing methods and report on the quantitative reliability. The goal of the research is to develop a nondestructive evaluation methodology to determine the bonding quality in adhesively bonded aircraft structures, and to evaluate the results achieved by the developed technique quantitatively. While some of the recent research works focused on developing an NDT methodology, such as extended NDT techniques, this work aims to utilize and improve the common nondestructive bonding evaluation techniques. Throughout the work, numerical and experimental investigations were performed with ultrasonic NDT methods and induction thermography extensively. The NDT inspections have been collected with original samples and experiments, which defines the characteristic of research methodology as a primary experimental research. Whilst the goal of the work was to achieve quantitative research results, the research starts with the evaluation of experimental and numerical results qualitatively during the first four chapters, and then moves to

quantitative analysis with statistical methods, namely, the probability of detection, in the fifth chapter.

In order to evaluate the quality of adhesive bonding in aircraft structures, different types and quality of adhesive joints were investigated in five scholarly articles. The single lap joint samples were manufactured at *Cotesa GmBH,* Germany. Composite-adhesive single-lap joints prior to bonding are shown in **Fig. 2**. The composite adherend was made of six layers of carbon-fiber reinforced epoxy (CFRP) from HexPly M21-5H Satin woven prepreg. The resulting laminates had a thickness of 2.22 mm. Aluminum-adhesive single-lap joints prior to bonding are shown in **Fig. 3**. Aluminum adherends were cut from 1.6 mm thick aluminum 2024 alloy sheets. In both composite and aluminum joints, 3 M Scotch-Weld AF163 k-red structural adhesive film epoxy with the nominal thickness of 0.24 mm was used as the adhesive layer.

The bonding quality is defined as the expected adhesive joint quality that would be achieved with manufacturing according to the regulations as applicable to surface preparation where no defect or inclusion is present. The perfect bond (PB) bonding quality represents the structure in the pristine state, however, in other cases, the quality of the bonding was decreased by adding inclusions to the adhesive-adherend interface. An artificial air gap or porosity at the bonding interface, also known as debonding (DB), was created by placing two-fold square release agent films (12.7 mm x 12.7 mm x 0.63 mm) to the adhesive-adherend interface. Additionally, interfacial debonding that might occur due to foreign material inclusions during manufacturing was displayed with brass film inclusions for two sizes: two-fold square big brass defects with 12.7 mm edge length (DB-brass-big) and two-fold square small brass defects with 6.35 mm edge length (DB-brass-small). As seen in **Fig. 2**. and **Fig. 3**, artificial debonding and brass inclusions were added as five identical squares with equal distribution. Moreover, the weak bond – where the bonding quality is reduced dramatically due to contamination or environmental factors – was considered to be of interest. Weak bonds due to liquid layer contamination were artificially created by spraying the adhesive interface with 0.6 mL release agent (WB-RA). For the composite-adhesive joint, during spraying, one side of the sample was masked with a plastic film to limit the amount of release agent contamination (WB-RA-less), while the other side did not have any mask on (WB-RA-more). When considering the curing cycle effects on the adhesive quality, weak bonds due to faulty curing (WB-FC) were created by doubling the speed to reach the curing temperature and decreasing the nominal curing (dwell) temperature of the epoxy adhesive from 125°C to 90°C (level 1) and 75°C (level 2).

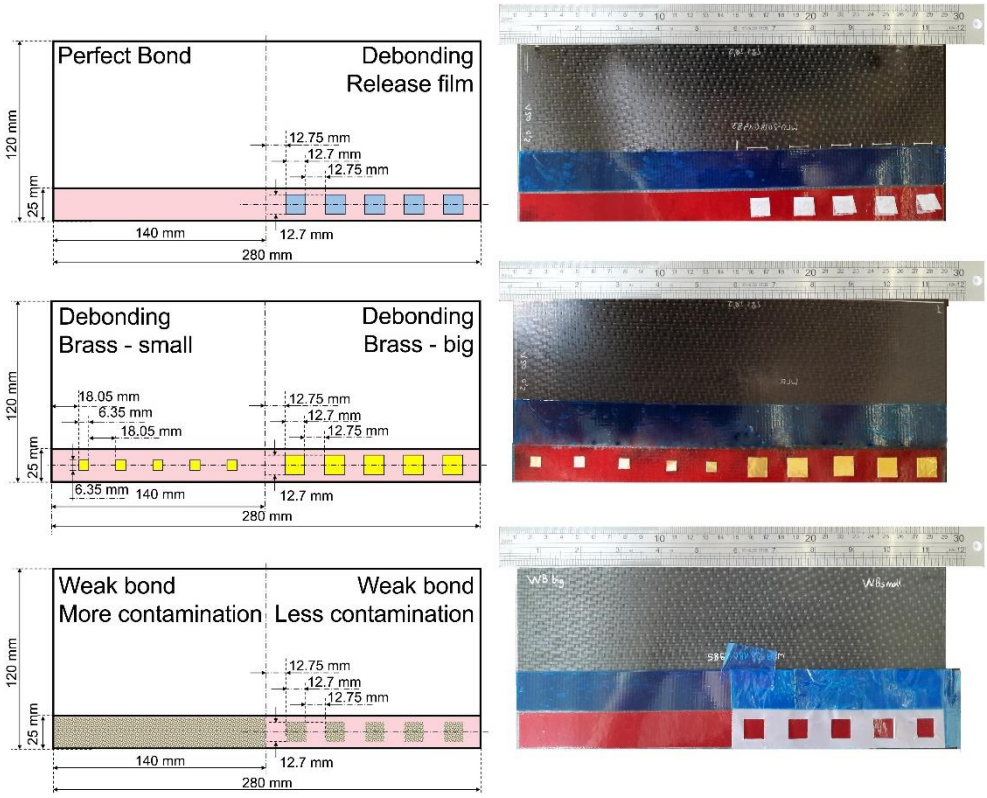

Fig. *2* Composite-adhesive single lap joints before bonding; sketches on the left, photos on the right

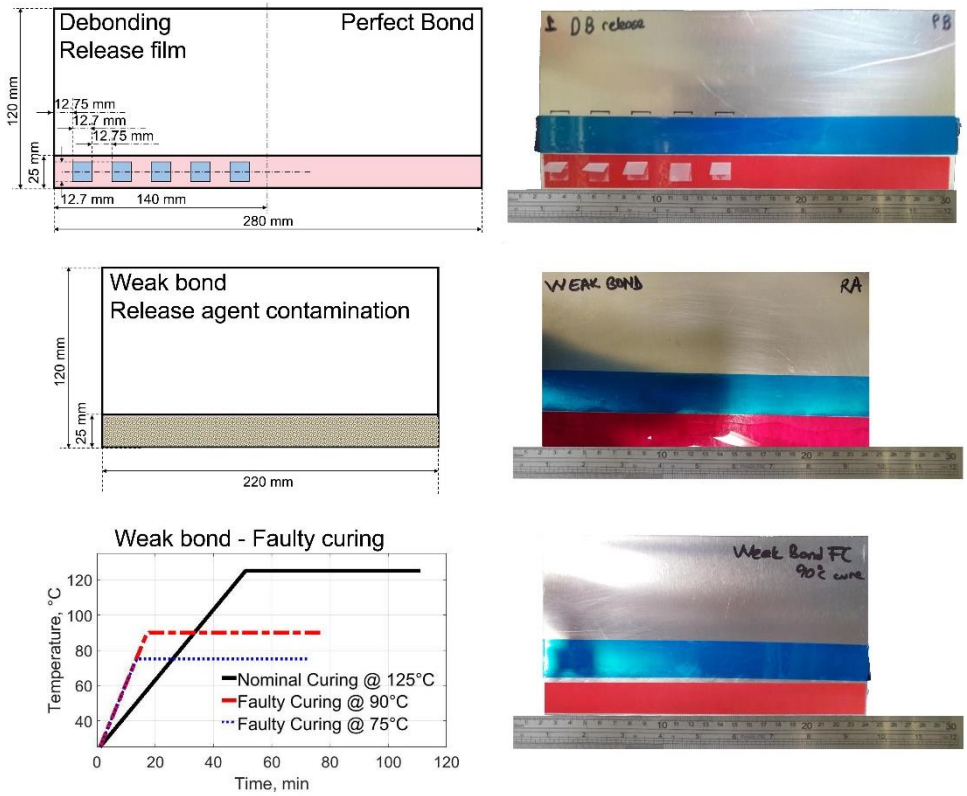

Fig. *3* Aluminum-adhesive single lap joints before bonding; sketches on the left, photos on the right.

The unified system of bonding qualities and nondestructive testing methods used in the articles is listed in Table 2. Additionally, the relationship in between the articles is highlighted with **Fig. 4** considering the NDT technique, the bonding quality, and the adhesive-adherend combination of interest. While in A1, A2 and A4, composite-adhesive single-lap joints were of interest, A3 and A5 focused on the aluminum-adhesive single-lap joints.

NDT techniques for each specimen were selected based on the applicability of each technique. Both composite-adhesive joints and aluminum-adhesive joints were investigated with scanning acoustic microscopy (A1, A5). Scanning acoustic microscopy was chosen so that to provide high resolution interface visualization in between the highly attenuating epoxy adhesive and the substrate. Eddy current (induction) thermography can only be applicable to composite-adhesive joints because recording the aluminum surface with an infrared camera is challenging due to the high thermal conductivity of aluminum. Eddy current induction thermography provides spatial information of adhesive joints, which can be exploited in fast and non-contact in-situ monitoring. Immersion ultrasonic NDT was used to investigate both composite-adhesive and aluminum-adhesive joints. Immersion ultrasonic NDT is a standard method that is used in aerospace industry manufacturing, hence, it was

selected to provide the base level information that can be compared with other techniques. Additionally, it was decided to compare and apply data fusion to ultrasonic immersion NDT and induction thermography, since the former is a standard technique that is used in the industry, and the latter is a developing NDT with such potential advantages as being fast and non-contact. For guided wave investigation, aluminum-adhesive joints were chosen as the structure under investigation to achieve the best possible representation with less attenuating and homogenous substrate compared to the composite. The GW technique is exploited with such features as being fast, accurate and being able to provide more information than longitudinal bulk waves. Air coupled ultrasonic NDT is used with aluminum-epoxy joints to demonstrate possible non-contact ultrasonic applications with two-sided access.

Table 2 Adhesives & adherends, bonding qualities and NDT techniques used in each article

	Adhesive& Adherend	Bonding Quality	NDT Techniques	Extracted Features
A1	CFRP-epoxy-CFRP	PB DB WB-RA	Scanning acoustic microscopy (SAM)	Time domain Amax Time delay Frequency Amax Frequency shift
A2	CFRP-epoxy-CFRP	PB DB DB-brass WB-RA	ECPuCT - Eddy-current (induction) pulse compression thermography	K-PCA (sliding) Impulse response Derivative Kurtosis Skewness
A3	Aluminum-epoxy-aluminum	DB	Immersion pulse-echo Immersion through transmission Scanning acoustic microscopy (SAM) Air-coupled ultrasonic through transmission Air-coupled to contact GW Contact-to-contact GW	Peak to peak amplitude
A4	CFRP-epoxy-CFRP	DB DB-brass	Immersion pulse-echo Induction thermography	Peak to peak amplitude
A5	Aluminum-epoxy-aluminum	PB DB WB-RA WB-FC	Scanning acoustic microscopy (SAM)	Peak to peak amplitude Time delay Frequency Amax Frequency Shift Attenuation

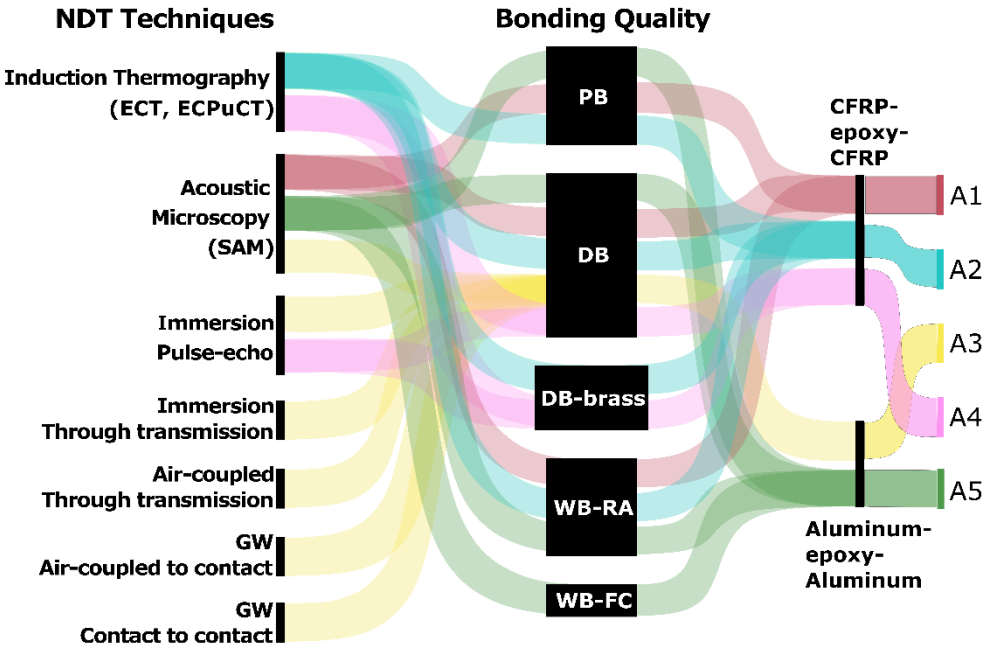

Fig. *4* Relationship between articles used in the dissertation considering NDT techniques, bonding quality and adhesive-adherend combinations

Scientific articles and their connections

In the first article (A1) *Advanced ultrasonic NDT for weak bond detection in composite-adhesive bonded structures* [11], four different ultrasonic parameters based on time and frequency domain analysis are determined after high frequency immersion pulse-echo ultrasonic inspection. Highly attenuating composite interface is visualized with high resolution by exploiting the high frequency scanning acoustic microscopy. Composite-adhesive single lap adhesive joints with three different conditions of bonding quality are investigated, and interface qualities are evaluated with the developed advanced NDT technique. It is shown that the novel post-processing algorithms enable weak bond detection in composite-adhesive joints.

In order to check the performance of electromagnetic NDT techniques, in the second article (A2) *Evaluation of debonding in CFRP-epoxy adhesive single-lap joints using eddy current pulse-compression thermography* [12], the composite-adhesive single lap joints with three different bonding quality – the ones that are used in Article 1 [11] as well – are investigated with the eddy current thermography technique. In order to increase the sensitivity of the thermal response, the pulse-compression technique is implemented. By developing advanced signal processing algorithms for eddy current pulsed-compression thermography results, non-uniform heating pattern is removed, and the relationship between inclusions within the samples and the electromagnetic parameters are determined based on kernel principal component analysis. The depth of artificial defects as well as their sizes are correlated with the electromagnetic thermal response. The results indicate that the weak bond

due to contamination plays a minor role in changing the electrical and thermal properties of a single-lap joint; however, it affects the thermal properties more than the electrical ones.

In order to widen the perspective on the evaluation of the bonding quality, a comparison of different ultrasonic techniques is reported in the third article (A3) *Air-coupled, contact and immersion ultrasonic nondestructive testing: comparison for bonding quality evaluation* [13]. Aluminum-epoxy single-lap joints with artificial debonding are investigated with the contact, immersion and air-coupled ultrasonic techniques including guided wave inspection. The best performance in defect sizing and localization is observed with bulk wave investigations. Particularly, the high frequencies in immersion perform better than the low frequency air-coupled ultrasonic testing, but air-coupled techniques allow samples to be investigated without contact. Also, guided waves can be effective when performing defect detection as opposed to their low defect sizing performance.

As the comparison of different ultrasonic investigations suggested, the advantages and limitations of the techniques differ. Hence, the best performance can be accessed by using information from different techniques with data fusion. In the fourth study (A4) *Evaluation of bonding quality with advanced NDT and data fusion* [14], a comparison and data fusion of nondestructive evaluation results obtained from two different techniques are reported for three different levels of bonding quality in composite-adhesive single lap joints. The ultrasonic immersion technique is selected as one of the NDT techniques since it is the most commonly used standard methodology. For the second data fusion source, adhesively bonded structures are inspected with the eddy current (induction) thermography set-up. While ultrasonic immersion NDT provides directional response from a specific point on the adhesive joint, induction thermography gives contactless and spatial information. Also, it is considered that while one data source depends on ultrasonic wave propagation, the other is based on electromagnetic waves and the thermal response. Advanced signal processing algorithms (average, difference, weighted average, Hadamard, and Dempster-Shafer) are applied to obtain different data fusion results. The results evaluated by the receiver operating characteristic curve show that data fusion can increase the detectability of artificial debonding in single-lap joints.

Last but not least, the reliability of the previously developed [11] post-processing algorithms is evaluated quantitatively with probability of detection curves in the fifth study (A5) *Model assisted reliability assessment for adhesive bonding quality evaluation with advanced ultrasonic NDT* [15]. In order to avoid the time-consuming expensive experimental probability of detection study, model assisted probability of detection is implemented for aluminum-epoxy single lap joints containing three different bonding quality. Five features depending on the frequency and amplitude response of ultrasonic inspection are considered as the signal response input in sensitivity analysis. It is shown that the reliability performance of debonding detection mostly depends on the gate selection and the ultrasonic amplitude response. Whereas, for weak bond detection, frequency based calculations and attenuation estimations are more important than amplitude based responses. MAPOD results agree with the previously obtained experimental results and demonstrate that it is

easier to detect debonding defects than weak bonds. In summary, the bonding quality in aircraft structures (composite and metal adhesive bonds) can be evaluated based on ultrasonic and electromagnetic thermal response parameters [11,12]. Also, comparison and data fusion for different techniques is reported for ultrasonic and electromagnetic NDT techniques [13,14]. Lastly, quantitative reliability analysis with the model based probability of detection curves is completed [15].

1. ADVANCED ULTRASONIC NDT FOR BONDING QUALITY EVALUATION

This chapter focuses on the relationship between ultrasonic parameters and the adhesive bonding quality. The bonding quality in carbon fiber composite-epoxy single lap joints was evaluated with numerical and experimental ultrasonic investigations. The novel post-processing algorithm that is able to detect weak bonds and debonding with high reliability is explained. This chapter is based on a review of the article *Advanced ultrasonic NDT for weak bond detection in composite-adhesive bonded structures* [11] that was written by the dissertation author Bengisu Yilmaz and co-author Elena Jasiuniene. The contribution from each co-author is reported at the end of the article. The first author as well as the corresponding author is the dissertation author, and she has developed the novel post processing algorithm to increase the detectability of weak bonds in composite adhesive joints and has applied the procedures to high-frequency ultrasonic investigations.

1.1. Numerical investigations

Developing advanced ultrasonic NDT techniques for adhesive bonding quality evaluation is a challenging task which requires several steps of investigation and innovation. In this work, the relationship between ultrasonic parameters and the bonding quality, including weak bond characteristics, is determined through numerical analysis and validated with experimental investigations. A novel post-processing algorithm to detect weak bonds and debonding in composite-adhesive single lap joints is implemented.

In order to determine the relationship between ultrasonic parameters and the adhesive bonding quality, wave propagation through different quality of bonding was simulated with semi analytical finite element (SAFE) based software *CIVA*. Three different conditions of bonding quality were investigated with 5 MHz central frequency contact pulse-echo ultrasonic testing. The Gaussian excitation signal is shown in **Fig. 1.1.1**.The non-defected model, also known as the perfect bond (PB), is represented where the composite adherend and the epoxy adhesive are completely in contact. The debonding (DB) defect is modeled as delamination at the top interface of the adhesive joint. The weak bond (WB) is simulated with an additional layer of thin liquid contamination between the adhesive and the top adherend interface. Two different composite-adhesive single-lap joint models were studied with different levels of adhesion and adherends: the thick model and the thin model. Meanwhile, the adherend and adhesive thickness for thick model is 5 mm and 1 mm, respectively; the thin model consists of 2.4 mm adherend and 0.15 mm adhesive. The model schematics and bonding quality representations are shown in **Fig. 1.1.2**. The thickness selection for the thick model is made to be able to decompose the ultrasonic echo signals from each interface, whereas the thin sample dimensions are chosen to be similar to the real case thickness.

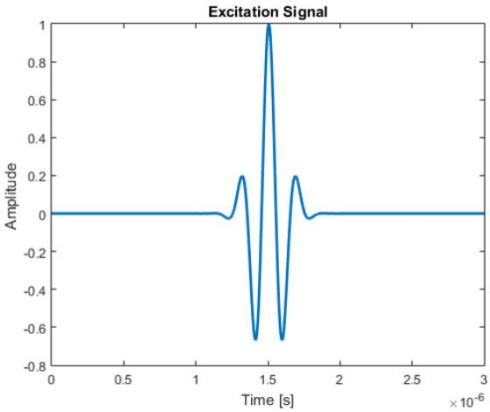

Fig. 1.1.1 Excitation signal used in the numerical model

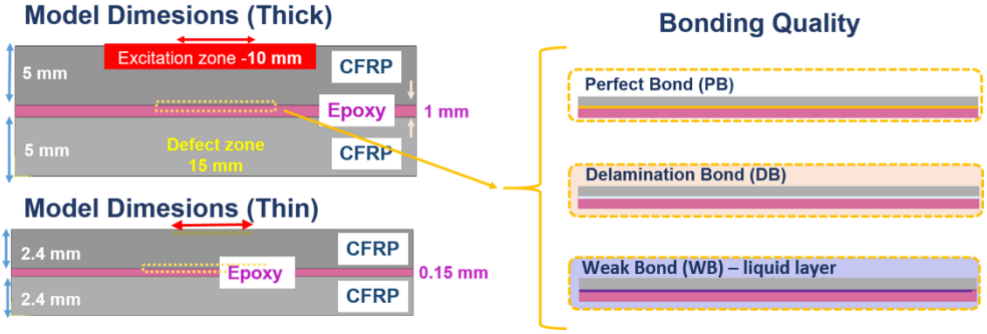

Fig. 1.1.2 Schematics of the thin and thick models and three bonding qualities that are simulated with ultrasonic wave propagation

The resulting ultrasonic pulse-echo responses that are calculated for the thick model with semi-analytical software *CIVA* are shown in **Fig. 1.1.3**. The ultrasonic amplitude response estimated by *CIVA* is calibrated – and not normalized – based on the highest response observed from the defect to obtain amplitude percentages. A-scan is divided into several time zones with longitudinal lines according to the time of flight calculations for each interface reflection, based on Formula (7), where ToF is the time-of-flight, Th is the thickness, and v is the acoustic wave velocity. On top of each divided zone, the schematic of the interface echo is shown. These schematics represent the corresponding interface reflections for the ultrasonic wave packet of interest. Specifically, the first interval indicates the surface reflection, the second interval is the reflection from the top interface of a single lap joint (the red continuous line), the third interface represents the bottom interface reflection (the blue dotted line), and so on. The thin model results are indicated in **Fig. 1.1.4**. As opposed to the thick model results, the thin model results indicate that the top and bottom reflection interface echoes are not separable. While the first ultrasonic wave packet echo received is a combination of the top reflection, the bottom reflection and a few multiple reflections within the adhesive layer; the second ultrasonic wave packet

consists of a double reflection at the top interface, a backwall echo and a double reflection at the bottom interface.

$$ToF = \frac{2 * Th}{v}. \tag{7}$$

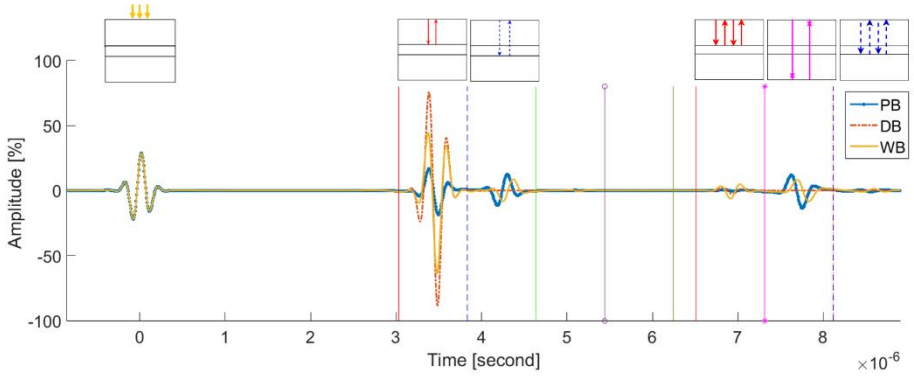

Fig. 1.1.3 A-scan SAFE results for thick CFRP bond

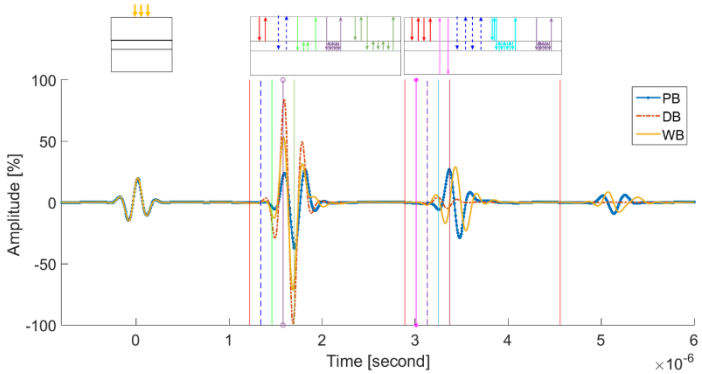

Fig. 1.1.4 A-scan SAFE results for thin CFRP bond

In order to compare the ultrasonic parameters, the first wave packet response after the surface reflection is investigated in the time and frequency domain for the thin and thick models (**Fig. 1.1.5**). For both models, the response amplitude in the time domain as well as in the frequency domain increases by the presence of debonding or a weak bond. It is also clearly seen that the frequency spectrum in the presence of debonding and a weak bond has widened, and that the central frequency of the maximum amplitude is shifted. The shift in the frequency of the maximum amplitude is usually associated with the attenuation of the specimen. The observed changes have similar effects in debonding and the weak bond, however, the amount of change is higher in the case of debonding than in the case of the weak bond.

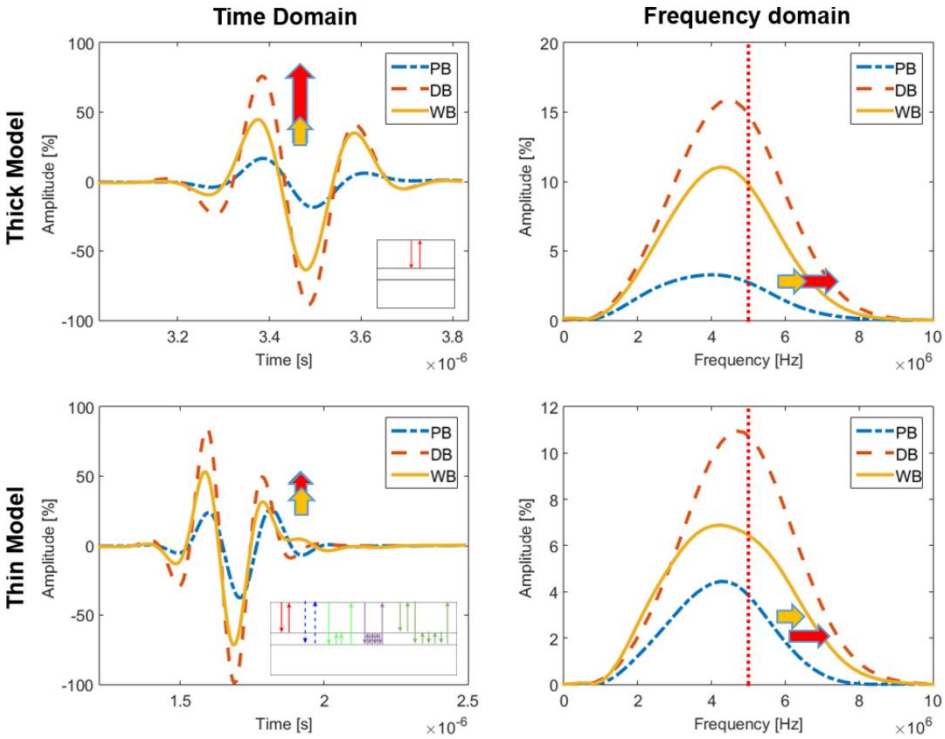

Fig. 1.1.5 First ultrasonic wave packet response in time domain and frequency domain for thick and thin models

The second ultrasonic wave packet after surface reflection for thin and thick models are investigated in detail (**Fig. 1.1.6**). It shows more variance in terms of the amplitude and phase responses than the previous case. Compared to the perfect bond, the weak bond response is shifted in the time domain for the thick and thin models; however, for the thin model, an almost completely opposite phase is observed. In the frequency domain, while there is some decrease in the amplitude and frequency shift on the weak bond case for the thick model, there is an increase of the amplitude in the thin case. For the case of debonding, the ultrasonic wave does not travel to the bottom interface because of complete blockage at the top interface. Hence, for this time interval, there is no response for the thick model. For the thin model, there are small variations in the time and frequency domains due to multiple reflections.

Based on numerical investigations, it is evident that there is a strong relationship between ultrasonic parameters and the adhesive bonding quality. Also, a comparison between thin and thick adhesive indicates that not only it is thickness dependent, but also the selection of the ultrasonic wavelength traveling through the structures plays a significant role when it is required to separate the top and bottom interface reflections, where the quality of adhesive bonding is has major impact on the output.

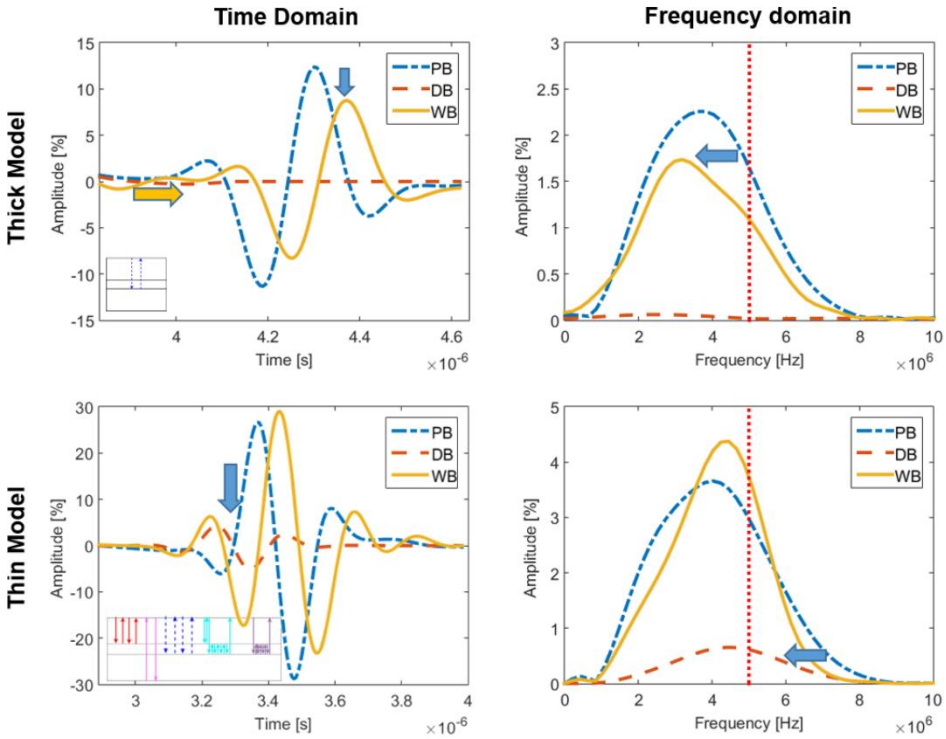

Fig. 1.1.6 Second ultrasonic wave packet response in time domain and frequency domain for thick and thin models

1.2. Experimental investigations

In the publication *Advanced ultrasonic NDT for weak bond detection in composite-adhesive bonded structures* [11], CFRP-epoxy single-lap joints containing three different levels bonding quality – debonding, a weak bond with less contamination, and weak bond with more contamination – in addition to the perfect bond were investigated with high-frequency high-resolution acoustic microscopy. Six layers of carbon-fiber reinforced epoxy from satin woven prepreg were selected as the adherend layers (120 mm length, 280 mm width, and 2.22 mm thickness). As commonly used in aerospace, structural adhesive film epoxy (25 mm length, 280 mm width and 0.24 mm thickness) is selected as the adhesive layer. A single-lap joint at the pristine state, also referred to the *perfect bond* (PB) is manufactured without any inclusion. In order to artificially represent debonding, two-folded release film square with 12.7 mm edge length is added at the adhesive-adherend interface prior to bonding. The weak bond is represented with 0.6 mL release agent contamination over the bonding area. Half of the bondline is masked during contamination addition, and referred to as the *weak bond-less contamination*. Non-masked part of the bonding area is called weak bond – more contamination. The region of interest (16.7 mm by 16.7 mm) was chosen at the bondline of each four levels of different levels of bonding quality. The focused transducer (3 mm diameter, 10 mm focal length and 50 MHz

central frequency) is selected for scanning acoustic microscopy. The ultrasonic pulse-echo response at the region of interest is recorded and used for post-processing.

In order to increase the debonding and contamination detection performance, a novel multi-level post-processing algorithm was developed (**Fig. 1.2.1**). Firstly, the advanced post-processing reduces the noise that is caused by a highly attenuating CFRP adherend and high frequency investigations. Then, the ultrasonic pulse-echo response signals are aligned according to surface reflection. Furthermore, the time window of interest is selected according to ToF calculations, and the signals are aligned at the maximum amplitudes within the chosen time window. Lastly, time and frequency domain based features are extracted as bonding quality features from ultrasonic pulse-echo responses. The selection of these features heavily depends on the changes observed in the ultrasonic pulse-echo response by performing numerical simulations. Four different interface visualizations were made with the extracted features (**Fig. 1.2.2**): C_{time} based on the time domain maximum amplitude, P_{time} based on the time domain phase shift of the maximum amplitude, $C_{frequency}$ based on the maximum amplitude observed in the frequency domain, $P_{frequency}$ based on the frequency shift of the maximum amplitude observed in the frequency domain.

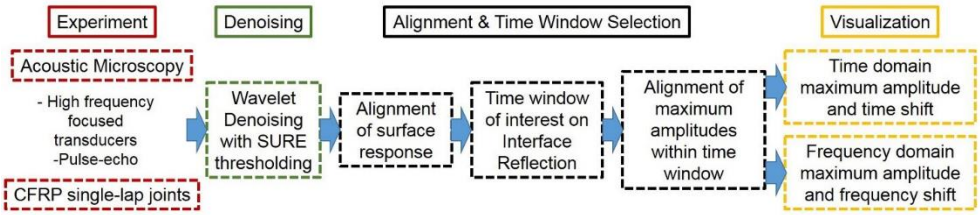

Fig. 1.2.1 System diagram for post-processing algorithm: experiment, denoising, alignment and time window selection, visualization [11]

C_{time}, similar to classical C-scan imaging, depends on the maximum ultrasonic response amplitude for each A-scan in the time domain within the determined time window. C_{time} visualization indicates no defect within the perfect bond, the square release film is clearly seen in debonding, and some deviation is observed for the weak bond with less contamination as well as the weak bond with more contamination, however, it is very difficult to label them as defected or low bonding quality samples.

P_{time} shows ToF deviations of the maximum amplitudes in the time domain within the chosen window of interest. , P_{time} visualizes the performance of the previously applied alignment algorithm. As seen in **Fig. 1.2.2**, having smaller values throughout the visualizations expresses that the alignment algorithm was reliably applied.

$C_{frequency}$ visualizes the bonding interface with the observed maximum amplitude after the frequency domain transformation. The interface visualizations for all bonding qualities are similar to the C_{time} imaging – which is expected since both are amplitude based visualizations, and the Fourier transform of the time domain data is amplitude dependent.

Each pixel value on $P_{frequency}$ images represents the frequency values that correspond to the observed maximum amplitude in the frequency domain. Perfect bond $P_{frequency}$ visualization exhibits that the sample is defect-free and that only small variations are detected due to the texture of the adhesive film layer. Meanwhile, artificial debonding can be clearly identified as a defect, weak bond contamination $P_{frequency}$ interface visualization reveals defective zones on the interface. Compared to the weak bond less contamination $P_{frequency}$ image, the weak bond more contamination $P_{frequency}$ image shows fewer defective zones.

These four different advanced novel interface visualization techniques were also evaluated quantitatively with the *bonding characteristic values* (BCV) – that is the mean-square likelihood of the observed values to the maximum observed value. The calculated BCV reflects the defect likelihood in each visualization because the maximum observed value corresponds to the high ultrasonic impedance difference at the interface. BCV values are reported on top of each interface visualization (**Fig. 1.2.2**). BCVs are in line with the qualitative image analysis and indicate that weak bond detection can be improved with the frequency phase based visualization $P_{frequency}$. Generally, the results show that high frequency focused transducers used in acoustic microscopy are a great choice to visualize the interface quality in bonded structures. Also, the developed post-processing algorithm performs well on the detection of the weak bond and is independent from the perfect bond inspection results.

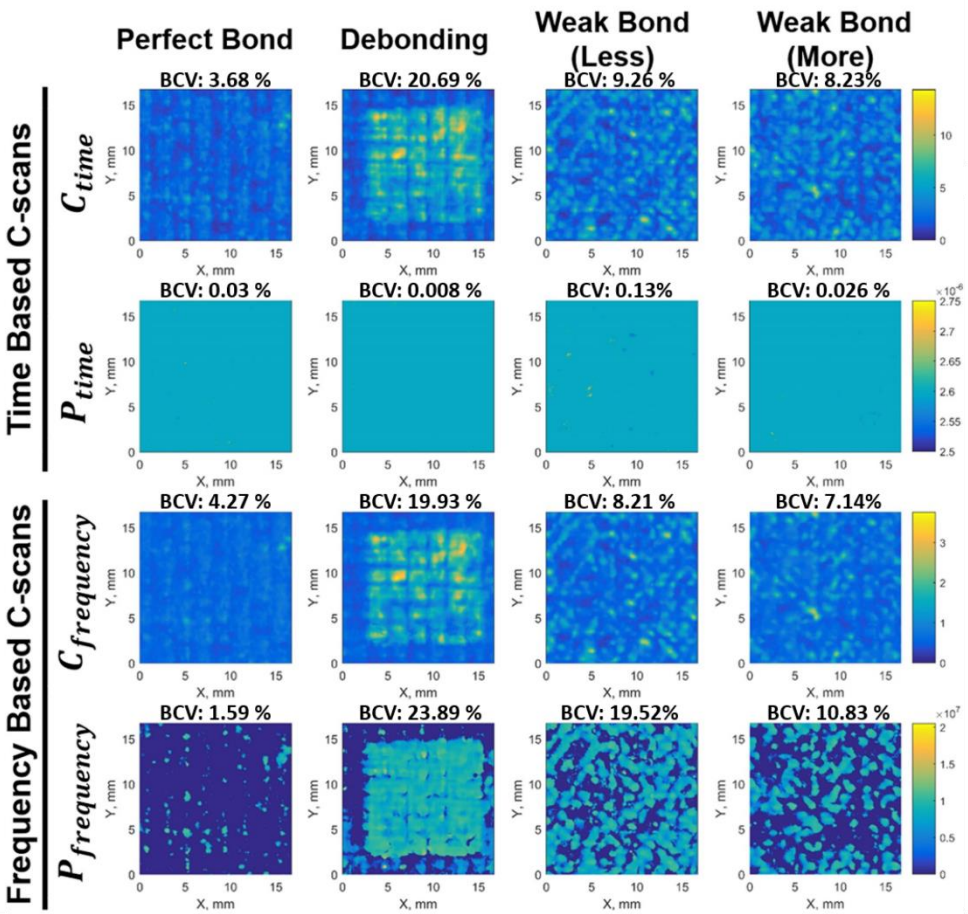

Fig. 1.2.2 Interface visualization with four different types of feature extraction [11]

1.3. Conclusions for Chapter 1

1. Based on numerical investigations, it was discovered that there is powerful relationship between the ultrasonic parameters and the adhesive bonding quality. Also, our comparison between the thin and thick numerical models indicates that not only the thickness of each layer but also the selection of the ultrasonic wavelength traveling through the structures plays a significant role when separating top and bottom interface reflections – where the adhesive bonding quality is strongly effective.
2. Among the four different extracted features, P_{time} visualization with low bonding characteristics values (BCV) values (less than 1%) shows that the alignment algorithm performed well in all cases of bonding quality. It is also seen that C_{time} and similarly $C_{frequency}$ demonstrate the defect presence for debonding clearly (debonding BCV is 4 to 5 times of the perfect bond), however their performance on weak bond detection is low (the weak bond BCV is 1 to 2 times of the perfect bond). On the other hand, $P_{frequency}$, as a result of the novel

post-processing algorithm, can visualize with higher accuracy the release agent contamination at the bonding interface, which might cause weak bonds (the weak bond BCV is 5 to 10 times of the perfect bond).

3. $P_{frequency}$ interface visualizations obtained by using the developed algorithm demonstrate that the less contaminated regions (BCV:19.52%) show two times more defective zones than the more contaminated regions (BCV:10.83%). It is expected that the diffusion of the release agent into the adhesive film was more dominant at the more contaminated regions of the sample; on the contrary, the less contaminated regions had more release agent on the interface.
4. It was shown that the novel post-processing algorithm extracts more information on the evaluation of bonding quality. By implementing the novel algorithm, the difference from the perfect bond is increased 3 times for debonding, and 3 to 6 times for weak bonds. The presented results prove that the high-frequency acoustic microscopy with the developed post-processing algorithm is a great candidate to evaluate the bonding quality and to detect weak bonds which occur due to bonding interface contamination. However, the limitations regarding structure dimensions and water immersion should be noted.

2. ADVANCED INNDUCTION THERMOGRAHY NDT FOR BONDING QUALITY EVALUATION

This chapter focuses on the relationship between electromagnetic (including thermography) parameters and adhesive bonding quality. In addition to the ultrasonic parameters discussed in the previous chapter, bonding quality relationship to electrical and thermal parameter was investigated in this chapter. Specifically, carbon fiber composite-epoxy single lap joints were evaluated with numerical and experimental eddy-current (induction) thermography investigations. The novel post-processing algorithm that is able to detect weak bonds and debonding is explained. This chapter is based on the review of the article *Evaluation of debonding in CFRP-epoxy adhesive single-lap joints using eddy current pulse-compression thermography* [12] which was written by the dissertation author Bengisu Yilmaz and her co-authors Qiuji Yi, Gui Yin Tian, Hamed Malekmohammadi, Stefano Laureti, Marco Ricci and Elena Jasiuniene. The third author is the dissertation author, and she contributed on the advanced post-processing of the data, the development of the feature extraction algorithm, the determination of the relationship between the extracted features and the bonding quality properties in both thermal and electrical parameters.

2.1. Numerical investigations

Adhesive bonding quality evaluation with electromagnetic NDT techniques is a challenging task that needs several steps of analysis. In this work, the finite element method (FEM) is used to simulate the electromagnetic and thermal response of a composite-adhesive single-lap joint with a brass debonding inclusion [92]. Active thermography with eddy current, also known as induction, is considered as the investigation technique. Six layer CFRP adherends bonded with 25 mm epoxy bondline were modeled with FEM. Square brass film inclusions with 12.7 mm edge length were modeled as artificial debonding at the adhesive adherend interface. Induction thermography simulation included the coupled electromagnetic and thermal problem [58,93]. Weak electromagnetic $\mathbf{A} - \varphi$ and nodal thermal formulations were used to calculate the eddy currents and temperature distribution on the surface of the specimen.

During the simulation, electromagnetic and thermal parameters were selected based on prior knowledge and the investigated material's data sheet. For the eddy current, an induction coil with five turns was placed behind the bondline with a 2 mm lift-off distance between the coil and the adhesive bonding (**Fig. 2.1.1**). In order to optimize the defect detection with the temperature evaluation curve, several measurement parameters of the electromagnetic field, such as the activation time, the activation current, the coil dimensions and the number of turns,were studied. The optimum power output was observed with the activation current selection being at 600 Amperes, and the frequency should be kept at minimum 100 kHz on the eddy-current system.

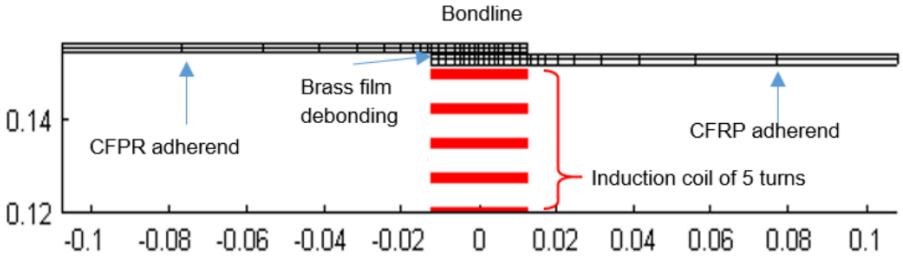

Fig. 2.1.1 Schematic of induction thermography modeling for composite-adhesive bond, side view

Furthermore, temporal evolution curves simulated for the optimized measurement parameters were studied. Two conditions, the defect free region with the perfect bond and debonding with the brass inclusion, were considered to be of interest. The brass film was selected for this simulation due to its high electrical conductivity. The simulated temperature at the surface at a frequency of 100 kHz and current 600 A is shown in **Fig. 2.1.2**, where the perfect bond is represented with the blue curve, and the brass debonding is shown with the red curve. In the simulation, the current was run for 2 seconds. The evolution of the temperature at the surface was calculated for one minute (60 seconds). As it is shown in **Fig. 2.1.2**, the temperature of the surface with a defect reached its maximum when the time was at 6 seconds, and the difference between the defect free case was the highest over almost the entire measurement period. In **Fig. 2.1.3**, the temporal evolution of the temperature at the middle of the brass film is shown. The brass film was heated well when the generator was running. The temperature reached its maximum when the time was equal to 2 seconds (the heating time). The maximum temperature was evaluated as 35 °C. After the generator was closed, the temperature at the middle of the metal foil began to decrease due to thermal convection.

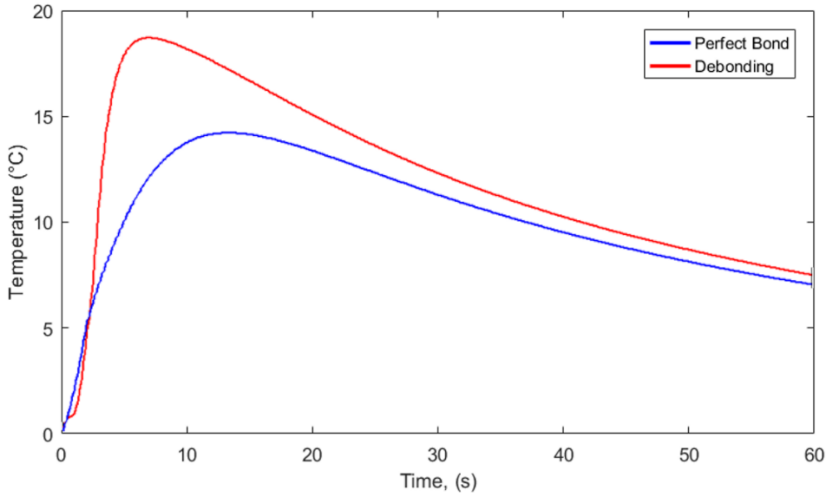

Fig. 2.1.2 Temporal evolution of the temperature at the center of the defect upper face, with and without defect presence [92]

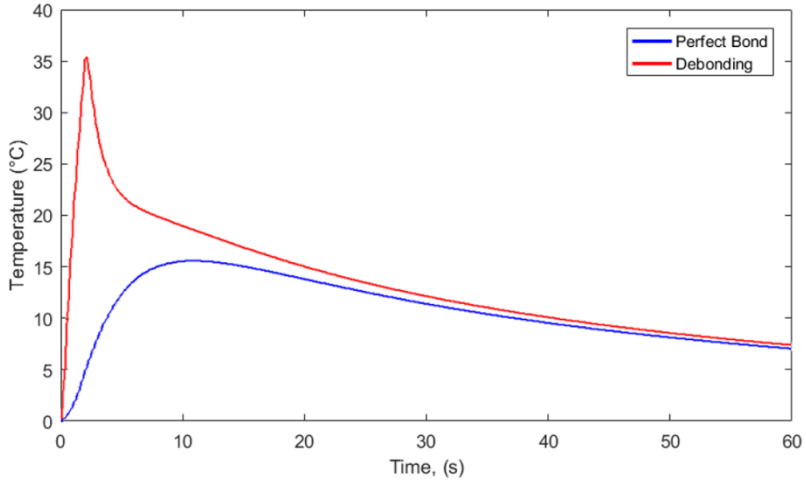

Fig. 2.1.3 Temporal evolution of the temperature at the middle of brass film [92]

2.2. Experimental investigations

Although eddy current thermography has such advantages as being a non-contact, responsive and fast NDT technique, numerical investigations suggested the that high contrast between the defect and the defect free zones can only be achieved by the optimized measurement parameters. In the publication *Evaluation of debonding in CFRP-epoxy adhesive single-lap joints using eddy current pulse-compression thermography* [12], composite-adhesive bonded structures with various types of interface contamination were studied with eddy-current pulse-compression thermography. Particularly, CFRP-epoxy single lap joints containing artificial

debonding with a release film, a brass film in addition to the weak bond representation of release agent contamination were investigated. Multi-level signal processing was applied in order to correlate the physical properties, such as the contamination depth, size and conductivity, with the observed electromagnetic and thermal response.

Firstly, the Barker code with the pulse compression technique was implemented for the inspection of bonded structures with eddy current thermography. Pulse compression – the impulse response of the recorded data calculated by the convolution of the matched filter – is known to be an improved level of resolution in the signals of RADAR and ultrasonic applications as well as in eddy current thermography. In eddy current pulse compression thermography (ECPuCT), the sample is excited with coded excitation (40 Amperes and 240 kHz carrier frequency in order not to damage the sample) (in this case with Barker Code No. 13 (BC)), and thermal images were collected for the overall time duration of heating and cooling with an infrared camera at a 50 frame per second recording rate. The step heating was removed from the recorded thermal response, and the convolution matched filter was applied (**Fig. 2.2.1**). The main advantage of ECPuCT compared to the classical eddy current thermography is that the impulse response can be estimated by delivering energy to the system in a significantly longer time. This flexibility can be exploited as, in the evaluation of cases of bonding quality, we can increase the signal to noise ratio by providing more energy than in the eddy current thermography experiments, or this allows us to use lower power heating sources while maintaining the same signal to noise ratio level.

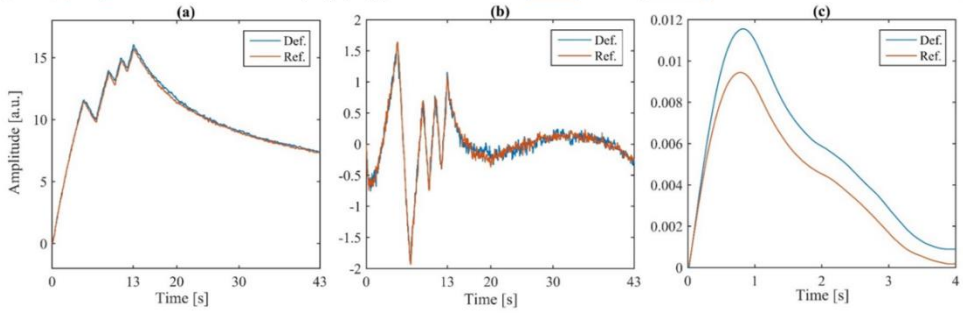

Fig. 2.2.1 Example signals for a reference point on the pristine state (perfect bond) and on the contaminated area (brass inclusion): (a) acquired raw signal, (b) raw signal after removal of step heating contribution, (c) impulse response after the pulse compression process [12]

During the next step, two different algorithms were applied to remove the non-uniform heating pattern that is caused by the material anisotropy and the coil shape: the perfect bond subtraction and the partial least square method. In order to remove the non-uniform heating pattern with the perfect bond subtraction method, a defect free sample was investigated with ECPuCT, then the perfect bond results are subtracted directly from the results of bonding with different contaminations. As the second method, the partial last square (PLS) technique was used to remove non-uniform heating. Three main steps were followed for the PLS technique: the recorded three-dimensional thermography data (x, y and time) reshaped into a two-dimensional set; partial least squares were calculated; partial least squares corresponding to non-uniform heating were removed, and the data was reconstructed.

In order to extract the relevant information on the bonding quality, the impulse responses were analyzed with sliding time windows. Within these windows, kernel based principal component analysis (K-PCA) projected image was calculated in order to determine the features that are correlated with the contamination size, depth and conductivity. The verification of the best image showing the contamination or the artificial defect was done with the derivatives and the time phase images of impulse response.

The size of different artificial debondings was estimated with spatial kurtosis. Kurtosis is a distribution shape based feature which is related to the tailedness of the data of interest. Brass film artificial debonding of two different sizes was determined by plotting the sum of special kurtosis values over the selected area (**Fig. 2.2.2**), while it is difficult to determine the exact sizes of debonding two peaks over the Gaussian curve. The size of artificial debonding with two identical defects was determined with kurtosis values as seen in **Fig. 2.2.3**. In this case, the Gaussian peaks are more separable, and the kurtosis values are similar to each other.

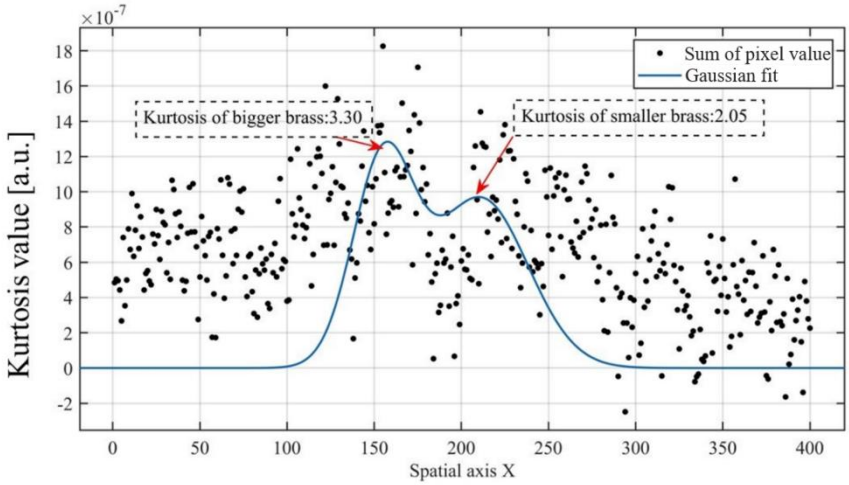

Fig. 2.2.2 Results for spatial kurtosis for sizing of bigger and smaller brass films [12]

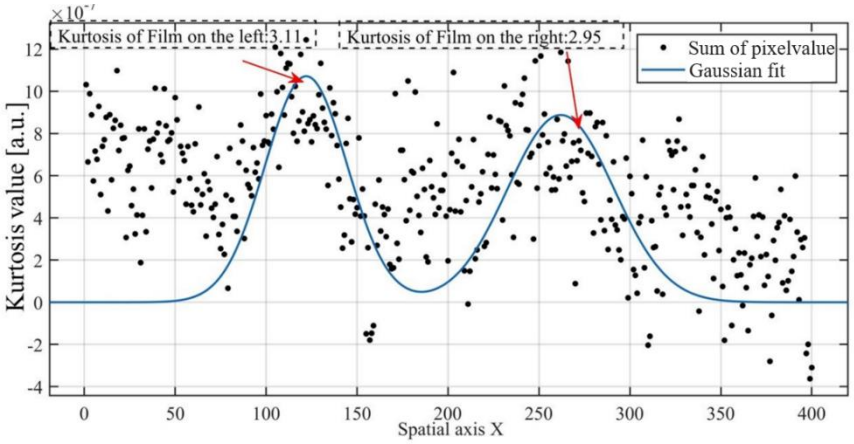

Fig. 2.2.3 Results of spatial kurtosis for sizing of release film artificial debondings [12]

Then, the depth of the contamination and the conductivity level were estimated based on the derivatives and the time-phase images of the impulse response along with the norm of the first kernel based principal component within the time window. **Fig. 2.2.4** shows that, while electrical conductivity is dominant in the first 15 frames, thermal conductivity takes the lead after 60 frames (the cooling stage). Since brass is an electrically conductive material, the electromagnetic response for the artificial brass debonding defect has the highest derivative during the first 15 frames. The thermal reflection time is observed to be similar for each defect where the defect depth is correlated in the same way for each specimen – since each artificial defect is placed at the same depth from the surface.

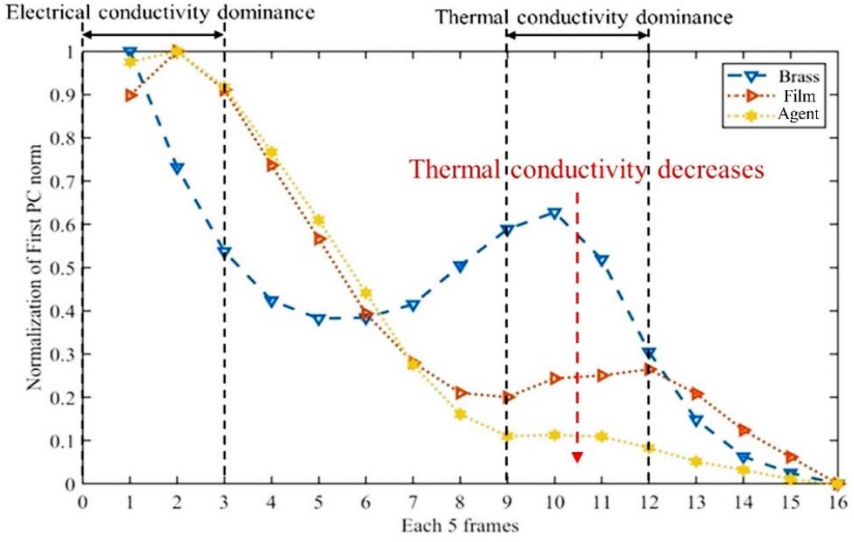

Fig. 2.2.4 First PC norm of different contaminations versus number of 5 frames (sliding window); where brass is debonding brass inclusion, film is release film debonding and agent is release agent contamination [12]

2.3. Conclusions of Chapter 2

1. Numerical investigations were used to evaluate the detectability of artificial brass film debonding at the composite-adhesive interface with eddy current thermography. It was shown that the electromagnetic (excitation frequency, heating current) and thermal (heating time, observation time etc.) parameters have to be optimized in order to achieve detectability with a high contrast. The results show that the maximum defect contrast can be achieved only in small time intervals.
2. Experimental investigations focused on the detection and evaluation of different contaminations in separate composite-adhesive single-lap joints with eddy current pulse compression thermography in order to optimize a high contrast in the defect response. Three physical features related to contamination, namely, the size, the depth and the conductivity, are determined by implementing the novel post-processing algorithm.
3. Experiments have established that partial least square subtraction of non-uniform heating performs better than perfect bond subtraction because, on the contrary to perfect bond subtraction, no spatial misalignment of experiments can affect the procedure.
4. After the successful implementation of the proposed novel post-processing algorithm, the sliding K-PCA features and the norm of principle component can differentiate the contamination layer in the heating and cooling stages. The first instant high contrast happens at the very beginning (first 300 ms) of the retrieved impulse responses due to the Joule heating effect in CFRP. This first instants indicate the difference in the electrical properties of contamination in adhesive joints. It has also been verified that the 60^{th} frame contains the maximum information about the contamination's thermal properties in the cooling stage.
5. It has been shown that contamination within the adhesive bond can be classified by using the derivatives of the impulse response at a specific time. While the release agent (10% change) has the minimum influence on the electrical and thermal properties compared to the brass film (50% change) and the release film (25% thermal, 10% electrical change), the thermal properties are more indicative in terms of detection of weak bonds due to the release agent than electrical properties.

3. COMPARISON OF DIFFERENT ULTRASONIC NDT TECHNIQUES FOR BONDING QUALITY EVALUATION

While in the previous chapters the determination of ultrasonic, electromagnetic and thermal parameters related to different types of inclusions in composite-adhesive bonds was investigated with the single NDT technique, this chapter focuses on the detailed comparison of different ultrasonic NDT techniques for debonding detection and sizing in metal-adhesive joints. Debonding is one of the most commonly occurring defects in adhesive joints that can lead to premature failures. This work demonstrates the application possibilities of different ultrasonic NDT techniques for the detection of debonding in aluminum-epoxy single-lap joints. While most of the aircraft components are gradually replaced by composite materials, a big percentage of the aircraft structures are still made of aluminum, hence there is need to develop NDT techniques for modern joining methodologies, such as adhesive bonding.

Artificial debonding placed in aluminum-epoxy single lap joints was investigated with a wide variety of inspection frequencies in air-coupled, contact, and immersion ultrasonic testing. This chapter is based on a review of the article *Air-coupled, contact and immersion ultrasonic nondestructive testing: comparison for bonding quality evaluation* [13] written by the dissertation author Bengisu Yilmaz and co-authors Aadhik Asokkumar, Elena Jasiuniene and Rymantas Jonas Kazys. The contribution from each co-author is reported at the end of the article. The first author as well as the corresponding author is the dissertation author, and she contributed by developing numerical models of the adhesive joint as well as by implementing a novel defect sizing error comparison technique based on ultrasonic wavelength.

3.1. Materials and ultrasonic testing

In the publication *Air-coupled, contact and immersion ultrasonic nondestructive testing: comparison for bonding quality evaluation* [13], various ultrasonic testing techniques were compared in the case of debonding detection metal-adhesive single lap joints. Specifically, aluminum-epoxy-aluminum single lap joints containing five square two-fold artificial debonding defects (12.7 mm edge length) placed at the interface were investigated with ultrasonic bulk waves when using the immersion through transmission, the immersion pulse-echo, the high frequency acoustic microscopy, and the air-coupled through-transmission techniques. In addition to the conventional bulk wave ultrasound, guided wave testing was also performed with two different set-ups: the contact-to-contact transducer, air-coupled excitation to the contact transducer.

For immersion pulse-echo and immersion through transmission inspections, 10 MHz focused transducers were selected, and the distance from one transducer to the sample has kept at 43.29 mm in order to focus at the interface where the debonding defects were located. In scanning acoustic microscopy (SAM) experiments, the adhesive bond was investigated with a 50 MHz focused transducer which was placed 2.94 mm away from the joint surface. The air-coupled ultrasonic through transmission method was tested by using 300 KHz flat transducers, and the sample was placed right after the end of the calculated near field.

Prior to conducting guided wave inspections, dispersion curves for the aluminum adherend plate were calculated. Also, a numerical study was performed with the three-dimensional finite element method on the aluminum-epoxy joint model with debonding. Ultrasonic wave propagation was simulated as excited with an air-coupled transducer and received with contact coupling. The numerical simulation results guided us to choose the experimental set-up parameters and identify the guided wave mode generation. Hence, the distance between the air-coupled and the contact transducer was set to 65 mm, and the angle of air-coupled excitation was kept at 10° to generate the A0 mode of guided waves. Similarly, contact-to-contact guided wave inspections were performed by keeping the distance between the two transducers at 100 mm.

The comparison of the ultrasonic NDT techniques that are used in the case study are given with their capabilities and limitations in **Table 3.1**. The advantages of immersion testing include megahertz range testing frequencies (up to 100 MHz with scanning acoustic microscopy), easy coupling with water, less wear of the probes, and easy focus for ultrasonic beams; however, it is limited for the types of materials and defects because water immersion might threaten the structural integrity and can cause corrosion. On the other hand, air-coupled testing offers purely non-contact inspection within the 50 kHz to 2 MHz testing frequency range and a possibility to focus the ultrasonic beam. Unfortunately, air-coupling causes high drops in the ultrasonic amplitude and relatively low signal to noise ratios due to impedance mismatch. Hence, air-coupled ultrasonic testing is usually applied as through transmission instead of pulse-echo. Contact testing with guided waves can operate up to 5 MHz, and it enables faster acquisition and superior coupling than air-coupled testing, yet it requires complex set-ups for angle excitations, transducers as well as structure surface may wear off due to the constant contact and difficult to inspect large areas. Furthermore, air-coupled excitation to contact reception for guided wave inspection can provide long-range inspection with the possibility of mode selection, but the signal to noise ratios are lower than those of contact-to-contact guided wave inspections.

Table 3.1 Comparison of different techniques [13]

Techniques	Capabilities	Limitations
Immersion testing	MHz range operating frequency, coupling uniformity, less wear for probes, focused beams	Limited materials due to corrosion
Air-coupled testing	50 kHz to 2 MHz operating frequency, contactless coupling, focused beams	High attenuation loss at higher frequencies, lower signal to noise ratio due to acoustic mismatch
Contact testing	Up to 5 MHz operating frequency, ability for faster inspection than air coupled, superior coupling over immersion and air-coupled methods hence higher transmissibility	Wear of transducers and material due to contact Requires special set-up for angle excitation

Air coupled excitation and contact reception of guided waves	Possibility of mode selection, directional wave front, long-range inspection	Lower signal to noise ratio

3.2. Results

In this work, a wide variety range of inspection frequencies resulting in different ultrasonic wavelengths, have been investigated.

Defect detection performance yielded better results in terms of immersion techniques than the air-coupled and contact methods. All the five debonding defects were separately identified with the immersion techniques and SAM, four were identified with the air-coupled through transmission technique. The last defect was close to the edge of the sample where the active part of the transducer was exposed outside the plate boundary; hence, the ultrasonic wave was directly transmitted to the receiver. Guided wave inspection with air-coupled excitation detected three defects, whilst four defects were identified with the guided wave contact to contact transducer method. A defect that is placed close to the edge is difficult to detect with guided wave ultrasonics because of the boundary reflections.

For each ultrasonic inspection technique, A-scan and the visualization of defects were reported, and the defect sizes were determined with the decibel drop methodology. According to this technique, the normalized amplitude from the observed C-scan or B-scan is crossed with a horizontal line at the desired decibel drop. For immersion ultrasonic NDT and SAM, C-scan images were used to visualize debonding at the bonding interface; therefore, the slice is selected at the middle of the defects (**Fig. 3.2.1**). For air coupled through transmission C-scans and guided wave generated B-scans, the slice was selected at the highest defect contrast observed (**Fig. 3.2.1**). The decibel dropping line and normalized values for each inspection are shown in **Fig. 3.2.2**. For all inspections except for air-coupled through transmission, -6dB decibel drop was used to calculate the defect size. The air-coupled through transmission defect sizing was performed with -12dB decibel drop due to unexpected positive interference on the edge defect (defect center is located around 40 mm on X axis).

Furthermore, according to the known defect size (12.7 mm), absolute errors were calculated for each technique while considering each defect. The average values of the calculated errors are shown in a bar graph with uncertainty (**Fig. 3.2.3**). According to the calculated related errors, the immersion techniques and SAM can size defects with higher precision than the air-coupled and contact techniques. Compared to the guided wave inspections, the air coupled through transmission shows almost a half of the relative error in defect sizing. Among the guided wave techniques, the contact-to-contact method offers better performance in determining the defect size than the air-coupled to contact method. However, the defect detection performance for the contact-to-contact method is inconsistent among the four detected defects.

Considering the ultrasonic wavelength traveling through an aluminum joint, the defect sizing performance of each NDT technique was normalized. This novel quantitative comparison depends on the ratio of the average absolute defect sizing

errors and the ultrasonic wavelength. It was shown that in between the immersion techniques and SAM, the immersion through transmission technique involves the lowest error, hence offering the highest performance. The air coupled through transmission indicates lower error values than the guided wave inspections. The contact to contact method performs better than the air-coupled to contact method. This method makes the immersion technique performance comparable to the air-coupled, guided wave and contact ultrasonic inspection. It is evident that, while the precision is very high in the SAM results, the defect sizing error per wavelength is higher than in the other techniques. It can be explained by the magnification of error due to the small wavelength transmission.

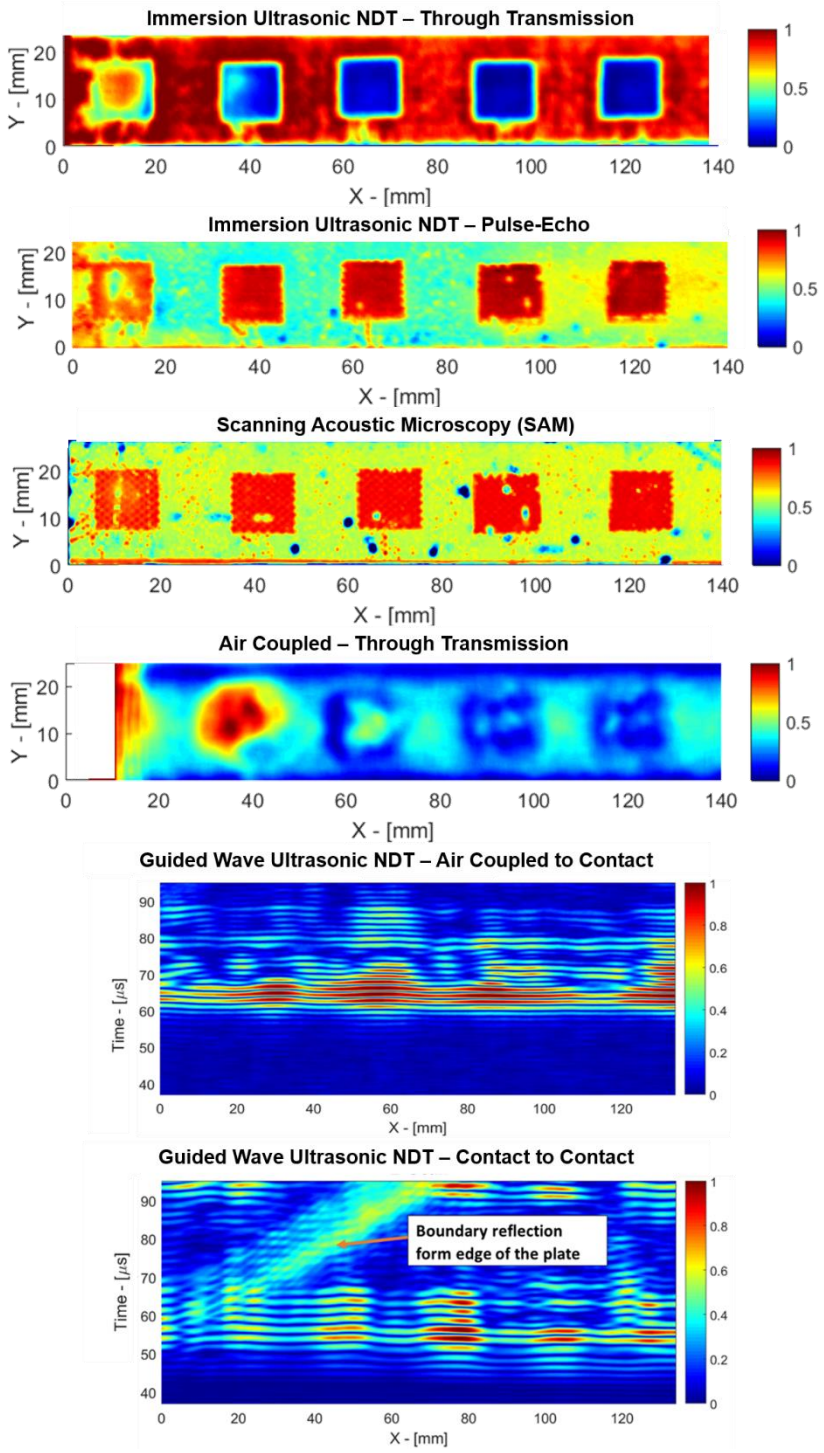

Fig. 3.2.1 C-scan and B-scan results for ultrasonic NDT inspections [13]

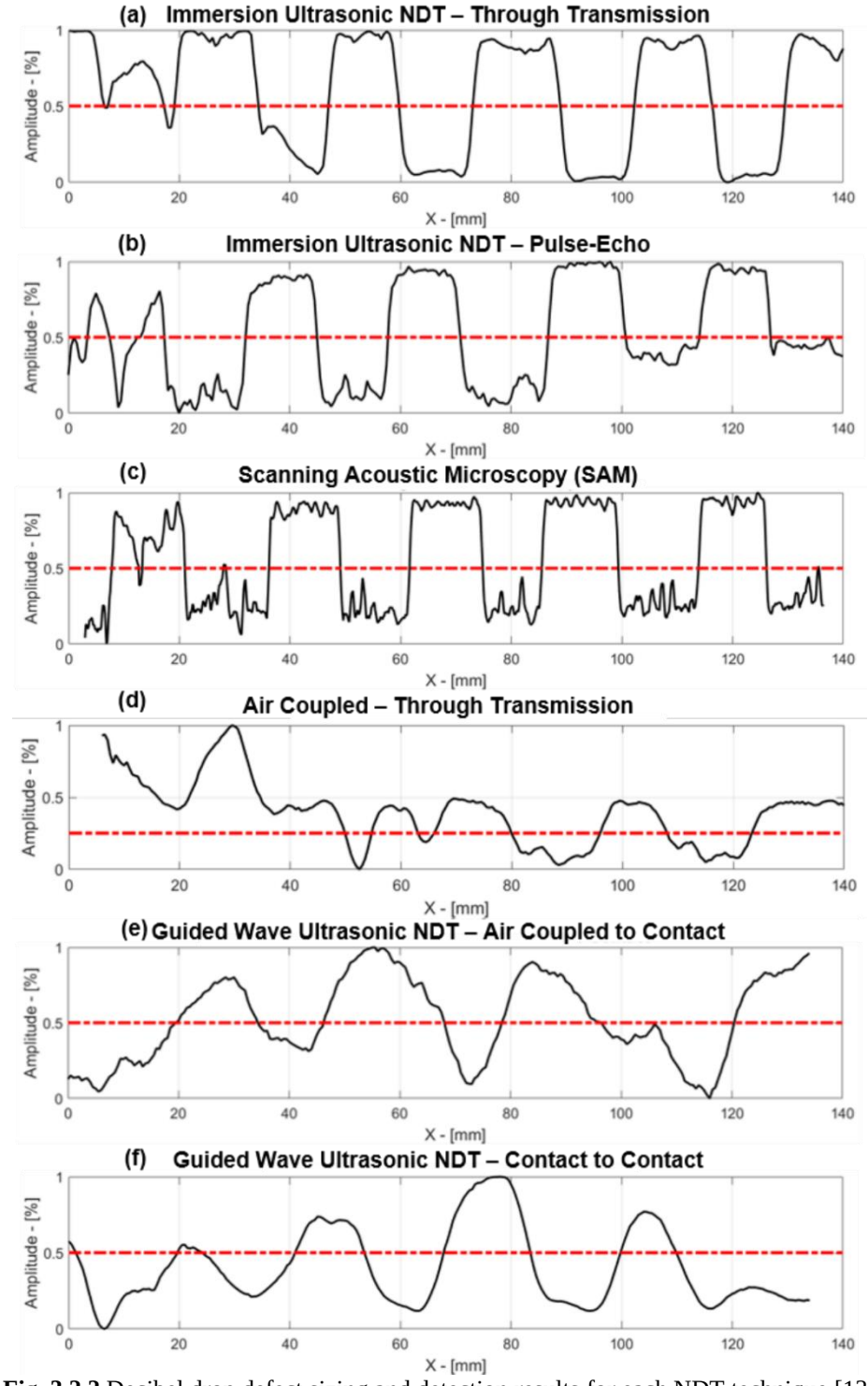

Fig. 3.2.2 Decibel drop defect sizing and detection results for each NDT technique [13]

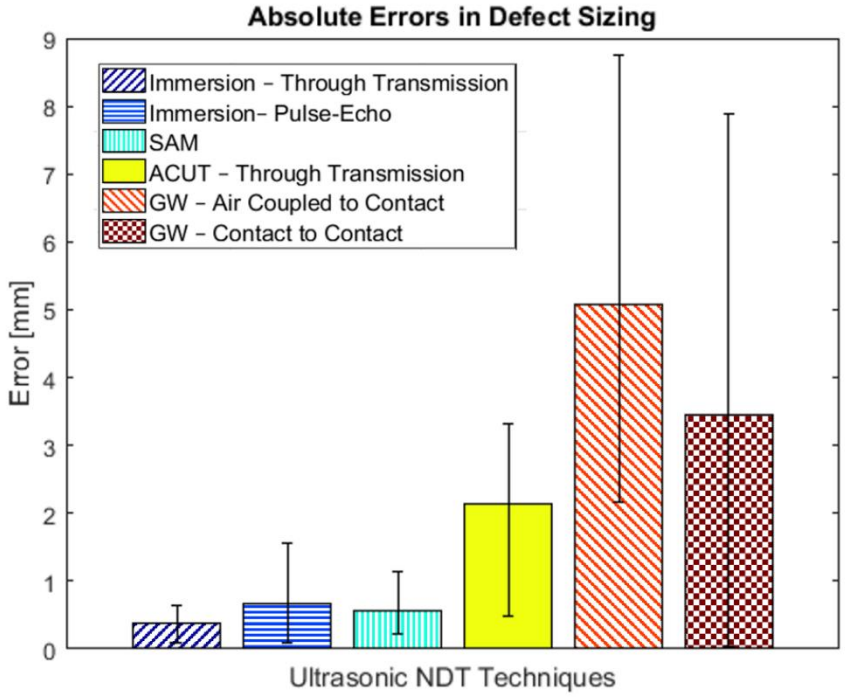

Fig. 3.2.3 Defect sizing errors in absolute values for each ultrasonic NDT technique

3.3. Conclusions for Chapter 3

1. The relative change in the recorded ultrasonic amplitude is an important criterion for different nondestructive testing techniques: for through transmission bulk wave inspection, the defect presence decreases the received amplitude, while in the case of guided waves and pulse-echo inspections, the amplitude increases when passing through a defect.
2. The bulk wave results show that the higher frequencies from 10 MHz to 50 MHz in the immersion testing perform significantly better in the case of defect detection as well as defect sizing when compared to air-coupled testing using 300 kHz. Whereas contact-to-contact guided wave inspections at 300 kHz show relatively lower accuracy in defect sizing, they are good enough to detect the presence of four out of five cases of debonding. Air coupled to contact guided wave inspection offers the lowest performance in terms of defect detection and defect sizing.
3. With error sizing calculations, the best performance is observed in the immersion through transmission technique (an average error is less than 0.5 mm), however, the high performance for SAM (less than 1 mm average error) and air-coupled through transmission (less than 3 mm average error) cannot be disregarded.

4. Immersion ultrasonic techniques and SAM achieve high precision in defect detection and sizing (all the five defects were detected with an error not exceeding 2 mm), however, the bonded structure needs to be immersed in water. Also, inspection systems are non-transportable and expensive. Although the air-coupled ultrasonic methods achieve less precision than the immersion techniques (3–4 defects were detected), they allow non-contact inspection. Since the air coupled through transmission technique requires two-sided inspection, guided wave inspections can be chosen for rapid or in-situ applications.

4. DATA FUSION OF ADVANCED ULTRASONIC NDT AND INDUCTION THERMOGRAPHY FOR BONDING QUALITY EVALUATION

This chapter focuses on the data fusion of ultrasonic immersion pulse-echo testing and induction thermography for determining different sizes and materials of artificial debonding placed in CFRP-epoxy single lap joints. As our comparison of ultrasonic NDT techniques in the previous chapter justified, each technique has indisputable advantages and limitations. In this chapter, NDT techniques which had already show promising results in debonding detection within composite-adhesive joints were synthesized with data fusion post-processing techniques. This chapter is based on a review of the article *Evaluation of bonding quality with advanced NDT and data fusion* [14] which was written by the dissertation author Bengisu Yilmaz and co-authors Abdoulaye Ba, Huu-Kien Bui, Elena Jasiuniene and Gerard Berthiau. The contribution from each co-author is reported at the end of the article. The first author as well as the corresponding author is the dissertation author, and she contributed by developing advanced post-processing algorithms for induction thermography investigations, as well as by developing, implementing, and evaluating data fusion techniques for the ultrasonic and induction thermography nondestructive evaluation of adhesive bonding quality.

4.1. Materials and NDT methods

In the publication *Evaluation of bonding quality with advanced NDT and data fusion* [14], composite-adhesive single lap joints containing three different cases of artificial debonding were investigated with pulse-echo ultrasonic inspection and induction thermography.

Two CFRP adherends where each of them was built of six layers of woven (satin weave) were bonded together with a structural epoxy film after surface preparation. The artificial debonding defects were introduced prior to bonding by putting two-folded square films on the epoxy adhesive layer. Three different debonding conditions were considered to be of interest: debonding with a release film (a two-folded square with 12.7 mm edge length and 0.063 mm thickness), debonding with a brass film (a two-folded square with 12.7 edge length and 0.05 mm thickness), small debonding with a brass film (a two-folded square with 6.35 mm edge length and 0.005 mm thickness).

Composite-adhesive single lap joints containing three different cases of artificial debonding were investigated with ultrasonic immersion pulse-echo NDT and transmission induction thermography separately.

Ultrasonic investigations were performed with a focused transducer having 10 MHz central frequency in the pulse-echo immersion settings. The distance between the transducer and the adhesive bond has kept at 46.3 mm so that to place the ultrasonic focus on the adhesive bonding line. The whole bonding area was scanned with the directional immersion set-up, and A-scans were saved with a 0.5 mm step-size.

Induction thermography (eddy current stimulated active thermography) was used for the investigation of composite-adhesive single-lap joints in the transmission mode – thus, the sample was placed in between the coil and the camera. The induction coil (helical design, inner diameter 15 mm, outer diameter 25 mm, height 30 mm, five turns) was oriented in such a way that the coil center was centering the defect location. During the experiments, 105 kHz carrier frequency was achieved by 200 Amperes excitation power of 1 second. Starting from the excitation, an infrared camera recorded the temperature variance of the sample surface with 25 frames per second for a 60-second period.

4.2. Data fusion results and evaluation

Data fusion is a post-processing method which synthesizes the data collected by multiple sources in order to improve the accuracy of the information. In this work, the raw data that was collected by two different NDT systems was pre-processed in order to satisfy the requirement of compatibility in data fusion. Multi-level pre-processing methods were applied to both ultrasonic NDT and induction thermography results.

Raw data of ultrasonic inspection consisted of local Cartesian coordinates (x, y) and the time of flight response; similarly, induction thermography results were three dimensional datasets with local Cartesian coordinates (x, y) and the time of recording. Firstly, in order to minimize the error multiplication due to noise, the raw data was filtered. Ultrasonic and induction thermography inspections took place in different environments, hence, the local coordinates for each inspection were transferred to a global matching coordinate system. While point-by-point matching on some coordinates was achieved by this transformation, the data needed to be scaled for complete alignment across the dataset. Therefore, ultrasonic data was interpolated to match the same coordinate values, and the recorded data was re-centered in the registration step. Then, the resulting ultrasonic and thermography datasets were normalized from 0 to 1.

After completing the pre-processing of the data for data fusion, based on an advanced processing algorithm, the feature matrices were extracted from the ultrasonic and thermography inspection results. For ultrasonic inspection, the extracted feature was selected as the interface reflection peak-to-peak amplitude, and, for the induction thermography response, the principal component analysis was applied. The extracted features were put into the data fusion application as a source.

Six different data fusion algorithms were applied on the extracted feature matrices on the pixel level, namely: average, difference, weighted average (1UT5TH), weighted average (5UT1TH), Hadamard product, and Dempster-Shafer rule of combination.

One of the many basic fusion methods – average – depends on the sum of two source values divided by half. The second basic fusion technique is the difference which represents the inverse correlation between two sources. The weighted average algorithm – where one data set is taken as five times more and imported in the sum of averages – was applied for ultrasonic data (5UT1TH) as well as for thermography data (1UT5TH) algorithms. Moreover, the Hadamard product, which is a simple

algebraic operation based on pixel-wise multiplication of same-size matrices, was used as a data fusion method.

As an information theory based data fusion method, the Dempster-Shafer (DS) rule of combination was applied on the dataset. While the DS theory treats the information from multiple sources as evidence of multiple events, the DS rule of combination lets us estimate unique mass evidence for a hypothesis by the evidence masses. In this work, these hypotheses were defected (positive), not defected (negative) and unsure if defected or not (doubt). DS combinations were calculated with the orthogonal sum of different hypotheses from each source which feature matrices obtained from ultrasonic inspection and thermography experiments. Three hypotheses – positive, doubt, and negative – were selected according to the cross-section of the local amplitude distribution over the global Gaussian of the feature matrix. The local distribution was calculated with the pixels and the values of the surrounding (8) pixels. DS also allows us to calculate contradiction percentage which indicates the source compatibility regarding the given task of defect detection.

The results for three different categories of interface debonding that were obtained with the feature matrix extraction from ultrasonic and thermography data as well as data fusion applications were evaluated both qualitatively and quantitatively. Interface visualizations where the defect must be present were reported for debonding with a release film, debonding with brass inclusion, and debonding with small brass inclusion. Quantitative comparison of each NDT technique and data fusion was reported with the area under response operating characteristic (ROC) curves – which shows the correlation between false positive rates and true positive rates calculated based on the known location and size of the debonding. The normalized interface visualizations were divided into 100 threshold values changing from 0 to 1. For each specific threshold value, the main characteristics were estimated:

- True positive (TP): total number of pixel values which are greater than the threshold within the defect position.
- False negative (FN): total number of pixel values which are smaller than the threshold within the defect position.
- True negative (TN): total number of pixel values which are smaller than the threshold outside of the defect position.
- False positive (FP): total number of pixel values which are greater than the threshold outside of the defect position.

According to this calculation, the true positive ratio (TPR) and the false positive ratios (FPR) are calculated by using Formula (8) and Formula (9). ROC curves were obtained by plotting false positive rates to true positive rates.

$$TPR = \frac{TP}{TP + FN}, \tag{8}$$

$$FPR = \frac{FP}{FP + TN}. \tag{9}$$

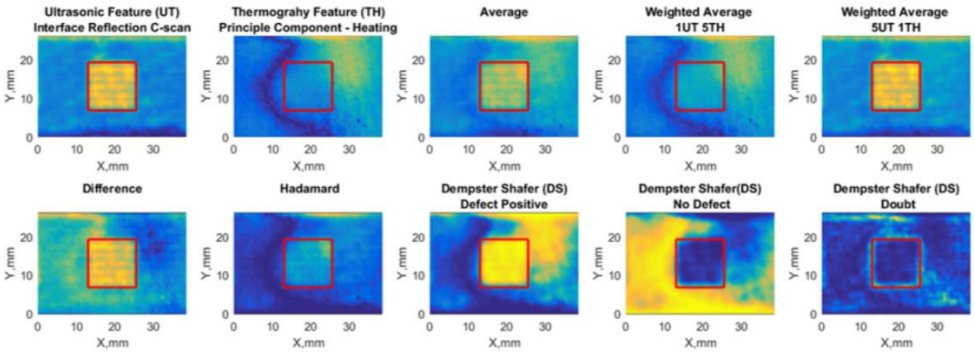

Fig. 4.2.1 Ultrasonic feature, thermography feature and data fusion results for release film debonding defect

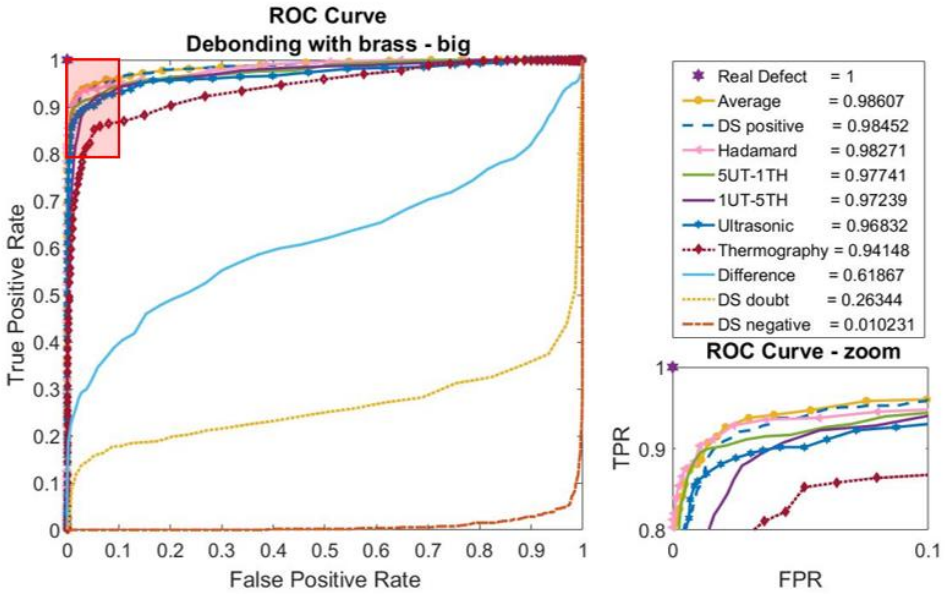

Fig. 4.2.2 ROC curve response of different features and data fusion results for release film debonding defect

For the visualizations of debonding with a release film, the ultrasonic feature is the best among all as it shows the defect region with a higher amplitude response than the surroundings (**Fig. 4.2.1**). No significant defect contrast was observed with induction thermography. With the averaging data fusion, the results got smoothened, but the observed defect contrast is much higher in the weighted average 5UT-1TH than for the other fusion results The difference fusion matrix shows a relatively high performance level on defect detection. The Hadamard fusion indicates a very low performance level in defect detection while DS performs well but delivers too many false positives. The area under ROC curve calculations is in line with the qualitative results and the ultrasonic feature has the highest performance with the follow-up of the weighted average 5UT-1TH, difference, and the average (**Fig. 4.2.2**).

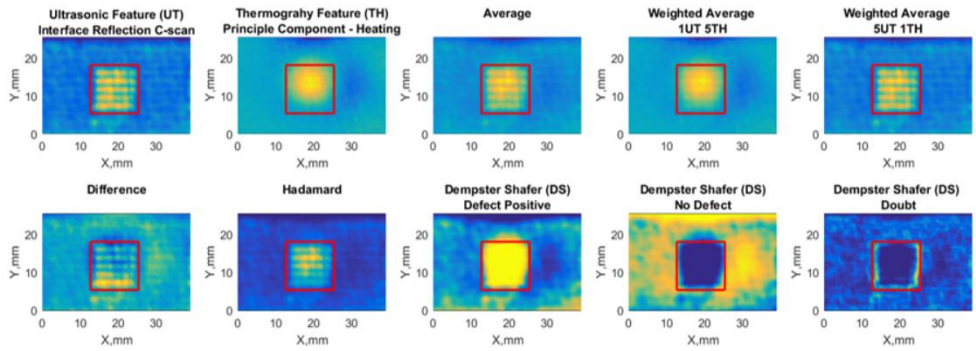

Fig. 4.2.3 Ultrasonic feature, thermography feature and data fusion results for big (12.7 mm) brass inclusion defect

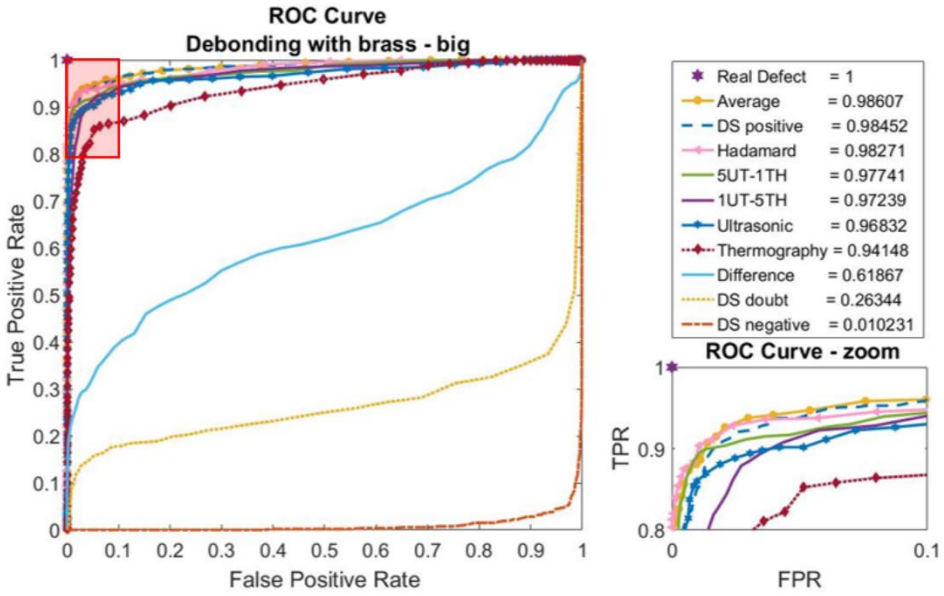

Fig. 4.2.4 ROC curve response of different features and data fusion results for big (12.7 mm) brass inclusion defect

Advanced NDT and data fusion results for debonding with brass inclusion (the large window) indicates that defect contrast has been achieved for all methods, while the information theory based DS performs the best (**Fig. 4.2.3**). The calculations for the quantitative area under the ROC curve also show that almost all features ranked similar values, and they were effective in defect detection (**Fig. 4.2.4**). Difference calculation shows low values, which indicates that no contradiction is observed between the sources.

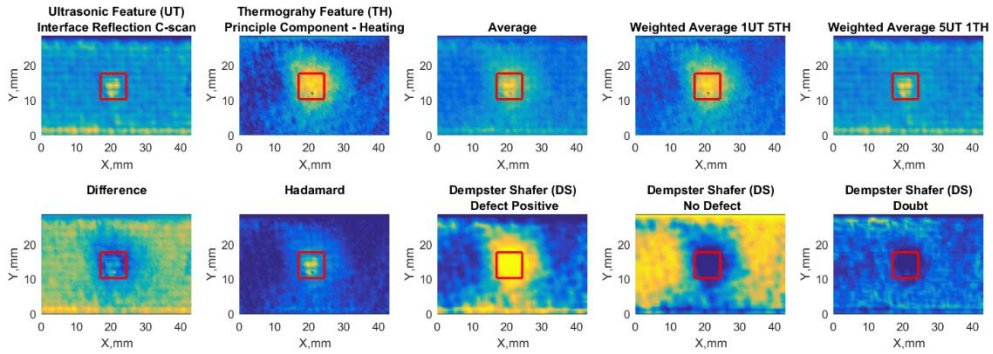

Fig. 4.2.5 Ultrasonic feature, thermography feature and data fusion results for small brass inclusion defect

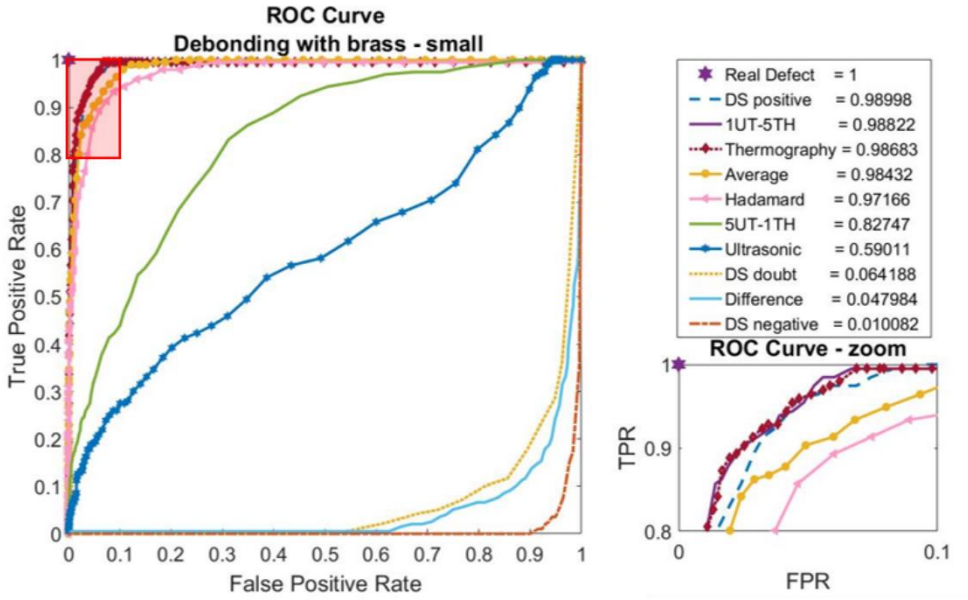

Fig. 4.2.6 ROC curve response of different features and data fusion results for small brass inclusion defect

Nondestructive evaluation results for adhesive bonding containing debonding with small brass film suggested that ultrasonic and induction thermography NDT features can detect the presence of a defect; while false negative ratios were present in the ultrasonic technique, false positives were effective in the induction thermography results (**Fig. 4.2.5**). The difference data fusion suggests that there is no contradiction in between the NDT techniques. According to the area under the ROC curve values, the ultrasonic feature and the weighted average with 5UT-1TH do not perform well in comparison to other options (**Fig. 4.2.6**). The DS-positive option seems to deliver the highest contrast in quantitative and qualitative analysis.

4.3. Conclusions of Chapter 4

1. For composite-adhesive single lap joints, the ultrasonic immersion pulse-echo NDT technique has advantages for debonding detection whereas induction thermography NDT only performs well when detecting electrically conductive inclusion.
2. It is evident that the quality of artificial debonding with small (6.35 mm) brass (electrically conductive material) elements in adhesive bonding can be better detected with induction thermography (AUC:0.98) than with the ultrasonic pulse-echo immersion NDT method (AUC:0.59).
3. Data fusion improves the performance of non-destructive evaluation if and only if the sources are not in contradiction.
4. Considering all the three studied different inclusions, the information theory-based fusion algorithm, the Dempster-Shafer rule of combination (AUC:0.98), and the Hadamard (AUC>0.97) method shows high performance, however, the performance of averaging (AUC>0.98) cannot be disregarded.
5. Nondestructive evaluation of adhesive bonding quality is a challenging task, but as long as the sources do not contradict each other, according to the area under the ROC curve, the calculation of data fusion increases the sensitivity and specificity of the inspection.

5. QUANTITATIVE RELIABILITY ANALYSIS OF ADVANCED ULTRASONIC NDT FOR BONDING QUALITY EVALUATION

This chapter focuses on the quantitative reliability assessment of advanced ultrasonic nondestructive testing for adhesive bonding quality evaluation. Probability of detection curves for high frequency ultrasonic evaluation of aluminum-epoxy single lap joints were estimated with a novel and cost-effective model based approach. The novel feature based interface visualization algorithm developed in the article *Advanced ultrasonic NDT for weak bond detection in composite-adhesive bonded structures* [11], as discussed in the first chapter, was applied to metal-adhesive single lap joins. The reliability of each proposed feature was evaluated with the model based probability of detection curves in terms of debonding and weak bond detection. This chapter is based on a review of the article *Model assisted reliability assessment for adhesive bonding quality evaluation with advanced ultrasonic NDT* [15] which was written by the dissertation author Bengisu Yilmaz and co-authors Damira Smagulova and Elena Jasiuniene. The contribution from each co-author is reported at the end of the article. The first author as well as the corresponding author is the dissertation author, and she contributed by implementing the developed advanced post-processing algorithms for probability of detection curve estimations, as well as by determining and implementing the characteristic values for nondestructive evaluation of weak bonds.

5.1. Materials and methods

In the publication *Model assisted reliability assessment for adhesive bonding quality evaluation with advanced ultrasonic NDT* [15], the reliability of advanced acoustic microcopy investigations in bonding quality evaluation was estimated with the model assisted probability of detection curves. Aluminum-epoxy-aluminum single lap joints with three bonding quality conditions were considered to be of interest for the reliability evaluation. Two identical 1.6 mm thick aluminum sheets were bonded with a structural adhesive epoxy film after surface preparation. As the pristine state reference, one sample was produced with the nominal settings; it was called the *perfect bond* (PB). In order to demonstrate debonding defects, two-fold release films were placed at the adhesive-adherend interface prior to bonding, which we refer to as *debonding* (DB). Additionally, release agent contamination was sprayed over the epoxy film in order to deteriorate the bonding quality, and we refer to it as *weak bond due to release agent* (WB-RA). In order to represent the possible deviations in the manufacturing protocol, the curing cycle for bonding epoxy was altered by reducing the curing temperature, and the samples were referred to as *weak bond due to faulty curing* (WB-FC).

In order to evaluate the reliability of aluminum-epoxy single lap joints with different levels of bonding quality, scanning acoustic microscopy (SAM) was selected as the ultrasonic nondestructive evaluation technique. The samples were investigated with the pulse-echo immersion technique in room temperature (25°C). A focused transducer (PT-50-3-10) of 50 MHz central frequency, 10 mm focal depth and 3 mm diameter was used for investigations. The distance between the transducer and the

sample was kept at 2.94 mm. The experimental results for PB, DB, WB-RA and WB-FC were saved and used in this work in order to validate numerical simulation results.

In order to build model assisted probability of detection (MAPOD) curves, several steps were taken, as shown in **Fig. 5.1.1**. At the first step, numerical models were built to represent adhesive bonding and different bonding quality conditions by using the semi-analytical finite element method based software CIVA. Adhesive bonding was simulated as a three-layered structure representing the same thickness and material properties of the sample: an aluminum adherend with a thickness of 1.6 mm and a longitudinal acoustic wave velocity of 6300 m/s, an epoxy adhesive of 0.16 mm thickness and a longitudinal acoustic wave velocity of 2990 m/s. To simulate ultrasonic wave propagation, a focused transducer was modeled (PT-50-3-10), and the excitation signal was selected as the reference recorded signal with the experimental set-up. The interface quality between the adhesive and the adherend was selected as connected for PB, whereas the delamination defect was placed at the interface layer for the DB case. The WB-RA model was represented with a thin oil layer inclusion at the interface. In the case of WB-FC, it was considered that the epoxy acoustic wave velocity was affected by the faulty curing. The numerical model results were calculated in two-dimension for each case of bonding quality, and the ultrasonic response in time and frequency domain was validated by similar behavior observed in experimental investigations.

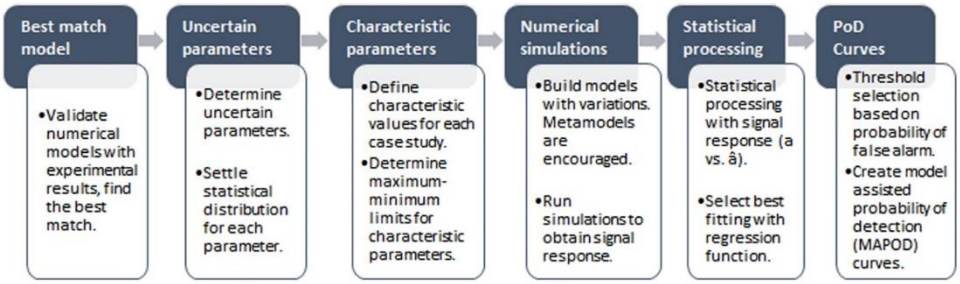

Fig. 5.1.1 Steps to obtain model assisted probability of detection curves [15]

As a second step to obtain MAPOD curves, uncertain parameters and their statistical distribution were determined. The uncertain parameters are the parameters that might be variant due to the specimen based, experimental, environmental, or human factors. In this work, eight influential parameters are marked as uncertain parameters, namely, epoxy thickness, epoxy acoustic velocity (longitudinal), aluminum thickness, aluminum acoustic wave velocity (longitudinal), water path, acoustic velocity of water, incidence angle, and defect position in depth. The distributions of each parameter were determined according to expert knowledge and experimental investigations (**Fig. 5.1.2**).

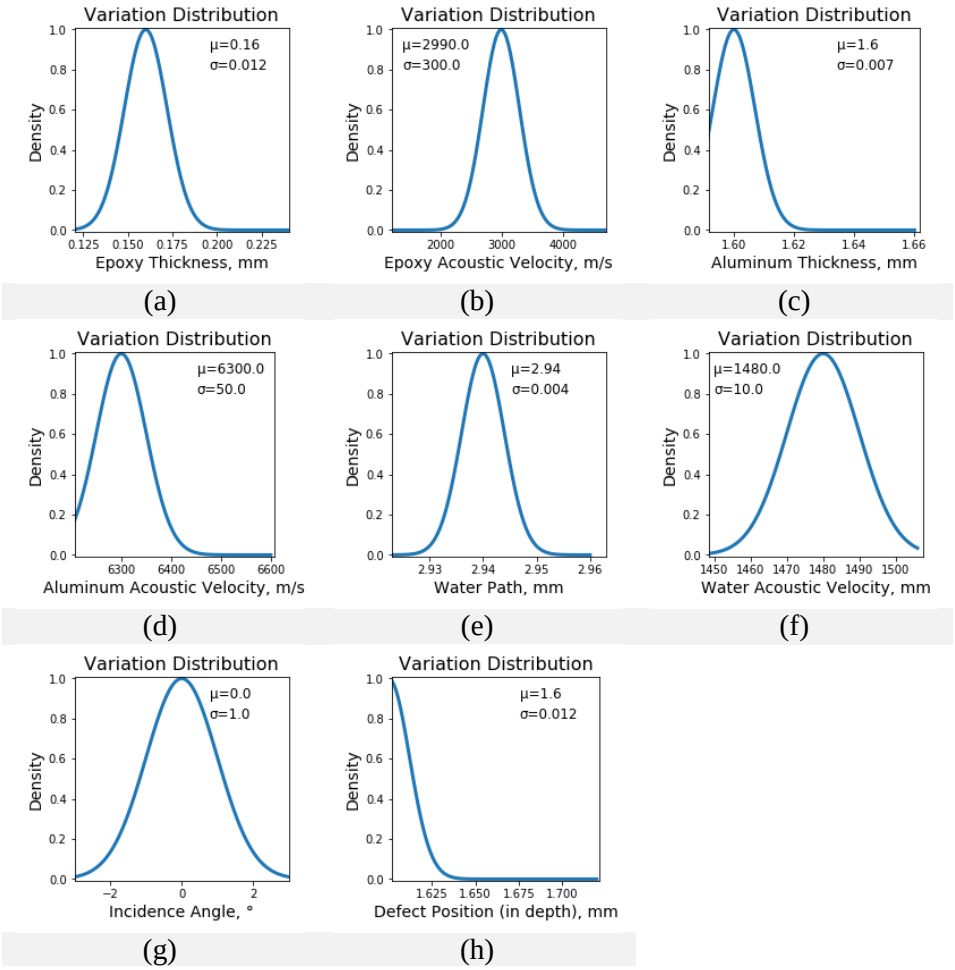

Fig. 5.1.2 Uncertain parameters and their statistical distribution: a) epoxy thickness, b) epoxy acoustic velocity, c) aluminum thickness, d) aluminum acoustic velocity, e) water path, f) water acoustic velocity, g) incidence angle of the transducer, h) defect position

In addition to the uncertain parameters, MAPOD calculations require characteristic values to be determined. Conventionally, the characteristic value for PoD curves was selected as the defect size that is under investigation. When considering the complexity of the bonding quality analysis and the physical reasons behind the weakening of the joint, the characteristic value for each case of bonding quality was determined. In the case of the debonding model (DB), debonding was represented with zero-thickness rectangular delamination placed at the interface; therefore, the defect size is considered as the characteristic value. For the weak bond due to release agent models (WB-RA), the thickness of oil addition was selected as the characteristic value. The characteristic value for the weak bond due to faulty curing (WB-FC) was decided as the epoxy acoustic velocity because epoxy properties are significantly affected by poor curing caused by elasticity changes. The limits to

the characteristic values were put in terms of physical behavior and observation based on experimental investigations.

Since the full factorial design of eight uncertain parameters and the characteristic value with a reasonable step-size in the defined limits would lead to extreme costs in terms of computational power, the validated numerical models were used to build metamodels which are mathematical approximations so that to reduce the computation time of a high degree of freedom of numerical simulations. Each metamodel was calculated with Kriging regression analysis over more than 1000 calculated data points.

Five different feature extraction algorithms were selected as the signal response in metamodel calculations in order to incorporate the advance ultrasonic post-processing algorithm:

- Peak to peak amplitude at the specified gate (Peak to Peak Amplitude);
- Time delay of absolute maximum amplitude (Time Delay);
- Maximum amplitude in frequency domain (Frequency Amax);
- Frequency shift of absolute maximum amplitude (Frequency Shift);
- Attenuation at the adhesive layer (Attenuation).

All of these features were estimated within the selected time gate over ultrasonic A-scan results. In numerical modeling, the surface reflection was not considered to be of interest. Since the bonding quality information mostly lies in the interface echoes, the gate of interest was selected considering the echoes from the top (first) and the bottom (second) epoxy interface. What concerns the case of debonding, the first interface reflection mostly represents the defect reflection which is selected in DB-OPTION1. In order to decrease the false-positive rates, a special gate selection algorithm was proposed and applied (DB-OPTION2). Normally (DB-OPTION1), the gate starts before the first interface reflection. In DB-OPTION2, if the maximum amplitude of the signal response envelope is less than 100 percent and the second reflection is observed, then the gate is placed at the second interface reflection. For the weak bond due to the release agent WB-RA and the weak bond due to faulty curing WB-FC, the second reflection (the wave packet observed after the top interface reflection) is of interest.

In order to obtain MAPOD curves, data plots based on each metamodel were created in the *CIVA* software thereby representing five features for three cases of bonding quality. In this step, the best fit of transformation combinations (logarithmic, normal, boxcox) was chosen based on the Berens' hypothesis and the calculated residual values. Outlier data points were put under 'noise' and 'saturation' in order to minimize the fitting errors and satisfy Beren's validity on linearity, homoscedasticity, normality, and variance.

One of the most influential parameters in MAPOD creation is the threshold selection. In this work, the Threshold values were selected by minimizing the probability of false alarms and taking the most of the response signal for all the five features and three bonding qualities. As referenced by many researchers, MH-1823 suggests that no probability of detection is considered to be sufficient if the probability of a false alarm is not calculated [75]. Most of the applications probability of false alarms (PFA) were calculated by comparing the results with the observed noise. In

this study, PFA is determined by building variation studies with the adhesive bonding holding no defect – which is also called the *perfect bond* (PB).

5.2. MAPOD results

The reliability of detecting debonding and a weak bond due to a release agent and a weak bond due to faulty curing of aluminum-epoxy single-lap joints was estimated based on numerical simulations. The model based probability of detection curves is reported for three different bonding qualities and five different features in **Fig. 5.2.1**.

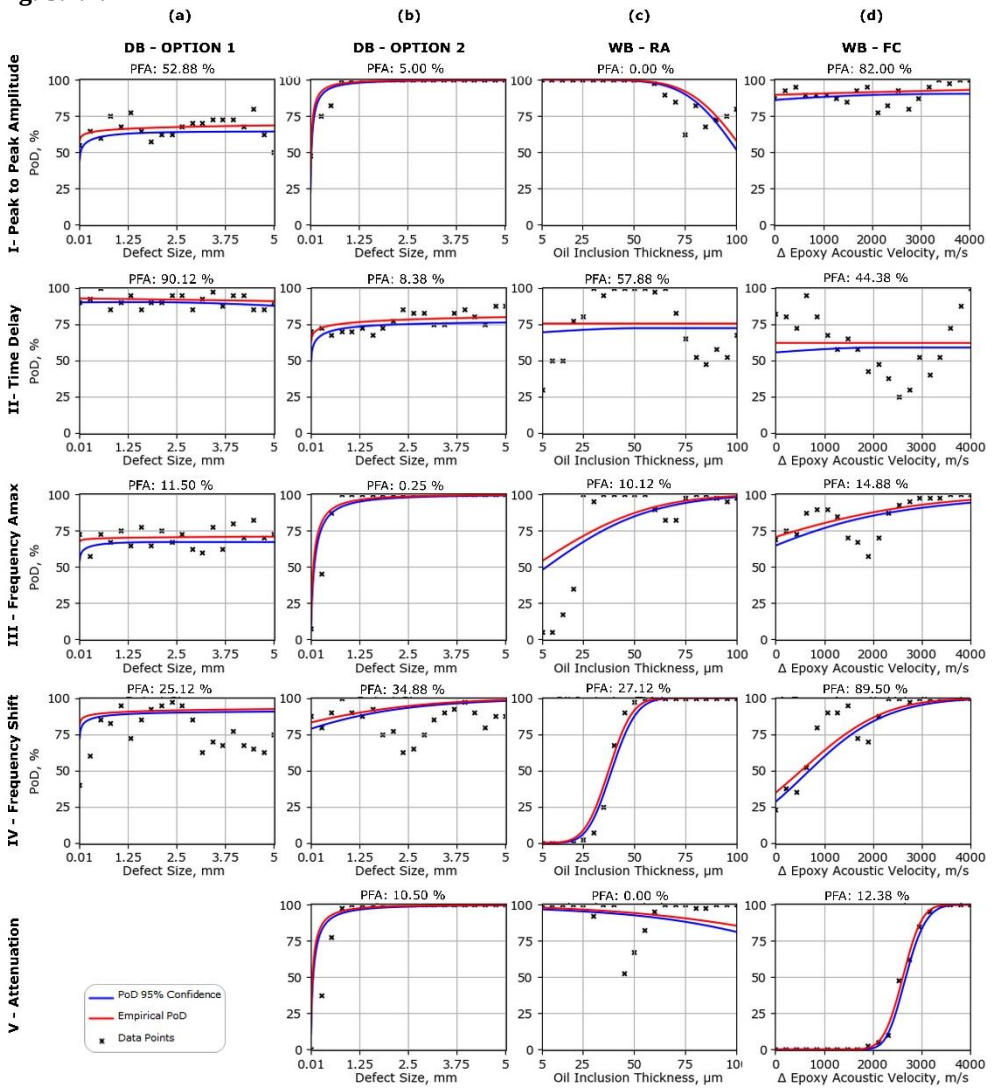

Fig. 5.2.1 Estimated MAPOD curves along with PFA values for four different bonding quality cases: (a) debonding DB-OPTION1, (b) debonding DB-OPTION2, (c) weak bond due to release agent WB–RA, (d) weak bond due to faulty curing WB–FC; considering five

signal response features on the rows I – peak to peak amplitude, II – time delay, III – frequency Amax, IV – frequency shift, V – attenuation [15]

The reliability of debonding detection was estimated with MAPOD while firstly considering the gate selection at the maximum observed amplitude (DB-OPTION1), then the smart gate algorithm was applied (DB-OPTION2). In DB-OPTION1, none of the MAPOD curves reached the critical stage where $a_{90/95}$can be calculated (**Fig. 5.2.1**-a). The PFA values for the peak to peak amplitude response was estimated to be as high as 53%, whereas in the time delay response, it nearly reached 90%. This is expected to be in relation to the gate selection related high level false positives. Compared to DB-OPTION1, DB-OPTION2 increased the reliability of detecting debonding in adhesive joints significantly (**Fig. 5.2.1**-b). Except from the time-delay response, it was observed that all other features can reach 100% probability of detection with the 5 mm defect size. Additionally, PFA values are significantly low – almost all features would deliver predictions with less than 10% false alarms.

The weak bond due to release agent case (WB-RA) was represented with the oil thickness as a characteristic value from 5 to 100 μm (**Fig. 5.2.1**-c). While the peak-to-peak amplitude change (I) and attenuation (V) signal responses suggested that the detection probability of a small layer of inclusion is higher than a thick layer, the frequency Amax (III) and frequency shift (IV) responses indicated the opposite.

The characteristic value for the weak bond due to faculty curing (WB-FC) was selected as the epoxy longitudinal wave velocity (**Fig. 5.2.1**-d). MAPOD curves showed that it is difficult to detect WB-FC with the peak-to-peak amplitude (I) and the time delay (II) response signals. While the frequency domain based responses (III-IV) might perform better, PFA values suggested that there might be too many false calls. On the contrary, by attenuation (V) percentage, the weak bond due to faulty curing can be detected with a low number of PFA values and high performance.

5.3. Conclusions for Chapter 5

1. It is evident that the reliability of detecting debonding in aluminum-epoxy single lap joints mostly depends on the gate selection algorithm and the observed ultrasonic echo amplitude.
2. Frequency based response feature calculations can improve the detection reliability of the weak bond due to release agent contamination, by implementing frequency response $a_{90/95}$ values decrease from 75 μm to less than 62 μm.
3. Among all the feature responses, the probability of detecting weak bonds caused by faulty curing is the highest with the attenuation feature.
4. Weak bond detection requires more delicate nondestructive evaluation than debonding detection in order to reach similar reliability. Although it is complicated to make this comparison due to different characteristic values, MAPOD curves indicate that the probability of the detection of a small size (less than 0.5 mm) debonding defect is higher than the detection of weak bonds (due to 60 μm oil inclusion, 2500 m/s change in the acoustic wave velocity).

5. What concerns debonding, the weak bond due to release agent and the weak bond due to faulty curing, the best performed signal response features are frequency responses and attenuation, while time delay is evaluated as the worst one.

6. CONCLUSIONS

1. Extensive literature review led to the determination of nondestructive testing methods to be used in the evaluation of adhesive bonding quality: ultrasonic non-destructive testing – specifically high-frequencies – and eddy-current thermography. The gap observed in literature directed the research towards developing novel post-processing techniques based on feature extraction and data fusion, as well as reliability estimations.
2. An advanced ultrasonic nondestructive testing methodology based on the extraction of features, namely, interface visualization with the ultrasonic amplitude, the frequency domain amplitude and the frequency shift was developed. Compared to the ultrasonic amplitude, the frequency shift feature selection improved the detection performance of artificial debonding by 3 times and the release agent contaminations by 3 to 6 times. The proposed bonding quality evaluation technique is a great candidate to detect interface defects as well as weak bonds based on liquid contamination.
3. The thermal and electrical properties of several contaminations within composite-adhesive joints were determined by using eddy current pulse-compression thermography. The depth of debonding defects was possible to detect with a derivative of the impulse response; skewness and kurtosis of the impulse response is used to verify the size and position of inclusions. According to the norm of kernel principal component analysis (K-PCA), a weak bond due to release agent contamination showed minimum change in the electrical and thermal properties of the bonding; however, thermal properties were affected more than electrical properties.
4. The performance evaluation of ultrasonic techniques in debonding defect detection and sizing is determined with the absolute error per wavelength calculations. The performance for the immersion techniques (including SAM) was higher than the air-coupled and guided wave methods; however, immersion systems are bulky, and the sample needs to be immersed in water. Relative to the ultrasonic wavelength during inspection, the air-coupled through transmission technique performed well in defect sizing while offering the advantage of non-contact inspection. Guided wave ultrasonic NDT could detect debonding defects that are not at the edge of the inspected structure with quick long-range inspections.
5. Data fusion algorithms (average, difference, weighted average, Hadamard, Dempster-Shafer) improved the detection performance for brass inclusions since ultrasonic and thermography results were not in contradiction. Specifically, the Dempster-Shafer rule of combination performs well, however, such basic data fusion techniques as averaging cannot be disregarded. Although nondestructive evaluation of adhesive bonding is still a challenging task, as long as the sources do not contradict each other, the proposed data fusion algorithms

increase the sensitivity and specificity of the inspection by 5 to 40 percent according to the area under ROC curves.

6. The reliability of the developed advanced ultrasonic NDT in debonding detection within aluminum-epoxy single lap joints depends mostly on the gate selection and the ultrasonic amplitude response: and peak-to-peak amplitude as well as frequency amplitude, and attenuation perform well. The probability of detecting weak bonds due to liquid contamination is higher in the frequency shift signal response. In order to detect weak bonds due to faulty curing, it is more reliable to estimate attenuation in the adhesive layer.

7. GUIDELINES FOR FUTURE RESEARCH

The methods presented in this research proposed an overall view on how to evaluate the quality of adhesive bonding with advanced nondestructive testing techniques and evaluate their reliability. However, some aspects of this study need further improvements, such as:

- Although the study covers the most commonly used material combinations in the aerospace industry (carbon fiber reinforced composite-epoxy and aluminum-epoxy joints), the proposed techniques should be experimented on different combinations of materials and dissimilar joints.
- In this work, single-lap joints were selected for both composite-adhesive and aluminum-adhesive bonding samples, however, one should consider the geometrical complexity in terms of the application of these nondestructive evaluation techniques.
- This work focuses on numerical and experimental investigation of the propagation of nondestructive waves through adhesive bonds. In order to formulate the proposed solutions, purely analytical analysis might be needed.
- The bonding quality of the samples used in the study is deteriorated from the perfect bond by adding various inclusions (release films, brass films, release agent contamination) at the adhesive-adherend interface; however, other defects, such as porosity, unwanted surface roughness, finger prints, or moisture might change the quality of bonding.
- The quantitative reliability analysis in this work is limited for ultrasonic wave propagation through aluminum-single lap joints. The statistical tools should be applied for further quantitative analysis for induction thermography and composite-adhesive investigations.
- This study focuses on the ultrasonic, thermal and electrical parameters that are related to the quality of adhesive bonding grounded on physics based feature extraction. It is possible for the future works to consider artificial intelligence tools, such as machine learning, to determine multiple new features as well as categorization application so that to determine bonding quality.

This thesis is presented in a way so that to serve as an open source for the further research topics in the field of nondestructive evaluation of the quality of adhesive bonding in aircraft structures.

8. SANTRAUKA

8.1. Įvadas

8.1.1. Tyrimo aktualumas

Klijavimas klijais yra veiksminga orlaivių konstrukcijų, pagamintų iš kompozitų [1] ir metalų [2], jungimo technologija. Klijais klijuotos konstrukcijos tinka aviacijos ir kosmoso pramonei dėl daugelio aspektų, pavyzdžiui, didelio stiprumo ir svorio santykio, tolygaus apkrovos pasiskirstymo, atsparumo korozijai, gebėjimo sujungti sudėtingas formas ir skirtingas medžiagas. O mechaninėms tvirtinimo detalėms, pavyzdžiui, varžtams, reikia pragręžti skyles, dėl to trūksta kompozitinės skaidulos, prarandamos mechaninės savybės, pažeidžiamas konstrukcijos vientisumas, gerokai padidėja konstrukcijos svoris, ji jautri nuovargiui ir liekamiesiems įtempiams [3].

Tarp orlaivio dalių sujungimai išlieka svarbiausiomis sudedamosiomis dalimis – dauguma konstrukcinių gedimų prasideda nuo jungčių. XXI amžiuje, pradėjus naudoti anglies pluoštu armuotą plastiką (CFRP), orlaivių jungčių klijavimas gerokai išaugo [4]. Pirmasis klijų panaudojimo atvejis užfiksuotas 1945 m. kaip skysto ir miltelių pavidalo klijai „Redux 775“,“, skirti „de Havilland Dove“ orlaiviui [5]. Be „de Havilland Dove“, 1955 m. tuos pačius klijus pirminėms konstrukcinėms dalims gaminti pradėta naudoti ir „Fokker“ lėktuvuose. Karšto kietėjimo epoksidiniai klijai 1963 m. pradėti naudoti „Boeing 727“ orlaiviuose. Be to, pirmajame „Airbus“ lėktuve A300 buvo naudojami karšto kietėjimo epoksidiniai klijai „Cytec FM123-2 “ [4]. Pradėjus naudoti karšto kietėjimo epoksidinius klijus, klijų naudojimas antrinėms apkrovos konstrukcijoms tvirtinti išaugo. Konkrečiai keliose „„Airbus A380“ konstrukcinėse dalyse, pavyzdžiui, aukščio vairuose ir užsparniuose, kaip matyti **8.1.1 pav.**, yra daug klijų [4].

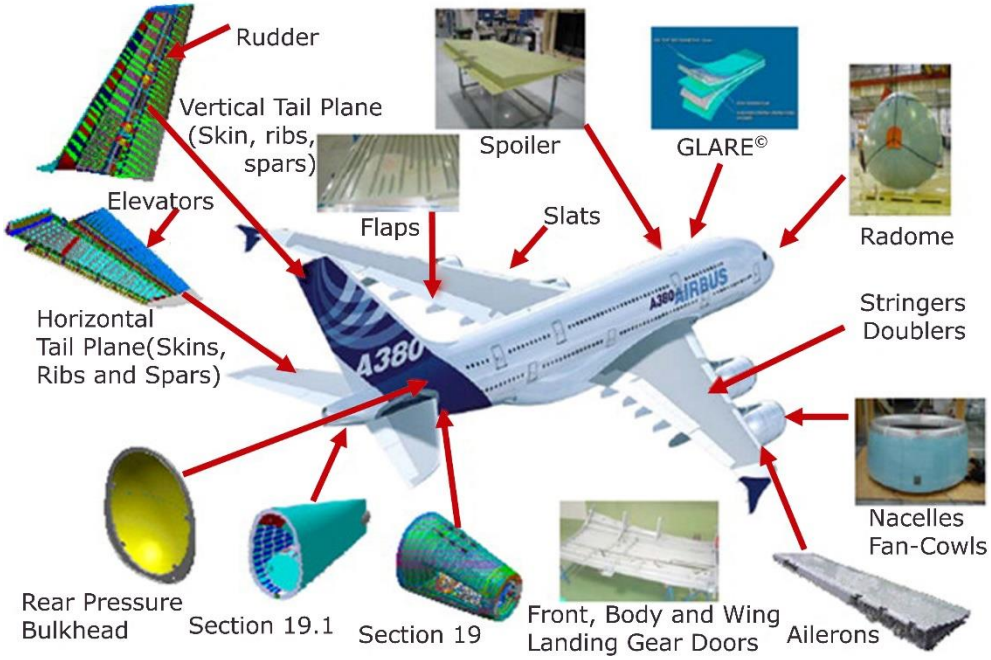

8.1.1 pav. „Airbus A380““ orlaivio dalys, kuriose yra klijų [4]

Nors klijuoti sujungimai yra patraukli jungimo technologija, klijuotų konstrukcijų naudojimas reguliuojamose pramonės šakose, tokiose kaip aviacijos ir kosmoso pramonė, yra ribotas [6]. Kelios priežastys ribojasujungimų klijais taikymą orlaiviuose: sujungimo kokybė labai priklauso nuo paviršiaus paruošimo, o klijuotų sujungimų ilgaamžiškumas yra ribotas [4]. Neardomaisiais bandymų metodais galima nustatyti paviršiaus paruošimo kokybę ir klijų patvarumą prieš naudojimą ir atliekant techninę priežiūrą. Tačiau aviacijos ir kosmoso pramonėje sujungimų klijais kokybės užtikrinimas priskiriamas „specialiems procesams“, kuriems reikalingi patikimi neardomosios kontrolės metodai. Klijais sujungtos konstrukcijos arba klijuotosios jungtys gali būti apibrėžiamos kaip dvi ar daugiau konstrukcijų, vadinamų adherendais, sujungtų struktūriniais klijais. Klijuotų sujungimų sukibimo kokybė priklauso nuo daugelio gamybos etapo veiksnių, t. y. nuo paviršiaus paruošimo, drėkinimo, aplinkos sąlygų ir kietėjimo proceso. Be to, eksploatacijos metu gali atsirasti kitų defektų, o anksčiau atsiradę defektai gali išplisti dėl nuovargio ir naudojimo. Klijuotų sujungimų negrįžtamą struktūrinį pažeidimą gedimą paprastai sukelia tokie defektai, kaip atsisluoksniavimas, porėtumas, drėgmė ir užterštumas [7]. Prieš gedimą dėl užterštumo gali atsirasti vadinamasis „kissing bond“ – kai adherendas ir klijai visiškai liečiasi, tačiau be jokio cheminio ryšio [8]. Tokio tipo defektus labai sunku nustatyti įprastais neardomaisiais bandymų metodais. Be to, dėl užterštumo, drėgmės ir gryno kietėjimo gali smarkiai sumažėti ne tik dviejų medžiagų ribos sujungimo kokybė, bet ir klijų sluoksnio vientisumas [9]. Šis drastiškas klijų sukibimo kokybės sumažėjimas, dar vadinamas silpnuoju sukibimu, sunkiai nustatomas neardomaisiais bandymų metodais. Negalint aptikti silpnų ryšių ir

nustatyti inkliuzijas klijų ir klijuotės sąsajoje, gali labai sumažėti stiprumas, taip pat atsirasti netikėtų katastrofinių pažeidimų gedimų. Todėl labai svarbu turėti patikimus neardomuosius bandymų metodus, kad būtų galima naudoti klijuojamąsias jungtis.

Klijų sukibimo neardomasis vertinimas yra sudėtingas uždavinys, nes sukibimas yra tarpfazinis reiškinys, apimantis labai ploną medžiagos sluoksnį, dažniausiai gerokai mažesnį už neardomojo bandymo metodo bangos ilgį [10]. Iki šiol klijavimo kokybei vertinti buvo taikomi keli neardomųjų bandymų metodai. Dažniausiai surištų konstrukcijų struktūrinis vientisumas nustatomas atliekant ultragarsinę patikrą ir aktyviąją termografiją. Vis dažniau naudojami pažangūs signalų apdorojimo algoritmai, įskaitant duomenų sintezę, todėl šie metodai yra efektyvesni siekiant vizualizuoti vidinę struktūrą ir nustatyti defektus. Tai leidžia kelti **mokslinę hipotezę**, kad gali būti sukurta nauja neardomojo vertinimo metodika klijuotų sujungimų kokybei tirti, kuri leistų patikimai įvertinti klijuotų konstrukcijų kokybę ir atskirti atsisluoksniavimą nuo silpno suklijavimo.

8.1.2. Tikslas ir uždaviniai

Disertacijos tikslas — sukurti ir įvertinti naują neardomojo vertinimo metodiką, skirtą klijais sujungtų orlaivių konstrukcijų sukibimo kokybei nustatyti, naudojant ultragarsinius, elektromagnetinius, termografinius metodus ir duomenų sintezę. Šiam tikslui pasiekti buvo numatyti šie uždaviniai:

1. Ištirti bangų sklidimą per gerus, atsisluoksniavusius ir silpnus klijuotus sujungimus, nustatyti perspektyvius neardomųjų bandymų metodus , galimus signalų apdorojimo algoritmus ir patikimumo vertinimo metodus skaitiniams ir eksperimentiniams tyrimams.
2. Ištirti ultragarso bangų sąveiką skaitmeniniu ir eksperimentiniu būdu klijais sujungtose struktūrose, nustatant ultragarso parametrus, kurie yra glaudžiai susiję su sujungimo kokybe, ir aptikti silpną sujungimą.
3. Nustatyti elektromagnetinius (įskaitant šiluminius) parametrus, kuriuose yra informacijos apie sukibimo kokybę, ir nustatyti sukibimo kokybę atliekant skaitinius ir eksperimentinius tyrimus.
4. Palyginti skirtingų ultragarsinių neardomųjų metodų efektyvumą nustatant defektus ir defektų dydį klijais klijuotose jungtyse.
5. Įdiegti ultragarso ir sūkurinės srovės termografijos neardomųjų bandymų metodų duomenų sintezę, siekiant pagerinti klijavimo kokybės vertinimą.
6. Kiekybiškai įvertinti įvairių ultragarsinių parametrų patikimumą, vertinant atsisluoksniavimą ar silpną sujungimą, taikant statistinius metodus, pavyzdžiui, aptikimo tikimybės (PoD) kreives.

8.1.3. Mokslinis naujumas

1. Nustatomos tokios ultragarsinės ir elektromagnetinės savybės ir parametrai, turintys įtakos sukibimo kokybei: ultragarsinių atspindėtų signalų amplitudė ir fazė laiko ir dažnių srityje, ultragarsinio signalo slopinimas klijų sluoksnyje, sūkurinių srovių termografijos principinė komponentė, sūkurinių srovių suspaustų signalų termografijos išvestinė, impulso atsako skirstinio simetriškumas (angl. *skewness)* ir kurtozė (angl. *kurtosis*.)

2. Nauji skaitmeniniai modeliai su skirtinga sukibimo kokybe, įskaitant silpną sukibimą, buvo sukurti taikant pusiau analitinį baigtinių elementų metodą (SAFE) ultragarso sklidimui ir baigtinių elementų metodą (FEM) sūkurinių srovių termografijai.
3. Sukurtas naujas signalų apdorojimo algoritmas, skirtas klijais surištų konstrukcijų aukšto dažnio ultragarsiniams tyrimams, remiantis laiko ir dažnio charakteristikomis, ir kiekybiškai įvertintas sukurtų metodų veiksmingumas.
4. Sukurtas naujas signalų apdorojimo algoritmas sūkurinių srovių suspaustų impulsų termografijai, skirtai adheziškai sujungtų konstrukcijų tyrimams, remiantis branduolio principinių komponenčių analize, impulso atsako skirstinio simetriškumu (angl. *skewness)* ir kurtoze (angl. *kurtosis*.). Rezultatai buvo kiekybiškai įvertinti, siekiant nustatyti klijų ir klijų sandūros sąsajoje esančių defektų dydį, gylį ir laidumą (elektrinį ir šiluminį).
5. Sukurtas naujas kiekybinio palyginimo metodas, skirtas skirtingų ultragarsinių tyrimų metodų efektyvumui įvertinti nustatant defektus ir defektų dydį, remiantis ultragarso bangos ilgiu klijuotame bandinyje. Be to, siekiant padidinti ultragarsinės ir sūkurinių srovių termografijos patikimumą vertinant klijavimo kokybę, buvo sukurtos duomenų sintezės programos.
6. Naudojant modelį apskaičiuotos silpnų sujungimų aptikimo tikimybės kreivės. Inovatyvūs skaitiniai modeliai buvo patvirtinti eksperimentiniais tyrimais. Anksčiau sukurti požymiais pagrįsti signalų apdorojimo algoritmai kiekybiškai įvertinti naudojant aptikimo tikimybės kreives.

8.1.4. Praktinė darbo vertė

1. Siūloma nauja signalų apdorojimo metodika su aukšto dažnio akustinės mikroskopijos tyrimais ir sūkurinių srovių suspaustų signalų termografija gali būti naudojama atsisluoksniavimui aptikti, inkliuzams klijuotame sujungime apibūdinti ir silpniems sujungimams prognozuoti.
2. Siūlomi ultragarsinių neardomųjų tyrimų metodai bei sūkurinių srovių termografija gali būti naudojami defektams nustatyti ir lokalizuoti. Sūkurinių srovių termografija ir su ultragarsiniai tyrimai per orą suteikia nekontaktinio tikrinimo privalumų, o imersiniai ultragarso metodai su nauju signalų apdorojimu leidžia tiksliai nustatyti defektus, medžiagas ir jų dydį.
3. Siūlomos ultragarso ir sūkurinių srovių termografijos duomenų sintezės programos, skirtos klijavimo kokybei vertinti, gali būti pritaikytos įvairiems daugiamačiams neardomiesiems vertinimams, jei atsako signalai neprieštarauja vienas kitam. Be to, pateiktos imtuvo operatoriaus charakteristikos ROC kreivės gali būti naudojamos duomenų sintezės programų patikimumui nustatyti, kai tiriami bandiniai su žinomais defektais.
4. Modeliu pagrįstos aptikimo tikimybės kreivės gali būti naudojamos bet kokiam neardomojo vertinimo metodui, kurį galima pavaizduoti baigtinių elementų modeliavimu, kad būtų galima palyginti patikimumą nustatant atsisluoksniavimą, ar atskirti silpną sujungimą dėl užterštumo nuo silpno sujungimo dėl netinkamo kietėjimo.

Kai kurios šio darbo dalys buvo panaudotos tarptautinio projekto NDTonAIR „Orlaivių konstrukcijų neardomasis bandymas ir konstrukcijų būklės stebėsena“ (H2020-2016-2020-722134) – Europos Sąjungos mokslinių tyrimų ir inovacijų programos „Horizontas 2020“ pagal Marie Sklodowskos-Curie pradinio mokymo tinklus – ataskaitose.

8.1.5. Ginti pateikiami rezultatai

1. Pažangi ultragarsinė neardomųjų bandymų metodika su nauju signalų apdorojimo metodu, skirtu sujungimo kokybei nustatyti ir aptikti silpną sujungimą.
2. Sujungimo kokybės įvertinimas naudojant suspaustų signalų sūkurinių srovių termografiją, grindžiamą branduolio principinių komponenčių analizės terminių ir elektrinių požymių išskyrimu.
3. Imersinių, kontaktinių ir per orą ultragarsinių neardomųjų metodų palyginimas nustatant atsisluoksniavimą metalo ir klijų sujungimuose.
4. Ultragarsinių atspindžio imersinių ir indukcinės termografijos neardomųjų vertinimų duomenų sintezė kompozito ir klijų jungtyse.
5. Sukurto požymiais pagrįsto neardomojo ultragarsinio signalų apdorojimo metodo patikimumo vertinimas naudojant modeliu pagrįstas aptikimo tikimybės kreives.

8.1.6. Tyrimų rezultatų aprobavimas

Disertacijos laikotarpiu moksliniai rezultatai paskelbti 8 publikacijose: pusė straipsnių paskelbta tarptautiniuose žurnaluose, įtrauktuose į ISI Web of Science, o kita pusė – recenzuojamuose tarptautinių konferencijų leidiniuose. Be to, rezultatai buvo skleisti 11 tarptautinių konferencijų, vykusių Vilniuje, Geteborge, Glazge, Bukarešte, Turine, Briugėje, Paryžiuje, Atėnuose ir internete. Remiantis tyrimų rezultatais, 2020 ir 2021 m. gauta Lietuvos mokslo tarybos teikiama doktorantūros stipendija. 2021 m. gauta tarptautinė studentų mokslinių tyrimų stipendija, kurią skyrė Amerikos akustikų draugijos (ASA) Tarptautinių tyrimų ir švietimo komitetas (CIRE).

8.1.7. Disertacijos struktūra

Disertaciją sudaro įvadas, penki skyriai, pagrįsti straipsnių apžvalga, išvados, literatūros sąrašas, gyvenimo aprašymas, publikacijų, be konferencijų, sąrašas ir mokslinių publikacijų kopijos. Visą disertaciją sudaro 212 puslapių, 31 paveikslas, 3 lygtys, 9 lentelės, 93 bibliografinių nuorodų ir penkios leidinių kopijos.

1. Pirmajame skyriuje nagrinėjamas ultragarsinių parametrų ir klijuotų sujungimų kokybės ryšys. Pateikiami klijuotų sujungimų skaitiniai modeliavimai ir eksperimentiniai tyrimai. Paaiškinamas naujas signalų apdorojimo algoritmas, galintis patikimai nustatyti silpnus sujungimus ir atsisluoksniavimą, ir pateikiamas anglies pluošto kompozito ir epoksidinio pluošto viengubo persidengiančio sujungimo atvejo tyrimas.
2. Antrajame skyriuje nagrinėjamas elektromagnetinių (įskaitant šiluminius) parametrų ir klijuotų sujungimų sukibimo kokybės ryšys. Pateikiami skaitiniai

ir eksperimentiniai kompozitinių- klijų sujungimų tyrimai. Atliekant atvejo tyrimą, naudojant impulsinę-kompresinę indukcinę termografiją, tiriamas atsisluoksniavimo aptikimas ir dydžio nustatymas bei inkliuzų, galinčių sukelti silpną sukibimą, nustatymas.

3. Trečiajame skyriuje išsamiai tiriami ir lyginami skirtingi ultragarsiniai neardomųjų bandymų metodai, skirti sukibimo kokybei įvertinti. Keletas ultragarsinių neardomųjų bandymų metodų, įskaitant nukreiptąsias bangas, ultragarsą per orą, imersinę impulsinę echoskopiją, imersinę praėjimo ir akustinę mikroskopiją, taikomi aliuminio ir epoksido viengubų persidengiančių sujungimų, kuriose yra surišimo defektų, atveju. Atliekant metalo ir klijų jungčių tyrimus, defektų aptikimo ir defektų dydžio nustatymo galimybės buvo įvertintos atsižvelgiant į ultragarso bangos ilgį, sklindantį per konstrukcijas.
4. Ketvirtajame skyriuje atliktas kompozito irepoksido viengubų persidengiančių sujungimų, kuriose yra įvairaus dydžio ir medžiagos dirbtinių defektų, tyrimas, naudojant ultragarsinį imersinį atspindžio metodą ir indukcinę termografiją. Siekiant išnaudoti kiekvieno metodo privalumus, taikyti keli duomenų sintezės algoritmai. Eksperimentinių tyrimų ir duomenų sintezės rezultatai buvo kiekybiškai įvertinti naudojant imtuvo operacinių charakteristikų (ROC) kreives.
5. Penktajame skyriuje aptariamas ultragarsinio neardomojo vertinimo patikimumas. Išsamiai išnagrinėtas kiekybinis pažangių ultragarsinių tyrimų patikimumas atliekant aukšto dažnio akustinės mikroskopijos tyrimus. Atvejo analizėje daugiausia dėmesio skiriama aliuminio-epoksido persidengiantiems sujungimams, kuriuose yra atsisluoksniavimas, silpnas sujungimas dėl užterštumo ir silpnas sujungimas dėl netinkamo kietinimo. Modeliu pagrįstos aptikimo tikimybės kreivės gautos atlikus daugybę pusiau analitinių baigtinių elementų modeliavimų.

Naudojamų straipsnių ryšys apibendrintas **8.1.2. pav**. A1, A2, A4 straipsniuose buvo domimasi kompozitiniais klijais klijuojamomis viengubomis jungtimis, o A3 ir A5 – aliuminio klijais klijuojamomis viengubomis jungtimis. Neardomieji bandymo metodai buvo parinkti atsižvelgiant į pritaikomumą ir našumą. Kompozitinės klijuotinės jungtys ir aliuminio klijuotinės jungtys buvo tiriamos skenuojamuoju akustiniu mikroskopu (A1, A5). Sūkurinių srovių (indukcinė) termografija gali būti taikoma tik kompozito ir klijų jungtims, nes dėl didelio šilumos laidumo sudėtinga infraraudonųjų spindulių kamera registruoti temperatūros gradientą aliuminio paviršiuje. Kompozito ir klijų bei aliuminio ir klijų sandūrų tyrimams buvo naudojamas imersinis ultragarsinis tyrimų metodas. Be to, nuspręsta palyginti ir taikyti duomenų sintezę ultragarsinei imersinei ir indukcinei termografijai, nes pirmoji yra pramonėje naudojamas standartinis metodas, o antroji – besivystantis neardomasis bandymo metodas, turinti potencialių privalumų, pavyzdžiui, yra greita ir bekontaktė. Nukreiptųjų bangų tyrimui atlikti buvo pasirinktos aliuminio ir klijų jungtys, kad būtų pasiektas geriausias įmanomas vaizdas su mažiau slopinančiu ir homogenišku pagrindu. Ultragarsiniai tyrimai per orą naudojami su aliuminio ir epoksidinėmis jungtimis, siekiant pademonstruoti galimus bekontakčius ultragarso taikymus su dvipuse prieiga.

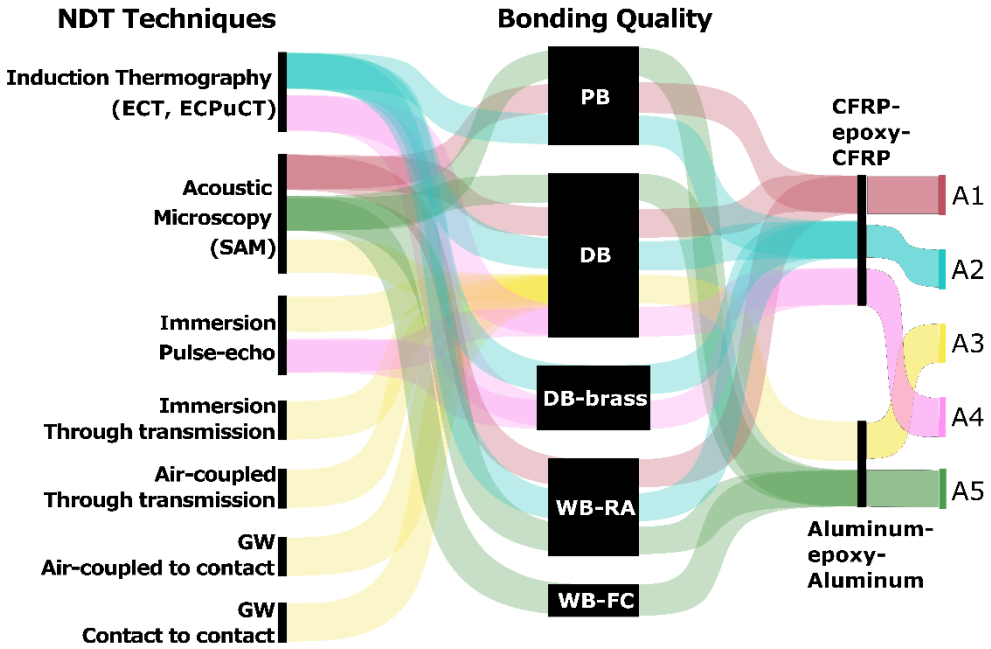

8.1.2 pav. Disertacijoje naudojamų gaminių (A1-A5) ryšys, atsižvelgiant į neardomųjų bandymų metodus, sukibimo kokybę ir klijų-adherendų derinius

8.1.8. Literatūros apžvalga apie surišimo kokybės vertinimą naudojant neardomųjų bandymų metodus

Klijavimo kokybei vertinti ultragarsinis neardomasis bandymo metodas yra vienas iš dažniausiai naudojamų metodų [19]. Pamerkimo per perdavimą ultragarsinis metodas laikomas etaloninu tarp ultragarsinių metodų, tačiau jis reikalauja, kad konstrukcijos būtų panardintos į vandenį ir prie jų būtų galima prieiti iš dviejų pusių [24]. Panardinimo impulsų echoskopijos metodas leidžia naudotojams tikrinti konstrukcijas tik su vienpusiu priėjimu, tačiau vis tiek reikia, kad jos būtų panardintos į vandenį [25]. Konkrečiai, panardinimo impulsų-echo ultragarsinis metodas buvo naudojama vizualizuojant klijavimo sąsają [26], nustatant atsiklijavimą [27], vertinant klijų kokybę [28], matuojant drėgmės ir ekstremalios drėgmės poveikį silpnam klijavimui [29], nustatant bučinius [30] ir silpnus klijus [31], nustatant defektų padėtį [3]. Taip pat skenuojamoji akustinė mikroskopija (SAM) impulsų echo režimu, pasižyminti greita patikra, didele skiriamąja geba ir dideliu dažniu, naudojama silpnam klijavimui holografiškai vertinti [32] ir porėtumui nustatyti nelygiagrečiose jungtyse [33]. Pranešama, kad su oru susieta ultragarsinė technika (ACUT) naudojama silpnų jungčių tarpfaziniam standumui apskaičiuoti [34] ir trijų sluoksnių aliuminio jungties sąsajai vizualizuoti [35]. Kai kuriuose tyrimuose buvo nagrinėjamas atskyrimas ir atsisluoksniavimas nustatant Lembo bangomis ir vibrometrija [36,37]; kituose aptariama nukreiptųjų bangų sklaida dėl sąsajos kokybės

pokyčių [38,39]. Be to, Lembo bangos naudotos silpnam ryšiui tirti, tikrinant atsako amplitudės pokytį [40]. Be to, netiesiniu ultragarsu išmatuotas netiesiškumo lygis siejamas su surišimo kokybe, ypač kai yra silpnas surišimas [41,42]. Lazerinis ultragarsas yra ypač perspektyvus metodas, leidžiantis aptikti surištų korių konstrukcijų atsiskyrimą, tačiau jame naudojamos didelės sužadinimo amplitudės, dėl kurių atsiranda didelis triukšmas ir sunku interpretuoti rezultatus.

Termografija yra vienas iš plačiai naudojamų neardomasis bandymo metodas, skirtų klijavimo kokybei vertinti [48–50], nes yra labai jautri, tinkama dideliems plotams ir leidžia atlikti bekontaktę patikrą. Tačiau termografija dažniausiai aptinkami paviršiaus ir po paviršiaus defektai. Siekiant padidinti patikros jautrumą, struktūros stimuliuojamos naudojant kelias galimybes pavyzdžiui, aktyviąją termografiją. Aktyvioji termografija plačiai naudojama gamybos defektams klijuotose jungtyse aptikti [51,52], [53,54], siekiant nustatyti, ar klijų jungtyse yra teršalų. Metalinėse klijinėse jungtyse paviršiaus nelygumai, dirbtiniai defektai ir grioveliai aptinkami naudojant aktyviąją termografiją su fiksavimu [55]. Įprastinei šviesa pagrįstai aktyviajai termografijai didelę įtaką daro šiluminė difuzija ir struktūrinė anizotropija. Taikant šį metodą, šiluminė energija sklinda nuo įkaitinto paviršiaus ir tada grįžta atgal į paviršių, kad ją užfiksuotų infraraudonųjų spindulių kamera. Siekiant veiksmingai aptikti defektus didesniame odos gylyje, galima naudoti sūkurinių srovių (indukcinę) impulsinę termografiją, nes ji užtikrina tūrinį elektrai laidžios struktūros kaitinimą [12,56]. Nors indukcinė termografija yra priimtinesnė, jos taikymą gali riboti klijuojamų konstrukcijų storis ir rezultatų matmenų sudėtingumas [57].

Panašiai kaip ir termografija, shearografija yra labai jautri ir per trumpą laiką gali aptikti didelius plotus, tačiau ji užtikrina veiksmingą paviršiaus ir po paviršiaus defektų aptikimą ir reikalauja didelio įtempių sužadinimo [44]. Pranešama, kad shearografija gerai veikia aptikdama aliuminio ir klijų jungčių atskyrimo ir požeminius defektus [49].

Rentgeno spinduliuotė ir rentgeno spindulių kompiuterinė tomografija (KT) yra galingi tyrimo metodai, skirti vidiniams defektams klijuotose konstrukcijose tirti [50]. Kompozitinių klijų jungčių atveju rentgeno spindulių kompiuterinė tomografija yra sudėtingas uždavinys ne tik dėl to, kad tai gerokai brangi ir didelių gabaritų sistema, bet ir dėl didelio konstrukcijų aspektų santykio bei panašių difrakcijos koeficientų [59]. Be to, rentgeno KT nėra labai veiksmingas metodas nulinio tūrio defektams, tokiems kaip atskyrimas, aptikti.

Naujausiuose tyrimuose aptariamos elektromechaninio impedanso NDT taikymo galimybės tikrinant sąsajų defektus [60] ir silpnus ryšius, atsirandančius dėl užterštumo, drėgmės ir gryno kietėjimo [61,62]. Be to, pranešama, kad lazeriu pagrįsti metodai, tokie kaip lazerinis smūginis sukibimo bandymas (LASAT) [63] ir lazerinis sukibimo tikrinimas LBI) [64], yra perspektyvūs metodai silpnoms jungtims aptikti. Nors išplėstiniai tyrimometodai yra perspektyvūs siekiant aptikti defektus lipniose jungtyse, šios sistemos yra brangios tiek įsigijimo, tiek priežiūros požiūriu.

Nors neardomasis klijų sujungimo vertinimas atliekamas keliais skirtingais metodais, visi jie turi privalumų ir trūkumų. Siekiant įveikti metodų apribojimus, galima sujungti iš skirtingų patikrinimų gautą informaciją taikant duomenų sintezę.

Duomenų sintezę į NDT įvedė Grosas ir kt.,,, ir tyrimai toliau plėtojami [66]. Konkrečiai Daryabor ir Safizadeh [74] tyrė ultragarsinio tikrinimo ir aktyviosios termografijos vaizdų sintezę, skirtą klijų kokybei vertinti tarp nepanašių jungčių. Jie palygino keletą pagrindinių ir sudėtingų sintezės algoritmų, būtent: minimumo, maksimumo, vidurkio, pagrindinių komponenčių analizės, banginės transformacijos ir piramidės.

Dažniausiai duomenų sintezė pagerina rezultatus, palyginti su atskiru NDT metodu, tačiau NDT metodo patikimumą reikėtų įvertinti statistiniais metodais. Paprastai NDT patikimumas matuojamas aptikimo tikimybės (PoD) kreivėmis [76], kurios defekto aptikimo tikimybę sieja su jo charakteristine verte [77]. Praktiškai atlikti eksperimentus, kad būtų gautos aptikimo tikimybės kreivės, yra brangu ir užima daug laiko, nes tam reikia daug mėginių, patikrinimų ir žmogiškųjų išteklių Vis dėlto PoD kreivių poreikis ir pripažinimas didėja dėl saugos reglamentų. Todėl besiformuojančios pramonės šakos, pavyzdžiui, aviacijos ir kosmoso pramonė, renkasi modeliavimu grindžiamą patikimumo analizę, modelio padedamąją aptikimo tikimybę (MAPOD) [80–82]. Plokščiojo dugno skylių aptikimo ultragarsinio NDT metodu atvejo tyrime pateikiama MAPOD įgyvendinimo procedūra ir iššūkiai [90]. Be to, Smagulova ir kt. tyrė atsiskyrimo aptikimo galimybes nepanašiose jungtyse atlikdami ultragarsinį bandymą, taikydami MAPOD [91].

8.2. Pažangus ultragarsinis neardomasis metodas, skirtas sukibimo kokybei vertinti

Šiame skyriuje daugiausia dėmesio skiriama aptarti ryšiui tarp ultragarsinių parametrų ir sukibimo kokybės. Anglies pluoštu sutvirtinto plastiko paprastosios jungties sukibimo kokybė buvo įvertinta skaitiniais ir eksperimentiniais ultragarsiniais tyrimais. Sukurtas inovatyvus duomenų apdorojimo algoritmas, galintis patikimai aptikti silpnus ryšius ir kompozitinių sluoksnių atskyrimą.

8.2.1. Skaitiniai tyrimai

Ultragarso bangų sklidimas per skirtingos kokybės sujungimus buvo modeliuojamas semi-analitine baigtinių elementų (SAFE) pagrįsta programine įranga CIVA. Bandiniai su trimis skirtingos surišimo kokybėmis ištirti atliekant 5 MHz centrinio dažnio kontaktiniu impulsiniu echo ultragarsiniu metodu.

Defektų neturintis modelis – tobulas sukibimas (PB) – buvo modeliuojamas kaip kompozitinis adherendas, ir epoksidiniai klijai pilnai liečiasi. Atskyrimo defektas (DB) modeliuotas kaip 15 mm delaminacija viršutinėje sąsajoje. Silpnas sukibimas (WB) modeliuojamas su papildomu plonu skystos alyvos užterštumo sluoksniu tarp klijų ir viršutinės adherendo sąsajos.

Buvo tiriami dviejų skirtingų matmenų kompozito ir klijų paprastosios sandūros modeliai: storas modelis ir plonas modelis. Storo modelio adherendo ir klijų storiai buvo atitinkamai 5 mm ir 1 mm; ploną modelį sudarė 2,4 mm adherendas ir 0,15 mm klijai. Modelių schemos ir klijavimo kokybės atvaizdai pateikti **8.2.1 pav.** Storo modelio storis parenkamas taip, kad būtų galima išskaidyti kiekvienos sąsajos ultragarsinio aido signalus, o plono bandinio matmenys parenkami panašūs į realaus atvejo storį.

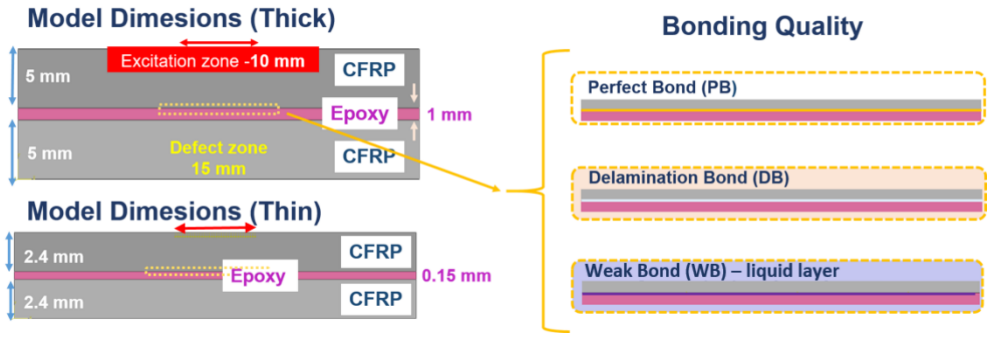

8.2.1 pav. Plonų ir storų modelių bei trijų surišimo savybių schemos, simuliuojamos ultragarso bangų sklidimu

Gauti ultragarsinio impulsinio echo A-skenavimo rezultatai buvo suskirstyti į kelis tipus pagal kiekvienos sąsajos atspindžio skrydžio laiko skaičiavimus. Šiose schemose pavaizduoti atitinkami susidomėjusio ultragarso bangų paketo sąsajos atspindžiai.

Storajame modelyje antrasis bangų paketas yra atspindys nuo viršutinės paprastosios jungties sąsajos, o trečiasis bangų paketo intervalas yra atspindys nuo apatinės sąsajos. Plono modelio rezultatai rodo, kad viršutinės ir apatinės sąsajos

atspindžio aidai nėra atskiriami. Pirmasis bangų paketo aidas yra viršutinio atspindžio, apatinio atspindžio ir kelių daugkartinių atspindžių klijų sluoksnyje derinys. Antrąjį ultragarso bangų paketą sudaro dvigubas atspindys viršutinėje sąsajoje, atgalinis aidas ir dvigubas atspindys apatinėje sąsajoje. Antrieji bangų paketai laiko ir dažnio erdvėse taip pat pavaizduoti **8.2.2 pav.** Lyginant DB ir WB su PB, laiko ir dažnio atsako amplitudė padidėja, o dažnių spektras išsiplečia. DB pokyčiai yra didesni nei PB. Trečiosios bangos paketo atsakas parodytas **8.2.3 pav.**

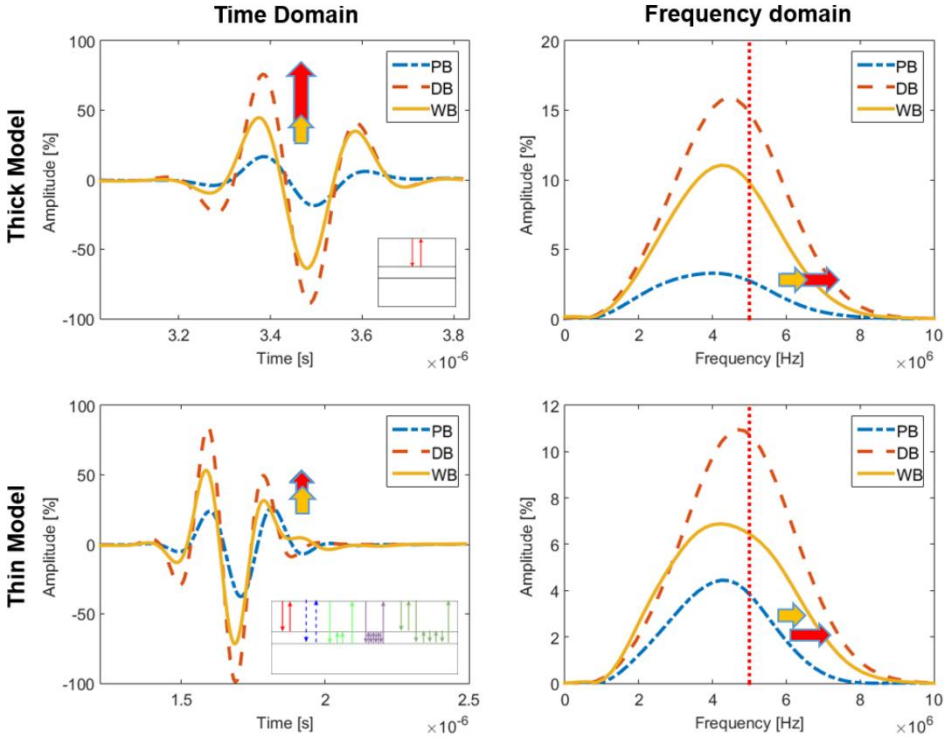

8.2.2 pav. Antrojo ultragarso bangos paketo atsakas laiko ir dažnio erdvėse (domenuose) storuose ir plonuose modeliuosemodeliuose

Palyginti su PB, WB atsakas pasislinko, ploname modelyje pastebimass beveik visiškas fazės pokytis. DB atveju ultragarso banga nepereina per dugno sąsają. Todėl storajame modelyje atsako nepastebima, o plonajame modelyje yra nedideli pokyčiai dėl kitų daugybinių atspindžių. Didžiausios amplitudės dažnio poslinkis paprastai siejamas su bandinio susilpnėjimu.

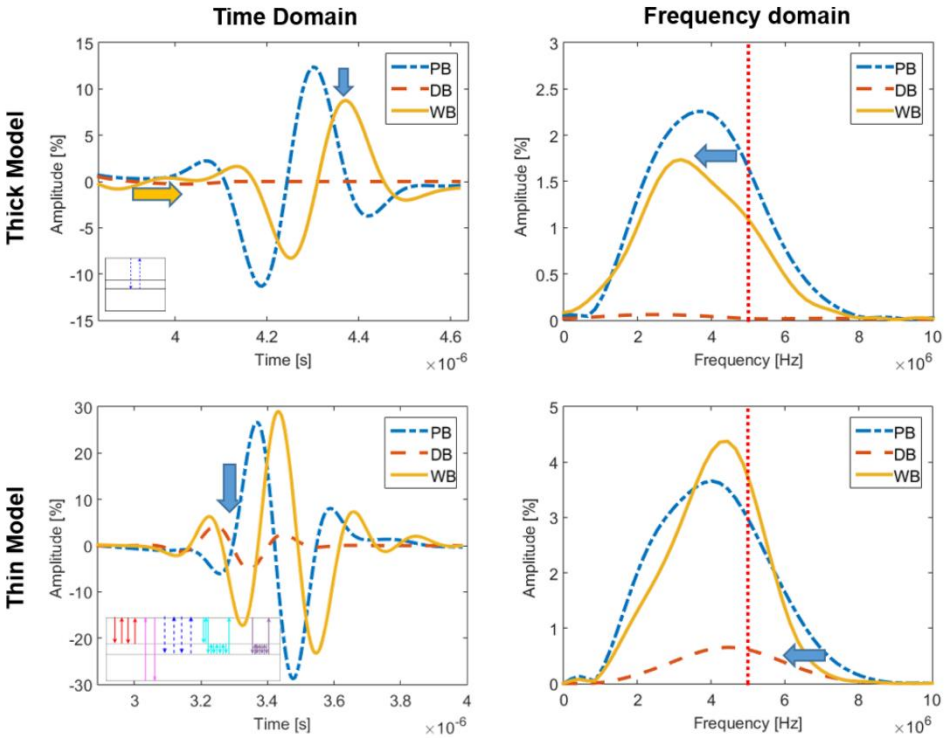

8.2.3 pav. Trečiojo ultragarso bangos paketo atsakas laiko ir dažnio erdvėse (domenuose) storuose ir plonuose modeliuosemodeliuose

8.2.2.Eksperimentiniai tyrimai

Kadangi skaitiniai tyrimai parodė stiprų ryšį tarp ultragarso parametrų (amplitudės ir poslinkio laiko ir dažnio domenuose) ir klijų sukibimo kokybės, buvo atlikti eksperimentiniai tyrimai su požymių išskyrimu. Kaip adherendas pasirinktas šešių sluoksnių anglies pluošto epoksidinis prepregas iš atlasinio audinio, kurio ilgis 120 mm, plotis 280 mm ir storis 2,22 mm. Kaip klijai pasirinkta 25 mm ilgio, 280 mm pločio ir 0,24 mm storio struktūrinė epoksidinė plėvelė. Kaip matyti **8.2.4 pav.**, tiriamos keturios skirtingos sukibimo kokybės bandiniai: tobulas sukibimas be defektų (PB), delaminavimo defektas (DB) – du kartus sulankstyta kvadratinė atskyrimo plėvelė, kurios kraštinės ilgis – 12,7 mm, silpno sukibimo defektas (WB) su didesniu užterštumu – 0,6 ml atpalaiduojamosios medžiagos sluoksnių sandūros vietoje kaip skystas užterštumas, silpnas sukibimo defektas su mažesniu užterštumu – 0,6 ml atpalaiduojamosios medžiagos sluoksnių klijavimo vietoje, uždengtoje kauke, kad būtų apribotas įterptojo skysčio pasiskirstymas paviršiuje.

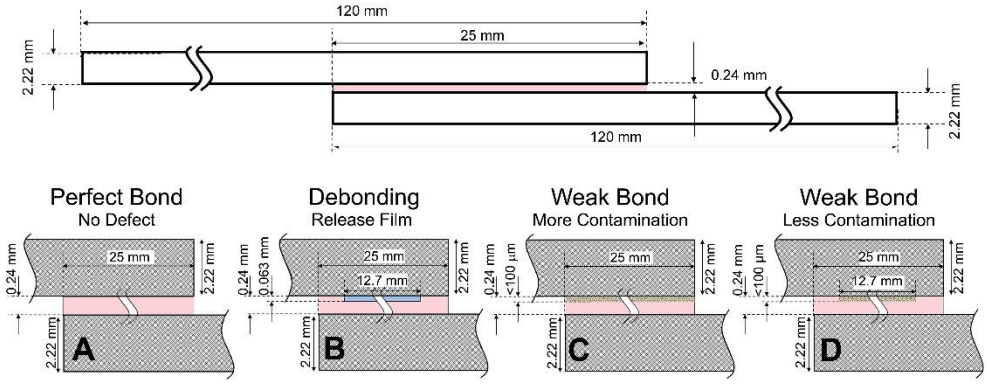

8.2.4 pav. Tiriamųjų pavyzdžių šoninio vaizdo schemos [11]

16,7 mm x 16,7 mm plotas buvo ištirtas ties kiekviena iš keturių skirtingų surišimo kokybės rišimo linija. Skenuojamajai akustinei mikroskopijai pasirinktas fokusuotas keitiklis (3 mm skersmens, 10 mm židinio nuotolio ir 50 MHz centrinio dažnio). Atlikti ultragarso impulso-echo rezultatai naudojami tolesniam apdorojimui atlikti.

Siekiant pagerinti atsiklijavimo ir užterštumo aptikimo efektyvumą, buvo sukurtas naujas daugiapakopis signalų apdorojimo algoritmas. Pirma, triukšmas, kurį sukelia stipriai signalus slopinantys CFRP klijai, buvo filtruojamas naudojant bangelės nutriukšminimą (**8.2.5 pav.**, a, b). Tada kiekvienas eksperimentas buvo išlygintas ties nuliniu paviršiaus atspindžio susikirtimu. Be to, pasirinktas dominantis laiko langas pagal ToF skaičiavimus ir signalai suderinami pagal maksimaliomis amplitudes pasirinktame laiko lange (**8.2.5 pav.**, c). Didžiausios amplitudės, pastebimos šiame laiko intervale, pasirinktos kaip C_{time} požymis, laikai, atitinkantys didžiausias amplitudes, buvo pažymėti kaip P_{time}. Tada ultragarsinis atsakas perkeliamas į dažnių sritį naudojant Furjė transformaciją (**8.2.5 pav.,** d). Didžiausios amplitudės, pastebimos dažnių srityje, pasirenkamos kaip $C_{frequency}$ požymis. Dažnio vertės, atitinkančios didžiausią vertę, pasirenkamos kaip $P_{frequency}$ požymis.

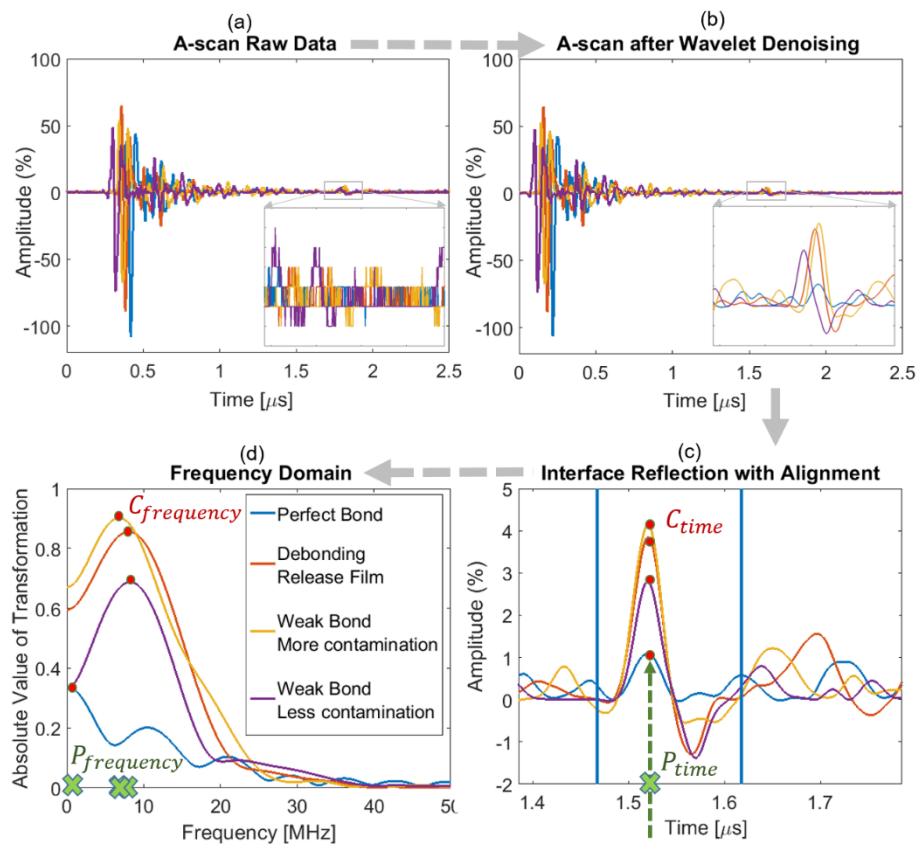

8.2.5 pav. Nauji tolesnio apdorojimo algoritmo etapai su požymių išskyrimu: a) neapdoroti ultragarsiniai duomenys, b) A skenavimas po bango laidinio denozavimo, c) sąsajos atspindys po išlyginimo, d) dažnių srities atsakas

C_{time} vizualizacija parodo defektų nebuvimą tobulo surišimo bandinyje (PB), kvadratinė atskyrimo plėvelė aiškiai matoma delaminuotame bandinyje (DB). Pastebimas tam tikras nuokrypis silpno surišimo su mažesniu užterštumu ir silpno surišimo su didesniu užterštumu atvejais, tačiau juos labai sunku įvardyti kaip bandinius su defektais ar prastos surišimo kokybės bandinius (**8.2.6 pav.**).

P_{time} vizualizuoja anksčiau taikyto lyginimo algoritmo našumą. Kaip matyti iš **8.2.6 pav.**, mažesnės reikšmės visose vizualizacijose rodo, kad lyginimo algoritmas buvo pritaikytas tinkamai.

Visų jungties savybių $C_{frequency}$ vizualizacijos yra panašios į C_{time} vaizdavimą – to ir tikimasi, nes abi vizualizacijos pagrįstos amplitude, o laiko srities duomenų Furjė transformacija priklauso nuo amplitudės (**8.2.6 pav.**).

Idealaus sąryšio (PB) $P_{frequency}$ vizualizacija rodo, kad bandinys yra be defektų, o dėl klijų plėvelės sluoksnio tekstūros aptinkami tik nedideli svyravimai. Nors dirbtinį atskyrimą galima aiškiai identifikuoti kaip defektą, silpno sukibimo užterštumo $P_{frequency}$ sąsajos vizualizacija atskleidžia defektines zonas sąsajoje. Palyginti su silpnojo surišimo mažesnio užterštumo $P_{frequency}$ vaizdu, silpnojo

surišimo didesnio užterštumo $P_{frequency}$ vaizde matyti mažiau defektinių zonų (**8.2.6 pav.**).

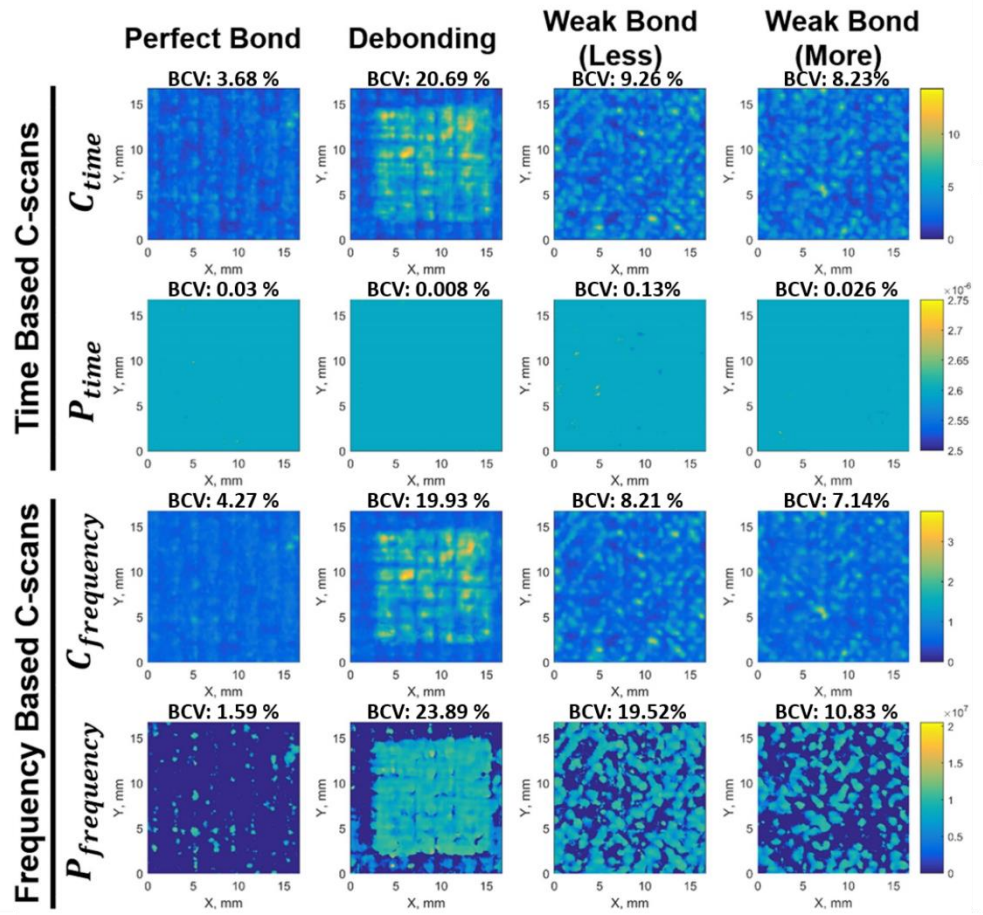

8.2.6 pav. Sąsajos vizualizacija su keturių skirtingų požymių išskyrimu [11]

Šie keturi skirtingi pažangūs inovatyvūs sąsajos vizualizavimo metodai taip pat buvo įvertinti kiekybiškai, naudojant surišimo charakteristines vertes (BCV), t. y. vidutinę kvadratinę pastebimųverčių tikimybę iki didžiausios pastebimos vertės. Apskaičiuota BCV atspindi defekto tikimybę kiekvienoje vizualizacijoje, nes didžiausia pastebėta vertė atitinka didelį ultragarsinio impedanso skirtumą sąsajoje (**8.2.1 lentelė**). BCV vertės pateikiamos kiekvienos sąsajos vizualizacijos viršuje. BCV atitinka kokybinę vaizdų analizę ir rodo, kad silpnų jungčių aptikimą galima pagerinti naudojant dažnio faze pagrįstą vizualizaciją $P_{frequency}$. Apskritai rezultatai rodo, kad akustinėje mikroskopijoje naudojami aukšto dažnio fokusuoti keitikliai yra puikus pasirinkimas sąsajos kokybei vizualizuoti surištose struktūrose. Be to, sukurtas vėlesnio apdorojimo algoritmas gerai atlieka silpno ryšio aptikimo funkciją, nepriklausomai nuo tobulo ryšio patikrinimo rezultatų.

8.2.1 lentelė. Sujungimų charakteristinės vertės (BCV) [11]

Sujungimo kokybė: / Dviejų medžiagų ribos vizualizacija		Geras sujungimas	Nesukibimas	Silpnas sujungimas, (daugiau užteršta)	Silpnas sujungimas, (mažiau užteršta)
Laiko domenas	C_{time}	3,68 %	20,69 %	8,23 %	9,26 %
	P_{time}	0,030 %	0,008 %	0,026 %	0,134 %
Dažnio domenas	$C_{frequency}$	4,27 %	19,93 %	7,14 %	8,21 %
	$P_{frequency}$	1,59 %	23,89 %	10,83 %	19,52 %

8.3. Pažangi indukcinė termografija, skirta klijavimo kokybei vertinti

Šiame skyriuje daugiausia dėmesio skiriama elektromagnetinių (įskaitant termografiją) parametrų ir klijų sukibimo kokybės ryšiui. Be ankstesniame skyriuje aptartų ultragarsinių parametrų, šiame skyriuje nagrinėjamas sukibimo kokybės ryšys su elektriniais ir termografiniais parametrais. Konkrečiai, anglies pluošto kompozito ir epoksidinio pluošto paprastieji sujungimai buvo vertinami atliekant skaitmeninius ir eksperimentinius sūkurinių srovių (indukcinės) termografijos tyrimus. Įdiegtas inovatyvus po apdorojimo (angl. *post-processing*) algoritmas, galintis aptikti silpnus ryšius ir delaminaciją.

8.3.1. Skaitiniai tyrimai

Baigtinių elementų metodas (BEM) taikomas modeliuojant kompozito ir klijų paprastojo sujungimo su 12,7 mm žalvario delaminaciniu intarpu sūkurinės srovės (indukcinės) termografijos reakciją [92]. Indukcinės termografijos modeliavimas apima susietą elektromagnetinę ir šiluminę problematiką [58,93]. Silpnosios elektromagnetinės A-φ ir nodinės šiluminės formulės naudojamos sūkurinėms srovėms ir temperatūros pasiskirstymui bandinio paviršiuje apskaičiuoti.

Sūkurinėms srovėms sužadinti penkių vijų indukcinė ritė uždedama 2 mm atstumu (**8.3.1 pav.**). Siekiant optimizuoti defektų aptikimą su temperatūros įvertinimo kreive, buvo ištirti keli elektromagnetinio lauko matavimo parametrai. Optimali išėjimo galia pastebėta pasirinkus 600 amperų aktyvacijos srovę, o sūkurinių srovių sistemos dažnis turėtų būti ne mažesnis kaip 100 kHz.

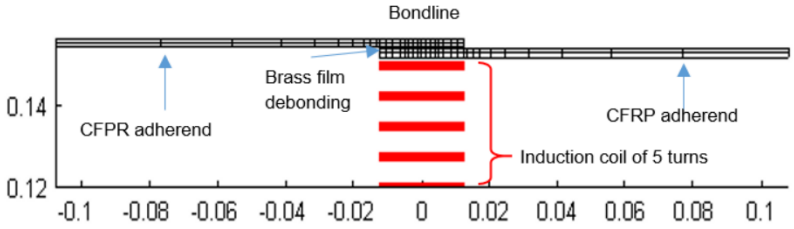

8.3.1 pav. Indukcinės termografijos modeliavimas, šoninis vaizdas

Be to, simuliuotos laiko priklausomybės kreivės buvo ištirtos su optimizuotais matavimo parametrais regionuose be defektų ir su žalvario inkliuzais. Modeliuojama paviršiaus temperatūra, esant 100 kHz dažniui ir 600 A srovei, parodyta **8.3.2 pav.** Simuliacijose elektros srovė buvo leidžiama 2 sekundes. Temperatūros kitimas paviršiuje apskaičiuotas vienai minutei (60 sekundžių). Didžiausia paviršiaus su defektu temperatūra pasiekta ties 6 sekunde, kai skirtumas nuo idealaus ryšio srities yra beveik didžiausias. **8.3.3 pav.** parodyta temperatūros priklausomybė nuo laiko žalvario plėvelės viduryje. Temperatūra pasiekė maksimumą per 2 s ir buvo 35 °C. Išjungus generatorių, temperatūra ties metalinės plėvelės viduriu pradeda mažėti dėl šiluminės konvekcijos.

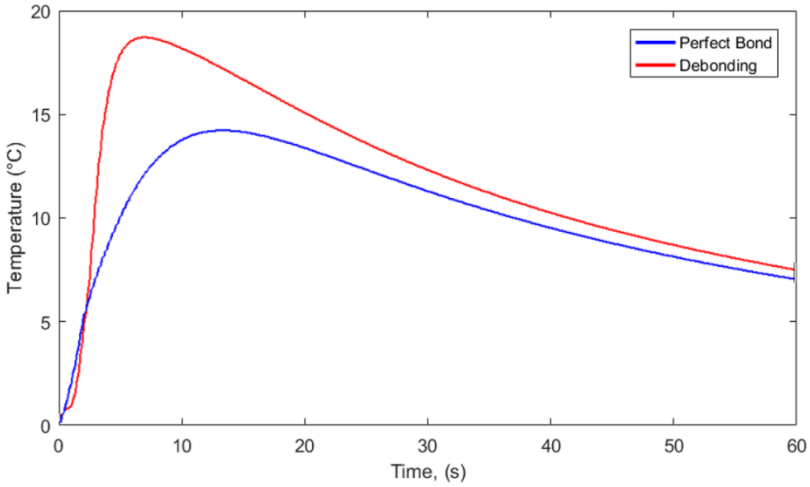

8.3.2 pav. Temperatūros kitimas laiko atžvilgiu paviršiaus centre, kai yra ir kai nėra defektų [92]

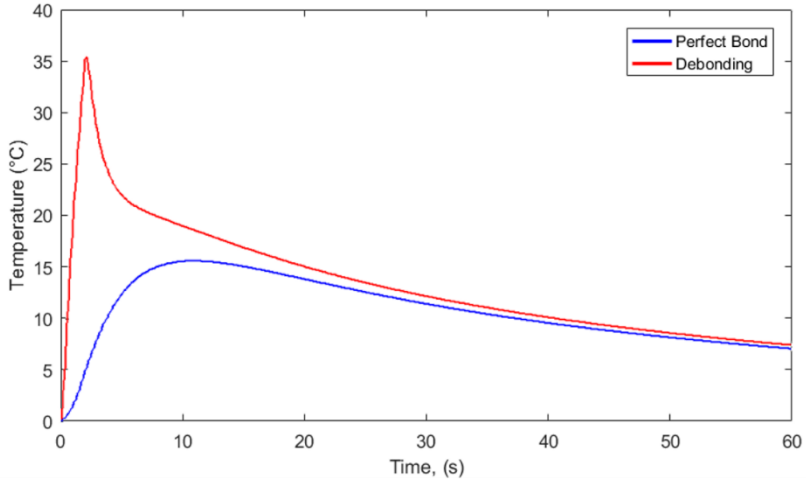

8.3.3 pav. Temperatūros kitimas žalvario plėvelės viduryje laike [92]

8.3.2.Eksperimentiniai tyrimai

CFRP-epoksido paprastojo sujungimo jungtys su dirbtine delaminacija naudojant atskyrimo plėvelę, žalvario plėvelė ir silpno ryšio defektai buvo tiriami naudojant sūkurinių srovių impulsinę suspaudimo termografiją. Daugiapakopis signalų apdorojimas taikytas siekiant susieti fizikines savybes, tokias kaip užterštumo gylis, dydis ir laidumas, su pastebėtu elektromagnetiniu ir terminiu atsaku.

Pirma, Barkerio kodas su impulsų kompresijos metodu buvo įdiegtas tiriant bandinius sūkurinių srovių termografijos metodu. Yra žinoma, kad impulsų kompresija (užfiksuotų duomenų impulsinis atsakas, apskaičiuojamas atliekant

konvoliuciją su atitinkamai suderintu filtru) pagerina skiriamąją gebą. Atliekant sūkurinių srovių impulsų suspaudimo termografiją (ECPuCT), bandinys sužadinamas atitinkamu kodu (40 amperų ir 240 kHz dažniu srove, kad nebūtų pažeistas bandinys), šiuo atveju – Barkerio kodu Nr. 13 (BC). Rezultatai fiksuojami infraraudonųjų spindulių kamera su 50 kadrų per sekundę įrašymo dažniu (**8.3.4 pav.**), o šiluminiai vaizdai renkami visą kaitinimo ir aušinimo laiką (**8.3.4 pav.**). Iš įrašyto šiluminio atsako pašalintas pakopinis kaitinimas ir pritaikomas konvoliucinis suderintas filtras (**8.3.5 pav.**).

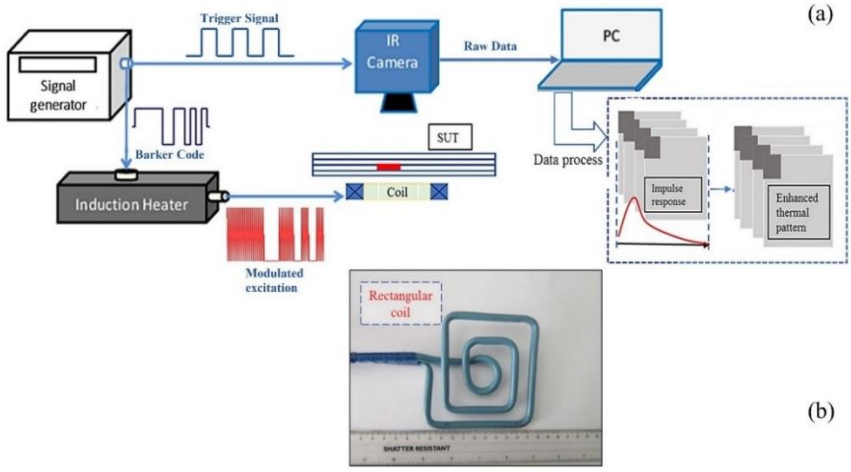

8.3.4 pav. Impulsinės kompresinės sūkurinių srovių termografijos eksperimentinė įranga (a) ir indukcinė spiralė (b) [12]

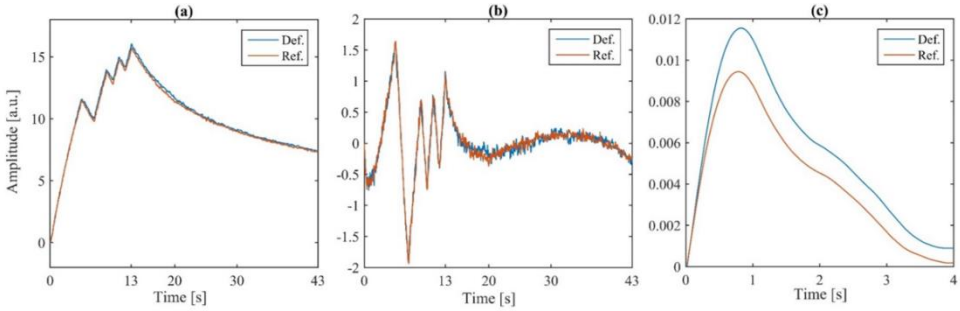

8.3.5 pav. Atraminio taško pavyzdys – signalai pirminės būklės (tobulas ryšys) ir užterštoje srityje (žalvario intarpai): a) gautas neapdorotas signalas, b) neapdorotas signalas, pašalinus pakopinio kaitinimo įtaką, c) impulsinis atsakas po impulsų suspaudimo proceso [12]

Kitame etape netolygiam kaitinimo modeliui, kurį lemia medžiagos anizotropija ir ritės forma, pašalinti buvo taikomi du skirtingi algoritmai: tobulo ryšio atėmimo ir dalinio mažiausių kvadratų (PLS) metodas. Taikant tobulo ryšio atimties metodą, ECPuCT metodu buvo tiriamas bandinys be defektų, tada tobulo ryšio rezultatai tiesiogiai atimami iš rezultatų su skirtingais užteršimais. PLS metodu buvo atliekami

trys pagrindiniai veiksmai: įrašyti trimačiai termografijos duomenys (x, y ir laikas) pertvarkyti į dvimatį duomenų rinkinį; apskaičiuoti daliniai mažiausi kvadratai; pašalinti daliniai mažiausi kvadratai, atitinkantys netolygų kaitinimą, ir vėl atkurti duomenys, pašalinus šiuos PLS narius. Šių dviejų metodų rezultatai pateikti (**8.3.6 pav.**).

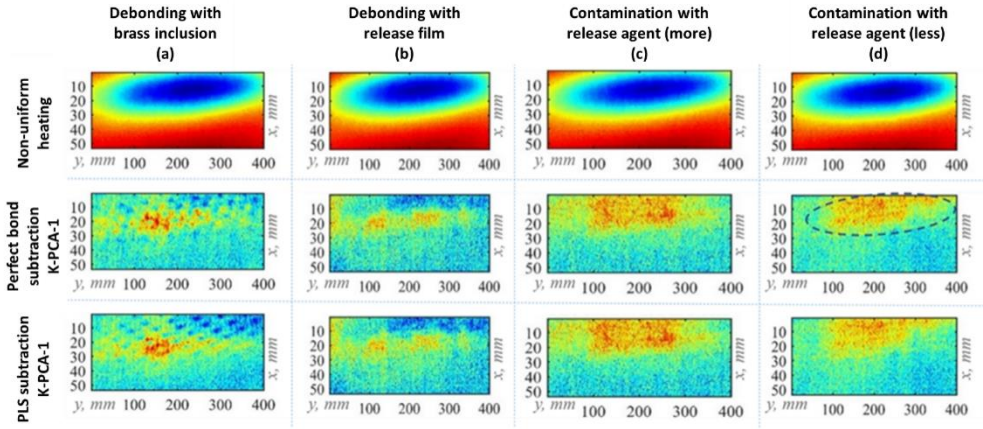

8.3.6 pav. Nevienodos kaitinimo reakcijos: a) nepašalinta, b) pašalinta su tobulo ryšio atimtimi, c) pašalinta su PLS atimtimi [12]

Be to, impulsų atsakai buvo analizuojami naudojant slankiojančius laiko intervalus ir KERNEL pagrįstą pagrindinių komponenčių analizę (K-PCA). Geriausias vaizdas, rodantis užterštumą arba dirbtinį defektą, buvo patikrintas naudojant išvestines ir impulsų atsako laiko fazės vaizdus.

Skirtingų dirbtinių defektų dydis buvo įvertintas pagal K-PCA rezultatų erdvinę kurtozę. Dviejų skirtingų dydžių žalvario plėvelė buvo nustatyta nubraižius erdvinės kurtozės reikšmių sumą virš pasirinktos srities (**8.3.7 pav.**), nors sunku nustatyti tikslias delaminacijos vertes dėl persidengusių dviejų Gauso pasiskirstymų viršūnių. Atpalaiduojamosios plėvelės delaminacijos dydis su dviem vienodo dydžio defektais buvo nustatytas pagal kurtozės reikšmes, kaip matyti **8.3.8 pav.** Šiuo atveju Gauso pasiskirstymo smailės yra labiau atskyrusios, o kurtozės reikšmės yra panašios.

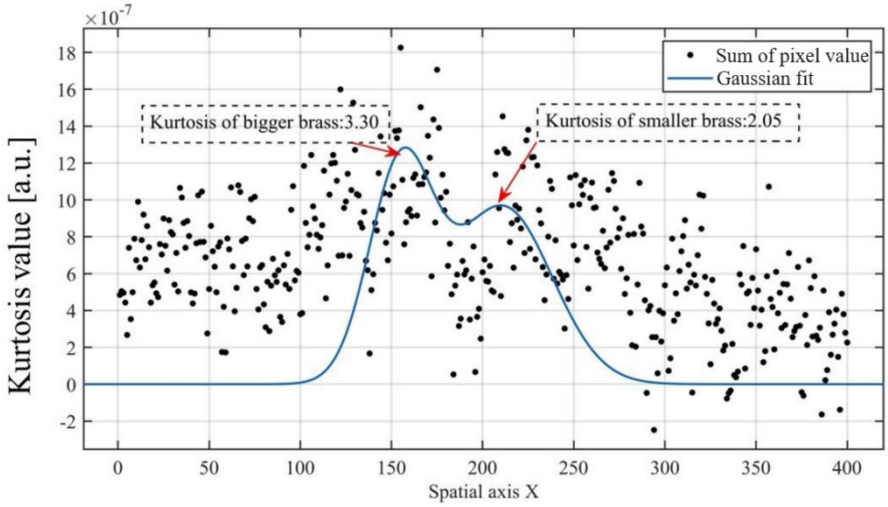

8.3.7 pav. Didesnių ir mažesnių žalvarinių plėvelių erdvinės kurtozės rezultatai [12]

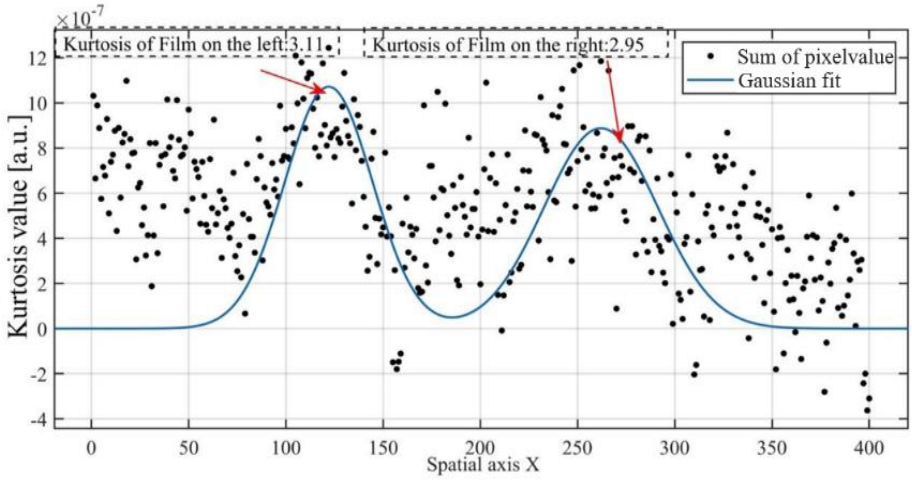

8.3.8 pav. Erdvinės kurtozės rezultatai nustatant atpalaiduojamosios plėvelės dirbtinių atskyrimų dydį [12]

Užterštumo gylis ir laidumas buvo apskaičiuoti pagal impulsų atsako išvestines ir laiko fazės vaizdus kartu su pirmojo K-PC laiko intervale. Elektrinis laidumas dominuoja pirmuosiuose 15 kadrų; šiluminis laidumas pirmauja po 60 kadrų (aušinimo etapas) (**8.3.9 pav**). Kadangi žalvaris yra elektrai laidi medžiaga, dirbtinio žalvario delaminacijos defekto elektromagnetinis atsakas labiausiai kinta per pirmuosius 15 kadrų. Pastebėta, kad kiekvieno defekto šiluminio atspindžio laikas yra

panašus, kai defekto gylis koreliuoja su kiekvienu bandiniu, nes kiekvienas dirbtinis defektas yra tame pačiame gylyje nuo paviršiaus.

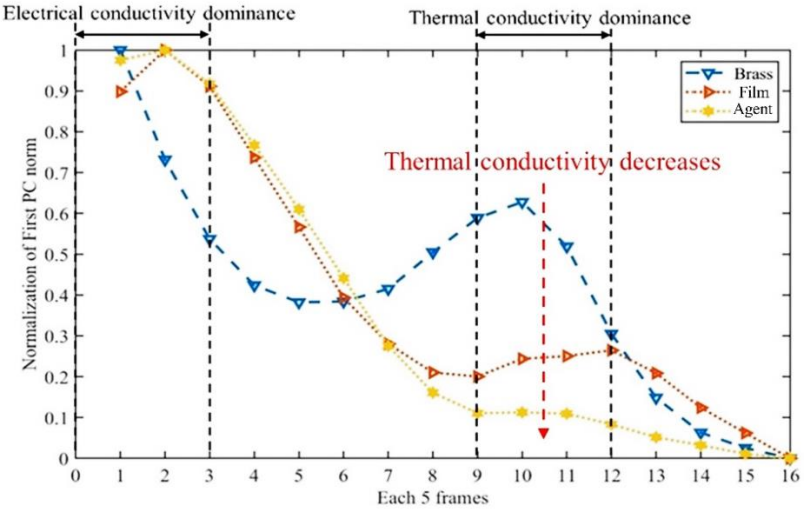

8.3.10 pav. Skirtingų užterštumų pirmoji PC norma, palyginti su 5 kadrų skaičiumi (slankiojantis langas); kur žalvaris – atsiklijuojantis žalvario intarpas, plėvelė – atsiklijuojančios plėvelės atsiklijavimas, o priemonė – atsiklijuojančios priemonės užterštumas [12]

8.4. Įvairių ultragarsinių nedestrukcinių tyrimo metodų, skirtų surišimo kokybei vertinti, palyginimas

Ankstesniuose skyriuose ultragarsinių, elektromagnetinių ir šiluminių parametrų, susijusių su įvairių tipų intarpais kompozito ir klijų jungtyse, nustatymas buvo tiriamas vienu NDT metodu, o šiame skyriuje daugiausia dėmesio skiriama išsamiam skirtingų ultragarsinių NDT metodų palyginimui, siekiant nustatyti metalo ir klijų jungčių atskyrimą ir dydį.

Aliuminio-epoksido-aliuminio paprastosios sandūros jungtys su penkiais kvadratiniais dvipusiais dirbtiniais atskyrimo defektais (12,7 mm ilgio briaunos), esančiais ties sąsaja, buvo tiriamos ultragarsinėmis tūrinėmis bangomis, naudojant panardinimo per perdavimą (angl. *immersion through transmission*), impulsų echo panardinimo (angl. *immersion pulse-echo*), aukšto dažnio akustinės mikroskopijos (SAM) ir oru susietu perdavimo (angl. *air-coupled through-transmission techniques*) metodais. Be to, taip pat buvo atliekami ir valdomųjų bangų tyrimai (GW) naudojant dvi skirtingas sąrankas: kontaktas prie kontaktinio keitiklio, su oru susietas sužadinimas su kontaktiniu keitikliu.

Imersinio bandymo privalumai – didelis bandymo dažnis ir lengvas sujungimas, tačiau dėl panardinimo į vandenį jis yra ribotas medžiagų ir defektų tipų atžvilgiu. Su oru susietas bandymas leidžia atlikti tik bekontaktį tikrinimą ir fokusuoti ultragarso spindulį, tačiau dėl impedanso neatitikimo labai sumažėja amplitudė. Kontaktinis bandymas su GW gali veikti iki 5 MHz dažniu, jis leidžia greičiau gauti duomenis ir užtikrina geresnį ryšį nei oro ryšys, tačiau jam reikia sudėtingų nustatymų ir sunku tikrinti didelius plotus. Su oru susietas sužadinimas su kontaktų priėmimu GW tikrinimo metu gali užtikrinti tolimą tikrinimą su galimybe pasirinkti režimą, tačiau mažas signalo ir triukšmo santykis nėra pageidautinas.

Panardinimo per perdavimą ir impulsinio echo tyrimai buvo atliekami naudojant 10 MHz fokusuotus keitiklius „TecScan“ matavimo sistema (**8.4.1 *pav***., a). Lipnusis sujungimas buvo tiriamas su SAM, kaip aprašyta 1.2 skyriuje ir parodyta **1.2.2 pav.** Su oru susietas ultragarsinis perdavimo metodas atliktas naudojant 300 KHz plokščius keitiklius, o bandinys padėtas iškart už apskaičiuoto artimojo lauko galo (**8.4.2 pav.**)

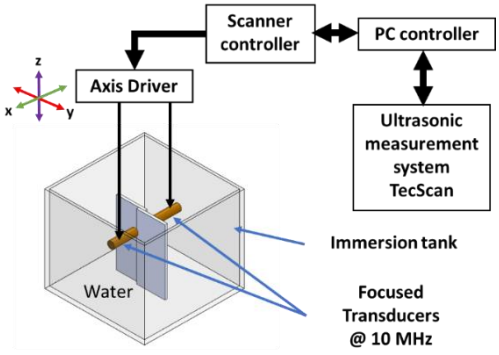

8.4.1 pav. Eksperimentinė sąranka: panardinamasis ultragarsinis NMT su transmisine (a) ir skenuojamąja akustine mikroskopija (b) [13]

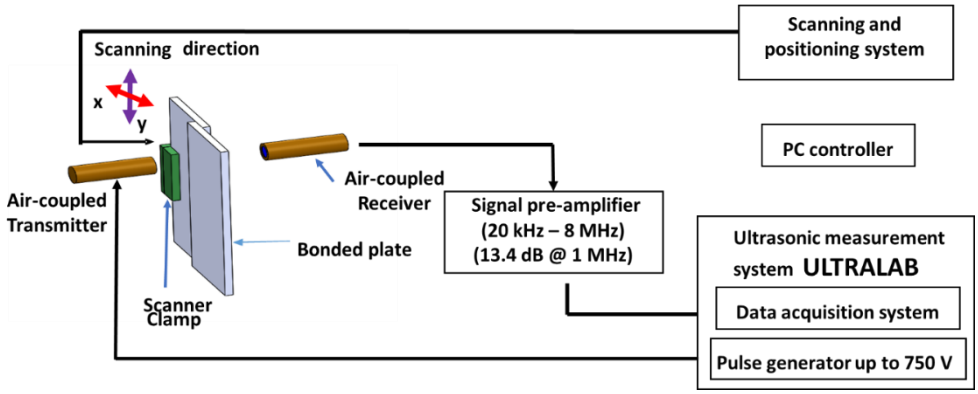

8.4.2 pav. Panardinimo per perdavimą su oru susieta eksperimentinė sąranka [13]

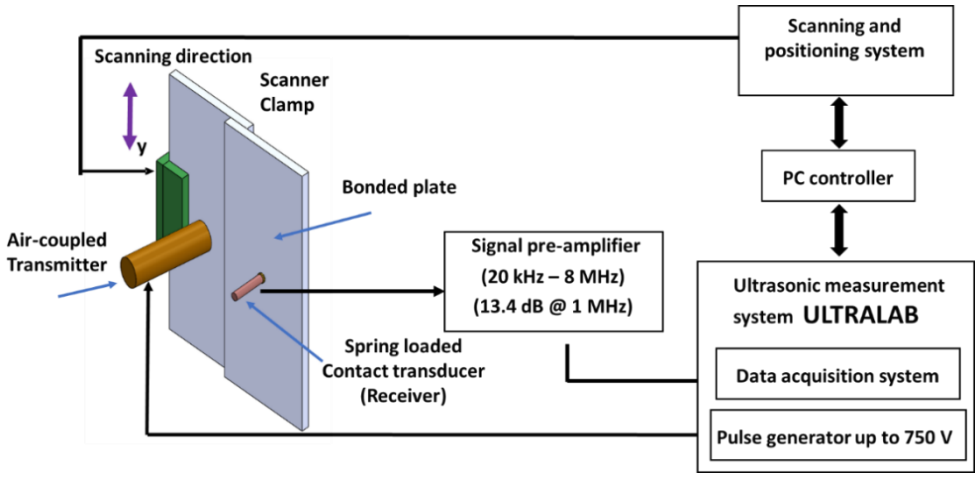

8.4.3 pav. Valdomųjų bangų tikrinimo sąranka su kontaktiniu ultragarso keitikliu, sujungtu su oru [13]

Prieš atliekant valdomųjų bangų patikrinimus, buvo apskaičiuotos aliuminio adherendinės plokštelės dispersijos kreivės. Taip pat buvo atliktas skaitinis tyrimas trimačiu baigtinių elementų metodu. Buvo modeliuojamas ultragarso bangų sklidimas, kai jos sužadinamos su oro jungtimi sujungtu keitikliu ir priimamos su kontaktine jungtimi. Taigi, šiame eksperimentine atstumas tarp oro ryšio ir kontaktinio keitiklio buvo nustatytas 65 mm, o oro ryšio sužadinimo kampas – 10°, kad būtų generuojama A0 valdomųjų bangų moda (**8.4.3 pav.**). Panašiai atliktos kontakto su kontaktu valdomų bangų patikros, išlaikant 100 mm atstumą tarp dviejų keitiklių (**8.4.4** pav.).

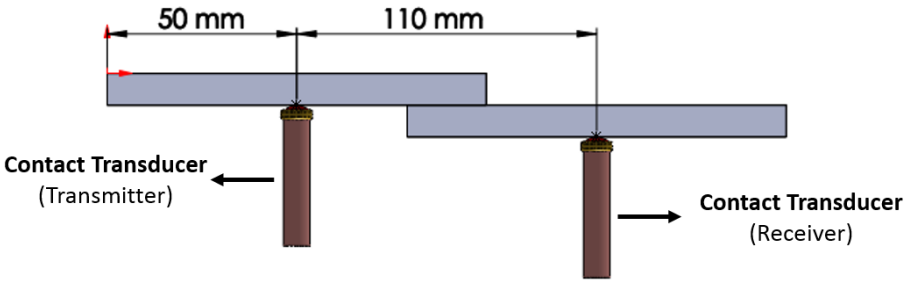

8.4.4 pav. Eksperimentinės sąrankos schema, skirta valdomosioms bangoms patikrinti, su dviem kontaktiniais ultragarso keitikliais [13]

Defektų aptikimo efektyvumas buvo geresnis taikant panardinimo metodus nei taikant oro ar kontaktinį metodus. Visi penki defektai atskirai buvo nustatyti taikant imersijos perdavimo, imersiniu impulsinio echo ir SAM metodus; keturi buvo nustatyti taikant oro ryšio perdavimo metodą (**8.4.5 pav.**)**..**). Kontroliuojant valdomosiomis bangomis, kai sužadinimo būdas yra oro ryšys, nustatyti trys defektai, o valdomųjų bangų kontakto su kontaktiniu keitikliu metodu nustatyti keturi defektai (**8.4.5 pav.**). Defektą, esantį arti krašto, sunku aptikti atliekant ultragarsinį tyrimą su valdomosiomis bangomis dėl ribinių atspindžių (**8.4.5 pav.**)**..**).

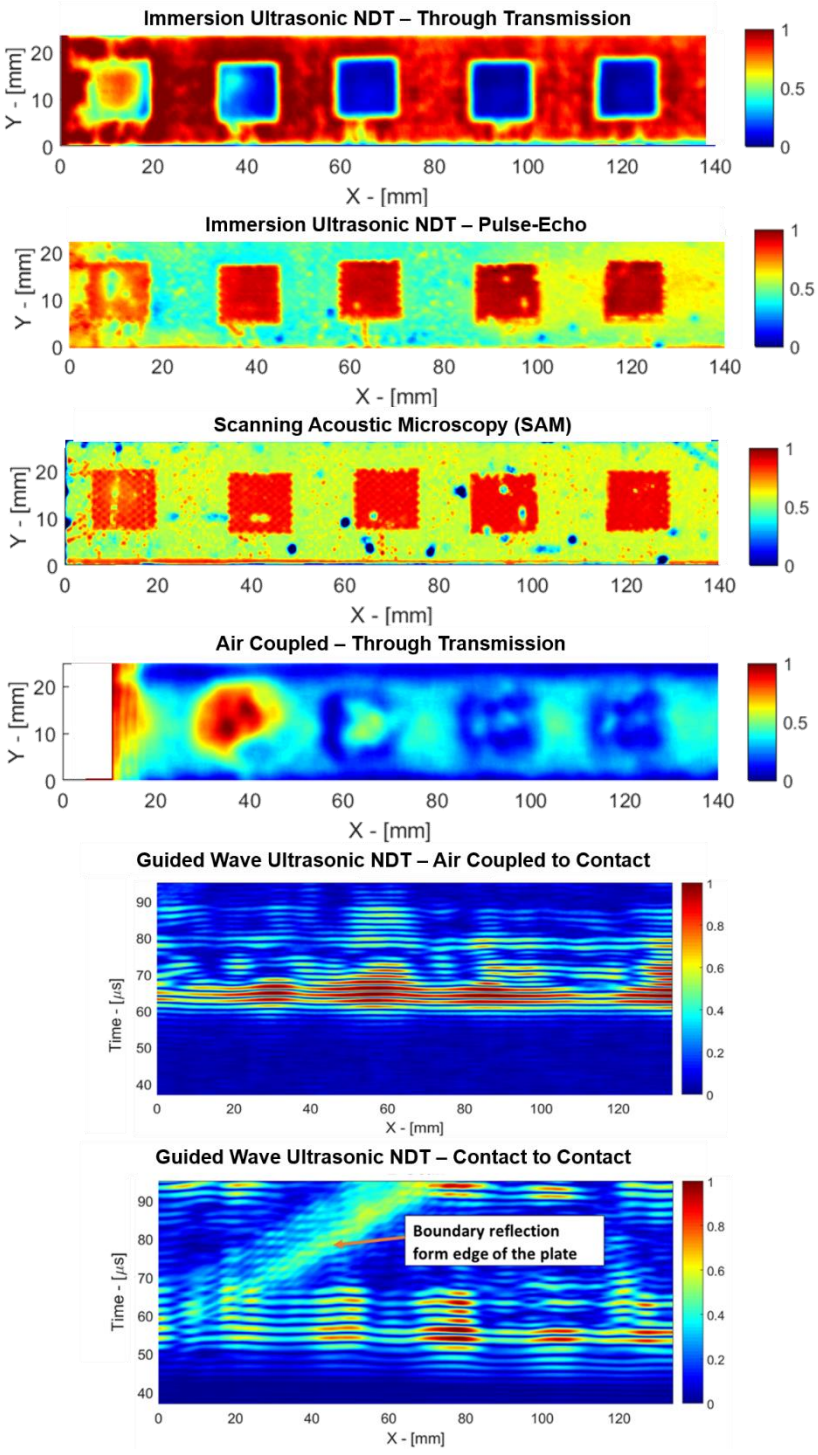

8.4.5 pav. C-skenavimo ir B-skenavimo rezultatai atliekant ultragarsinius NDT patikrinimus

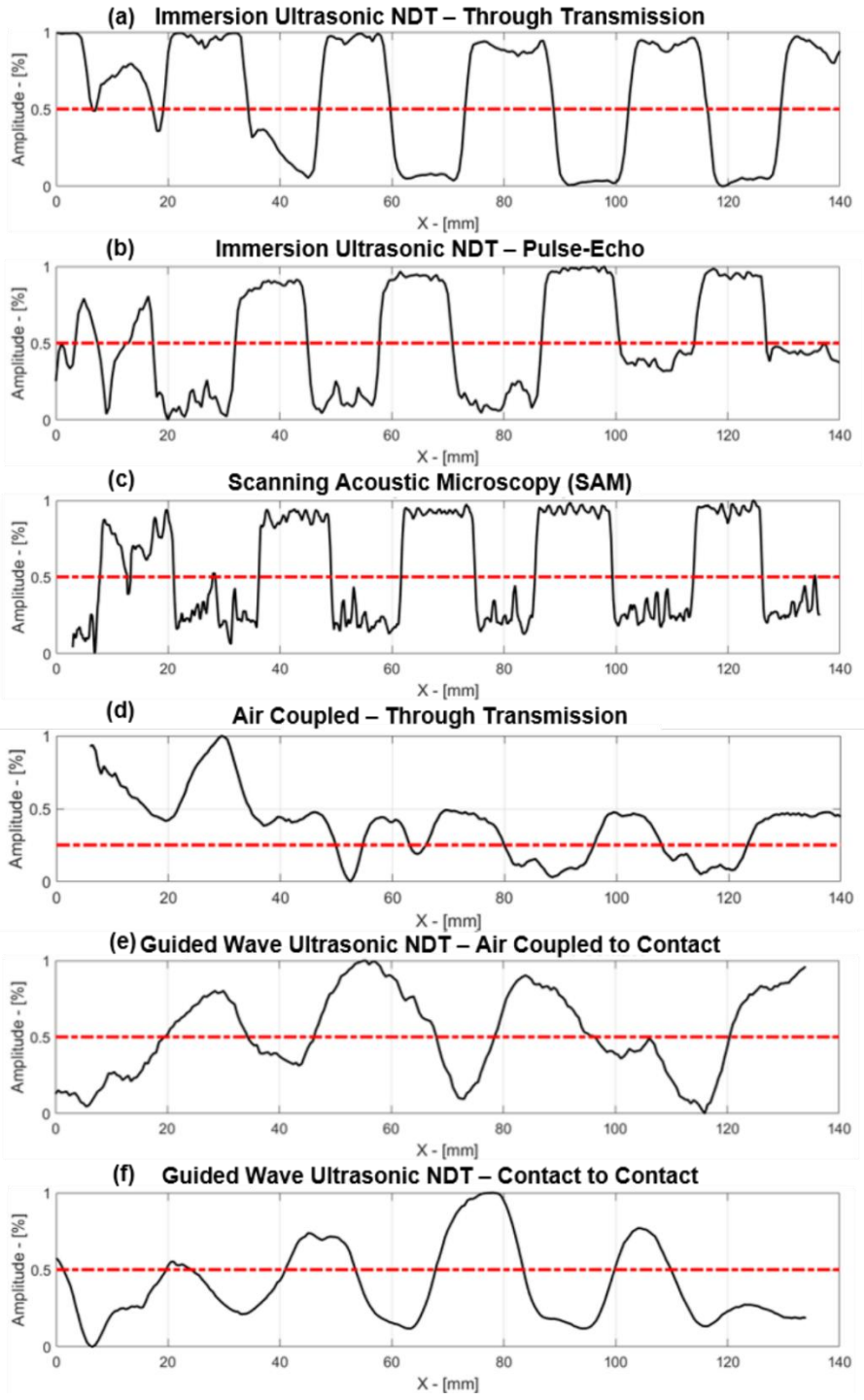

8.4.6 pav. Decibelų kritimo defektų dydžio nustatymo ir aptikimo rezultatai taikant kiekvieną metodą

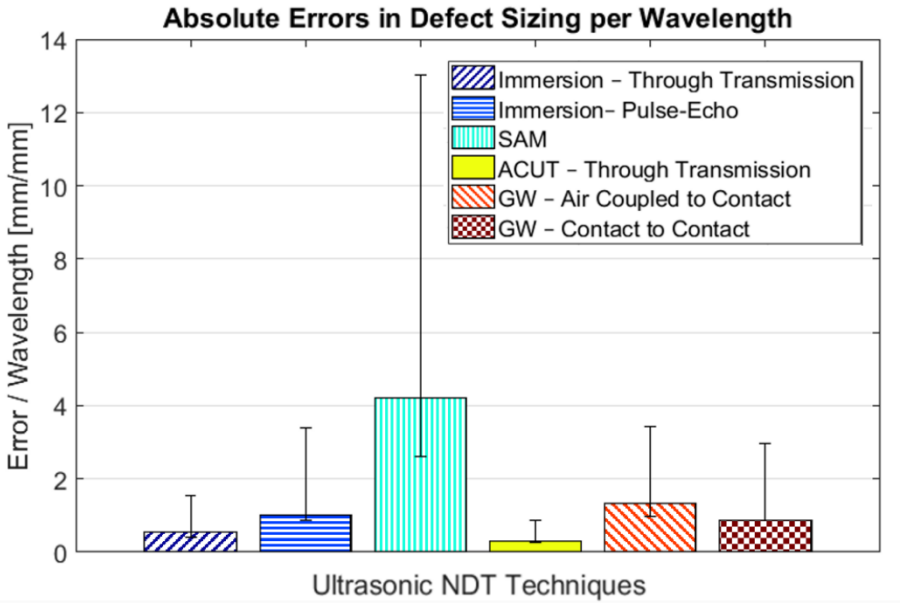

8.4.7 pav. Defektų dydžio nustatymo normalizuotos absoliutinės paklaidos pagal bangos ilgį ir ultragarsiniai metodai

Kiekvieno metodo defektų dydžiai buvo nustatyti taikant decibelų kritimo metodiką (**8.4.6 pav.**)**..**). Be to, pagal žinomą defekto dydį (12,7 mm) buvo apskaičiuotos kiekvieno metodo absoliučiosios paklaidos (**8.4.7 pav.**). Atsižvelgiant į ultragarso bangos ilgį, kiekvieno metodo defektų dydžio nustatymo rodikliai buvo normalizuoti. Šis palyginimas priklauso nuo vidutinių absoliutinių defektų dydžio nustatymo paklaidų ir ultragarso bangos ilgio santykio. **8.4.7. pav.** parodyta, kad tarp imersijos metodų ir SAM mažiausia paklaida yra imersijos per perdavimo metodą (angl. *immersion through transmission*). Perdavimas per oro sąsają rodo mažesnes paklaidų vertes nei valdomomis bangomis. Kontaktinis-kontaktinis metodas veikia geriau nei su oro-kontaktinis metodas.

8.5. Pažangiosios ultragarsinės ir indukcinės termografijos duomenų sintezė ryšio kokybei vertinti

Šiame skyriuje daugiausia dėmesio skiriama ultragarsinio imersinio echo impulsinio metodo ir indukcinės termografijos duomenų sintezei, siekiant nustatyti skirtingų dydžių ir medžiagų dirbtinį atskyrimą, esantį CFRP-epoksido paprastojo sujungimo sandūrose. Kaip nurodyta ankstesniame skyriuje, lyginant ultragarsinius metodus matoma, kad kiekvienas metodas turi neginčijamų privalumų ir apribojimų. Šiame skyriuje atlikta ultragarsinės imersinės echo impulsinės ir indukcinės termografijos metodų sintezė, taikant post-processing (po abdorojimo) duomenų apdorojimo metodus.

Kompozitinės-klijuotinės paprastosios jungtys su skirtingais dirbtiniais defektais, kaip aprašyta 1.2 skyriuje ir parodyta **1.2.1 pav.,.,** buvo tiriamos ultragarsiniu imersiniu echo-impulsiniu metodu ir transmisine indukcine termografija. Ultragarsiniai tyrimai atlikti naudojant 10 MHz centrinio dažnio fokusuotąjį keitiklį imersiniu echo-impulsiniu režimu (**8.5.1 pav., a**). Visas klijavimo plotas buvo nuskenuotas naudojant kryptinio panardinimo nustatymus, o A-skenavimo rezultatai atlikti 0,5 mm žingsniu. Indukcinės termografijos tyrimai buvo atliekami perdavimo režimu – bandinys padėtas tarp ritės ir kameros (**8.5.1 pav., b**). Indukcinė ritė (spiralinės konstrukcijos, vidinis skersmuo 15 mm, išorinis skersmuo 25 mm, aukštis 30 mm, penkių vijų) buvo orientuota taip, kad ritės centras būtų defekto vietos centre. Eksperimentų metu 105 kHz nešančiuoju dažniu pasiekta 200 amperų sužadinimo galia per 1 sekundę. Bandinio paviršiaus temperatūros pokyčiai buvo registruojami infraraudonųjų spindulių kamera 60 sekundžių laikotarpiu, 25 kadrais per sekundę.

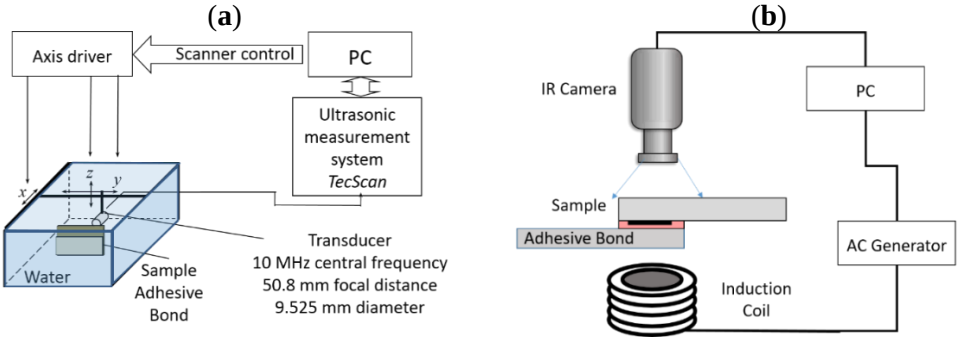

8.5.1 pav. Eksperimentinės sąrankos schemos: (a) ultragarsinis neardomasis bandymas (NDT) ir (b) indukcinė termografija [14]

Siekiant atlikti duomenų sintezę, daugiapakopiai išankstinio apdorojimo metodai buvo pritaikyti ultragarsinio NDT ir indukcinės termografijos rezultatams apdoroti (**8.5.2 pav.**) Pirmiausia neapdoroti duomenys buvo filtruojami. Kadangi tyrimai vyko skirtingose aplinkose, kiekvieno tyrimo vietinės koordinatės perkeltos į pasaulinę sutampančią koordinačių sistemą. Tada ultragarsiniai duomenys buvo interpoliuoti, kad atitiktų tas pačias mastelio koordinačių vertes registravimo etape.

Tada gauti ultragarso ir termografijos duomenų rinkiniai buvo normalizuoti skalėje nuo 0 iki 1.

Kitame etape, remiantis pažangiu apdorojimo algoritmu, iš ultragarsinės ir termografinės patikros rezultatų buvo išskirtos požymių matricos. Atliekant ultragarsinę patikrą išskirtas požymis – sąsajos atspindžio amplitudė nuo smailės iki smailės, o indukcinės termografijos atsakui buvo taikoma pagrindinių komponenčių analizė. Išskirti požymiai buvo įtraukti į duomenų sintezės programą kaip šaltinis.

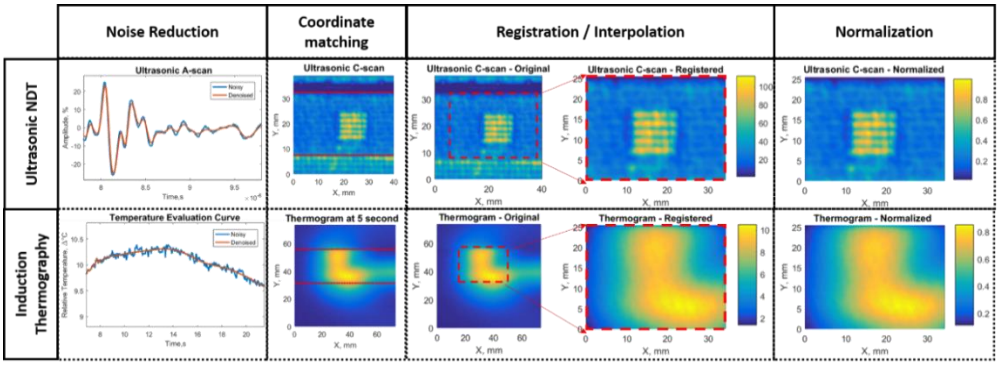

8.5.2 pav. Duomenų gavimo pirminio apdorojimo etapai: triukšmo mažinimas, koordinačių atitikimas, registracija (interpoliavimas), normalizavimas [14]

Išskirtoms pikselių lygmens požymių matricoms buvo taikomi šeši skirtingi duomenų sintezės algoritmai (**8.5.1 lentelė**): vidurkis (1), skirtumas (2), svertinis vidurkis (1UT5TH) ir (5UT1TH) (3), Hadamardo sandauga (4) ir Dempsterio ir Šaferio derinimo taisyklė (5).

8.5.1 lentelė Duomenų suliejimo algoritmai [14]

Duomenų sintezės algoritmai	**Aprašymas**	**Matematinė formulė**	
Vidurkis	pikselių lygmenyje dviejų šaltinių: UT[1] ir TH[2] vidurkis	$(UT + TH)/2;$	(1)
Skirtumas	pikselių lygmenyje , vienos matricos (TH) atėmimas iš kitos (UT)	$(UT - TH);$	(2)
Svertinis vidurkis	pikselių lygmenyje , svertinis vidurkis, kai viena matrica turi keturis kartus didesnį svorį nei kita	$((5xUT) + TH)/6;$ $\big(UT + (5xTH)\big)/6;$	(3)
Hadamardo sandauga	vienodo dydžio matricų daugyba	$(UT \circ TH)_{ij} = (UT)_{ij}(TH)_{ij};$	(4)

Dempsterio ir Šaferio derinimo taisyklė	įrodymų teorija, pagrįsta masės, tikėjimo ir tikėtinumo funkcijomis	$(m_1 \oplus m_2)(A) = \frac{1}{K-1} \sum_{B \cap C = A \neq \emptyset} m_1(B) m_2(C)$; $where$ $K = \sum_{B \cap C = \emptyset} m_1(B) m_2(C).$	(5)

Kokybiškai ir kiekybiškai įvertinti trijų skirtingų sąsajų atskyrimo rezultatai, gauti taikant požymių matricos išskyrimą iš ultragarso ir termografijos duomenų bei duomenų sintezės programas. Kiekybinis kiekvieno NDT metodo ir duomenų sintezės algoritmo palyginimas buvo įvertintas naudojant plotą pagal atsako veikimo charakteristikos (ROC) kreives.

Atitrūkimo su atskyrimo plėvele vizualizavimas, ultragarso funkcija yra geriausia iš visų (**8.5.3 pav.**). Naudojant indukcinę termografiją, nepastebėta jokio reikšmingo defektų kontrasto. Naudojant duomenų vidurkių sintezės rezultatus gautas išlygintas požymis, tačiau pastebėtas defektų kontrastas yra daug didesnis 5UT-1TH svertinio vidurkio atveju nei kitų. Skirtumų sintezės matrica rodo santykinai didelį defektų aptikimo efektyvumą. Hadamardo sintezė rodo labai mažą defektų aptikimo efektyvumą, o DS veikia gerai, tačiau turi per daug klaidingai teigiamų rezultatų. Plotas pagal ROC kreivės skaičiavimus atitinka kokybinius rezultatus, o ultragarsinis požymis pasižymi aukščiausiu našumu, stebint svertinio vidurkio 5UT-1TH, skirtumo ir vidurkio rezultatus (**8.5.4 pav.**).

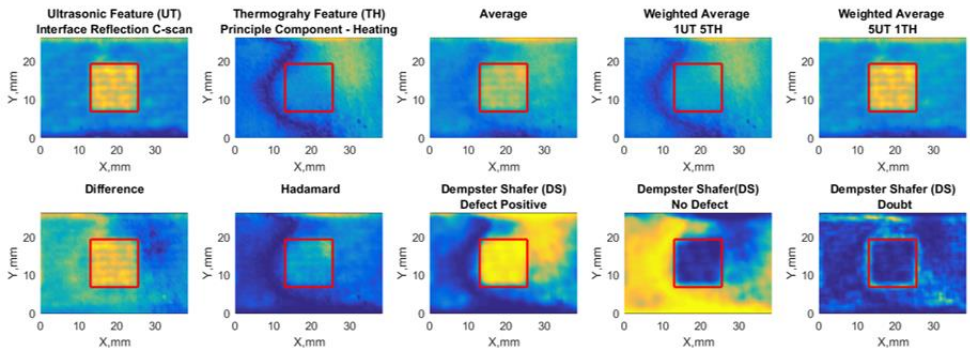

8.5.3 pav. Atitrūkimo su apsaugine plėvele (12,7 mm briaunos dydis) požymiais pagrįsto duomenų sintezės algoritmo rezultatai [14]

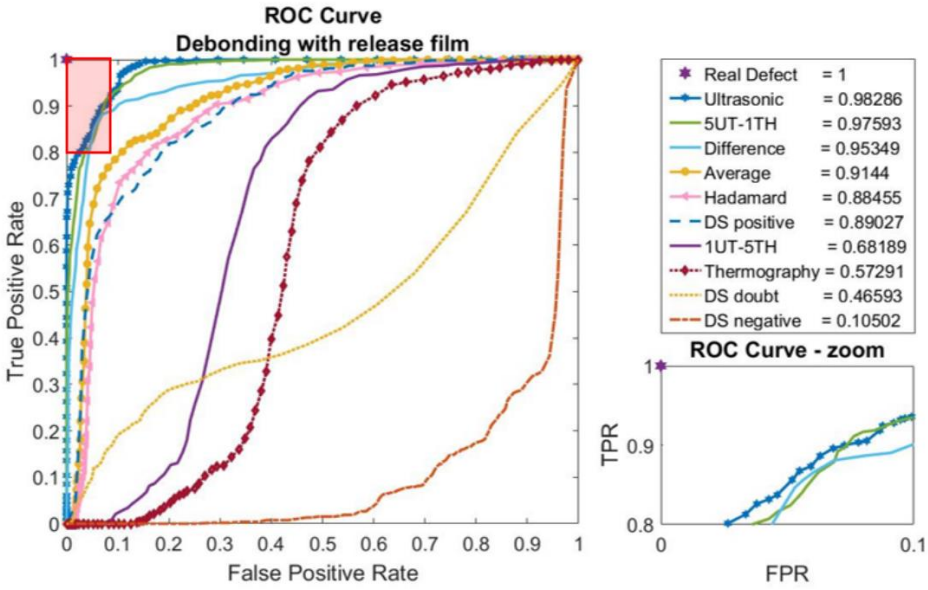

8.5.4 pav. Atitrūkimo su atskyrimo plėvele (12,7 mm krašto dydis) požymių sintezės duomenų vertinimo rezultatai su: a) imtuvo operacinės charakteristikos kreive (ROC) ir b) ploto po kreive (AUC) skaičiavimais su padidintu ROC kreivės vaizdu [14]

Išplėstinio NDT ir duomenų sintezės rezultatai, susiję su defektų šalinimu su žalvario intarpais (dideliais), rodo, kad defektų kontrastas buvo pasiektas visais metodais, o informacijos teorija pagrįstas DS veikia geriausiai (**8.5.5 pav.**)..). Kiekybiniai ploto po ROC kreive skaičiavimai taip pat rodo, kad beveik visi požymiai užėmė panašias vertes ir buvo veiksmingi nustatant defektus (**8.5.6 pav.**)..). Skirtumo skaičiavimai rodo mažas reikšmes, o tai rodo, kad tarp šaltinių nėra prieštaravimų.

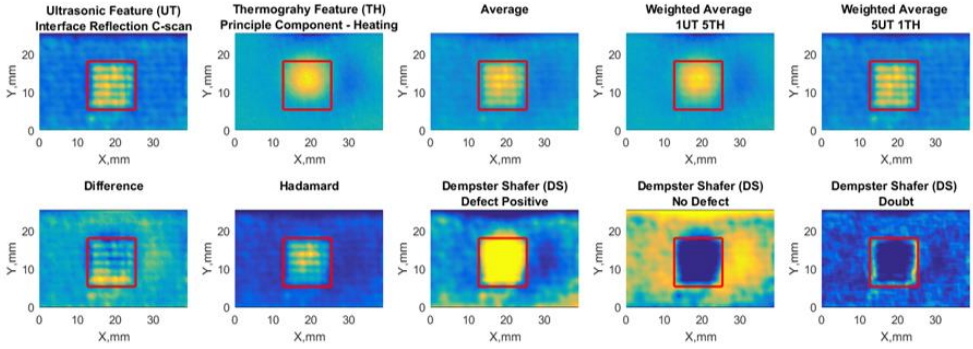

8.5.5 pav. Atitrūkimo su žalvario intarpu (12,7 mm krašto dydis) požymiais pagrįsto duomenų sintezės algoritmo rezultatai [14]

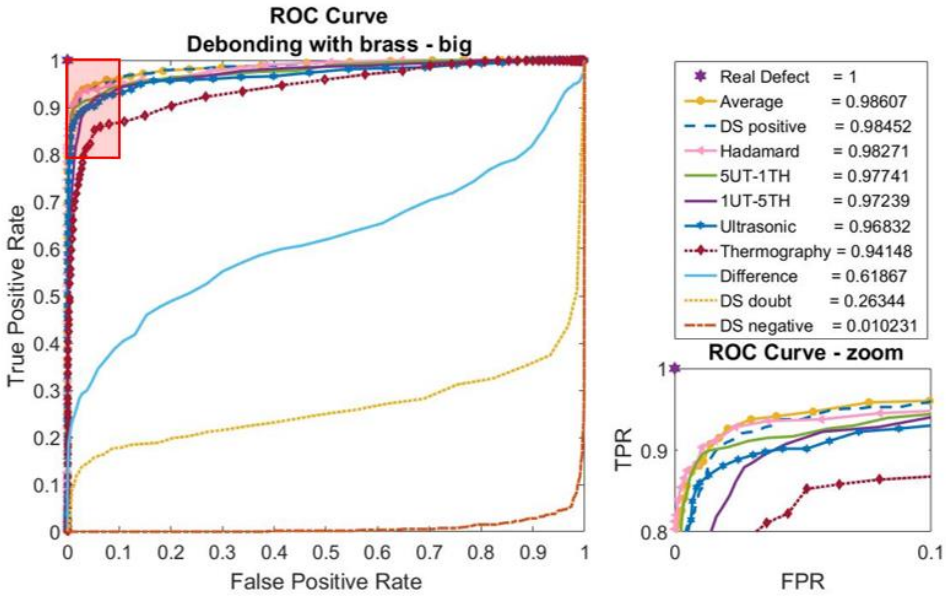

8.5.6 pav. Nesukibimas su žalvario inkliuzu (12,7 mm briaunos dydis) požymių sintezės duomenų vertinimo rezultatai su: (a) imtuvo operacinės charakteristikos kreive (ROC) ir (b) ploto po kreive (AUC) skaičiavimais su padidintu ROC kreivės vaizdu [14]

8.6. Pažangiųjų ultragarsinių neardomųjų tyrimų metodų kiekybinė analizė ryšio kokybei nustatyti

Šiame skyriuje daugiausia dėmesio skiriama kiekybiniams patikimumo vertinimams, atliekant pažangius ultragarsinius neardomuosius bandymus, skirtus klijų klijavimo kokybei įvertinti. Aukšto dažnio ultragarsinio aliuminio ir epoksidinių viengubo klijavimo jungčių vertinimo tikimybės aptikimo kreivės buvo įvertintos taikant naują ir ekonomiškai efektyvų modeliais pagrįstą metodą. Pirmajame skyriuje aprašytas naujas požymiais pagrįstas sąsajos vizualizavimo algoritmas buvo pritaikytas metalui ir klijams skirtoms vienguboms jungtims. Kiekvieno pasiūlyto požymio patikimumas įvertintas modeliu pagrįstomis aptikimo tikimybės (MAPOD) kreivėmis, atsižvelgiant į atskyrimą ir silpno sujungimo aptikimą.

Pažangios akustinės mikroskopijos tyrimų patikimumas vertinant sukibimo kokybę įvertintas modeliu paremtomis aptikimo tikimybės kreivėmis. Buvo tiriamos aliuminio-epoksido-aliuminio viengubo sujungimo jungtys su keturiomis sukibimo kokybės sąlygomis: nepriekaištingas sukibimas (PB), atskyrimas (DB), silpnas sukibimas dėl atpalaiduojamosios medžiagos (WB-RA), silpnas sukibimas dėl netinkamo kietėjimo (WB-FC).

SAM pasirinktas kaip ultragarsinis neardomasis vertinimo metodas, kaip aprašyta 9.2.2 skyriuje.

MAPOD kreivėms apskaičiuoti buvo atlikti keli žingsniai (**8.6.1 pav.)..**). Pirma, kiekvieno atvejo skaitmeniniai modeliai buvo apskaičiuoti pusiau analitine baigtinių elementų programine įranga CIVA. Skaitmeninio modelio rezultatai apskaičiuoti dvimatėje erdvėje kiekvienu klijavimo kokybės atveju, o ultragarsinis atsakas patvirtintas eksperimentiniais tyrimais (**8.6.2 pav.**).

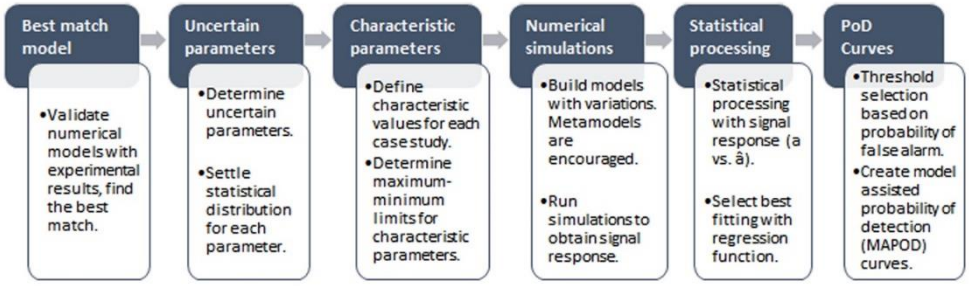

8.6.1 pav. Aptikimo tikimybės kreivių gavimo pagal modelį metodiniai etapai [15]

Apskaičiuojant MAPOD, atsižvelgiama į aštuonis neapibrėžtus parametrus, kurie kinta dėl bandinio, eksperimentinių, aplinkos ar žmogiškųjų veiksnių, būtent: epoksidinės medžiagos storio, epoksidinės medžiagos akustinių bangų greičio (išilginio), aliuminio storio, aliuminio akustinių bangų greičio (išilginio), vandens kelio, vandens akustinių bangų greičio, kritimo kampo ir defekto padėties gylyje (**8.6.1** lentelė).

8.6.1 lentelė. Neapibrėžtų parametrų ribos ir pasiskirstymo charakteristikos [15]

Pavadinimas	Apibrėžimas	Vidutinė reikšmė	Standartinis nuokrypis	Min reikšmė	Max reikšmė	Vienetas [SI]

Epoksido storis	Klijų storis	0,16	0,012	0,12	0,24	mm
Ultragarso bangų greitis epokside	Išilginių ultragarso bangų greitis	2990	300	1186	4706	m/s
Aluminio storis	Aluminio storis (viršutinės plokštelės)	1,6	0,007	1,59	1,66	mm
Ultragarso bangų greitis aliuminyje	Išilginių ultragarso bangų greitis (viršutinėje plokštelėje)	6300	50	6200	6600	m/s
Atstumas vandenyje	Atstumas tarp keitiklio ir bandinio	2,94	0,004	2,92	2,96	mm
Ultragarso banogs greitis vandenyje	Išilginių ulgtragarso bangų greitis vandenyje	1480	10	1447	1506	m/s
Kritimo kampas	Keitiklio pasvirimo kampas	0	1	-3	3	degree (angle)
Defekto gylis	Defekto atstumas nuo paviršiaus	1,6	0,012	1,6	1,72	mm

Be neapibrėžtų parametrų, atliekant MAPOD skaičiavimus reikia nustatyti charakteristines vertes. DB modelyje defekto dydis laikomas charakteringa verte. Silpno sukibimo dėl atpalaiduojamosios medžiagos modeliuose (WB-RA) kaip būdinga vertė pasirinktas alyvos įmaišymo storis. Silpno ryšio dėl netinkamo kietėjimo (WB-FC) modeliams būdinga verte nuspręsta laikyti epoksidinės medžiagos akustinį greitį.

Siekiant optimizuoti skaičiavimo sąnaudas, metamodeliams sudaryti buvo naudojami patvirtinti skaitiniai modeliai. Kiekvienas metamodelis buvo apskaičiuotas taikant Krigingo regresijos analizę daugiau kaip 1000 apskaičiuotų duomenų taškų.

Penki skirtingi požymių išskyrimo algoritmai buvo pasirinkti kaip signalo atsakas atliekant metamodelių skaičiavimus, kad būtų galima įtraukti pažangų ultragarsinio tolesnio apdorojimo algoritmą:

- Amplitudė nuo smailės iki smailės esant nurodytai užtvarai (angl. *Peak to Peak Amplitude*)
- Absoliučios didžiausios amplitudės uždelsimo laikas (angl. *Time Delay*)
- Didžiausia amplitudė dažnių srityje (angl. *Frequency Amax*)
- Absoliučios didžiausios amplitudės dažnio poslinkis (angl. *Frequency Shift*)
- Slopinimas lipniajame sluoksnyje (angl. *Attenuation*)

Visi šie požymiai buvo apskaičiuoti per pasirinktą laiko tarpą pagal ultragarsinio A-skenavimo rezultatus. Kadangi informacija apie sukibimo kokybę daugiausia yra sąsajos aiduose, dominanti užtvara buvo pasirinkta atsižvelgiant į viršutinės (pirmosios) ir apatinės (antrosios) epoksidinės medžiagos sąsajos aidus. DB atveju

pirmasis sąsajos atspindys pasirinktas DB-OPTION1. Siekiant sumažinti klaidingai teigiamų rezultatų skaičių, buvo pasiūlytas ir pritaikytas specialus vartų atrankos algoritmas (DB-OPTION2). DB-OPTION1 atveju vartai pradedami rinktis prieš pirmąjį sąsajos atspindį. Pagal DB-OPTION2, jei didžiausia signalo atsako apvalkalo amplitudė yra mažesnė nei 100 % ir pastebėtas antrasis atspindys, užtvara dedama ties antruoju sąsajos atspindžiu. WB-RA ir WB-FC atveju domina antrasis atspindys (bangų paketas, pastebimas po viršutinio sąsajos atspindžio).

Siekiant gauti MAPOD kreives, kiekvieno metamodelio atsako duomenys buvo nubraižyti CIVA programine įranga. Remiantis Bereno hipoteze, buvo pasirinktas geriausiai tinkantis transformacijos derinys (logaritminis, normalusis, Boxcox) ir apskaičiuotos liekanų vertės. Nukrypstantys duomenų taškai buvo priskirti prie „triukšmo“ ir „prisotinimo“, kad būtų sumažintos tinkavimo paklaidos ir patenkintas Bereno tiesiškumo, homoskedastiškumo, normalumo ir dispersijos pagrįstumas. Aptikimo slenkstis parinktas taip, kad būtų sumažinta klaidingo pavojaus reikšmių tikimybė, atsižvelgiant į daugumą apskaičiuotų duomenų. PFA ir atsako duomenų pasiskirstymas kartu su aptikimo slenksčiu parodytas **8.6.2 pav.** PFA nustatomas atliekant pastato variacijos tyrimus su PB jungtiniu modeliu, kuriame nėra defekto.

Gautos MAPOD kreivės pateikiamos trims skirtingoms surišimo savybėms ir penkioms skirtingoms savybėms 5.4 pav.

Nė viena MAPOD kreivė nepasiekė kritinės stadijos, kad būtų galima apskaičiuoti $a_{90/95}$ (**8.6.3 pav., a**), o PFA procentinė dalis yra didelė (**8.6.2 pav., a**). DB-OPTION2, palyginti su DB-OPTION1, padidino patikimumą aptikti adhezinių jungčių atskyrimą (**8.6.3 pav., b**). Pastebėta, kad visos DB-OPTION2 funkcijos, išskyrus laiko vėlinimo reakciją, gali pasiekti 100 % MAPOD su mažesnėmis PFA reikšmėmis (išskyrus dažnio poslinkio IV atvejį).

WB-RA buvo pavaizduotas su alyvos storiu kaip charakteringa verte nuo 5 iki 100 μm (**8.6.3 pav., c**). Nors amplitudės pokyčio nuo smailės iki smailės (I) ir slopinimo (V) signalų atsakymai rodė, kad mažo inkliuzijos sluoksnio aptikimo tikimybė yra didesnė nei storo sluoksnio, dažnio Amax (III) ir dažnio poslinkio (IV) atsakymai rodė priešingai.

Silpno ryšio dėl fakultatyvinio kietėjimo (WB-FC) būdinga vertė buvo pasirinkta kaip epoksidinės išilginės bangos greitis (**8.6.3 pav., d**). MAPOD kreivės parodė, kad WB-FC sunku aptikti naudojant amplitudės nuo smailės iki smailės (I) ir laiko vėlinimo (II) atsako signalus. Nors dažnių sritimi pagrįsti atsakymai (III–IV) gali būti geresni, PFA vertės rodo, kad gali būti per daug klaidingų skambučių. Priešingai, pagal silpnėjimo (V) procentą silpną jungtį, atsiradusią dėl netinkamo kietinimo, galima aptikti su mažomis PFA vertėmis ir aukštu efektyvumu.

Be to, PFA ir $a_{90/95}$ – 90 proc. aptikimo tikimybė su 95 proc. patikimumu – reikšmės kiekvienam išskirtam požymiui pateiktos **8.6.2 lentelėje**.

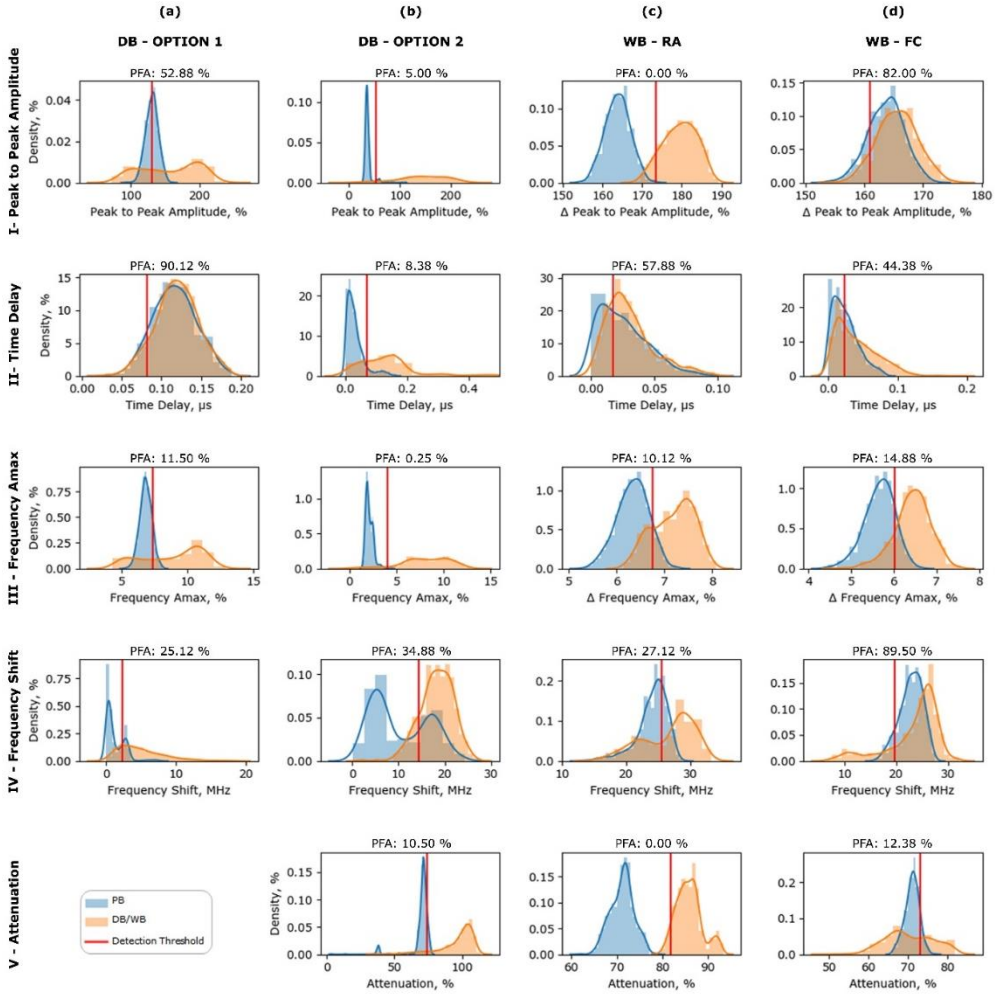

8.6.2 pav. Tobulo surišimo duomenų pasiskirstymas kartu su surišimo ir silpno surišimo duomenimis kiekvienam signalo atsakui, siekiant nustatyti slenkstinę vertę ir apskaičiuoti klaidingų pavojaus signalų tikimybę (PFA) surišimo DB-OPTION 1(a), surišimo DB-OPTION2 (b), silpno surišimo dėl atpalaiduojančios medžiagos WB-RA (c), silpno surišimo dėl netinkamo kietinimo WB-FC (d); penkioms skirtingoms signalo atsako savybėms I – amplitudė nuo smailės iki smailės, II – laiko vėlinimas, III – dažnio Amax, IV – dažnio poslinkis, V – slopinimas[15]

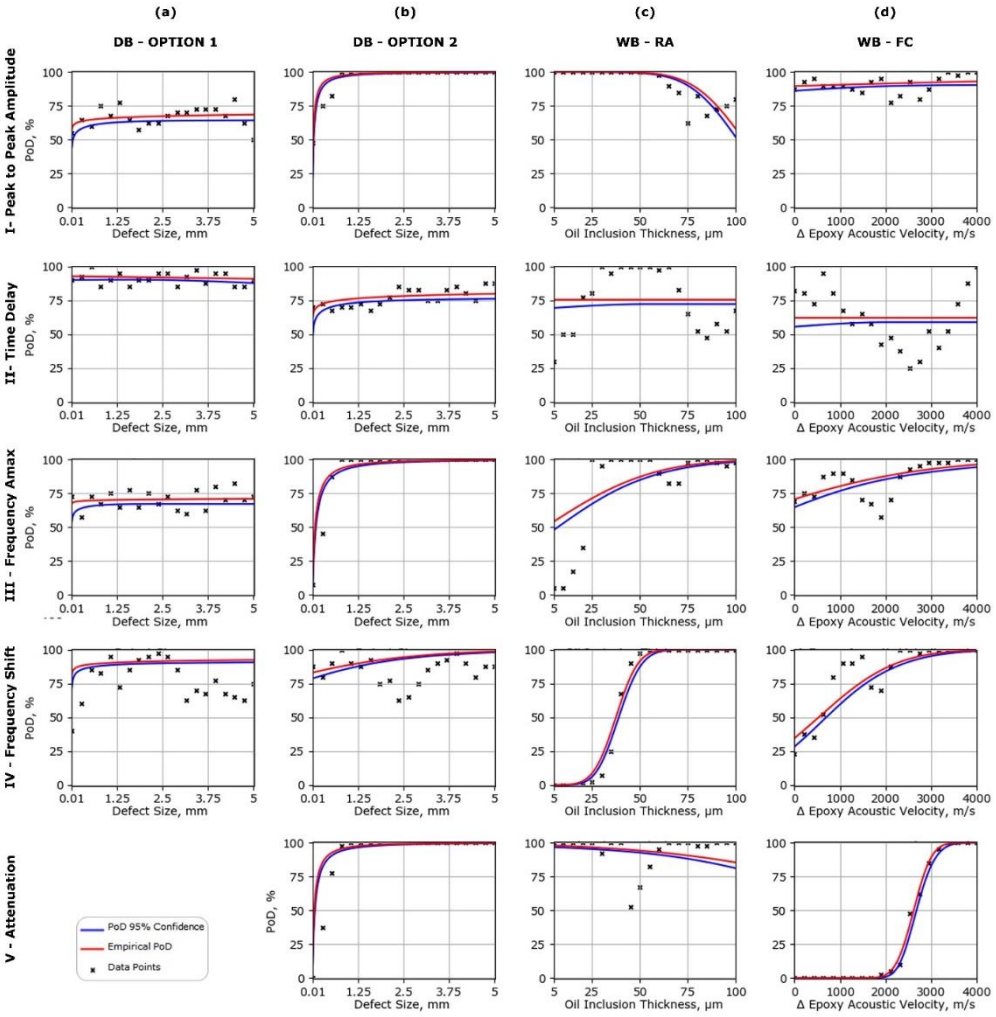

8.6.3 pav. Apskaičiuotos MAPOD kreivės keturiems skirtingiems surišimo kokybės atvejams: a) atskyrimas DB-OPTION1, b) atskyrimas DB-OPTION2, c) silpnas surišimas dėl atpalaiduojančios medžiagos WB - RA, d) silpnas surišimas dėl netinkamo kietinimo WB-FC; atsižvelgiant į penkias signalo atsako savybes eilutėse I – amplitude, II – laikas III – dažnio Amax, IV – dažnio poslinkis, V — slopinimas[15]

8.6.2 lentelė Apskaičiuotos POD rodiklio a-90/95 reikšmės ir klaidingų pavojaus signalų tikimybė kiekvienam klijavimo kokybės nuokrypiui ir kiekvienam požymiui [15]

Sujungimo kokybė / **Požymiai**	DB – var1		DB –var2		WB-RA		WB-FC	
	$a_{90/95}$ mm	PFA	$a_{90/95}$ mm	PFA	$a_{90/95}$ μm	PFA	$a_{90/95}$ m/s	PFA
Amplitudė	--	0,53	0,312	0,10	74,912	0,00	2618	0,82

Laikas	--	0,90	--	0,35	--	0,58	--	0,44
Dažnio Amax	--	0,12	0,687	0,00	61,537	0,10	2828	0,15
Dažnio poslinkis	--	0,25	1,685	0,08	51,386	0,27	2419	0,90
slopinimas	NA	NA	0,506	0,05	66,134	0,00	3118	0,12

8.7. Išvados

1. Atlikus išsamią literatūros apžvalgą, buvo nustatyti neardomieji bandymų metodai, naudotini klijų sukibimo kokybei vertinti: ultragarsinis neardomasis bandymas, ypač aukšto dažnio, ir sūkurinės srovės termografiją. Literatūros spragos nukreipė tyrimus į naujų signalų apdorojimo metodų, pagrįstų požymių išskyrimu ir duomenų sujungimu, taip pat patikimumo įvertinimu, kūrimą.
2. Sukurta pažangi ultragarsinio neardomojo bandymo metodika, pagrįsta požymių išskyrimu, t. y. dviejų medžiagų ribos vizualizacija ultragarso amplitude, dažnių srities amplitude ir dažnio poslinkiu. Palyginti su ultragarso amplitude, dažnio poslinkio požymių parinkimas pagerino nesukibimo aptikimo efektyvumą 3 kartus, o atskyrimo užterštumo aptikimo efektyvumą – nuo 3 iki 6 kartų. Siūlomas sujungimų kokybės vertinimo metodas yra puikus sujungimų defektams, taip pat silpniems sujungimams surišimams, užterštiems skysčiais, aptikti.
3. Naudojant sūkurinių srovių suspaustų signalų termografiją, buvo nustatytos suklijuotų sujungimų šiluminės ir elektrinės savybės. Nesukibimo defektų gylį buvo galima nustatyti naudojant impulsinio atsako išvestinę; impulsinio atsako skirstinio simetriškumas (angl. *skewness)* ir kurtozė (angl. *kurtosis*.) naudojami norint nustatyti defektų dydį ir padėtį. Pagal branduolio principinių komponenčių analizės (K-PCA) normą, silpnas sujungimas dėl užteršimo pasižymėjo minimaliu sujungimo elektrinių ir šiluminių savybių pokyčiu, tačiau šiluminės savybės buvo paveiktos labiau nei elektrinės.
4. Ultragarsinių metodų efektyvumo įvertinimas nustatant nesukibimo defektus ir jų dydžius nustatomas apskaičiuojant absoliučiąją paklaidą pagal bangos ilgį. Imersinių metodų (įskaitant SAM) našumas buvo didesnis nei tyrimų per orą ir nukreiptųjų bangų metodų, tačiau imersinės sistemos yra didelių gabaritų ir bandinį reikia panardinti į vandenį. Atsižvelgiant į ultragarso bangos ilgį tikrinimo metu, perdavimo metodas per orą buvo tinkamas nustatant defektų dydį, kartu suteikė bekontakčio tikrinimo pranašumą. Ultragarsinė NDT su nukreiptosiomis bangomis galėtų aptikti nesukibimo defektus, kurie nėra tikrinamos konstrukcijos krašte, greitai atliekant patikras dideliais atstumais.
5. Duomenų sintezės algoritmai (vidurkio, skirtumo, svertinio vidurkio, Hadamardo, Dempsterio ir Šaferio) pagerino žalvario intarpų aptikimo rezultatus, nes ultragarso ir termografijos rezultatai neprieštaravo vieni kitiems. Konkrečiai Dempsterio ir Šaferio derinio taisyklė veikia gerai, tačiau negalima neatsižvelgti į pagrindinius duomenų sujungimo metodus, pavyzdžiui, vidurkinimą. Nors neardomasis klijuotų sujungimų vertinimas vis dar yra sudėtingas uždavinys, kol šaltiniai neprieštarauja, siūlomi duomenų sintezės algoritmai padidina patikros jautrumą ir specifiškumą nuo 5 iki 40 proc. pagal plotą po ROC kreivėmis.

6. Sukurtos pažangios ultragarsinės NDT patikimumas aptikti aliuminio epoksidinių persidengiančių sujungimų nesukibimą labiausiai priklauso nuo laiko intervalo parinkimo ir ultragarso signalo amplitudės. Tikimybė aptikti silpnus sujungimus dėl skysčio užterštumo yra didesnė naudojant dažnio poslinkio signalo atsakui. Norint aptikti silpną sujungimą dėl nekokybiško kietinimo, patikimiau įvertinti signalo slopinimą klijų sluoksnyje.

9. REFERENCES

[1] Budhe S, Banea MD, de Barros S, da Silva LFM. An updated review of adhesively bonded joints in composite materials. Int J Adhes Adhes 2017;72:30–42. https://doi.org/10.1016/j.ijadhadh.2016.10.010.

[2] Cavezza F, Boehm M, Terryn H, Hauffman T. A Review on Adhesively Bonded Aluminium Joints in the Automotive Industry. Metals (Basel) 2020;10. https://doi.org/10.3390/met10060730.

[3] Jasiūnienė E, Mažeika L, Samaitis V, Cicėnas V, Mattsson D. Ultrasonic non-destructive testing of complex titanium/carbon fibre composite joints. Ultrasonics 2019. https://doi.org/10.1016/j.ultras.2019.02.009.

[4] Tserpes K. Adhesive Bonding of Aircraft Structures. Revolutionizing Aircr. Mater. Process., Cham: Springer International Publishing; 2020. https://doi.org/10.1007/978-3-030-35346-9_12.

[5] Higgins A. Adhesive bonding of aircraft structures. Int J Adhes Adhes 2000;20:367–76. https://doi.org/10.1016/S0143-7496(00)00006-3.

[6] Tornow C., Schlag M, Lima LCM. b, Stübing D., Hoffmann M., Noeske P-LM., et al. Quality assurance concepts for adhesive bonding of composite aircraft structures-characterisation of adherent surfaces by extended NDT. J Adhes Sci Technol 2015;29:2281–94. https://doi.org/10.1080/01694243.2015.1055062.

[7] Adams RD, Cawley P. A review of defect types and nondestructive testing techniques for composites and bonded joints. NDT E Int 1991;24:105. https://doi.org/10.1016/0963-8695(91)90924-R.

[8] Nagy PB. Ultrasonic detection of kissing bonds at adhesive interfaces. J Adhes Sci Technol 1991;5:619–30. https://doi.org/10.1163/156856191X00521.

[9] Jeenjitkaew C, Guild FJ. The analysis of kissing bonds in adhesive joints. Int J Adhes Adhes 2017;75:101–7. https://doi.org/10.1016/j.ijadhadh.2017.02.019.

[10] Vine K, Cawley P, Kinloch AJ. The correlation of non-destructive measurements and toughness changes in adhesive joints during environmental attack. J Adhes 2001;77:125–61. https://doi.org/10.1080/00218460108030735.

[11] Yılmaz B, Jasiūnienė E. Advanced ultrasonic NDT for weak bond detection in composite-adhesive bonded structures. Int J Adhes Adhes 2020;102:102675. https://doi.org/10.1016/j.ijadhadh.2020.102675.

[12] Yi Q, Tian GYY, Yilmaz B, Malekmohammadi H, Laureti S, Ricci M, et al. Evaluation of debonding in CFRP-epoxy adhesive single-lap joints using eddy current pulse-compression thermography. Compos Part B Eng 2019;178:107461. https://doi.org/10.1016/j.compositesb.2019.107461.

[13] Yilmaz B, Asokkumar A, Jasiūnienė E, Kažys RJ. Air-coupled, contact, and immersion ultrasonic non-destructive testing: Comparison for bonding quality evaluation. Appl Sci 2020;10:1–22. https://doi.org/10.3390/app10196757.

[14] Yilmaz B, Ba A, Jasiuniene E, Bui H-K, Berthiau G. Evaluation of Bonding Quality with Advanced Nondestructive Testing (NDT) and Data Fusion. Sensors 2020;20:5127. https://doi.org/10.3390/s20185127.

[15] Yilmaz B, Smagulova D, Jasiūnienė E. Model assisted reliability assessment for adhesive bonding quality evaluation with advanced ultrasonic NDT. NDT E Int 2021. https://doi.org/10.5281/zenodo.5464133.

[16] Adams RD, Cawley P. Defect types and non-destructive testing techniques for composites and bonded joints. Constr Build Mater 1989;3:170–83. https://doi.org/10.1016/0950-0618(89)90011-1.

[17] Jiao D, Rose JL. An ultrasonic interface layer model for bond evaluation. J Adhes Sci Technol 1991;5:631–46. https://doi.org/10.1163/156856191X00530.

[18] Yan D, Drinkwater BW, Neild SA. Measurement of the ultrasonic nonlinearity of kissing bonds in adhesive joints. NDT E Int 2009;42:459–66. https://doi.org/10.1016/j.ndteint.2009.02.002.

[19] Asif M, Khan MA, Khan SZ, Choudhry RS, Khan KA. Identification of an effective nondestructive technique for bond defect determination in laminate composites—A technical review. J Compos Mater 2018;52:3589–99. https://doi.org/10.1177/0021998318766595.

[20] Morlet J, Arens G, Fourfgeau E, Giard D. Wave propagation and sampling theory-Part I: Complex signal and scattering in multilayered media. Geophysics 1982;47:203–21.

[21] Bouchon M, Campillo M, Gaffet S. A boundary integral equation-discrete wavenumber representation method to study wave propagation in multilayered media having irregular interfaces. Geophysics 1989;54:1134–40. https://doi.org/10.1190/1.1442748.

[22] Brekhovskikh LM, Godin O a. Acoustics of layered media I : plane and quasi-plane waves. 1990.

[23] Anastasi R, Roberts M. Acoustic Wave propagation in an adhesive bond model with degrading interfacial layers. 1992.

[24] Ehrhart B, Valeske B, Muller C-E, Bockenheimer C. Methods for the Quality Assessment of Adhesive Bonded CFRP Structures - A Resumé. Proc Int 2010:1–9. https://doi.org/10.1109/TUFFC.924.

[25] Raišutis R, Kažys R, Mažeika L. Application of the ultrasonic pulse-echo technique for quality control of the multi-layered plastic materials. NDT E Int 2008;41:300–11. https://doi.org/10.1016/j.ndteint.2007.10.008.

[26] Tamborrino R, Palumbo D, Galietti U, Aversa P, Chiozzi S, Luprano VAM. Assessment of the effect of defects on mechanical properties of adhesive bonded joints by using non destructive methods. Compos Part B Eng 2016;91:337–45. https://doi.org/10.1016/j.compositesb.2016.01.059.

[27] Scarselli G, Nicassio F. Analysis of debonding in single lap joints based on employment of ultrasounds 2017;1017020:1017020. https://doi.org/10.1117/12.2260041.

[28] Galy J, Moysan J, El Mahi A, Ylla N, Massacret N. Controlled reduced-strength epoxy-aluminium joints validated by ultrasonic and mechanical measurements. Int J Adhes Adhes 2017;72:139–46. https://doi.org/10.1016/j.ijadhadh.2016.10.013.

[29] Markatos DN, Tserpes KI, Rau E, Markus S, Ehrhart B, Pantelakis S. The effects of manufacturing-induced and in-service related bonding quality reduction on the mode-I fracture toughness of composite bonded joints for aeronautical use. Compos Part B Eng 2013;45:556–64. https://doi.org/10.1016/j.compositesb.2012.05.052.

[30] Wood M, Charlton P, Yan D. Ultrasonic Evaluation of Artificial Kissing Bonds in CFRP Composites. E-Journal Nondestruct Test 2014;19:1–10.

[31] Ding J, Wu B, He C. Reflection and transmission coefficients of the SH0 mode in

the adhesive structures with imperfect interface. Ultrasonics 2016;70:248–57. https://doi.org/10.1016/j.ultras.2016.05.010.

[32] Twerdowski E, von Buttlar M, Grill W. Scanning acoustic defocused transmission microscopy with vector contrast combined with holography for weak bond imaging. Heal Monit Smart Nondestruct Eval Struct Biol Syst V 2006;6177:617718. https://doi.org/10.1117/12.657881.

[33] Jasiūnienė E, Žukauskas E, Dragatogiannis DA, Koumoulos EP, Charitidis CA. Investigation of dissimilar metal joints with nanoparticle fillers. NDT E Int 2017. https://doi.org/10.1016/j.ndteint.2017.08.005.

[34] Wu W-L, Wang X-G, Huang Z-C, Wu N-X. Measurements of the weak bonding interfacial stiffness by using air-coupled ultrasound. AIP Adv 2017;7:125316. https://doi.org/10.1063/1.5001248.

[35] Sunarsa TY, Aryan P, Jeon I, Park B, Liu P, Sohn H. A reference-free and non-contact method for detecting and imaging damage in adhesive-bonded structures using air-coupled ultrasonic transducers. Materials (Basel) 2017;10:1–16. https://doi.org/10.3390/ma10121402.

[36] Marks R, Clarke A, Featherston C, Paget C, Pullin R. Lamb Wave Interaction with Adhesively Bonded Stiffeners and Disbonds Using 3D Vibrometry. Appl Sci 2016;6:12. https://doi.org/10.3390/app6010012.

[37] Sherafat MH, Guitel R, Quaegebeur N, Lessard L, Hubert P, Masson P. Guided wave scattering behavior in composite bonded assemblies. Compos Struct 2016;136:696–705. https://doi.org/10.1016/j.compstruct.2015.10.046.

[38] Leiderman R, Figueroa JC, Braga AMB, Rochinha FA. Scattering of ultrasonic guided waves by heterogeneous interfaces in elastic multi-layered structures. Wave Motion 2016;63:68–82. https://doi.org/10.1016/j.wavemoti.2016.01.006.

[39] Leiderman R, Braga AMB. Scattering of guided waves by defective adhesive bonds in multilayer anisotropic plates. Wave Motion 2017;74:93–104. https://doi.org/10.1016/j.wavemoti.2017.05.007.

[40] Cho H, Hara Y, Matsuo T. Evaluation of the thickness and bond quality of three-layered media using zero-group-velocity lamb waves. J Phys Conf Ser 2014;520. https://doi.org/10.1088/1742-6596/520/1/012023.

[41] Yan D, Drinkwater BW, Neild SA. Measurement of the ultrasonic nonlinearity of kissing bonds in adhesive joints. NDT E Int 2009;42:459–66. https://doi.org/10.1016/j.ndteint.2009.02.002.

[42] Scarselli G, Ciampa F, Ginzburg D, Meo M. Non-destructive testing techniques based on nonlinear methods for assessment of debonding in single lap joints. Proc SPIE Vol 9437 2015. https://doi.org/10.1117/12.2085654.

[43] Zhang K, Zhou Z, Zhou J, Sun G. Characteristics of laser ultrasound interaction with multi-layered dissimilar metals adhesive interface by numerical simulation. Appl Surf Sci 2015;353:284–90. https://doi.org/10.1016/j.apsusc.2015.06.103.

[44] Ehrhart B, Valeske B, Bockenheimer C. Non-destructive evaluation (NDE) of aerospace composites: methods for testing adhesively bonded composites. Non-Destructive Eval Polym Matrix Compos 2013:220–37. https://doi.org/10.1533/9780857093554.2.220.

[45] Grimberg R, Savin A, Steigmann R, Serghiac B, Bruma A. Electromagnetic non-destructive evaluation using metamaterials. Insight Non-Destructive Test Cond

Monit 2011;53:132–7. https://doi.org/10.1784/insi.2011.53.3.132.

[46] Sophian A, Tian GY, Taylor D, Rudlin J. Electromagnetic and eddy current NDT in weld inspection: A review. Insight Non-Destructive Test Cond Monit 2001;43:302–6. https://doi.org/10.1784/insi.2015.57.6.337.

[47] Palka N, Miedzinska D. Detailed non-destructive evaluation of UHMWPE composites in the terahertz range. Opt Quantum Electron 2014;46:515–25. https://doi.org/10.1007/s11082-013-9836-4.

[48] Grosso M, Marinho CA, Nesteruk DA, Rebello JMA, Soares SD, Vavilov VP. Evaluating quality of adhesive joints in glass fiber plastic piping by using active thermal NDT. Proc SPIE - Int Soc Opt Eng 2013;8705:1–11. https://doi.org/10.1117/12.2016762.

[49] Hung MYY. Review and comparison of shearography and pulsed thermography for adhesive bond evaluation. Opt Eng 2007;46:051007. https://doi.org/10.1117/1.2741277.

[50] Genest M, Martinez M, Mrad N, Renaud G, Fahr A. Pulsed thermography for non-destructive evaluation and damage growth monitoring of bonded repairs. Compos Struct 2009. https://doi.org/10.1016/j.compstruct.2008.02.010.

[51] Waugh RC, Dulieu-Barton JM, Quinn S. Pulse Phase Thermography and its Application to Kissing Defects in Adhesively Bonded Joints. Appl Mech Mater 2011;70. https://doi.org/10.4028/www.scientific.net/AMM.70.369.

[52] Shin PH, Webb SC, Peters KJ. Pulsed phase thermography imaging of fatigue-loaded composite adhesively bonded joints. NDT E Int 2016;79. https://doi.org/10.1016/j.ndteint.2015.11.008.

[53] Yang R, He Y. Optically and non-optically excited thermography for composites: A review. Infrared Phys Technol 2016;75. https://doi.org/10.1016/j.infrared.2015.12.026.

[54] Milovanović B, Banjad Pečur I. Review of Active IR Thermography for Detection and Characterization of Defects in Reinforced Concrete. J Imaging 2016;2. https://doi.org/10.3390/jimaging2020011.

[55] Waugh RC, Dulieu-Barton JM, Quinn S. Thermographic Identification of Defects in Adhesively Bonded Joints, 2014. https://doi.org/10.1007/978-3-319-00768-7_45.

[56] Bui HK, Wasselynck G, Trichet D, Ramdane B, Berthiau G, Fouladgar J. 3-D modeling of thermo inductive non destructive testing method applied to multilayer composite. IEEE Trans Magn 2013;49:1949–52. https://doi.org/10.1109/TMAG.2013.2241037.

[57] Cheng L, Gao B, Tian GY, Woo WL, Berthiau G. Impact damage detection and identification using eddy current pulsed thermography through integration of PCA and ICA. IEEE Sens J 2014;14:1655–63. https://doi.org/10.1109/JSEN.2014.2301168.

[58] Bui HK, Berthiau G, Trichet D, Wasselynck G. Inductive thermography nondestructive testing applied to carbon composite materials: multiphysics and multiscale modeling. 8th Int Conf Electromagn Process Mater 2015:403–6.

[59] Kiziltaş G, Papila M, Yilmaz B, Bilge K. Challenges in Micro-CT Characterization of Composites. Micro-Computed Tomogr Med Eng 2020:225–46. https://doi.org/10.1007/978-3-030-16641-0_14.

[60] Kim C-H, Choi J-H, Kweon J-H. Defect detection in adhesive joints using the

impedance method. Compos Struct 2015;120:183–8. https://doi.org/10.1016/j.compstruct.2014.09.045.

[61] Malinowski PH, Wandowski T, Ostachowicz WM. Characterisation of CFRP adhesive bonds by electromechanical impedance 2014;9064:906415. https://doi.org/10.1117/12.2042868.

[62] Dugnani R, Chang FK. Analytical model of lap-joint adhesive with embedded piezoelectric transducer for weak bond detection. J Intell Mater Syst Struct 2017;28:124–40. https://doi.org/10.1177/1045389X16645864.

[63] Ehrhart B, Ecault R, Touchard F, Boustie M, Berthe L, Bockenheimer C, et al. Development of a laser shock adhesion test for the assessment of weak adhesive bonded CFRP structures. Int J Adhes Adhes 2014;52:57–65. https://doi.org/10.1016/j.ijadhadh.2014.04.002.

[64] Bossi R, Lahrman D, Sokol D, Walters C. Laser Bond Inspection for adhesive bond strength. Int. SAMPE Tech. Conf., 2011.

[65] Twerdowski E, von Buttlar M, Razek N, Wannemacher R, Schindler A, Grill W. Combined surface-focused acoustic microscopy in transmission and scanning ultrasonic holography. Ultrasonics 2006. https://doi.org/10.1016/j.ultras.2006.05.031.

[66] Gros XE, Strachan P, Lowden DW. Theory and implementation of NDT data fusion. Res Nondestruct Eval 1995;6:227–36. https://doi.org/10.1007/BF01606384.

[67] Ploix M, Garnier V, Breysse D, Moysan J. NDE data fusion to improve the evaluation of concrete structures. NDT E Int 2011;44:442–8. https://doi.org/10.1016/j.ndteint.2011.04.006.

[68] Völker C, Shokouhi P. Clustering Based Multi Sensor Data Fusion for Honeycomb Detection in Concrete. J Nondestruct Eval 2015;34:1–10. https://doi.org/10.1007/s10921-015-0307-7.

[69] Cotič P, Jagličić Z, Niederleithinger E, Stoppel M, Bosiljkov V. Image Fusion for Improved Detection of Near-Surface Defects in NDT-CE Using Unsupervised Clustering Methods. J Nondestruct Eval 2014;33:384–97. https://doi.org/10.1007/s10921-014-0232-1.

[70] Völker C, Shokouhi P. Multi sensor data fusion approach for automatic honeycomb detection in concrete. NDT E Int 2015;71:54–60. https://doi.org/10.1016/j.ndteint.2015.01.003.

[71] Gusenbauer C, Reiter M, Plank B, Salaberger D, Senck S, Kastner J. Porosity Determination of Carbon and Glass Fibre Reinforced Polymers Using Phase-Contrast Imaging. J Nondestruct Eval 2019;38:1–10. https://doi.org/10.1007/s10921-018-0529-6.

[72] Cuadra J, Vanniamparambil PA, Hazeli K, Bartoli I, Kontsos A. Damage quantification in polymer composites using a hybrid NDT approach. Compos Sci Technol 2013;83:11–21. https://doi.org/10.1016/j.compscitech.2013.04.013.

[73] Cao Y, Dong Y, Cao Y, Yang J, Yang MY. Two-stream convolutional neural network for non-destructive subsurface defect detection via similarity comparison of lock-in thermography signals. NDT E Int 2020;112:102246. https://doi.org/10.1016/j.ndteint.2020.102246.

[74] Daryabor P, Safizadeh MS. Image fusion of ultrasonic and thermographic inspection of carbon/epoxy patches bonded to an aluminum plate. NDT E Int 2017;90:1–10.

https://doi.org/10.1016/j.ndteint.2017.04.004.

[75] USA Department of Defense. Nondestructive Evaluation System Reliability Assessment. Department of Defense Handbook. MIL-HDBK-1823. 2009.

[76] Schneider CRA, Rudlin JR. Review of statistical methods used in quantifying NDT reliability. Insight Non-Destructive Test Cond Monit 2004;46:77–9. https://doi.org/10.1784/insi.46.2.77.55549.

[77] Bato MR, Hor A, Rautureau A, Bes C. Experimental and numerical methodology to obtain the probability of detection in eddy current NDT method. NDT E Int 2020;114. https://doi.org/10.1016/j.ndteint.2020.102300.

[78] Holstein R, Bertovic M, Kanzler D, Müller C. NDT reliability in the organizational context of service inspection companies. Mater Test 2014;56:607–10. https://doi.org/10.3139/120.110601.

[79] Bato MR, Hor A, Rautureau A, Bes C. Impact of human and environmental factors on the probability of detection during NDT control by eddy currents. Meas J Int Meas Confed 2019;133:222–32. https://doi.org/10.1016/j.measurement.2018.10.008.

[80] Aldrin JC, Medina EA, Lindgren EA, Buynak C, Steffes G, Derriso M, et al. MODEL-ASSISTED PROBABILISTIC RELIABILITY ASSESSMENT FOR STRUCTURAL HEALTH MONITORING SYSTEMS, 2010, p. 1965–72. https://doi.org/10.1063/1.3362348.

[81] Foucher F, Fernandez R, Leberre S, Calmon P. New Tools in CIVA for Model Assisted Probability of Detection (MAPOD) to Support NDE Reliability Studies. NDE Aerosp Mater Struct 2018 2018:32–43.

[82] Chapuis B, Calmon P, Jenson F. Best Practices for the Use of Simulation in POD Curves Estimation. Cham: Springer International Publishing; 2018. https://doi.org/10.1007/978-3-319-62659-8.

[83] Thompson RB, Brasche L, Forsyth D, Lindgren E, Swindell P, Winfree W. Recent Advances in Model-Assisted Probability of Detection. Proc 4th Eur Work Reliab NDE, Berlin, Ger 2009:23–26.

[84] Rosell A, Persson G. Model based capability assessment of an automated eddy current inspection procedure on flat surfaces. Res Nondestruct Eval 2013;24:154–76. https://doi.org/10.1080/09349847.2013.779401.

[85] Azzabi Zouraq B, Bui HK, Peterzol A, Wasselynck G, Berthiau G, Trichet D, et al. A Model-Assisted Probability of Detection Study on Induction Thermography Technique. IEEE Trans Magn 2019;55:2019–22. https://doi.org/10.1109/TMAG.2019.2898733.

[86] Carboni M, Cantini S. A " Model Assisted Probability of Detection " approach for ultrasonic inspection of railway axles. 18th World Conf Nondestruct Test 2012:16–20.

[87] Meyer RM, Crawford SL, Lareau JP, Anderson MT. Review of Literature for Model Assisted Probability of Detection - PNNL-23714 2014:1–20.

[88] Baskaran P, Pasadas DJ, Ramos HG, Ribeiro AL. Integration of multiple response signals into the probability of detection modelling in eddy current NDE of flaws. NDT E Int 2021;118:102401. https://doi.org/10.1016/j.ndteint.2020.102401.

[89] Jarvis R, Cawley P, Nagy PB. Performance evaluation of a magnetic field measurement NDE technique using a model assisted Probability of Detection framework. NDT E Int 2017;91:61–70.

https://doi.org/10.1016/j.ndteint.2017.06.006.

[90] Rentala VK, Mylavarapu P, Gautam JP. Issues in estimating probability of detection of NDT techniques – A model assisted approach. Ultrasonics 2018;87:59–70. https://doi.org/10.1016/j.ultras.2018.02.012.

[91] Smagulova D, Mazeika L, Jasiuniene E. Novel Processing Algorithm to Improve Detectability of Disbonds in Adhesive Dissimilar Material Joints. Sensors 2021, Vol 21, Page 3048 2021;21:3048. https://doi.org/10.3390/S21093048.

[92] Ba A, Yilmaz B, Bui HK, Jasiuniene E, BERTHIAU G. Development of multi-physics multi-scale modelling platform for CFRP composites using inductive thermography techniques. AeroNDT 2018 10th Int. Symp. NDT aerospace, 24-26 Oct. 2018, Dresden, Ger., 2018, p. 1–8.

[93] Ramdane B, Trichet D, Belkadi M, Saidi T, Fouladgar J. 3D numerical modeling of a new thermo-inductive NDT using pulse mode and pulsed phase methods. Eur Phys J Appl Phys 2010;52:23301. https://doi.org/10.1051/epjap/2010049.

CURRICULUM VITAE

Name, Surname: Bengisu Yilmaz
Website: https://sites.google.com/view/bengisu-yilmaz/
E-mail: bbengisuyilmaz@gmail.com

Education

November 2017 – October 2021
Electrical & Electronics Engineering, PhD
Kaunas University of Technology
Evaluation of bonding quality in aircraft structures by using different nondestructive testing techniques

September 2014 – January 2017
Mechatronics Engineering, MSc
Sabanci University
Tracing visual and acoustic signatures of mechanical behavior of composites

September 2009 – June 2014
Mechatronics Engineering, BSc
Sabanci University
Design and Demonstration of Vertical Axis Wind Turbine (VAWT)

Work Experience

May 2017 – May 2020
Junior Researcher
Prof. K. Barsauskas Ultrasound Research Institute
Kaunas University of Technology
Nondestructive testing and structural health monitoring of aircraft structures (NDTonAIR)

September 2014 – April 2017
Research Assistant
Sabanci University
M. Papila Composite Research Group

Organizations:
Marie Curie Alumni Association
Acoustic Society of America
Association for Women in Mathematics

Research Interests:
Nondestructive testing and evaluation,
Ultrasonic / Thermography / X-ray μCT,
Composite materials, Adhesive Joints,
FEM, SAFE, DSP

PUBLICATION LIST

Articles published in peer-reviewed scientific publications

Indexed in the Web of Science with Impact Factor

1. Yilmaz, Bengisu; Jasiūnienė, Elena. Advanced ultrasonic NDT for weak bond detection in composite-adhesive bonded structures // International journal of adhesion and adhesives. Oxford : Elsevier. ISSN 0143-7496. eISSN 1879-0127. 2020, vol. 102, art. no. 102675, p. 1-10. DOI: 10.1016/j.ijadhadh.2020.102675. [Science Citation Index Expanded (Web of Science); Scopus] [IF: 2,671; AIF: 5,014; IF/AIF: 0,532; Q2 (2019, InCites JCR SCIE)]
2. Yi, Q.; Tian, G.Y.; Yilmaz, B.; Malekmohammadi, H.; Laureti, S.; Ricci, M.; Jasiuniene, E. Evaluation of debonding in CFRP-epoxy adhesive single-lap joints using eddy current pulse-compression thermography // Composites Part B: Engineering. Oxford : Elsevier. ISSN 1359-8368. eISSN 1879-1069. 2019, Vol. 178, art. no. 107461, p. 1-12. DOI: 10.1016/j.compositesb.2019.107461. [Science Citation Index Expanded (Web of Science); Scopus] [IF: 7,635; AIF: 3,631; IF/AIF: 2,102; Q1 (2019, InCites JCR SCIE)]
3. Yilmaz, Bengisu; Asokkumar, Aadhik; Jasiūnienė, Elena; Kažys, Rymantas Jonas. Air-coupled, contact, and immersion ultrasonic non-destructive testing: comparison for bonding quality evaluation // Applied sciences. Basel : MDPI. ISSN 2076-3417. 2020, vol. 10, iss. 19, art. no. 6757, p. 1-22. DOI: 10.3390/app10196757. [Science Citation Index Expanded (Web of Science); Scopus; DOAJ] [IF: 2,474; AIF: 4,705; IF/AIF: 0,525; Q2 (2019, InCites JCR SCIE)]
4. Yilmaz, Bengisu; Ba, Abdoulaye; Jasiuniene, Elena; Bui, Huu-Kien; Berthiau, Gérard. Evaluation of bonding quality with advanced nondestructive testing (NDT) and data fusion // Sensors. Basel : MDPI. ISSN 1424-8220. 2020, vol. 20, iss. 18, art. no. 5127, p. 1-17. DOI: 10.3390/s20185127. [Science Citation Index Expanded (Web of Science); Scopus; DOAJ] [IF: 3,275; AIF: 3,581; IF/AIF: 0,914; Q1 (2019, InCites JCR SCIE)]
5. Yilmaz, Bengisu; Smagulova, Damira; Jasiuniene, Elena. Model assisted reliability assessment for adhesive bonding quality evaluation with advanced ultrasonic NDT // NDT &E International. Elsevier. ***UNDER REVIEW.***

Articles published in conference proceedings

1. Smagulova, Damira; Yilmaz, Bengisu; Papanaboina, Mastan Raja; Jasiuniene, Elena. Investigation on complex shaped aerospace structure: reliability and cost balance // AeroNDT 2019: 11th international symposium on NDT in aerospace, November 2019, Paris-Saclay, France. Bad Breisig : NDT.net. 2020, iss. 2, p. 1-9.
2. Yilmaz, Bengisu; Ba, Abdoulaye; Jasiuniene, Elena; Bui, Huu Kien; Berthiau, Gerard. Comparison of different non-destructive testing techniques for bonding quality evaluation // IEEE 5th international workshop on metrology for AeroSpace (MetroAeroSpace), Torino, Italy, June 19-21, 2019: proceedings.

Piscataway, NJ : IEEE, 2019. ISBN 9781728113456. eISBN 9781728113449. ISSN 2575-7490. p. 92-97. DOI: 10.1109/MetroAeroSpace.2019.8869692. [Scopus; INSPEC]

3. Ba, Abdoulaye; Yilmaz, Bengisu; Bui, Huu Kien; Jasiuniene, Elena; Berthiau, Gerard. Development of multi-physics multi-scale modelling platform for CFRP composites using inductive thermography techniques // AeroNDT 2018: 10th international symposium on NDT in aerospace, 24-26 October 2018, Dresden, Germany. Bad Breisig : NDT.net. 2018, p. 1-8.

Reviews, surveys and articles of represented co-authorship

In other peer-reviewed scientific publications

1. Yilmaz, Bengisu; Jasiūnienė, Elena; Mažeika, Liudas. Evaluation of bonding quality by using ultrasonic waves // 12th European Conference on Non-Destructive Testing (ECNDT 2018), Gothenburg, Sweden, 2018, June 11-15: proceedings / European Federation for Non-Destructive Testing (EFNDT). Bad Breisig : NDT.net, 2018. ISBN 9789163962172. ISSN 1435-4934. p. 1-3.

Works of art and their publication

Other conference abstracts and non-peer reviewed conference papers

1. Yilmaz, Bengisu; Smagulova, Damira; Jasiuniene, Elena. Model assisted probability of detection in adhesive joints // 6th International conference on structural adhesive bonding AB2021: 8-9 July 2021, Faculty of Engineering – University of Porto, Porto, Portugal: book of abstracts. Porto: Quântica Editora, 2021. ISBN 9789899017641. p. 181.
2. Yilmaz, Bengisu; Jasiuniene, Elena; Ba, Abdoulaye; Bui, Huu Kien; Berthiau, Gerard. Non-destructive evaluations of composite adhesive bonding with data fusion // 10th EASN virtual international conference on innovation in aviation & space to the satisfaction of the European citizens, 2-4 September 2020: book of abstracts. [S.l.] : EASN. 2020, p. 69.
3. Yilmaz, Bengisu. Rethinking joints: evaluation of adhesive bonding quality with advanced nondestructive testing techniques // TRA2020 (Transport Research Arena): due to the Covid-2019 pandemic, international conference TRA2020 scheduled on 27-30 April 2020, was cancelled but has been held online: NDTonAIR & SAFE-FLY webinar “Air transport safety: the role of structural health monitoring and nondestructive testing”, June 10th, 2020. [S.l.] : [s.n.]. 2020, p. 1-4.
4. Yilmaz, Bengisu. Innovative ultrasonic nondestructive testing technique for bonding quality evaluation // 11th international symposium on NDT in aerospace, 13-15, November, 2019, Paris, France: catalog of abstracts. Paris : COFREND. 2019, p. 104.
5. Yilmaz, Bengisu; Zukauskas, Egidijus; Jasiuniene, Elena. Interface quality evaluation of adhesive joints with acoustic microscopy // 2019 International

Congress on Ultrasonics, Bruges, Belgium, 3-6 September 2019: book of abstracts. [Bruges] : [s.n.]. 2019, p. 11.
6. Vyas, Jaishree; Yilmaz, Bengisu; Jasiuniene, Elena; Kazys, Rymantas J. Non-destructive testing and evaluation for carbon fibre epoxy bonded laminates using ultrasonic measurement techniques // 9th EASN international conference on innovation in aviation & space, 3 to 6 September, 2019, Athens, Greece: booklet of abstracts / organised by European Aeronautics Science Network. Athens : EASN. 2019, S-16, p. 100.
7. Yilmaz, Bengisu; Jasiuniene, Elena. Importance of non-destructive testing and evaluation for secure joints in aircrafts // AERODays 2019: 8th European Aeronautics Days, Bucharest, Romania, 27 - 30 May, 2019. Bucharest : [s.n.]. 2019, p. 1.
8. Yilmaz, Bengisu; Jasiūnienė, Elena. Evaluation of bonding quality with different nondestructive testing techniques : poster // Open Readings 2019: 62nd international conference for students of physics and natural sciences, March 19-22, Vilnius, Lithuania: abstract book. Vilnius : Vilnius University, 2019, P3-44. ISBN 9786090701379. p. 320.
9. Yilmaz, Bengisu; Jasiuniene, Elena. The relationship between ultrasonic wave parameters and the bonding quality // 8th EASN – CEAS international workshop on manufacturing for growth & innovation, 4-7 September 2018, Glasgow, UK: booklet of abstracts. [Glasgow] : [University of Glasgow]. 2018, ID 160, p. 17.
10. Amato, S.; Ba, A.; Chebbi, H.; Gartsev, S.; Kim, Y.; Malekmohammadi, H.; Rizwan, M.K.; Seresini, T.; Stamm, M.; Sunetchiieva, S.; Vyas, J.; Waters, S.; Yi, Q.; Yilmaz, B.; Zitoun, A.; Angulo, A.; Berthiau, G.; Burgholzer, P.; Burrascano, P.; Dixon, S.; Glorieux, C.; Hutchins, D.A.; Jasiuniene, E.; Kazys, R.; Köhler, B.; Laureti, S.; Mažeika, L.; Pfeiffer, H.; Premel, D.; Reboud, C.; Reynaert, J.; Ricci, M.; Soua, S.; Tian, G.Y.; Wevers, M. NDTonAIR: Training network in non-destructive testing and structural health monitoring of aircraft structures // 10th international symposium on NDT in Aerospace, 24-26 October 2018, Dresden, Germany: programme and abstracts. [S.l.] : [s.n.]. 2018, Th.6.B.1, p. 31.
11. Amato, S.; Ba, A.; Chebbi, H.; Gartsev, S.; Kim, Y.; Malekmohammadi, H.; Rizwan, M.K.; Seresini, T.; Stamm, M.; Sunetchiieva, S.; Vyas, J.; Waters, S.; Yi, Q.; Yilmaz, B.; Zitoun, A.; Angulo, A.; Berthiau, G.; Burgholzer, P.; Burrascano, P.; Dixon, S.; Glorieux, C.; Hutchins, D.A.; Jasiuniene, E.; Kažys, R.; Koehler, B.; Laureti, S.; Mazeika, L.; Pfeiffer, H.; Premel, D.; Reboud, C.; Reynaert, J.; Ricci, M.; Soua, S.; Tian, G.Y.; Wevers, M. NDTonAIR: Training network in non-destructive testing and structural health monitoring of aircraft structures: overview // 8th EASN – CEAS international workshop on manufacturing for growth & innovation, 4-7 September 2018, Glasgow, UK: booklet of abstracts. [Glasgow] : [University of Glasgow]. 2018, p. 16.
12. Malekmohammadi, Hamed; Laureti, Stefano; Ricci, Marco; Wevers, Martine; Tian, Gui Yun; Premel, Denis; Hutchins, David; Glorieux, Christ; Dixon, Steven; Burrascano, Pietro; Burgholzer, Peter; Jasiuniene, Elena; Mazeika, Liudas; Berthiau, Gerard; Pfeiffer, Helge; Reboud, Christophe; Reynaert,

Johan; Koehler, Bernd; Soua, Slim; Angulo, Angela; Amato, Silvio; Ba, Abdoulaye; Chebbi, Houssem; Gartsev, Sergey; Kim, Yongtak; Rizwan, Muhammad Khalid; Seresini, Tommaso; Stamm, Micheal; Sunetchiieva, Sevilia; Vyas, Jaishree; Yilmaz, Bengisu; Waters, Shaun; Yi, Quiji; Zitoun, Akram; Kazys, Rymantas. NDTonAIR: Training network in non-destructive testing and structural health monitoring of aircraft structures // QIRT 2018: 14th quantitative InfraRed thermography (QIRT) conference, 25 – 29 June 2018, Berlin, Germany. [S.l.] : [s.n.]. 2018, P46, p. 1.

COPIES OF PUBLICATIONS

International Journal of Adhesion & Adhesives 102 (2020) 102675

Contents lists available at ScienceDirect

International Journal of Adhesion and Adhesives

journal homepage: http://www.elsevier.com/locate/ijadhadh

Advanced ultrasonic NDT for weak bond detection in composite-adhesive bonded structures

Bengisu Yılmaz [a,*], Elena Jasiūnienė [a,b]

[a] Prof. K. Baršauskas Ultrasound Research Institute, Kaunas University of Technology, K. Baršausko St. 59, LT, 51423, Kaunas, Lithuania
[b] Department of Electronics Engineering, Kaunas University of Technology, Studentu St. 48, LT, 51367, Kaunas, Lithuania

ARTICLE INFO

Keywords:
Composites
Non-destructive testing
Acoustic microscopy
Adhesive joints

ABSTRACT

Weak bond detection in composite-adhesive joints is a highly challenging task in the non-destructive testing (NDT) community. This paper aims to evaluate the bonding quality in composite-adhesive bonded structures with high-frequency high-resolution acoustic microscopy. Carbon fibre reinforced epoxy-epoxy bonded single-lap joints containing three different bonding quality -debonding, weak bond with less and more contamination, in addition to perfect bond were investigated. Shape-based feature extraction algorithm in the frequency domain was developed in order to detect weak bonds. The results show that high frequency focused transducers used in acoustic microscopy is a great choice to visualize interface quality in bonded structures. Developed post-processing algorithm performs well on the detection of weak bond, independent from the perfect bond inspection results.

1. Introduction

In emerging technologies such as aerospace, automotive, and marine, the usage for high strength-low weight engineering materials like composite materials has increased drastically as reported by Scarselli et al. [1]. Efficient bonding technologies for these materials is challenging because of their natural inhomogeneous design. As stated in the comprehensive review by Budhe et al. [2], adhesively bonded structures not only create high strength to weight ratio, but also allow homogenous load distribution, protect the structure against galvanic corrosion, preserve the structural integrity of composites, and keep the structure surface smooth. Moreover, adhesive joints allow to design complex shape bonded structures and join dissimilar materials. As Jasiuniene et al. [3] stated adhesive bonds in-between composite substrates has become more popular due to the potential fibre breakage, local damages, and residual stress occurring around rivets. Tornow et al. [4] agrees with the early work of Adams and Drinkwater [5] and declares the adhesive bonding as the optimum method to bond composite structures, however, its usage is limited due to inadequate evaluation of bonding quality by non-destructive testing methods.

Vine et al. [6] showed that non-destructive evaluation of adhesive joints is a complex task since the bonding is an interfacial phenomena that involves a very thin layer of material, mostly significantly lower than the ultrasonic wavelength that is used for inspection. Bonding quality depends on various factors in production phase such as surface preparation, wettability, environmental conditions (temperature – pressure – humidity), and the curing process. In addition, other defects may initiate or the previous defects might propagate in bonded structure as a result of fatigue and usage. Adams and Cawley [7] discusses the defect types and causations that can lead to structural failures in bonded structures such as delamination, porosity, moisture, and contamination. As Nagy [8] described, contamination may lead to the kissing bond - where adherend and adhesive bond are in intimate contact; however, there is no physical bonding at the interface. In other words, kissing bonds have complete physical contact with inadequate chemical bonding. While Brotherhood et al. [9] has categorized kissing bond as dry-contact and liquid layer, Jeenjitkaew and Guild [10] studied the drastic decrease in the integrity of adhesive and the bonding quality due to contamination, moisture and pure curing. After the work carried by Dillingham et al. [11] proposed the detection technique of the contaminations on the adherend surfaces prior to bonding with novel surface energy measurements via liquid drops, Crane et al. [12] studied to detect both airborne and contact type contaminations with this technique. Hereinafter called *weak bonds* precipitate unreliable behaviour and they are hardly detectable with NDT techniques as well as kissing bonds. In order to overcome the application limitations of adhesive

* Corresponding author.
E-mail address: bengisu.yilmaz@ktu.lt (B. Yılmaz).

https://doi.org/10.1016/j.ijadhadh.2020.102675
Received 24 April 2020; Accepted 12 June 2020
Available online 1 July 2020

joints and meet the safety requirements, it is essential to have reliable non-destructive testing methods.

There are numerous studies that discuss the evaluation of bonding quality with various non-destructive testing methods, yet only some of them focuses on the non-destructive detection and evaluation of weak bonds. Although longitudinal ultrasonic wave propagation is a conventional ultrasonic technique, the C-scan images have been used to demonstrate the manufacturing defects caused by moisture and humidity in adhesive joints by Markatos et al. [13]. It is stated that the change in quality reduction at the bonding interface can be detected if and only if the level of moisture is high enough. In addition, Titov et al. [14] uses pulse-echo ultrasonic non-destructive testing technique has been used to evaluate bonding quality with ultrasonic wave features and transmission-reflection coefficient calculations. Furthermore, Wang et al. [15] calculate the interfacial stiffness and transverse stiffness in order to evaluate weak bonds in PMMA-epoxy bonded structures has been studied with air-coupled ultrasound analytical models. However, the results are not always correlated with the experimental studies and the application to composites is very unlikely due to their nature of inhomogeneity and variety. Application of air-coupled ultrasound to evaluate bonding quality is limited due to high attenuation in air, high wavelength and low bandwidth nature; especially for composite bonded structures. Wu et al. [16] recently used air-coupled ultrasonic NDT systems to calculate interfacial stiffness of weak bonds in composite bonded structures during curing, however, the sensitivity of the study is only limited to curing related defects and the results need to be improved. Moreover, guided waves, especially lamb waves are used to evaluate the surface treatment effects not only on metal-adhesive bonded structures by Gauthier et al. [17] but also in composite-bonded structures by Ren and Lissenden [18]. The application of lamb wave investigations to composite materials is limited due to variations in dispersion curves of each structure. Moreover, the bond quality reduction had been correlated with nonlinearity level and had been investigated with nonlinear ultrasound by Yan et al. [19]. However, the application of the nonlinear ultrasonics is challenging in industrial applications. Additionally, Bossi et al. [20] has established that the laser bond inspection (LBI) could be used to eliminate weak and kissing bonds via transmitting concentrated shock waves into the adhesive layer. Furthermore, the detailed damage tolerance study of laser shock adhesion test (LASAT) technique for weak bond assessment was carried out by Ecault et al. [21] and Ehrhart et al. [22]. However, laser shock adhesion test (LASAT) and laser bond inspection (LBI) techniques are not yet universally available because the testing systems are expensive and costly to maintain. On the other hand, acoustic microscopy, with the high resolution as a result of high-frequency transducers and short wavelength, is found to be a promising ultrasonic NDT technique to investigate interface quality in bonded structures. Acoustic microscopy has been used as a non-destructive testing methodology for friction stir weld quality investigations with the combination of different NDT techniques such as X-ray tomography by Jasiuniene et al. [23] and holographic imaging by Twerdowski et al. [24].

The aim of this work is to evaluate the interface quality of composite-epoxy-composite single-lap joints with high-frequency acoustic microscopy. Novel post-processing algorithm has been proposed to highlight the weak bond determination in carbon fibre reinforced composite-epoxy single-lap joints. Three composite-adhesive joints having different bonding quality have been investigated along with the reference sample under laboratory conditions. The results show that the bonding quality variations, specifically interface quality variations, are clearly observed with high bonding characteristic values by the proposed techniques.

2. Sample description

Carbon fibre reinforced epoxy (CFRP)-epoxy-CFRP single-lap joints, containing four different bonding quality, have been produced at COTESA GmBH, Germany. Six layers of carbon-fibre reinforced epoxy from HexPly M21-5H Satin woven prepreg was manufactured as adherend. Resulting laminates have a thickness of 2.22 mm. Residual stress during lamination process caused variation in the thickness of composite plates in the range of 10^{-6} m. 3 M Scotch-Weld AF163 k-red structural adhesive film epoxy with the thickness of 0.24 mm has been selected as adhesive layer. The film adhesive has been placed on top of the CFRP adherends after surface preparation with acetone and grinding. Single-lap joints, containing four different bonding quality, including pristine state, had been produced. Adhesive bonding at pristine state has been manufactured without any inclusion as a reference sample and named “perfect bond” (Fig. 1 (A)). Secondly, five two-fold Wrigtlon 4600 release film inclusions having 12.7 mm edge length and 0.063 mm thickness has been placed on the interface of in between epoxy and top adherend to demonstrate “debonding” (Figs. 1, 2 (B)). Additionally, the adhesive film surface contaminated with the total amount of 0.6 mL of release agent Marbocote 45 using a spray as a representation of weak bond. Half of the sample has been masked during contamination in order to limit the amount of release agent contamination. The mask has been removed before the placement of the second adherend layer. The sample has been marked as “weak bond-less contamination” (Figs. 1, 2 (D)). On the other half of the sample, release agent uniformly diffused to the uncured epoxy layer and marked as “weak bond-more contamination” (Figs. 1, 2 (C)).

3. Scanning acoustic microscopy

Adhesively bonded CFRP-epoxy-CFRP single-lap joints containing four different bonding quality have been investigated with scanning acoustic microscopy (KSI GmBH) located in Ultrasound Research Institute, Kaunas University of Technology, Lithuania. The experimental set up shown in Fig. 3 has been used to save the ultrasonic response of the selected bonding areas of the samples. In the region of interest (16.7 mm $\times$ 16.7 mm square area on the bondline), 250 points on each Cartesian axis (x and y) has been measured and full time-scale A-scan response is recorded. Samples have been investigated with a 50 MHz focused ultrasonic transducer PT-50-3-10 under immersion with pulse-echo technique. Ultrasonic transducer aperture is 3 mm, and the focal distance in water is 10 mm (Fig. 3). During measurements, samples have been placed perpendicular to the transducer. The distance between the transducer and samples have been selected as 5.5 mm in order to focus the ultrasonic field on the interface of the sample.

Physical parameters such as the thickness and the ultrasonic wave velocity of the adherend play a significant role in order to select the correct transducer frequency that will be used for inspection. The higher the acoustic velocity in the adherend material, the shorter the time travel of acoustic wave; as well as thin adherend leads to shorter time travel of the acoustic wave. The conditions like high acoustic velocity and the small thickness of the adherend material create the need for ultrasonic inspections with higher frequency transducers.

It should be noted that high frequency investigations on highly attenuated materials such as composites depend on ultrasonic pulse ability to reach an interface of interest. The ratio between the thickness of the adherend, attention levels, and the focal distance of the transducer plays a significant role in the experimental performance.

4. Advanced post-processing algorithm

The high-frequency transducer selection combined with highly attenuating materials results in higher noise in the received signals. Therefore, the post-processing algorithms play a significant role in displaying meaningful ultrasonic responses of thin composite-adhesive bonded structures.

In this work, multi-level post-processing algorithm is used in order to evaluate bonding quality and detect weak bonds in composite-adhesive single-lap joints. The system diagram for the post-processing algorithm

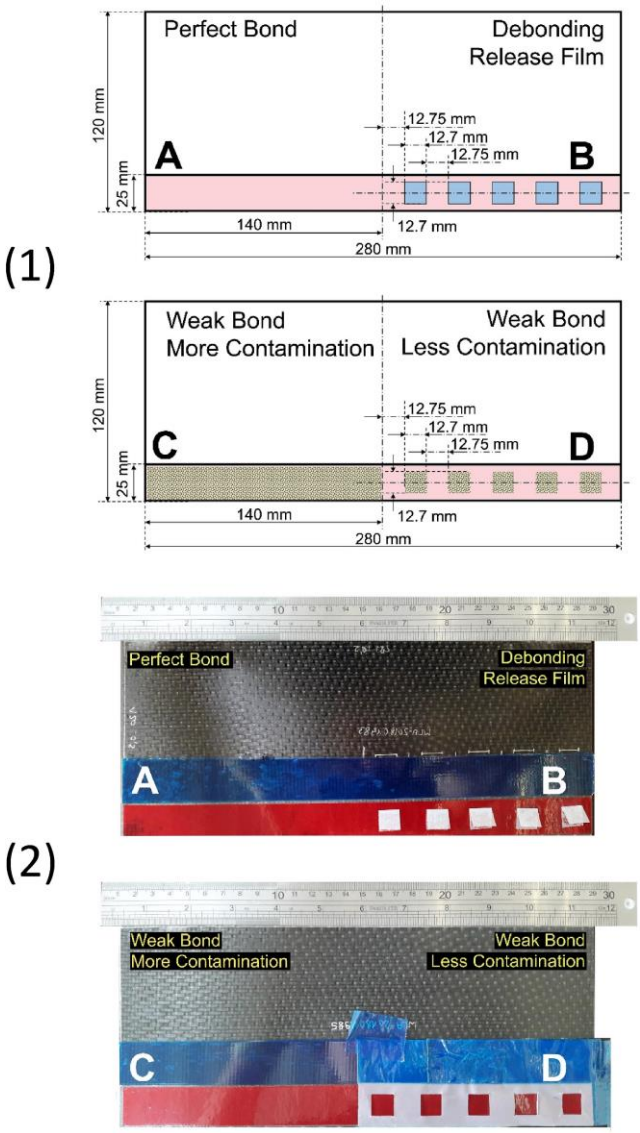

Fig. 1. CFRP-epoxy single-lap joints schematics (1) and pictures prior to bonding (2): (A) perfect bond, (B) debonding - release film inclusion, (C) weak bond with more release agent contamination, (D) weak bond - less release agent contamination.

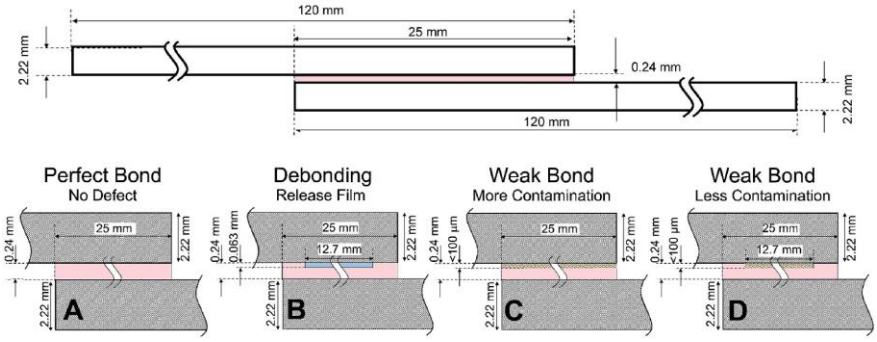

Fig. 2. CFRP-epoxy single-lap joints cross-section (not to scale) schematics: side view (top) and side view with zoom on the interface (bottom): (A) perfect bond, (B) debonding - release film inclusion, (C) weak bond with more release agent contamination, (D) weak bond with less release agent contamination.

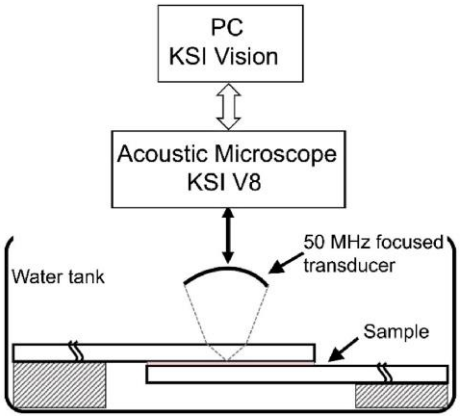

Fig. 3. Experimental set-up sketch for acoustic microscopy inspection of bonded specimens.

is shown in Fig. 4. As a start, A-scans have been recorded on the region of interest of bonded specimens. The electrical and structural noise has been removed from recorded A-scans with Wavelet denoising technique, suggested by Lazaro [25], where the level of denoising can be selected according to the input signal and central frequency of the transducer. Denoised signals have been aligned according to the surface reflection in order to eliminate the small variances due to the misplacement of the sample. Then, the time window of interest has been selected according to the calculated theoretical interface reflection of the bonded samples. In the time window of interests, the maximum values of A-scans have been aligned to be at the same time. Afterwards, amplitude and phase shift based visualization techniques have been applied to the data on time and frequency domains separately. As a result, four different two-dimensional images have been obtained to visualize the interface on the composite-adhesive bonded specimens.

4.1. Denoising

The recorded ultrasonic signal is noisy and scatters due to the anisotropic structure of the composite specimen, where the high-frequency transducer reckons more to the electronic noise. Therefore, there is a need for advanced denoising algorithm. Lazaro [25] studied the wavelet denoising which improves the detection rates in ultrasonic NDT and offers great flexibility. In this study, Symbol 3 – level 5 wavelets have been used with Stein's unbiased risk estimator (SURE) soft thresholding – which is data adaptive threshold estimator, where the residuals are kept at a minimum. Recorded A-scan signal with the denoised signal plotted on top is shown in Fig. 5.

4.2. Alignment and time window selection

In order to eliminate the small variations in the distance of sample surface position to the ultrasonic transducer, ultrasonic time of flight (ToF) of the surface reflection has been aligned according to −20 dB reflections. In the following equation, x is received ultrasonic surface reflection, i and j are the Cartesian coordinates of the transducer position

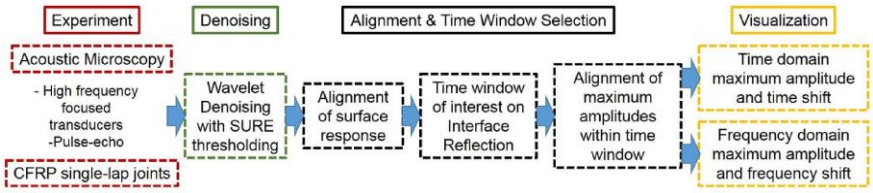

Fig. 4. System diagram for post-processing algorithm: Experiment, denoising, alignment and time window selection, visualization.

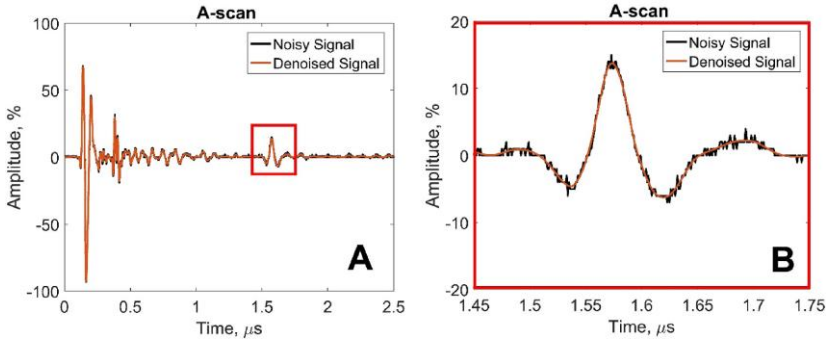

Fig. 5. Recorded A-scan example. Full time scale (A) and zoom on the interface reflection (B).

inside the region of interest, t is recorded time and t_0 is the time of flight where the zero crossing of each signal recorded (Equation (1)).

$$\tilde{x}^{ij}(t) = \begin{cases} x^{ij}(t)\,, & if\ x^{ij}(t_0) = -20\,dB \\ x^{ij}(t+a)\,, & if\ x^{ij}(t_0-a) = -20\,dB \end{cases} \qquad \exists\, a : t \tag{1}$$

After eliminating surface abnormalities and the transducer position uncertainties from the data, theoretical time of flight (ToF) for interface reflection has been calculated in order to obtain interface quality information. As it is discussed in the previous section, transducer frequency plays an important role in order to be able to separate the interface reflection from internal reflections (Fig. 6). Also, derived from equation (2), the adherend thickness (T) and the ultrasonic wave velocity (c) inside the adherend determines the beginning of the time window of interest (t_{open}). In order to be consistent with the values of recorded signals, zero-crossing time has been added to the theoretically calculated time of flight.

$$t_{open} = t_0 + \frac{2T}{c} \tag{2}$$

The time window of interest begins with the calculated time of flight for the interface reflection (t_{open}). For closing the gate, the time duration of excitation pulse has been referenced and the time window length has been set to 150 ns in this case. Within the time window of interest, the data has been aligned for the second time according to the time corresponding to the maximum amplitude inside the time window of interest [3]. Following equations (equation (3), equation (4), equation (5)) demonstrate the alignment algorithm, where t_{max} is time value where the maximum ultrasonic response has been recorded within the time window of interest, x being the ultrasonic signal, t_{open} and t_{close} are the time window of interest opening and closing times respectively t_{center} is the mid-time inside the window of interest. As an example, recorded A-scan signals has been shown in Fig. 7 before and after the application of the alignment algorithm.

$$t_{center} = t_{open} + \left(\frac{t_{close} - t_{open}}{2}\right) \tag{3}$$

$$\max\left(\left|x^{ij}(t)\right|\right) = \mp\, x^{ij}(t_{max})\,, \quad t_{open} \le t \le t_{close} \tag{4}$$

$$\tilde{x}^{ij}(t) = \begin{cases} x^{ij}(t)\,, & if\ t_{center} = t_{max} \\ x^{ij}(t-a)\,, & if\ t_{center} = t_{max} + a \end{cases} \qquad \exists\, a : t \tag{5}$$

4.3. Interface visualization with data in time domain

After the alignments, two different interface quality representations in time domain has been obtained from data inside the time window of interest. Firstly, maximum amplitudes in the time window of interest have been calculated for each A-scan coordinate (C_{time}). Secondly, the deviation of the time of flight values where the maximum amplitude is observed within the time window with respect to t_{center}, which is the mid-time inside the window of interest, has been represented in order to check the performance of alignment algorithm at interface (P_{time}). Amplitude-time based interface visualization C_{time} is the C-scan image

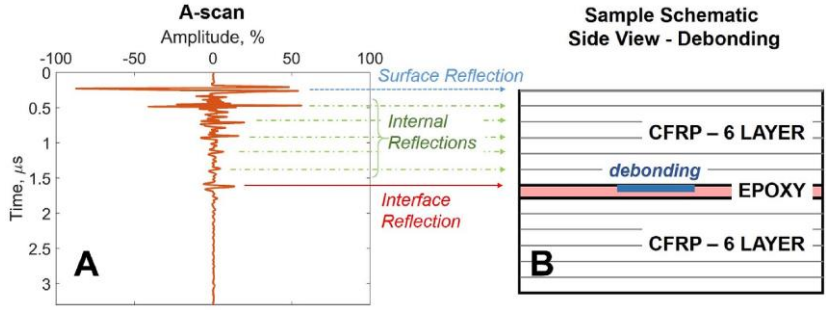

Fig. 6. Surface, internal, and interface reflections on the recorded A-scan signal (A) and the schematic of the sample (B).

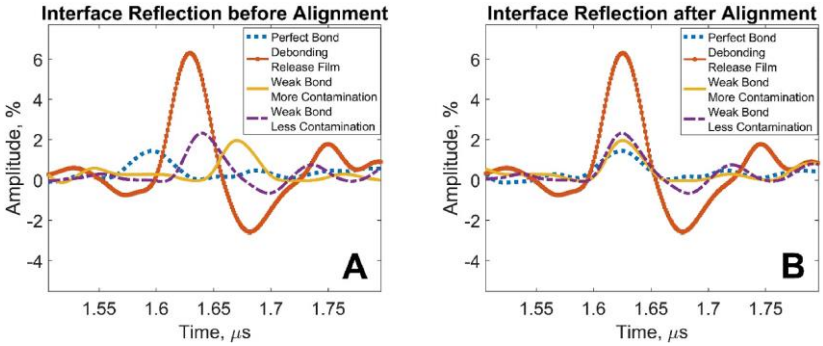

Fig. 7. A-scan signals on the time window of interest: (A) before alignment application (B) after alignment application.

values based on the maximum amplitudes in the time window of interest, phased-time based interface visualization P_{time} is the time shift based visualization to check the performance of the alignment, N is the number of recorded measurements i on lateral Cartesian coordinate, M is the number of recorded measurements j on longitudinal Cartesian coordinate.

$$C_{time}^{ij} = x^{ij}\,[t_{max}],\quad \forall i\,\varepsilon\{1\ldots N\},\quad \forall j\,\varepsilon\{1\ldots M\} \tag{6}$$

$$P_{time}^{ij} = |t_{max} - t_{center}|,\quad \forall i\,\varepsilon\{1\ldots N\},\quad \forall j\,\varepsilon\{1\ldots M\} \tag{7}$$

Equations (6) and (7) explains how the C-scan images from the data in the time domain have been obtained (amplitude-time based is in equation (6), phased-time based is in equation (7)). Fig. 8 shows how the pixel values for $\boldsymbol{C}_{time}$and t_{max} values that is used to calculate $\boldsymbol{P}_{time}$ visualizations have been obtained from an example measurement point (i,j).

4.4. Interface visualization with data in frequency domain

After the alignments, two different interface quality representations in frequency domain has been obtained from the data within the time window of interest. Before visualization, data in the interface time window has been converted to the frequency spectrum. Next, amplitude-based representation from the maximum values that are observed in the frequency spectrum created amplitude-frequency based interface visualization $C_{frequency}$. Lastly, the frequency values that are corresponding to the maximum amplitude in the frequency domain have been represented as phase-frequency based interface visualization $P_{frequency}$.

$$\mathcal{F}\{x^{ij}[k]\} = Y^{ij}[k] = \sum_{m=0}^{n-1} x^{ij}[k]\omega_n^{jk},\quad \forall i\,\varepsilon\{1\ldots N\},\quad \forall j\,\varepsilon\{1\ldots M\} \tag{8}$$

In equation (8), Fourier transform has been shown by $\mathcal{F}\{x^{ij}\}$; where $\omega_n = e^{-2\pi\sqrt{-1}/n}$, $0 \le k < n$ and n is being the time duration inside the time window of interest ($t_{close} - t_{open}$) over sampling frequency.

$$\left|Y^{ij}\left[f_{max}^{ij}\right]\right| = \max\left(\left|Y^{ij}[f]\right|\right) \tag{9}$$

$$C_{frequency}^{ij} = Y^{ij}\left[f_{max}^{ij}\right],\ \forall i\,\varepsilon\{1\ldots N\},\ \forall j\,\varepsilon\{1\ldots N\} \tag{10}$$

$$P_{frequency}^{ij} = f_{max}^{ij},\quad \forall i\,\varepsilon\{1\ldots N\},\quad \forall j\,\varepsilon\{1\ldots N\} \tag{11}$$

Equations (10) and (11) demonstrates how the interface visualization from frequency domain based data has been obtained (amplitude-frequency based is in equation (10), phased-frequency based is in equation (11)). Fig. 9 shows how the pixel values for $\boldsymbol{C}_{frequency}$ and $\boldsymbol{P}_{frequency}$ visualizations has been obtained from an example measurement point (i,j).

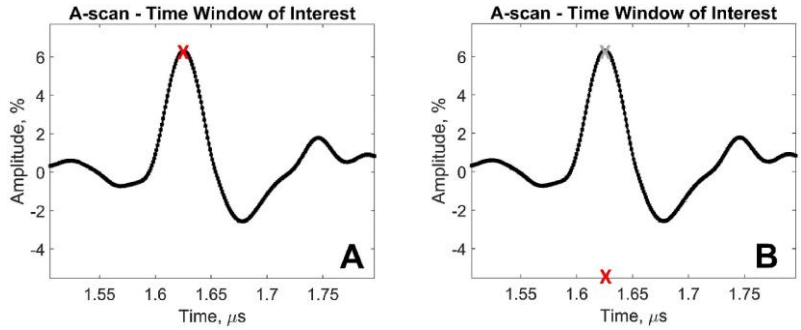

Fig. 8. A-scan signal on the time window of interest and the single point data that are used to visualize interface: for time-amplitude based interface visualization (A), for time-phased based visualization (B).

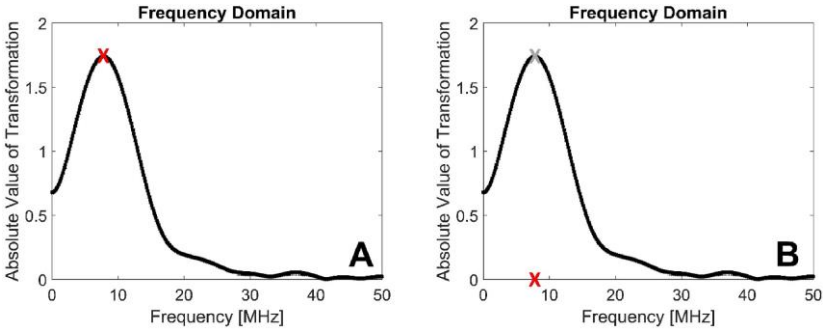

Fig. 9. F-scan signal on (signal in the time window of interest after Fourier transform) and the single point data that are used to visualize interface: for frequency-amplitude based interface visualization (A), for frequency-phased based visualization (B).

5. Non-destructive evaluation

Non-destructive evaluation of bonding quality has been performed on the scanning acoustic microscopy data by implementing the multi-level novel post-processing algorithm as the system diagram was shown in Fig. 4. After the application of multi-level post-processing algorithm, four different interface visualizations have been obtained ($\boldsymbol{C}_{time}$, $\boldsymbol{P}_{time}$, $\boldsymbol{C}_{frequency}$, $\boldsymbol{C}_{phase}$).

The first image obtained is time-amplitude based interface visualization $\boldsymbol{C}_{time}$ can be seen in Fig. 10 (A). This visualization depends on the maximum amplitude of ultrasonic response on each A-scan in the time domain within the time window of interest. As seen in Fig. 10 (A1), $\boldsymbol{C}_{time}$ visualization of perfect bond indicates no visible defect. On the other hand, Fig. 10 (A2) shows that debonding with release film can be detected by $\boldsymbol{C}_{time}$ visualization in composite-adhesive bonded structures with acoustic microscopy. Interface visualizations for the samples with weak bond with less contamination and weak bond with more contamination indicate some deviation compared to perfect bond visualization, however, it is very difficult to label them as defected or low bonding quality samples (Fig. 10 A3, A4).

Secondly, time-phased based interface visualization $\boldsymbol{P}_{time}$ shows the time of flight deviations of the observed maximum amplitudes in the time domain within the time window of interest (Fig. 10 (B)). This image visualizes the success or failure of the alignment procedure that has been applied in the time window of interest to interface reflection. As seen in Fig. 10 (B), having smaller values throughout the visualizations illustrates better reliability of the alignment algorithm since the algorithm requires that all maximum amplitudes (t_{max}) appear on the mid-time (t_{center}).

Third interface visualization $\boldsymbol{C}_{frequency}$ is amplitude-frequency based interface visualization where the observed maximum amplitude after the transition of the signal to frequency domain are represented (Fig. 10 (C)). The images for four different bonding quality, perfect bond, debonding with release film, weak bond less contamination and weak bond more contamination display quite similar results to the respective $\boldsymbol{C}_{time}$ interface visualizations. These similarities are expected since both $\boldsymbol{C}_{time}$ and $\boldsymbol{C}_{frequency}$ images are amplitude based visualizations, and the Fourier transform of the time domain data is amplitude dependent.

Last but not least, fourth interface image is obtained via phase-frequency based interface visualization $\boldsymbol{P}_{frequency}$ (Fig. 10 (D)). Pixel values on $\boldsymbol{P}_{frequency}$ images are the frequency values that is corresponding to the observed maximum amplitude in the frequency domain. In Fig. 10 (D1), perfect bond $\boldsymbol{P}_{frequency}$ image exhibits the sample is defect-free, while some variations are observed due to texture of the adhesive film layer. In Fig. 10 D2, debonding at the interface can be clearly identified as a defect. Weak bond less-contamination $\boldsymbol{P}_{frequency}$ interface visualization reveals defective zones on the interface (Fig. 10 D3). Compared to weak bond less contamination $\boldsymbol{P}_{frequency}$ image, weak bond more contamination $\boldsymbol{P}_{frequency}$ image shows less defective zones (Fig. 10 D4). This difference is expected due to the physical diffusion phenomenon of release agent contamination on the adhesive layer. It is expected that the mask used during the contamination procedure of weak bond less contamination sample has interrupted the diffusion procedure of release agent contaminant.

6. Quantitative performance evaluation of post-processing techniques

Both time and frequency based interface visualizations have been quantified according to the *bonding characteristic values* (BCV) which depend on the mean-square likelihood of observed values to the maximum observed value. Since maximum observed value corresponds to the high ultrasonic impedance difference at the interface, calculated bonding characteristic values results indicate the defect likelihood in each image. Results showing BCV ratios of four different bonding quality for four different post-processed visualizations have been reported in Table 1.

Bonding characteristic values for time-phase based interface visualization $\boldsymbol{P}_{time}$ evaluates the goodness of the alignment algorithm. Every pixel in $\boldsymbol{P}_{time}$ represents the deviation from mid-time where the algorithm supposed to align maximum ultrasonic amplitudes. Therefore, the smaller the values calculated by equation (12) indicates better performance in alignment algorithm.

For $\boldsymbol{C}_{time}$, $\boldsymbol{C}_{frequency}$, and $\boldsymbol{P}_{frequency}$ post-processing results, bonding characteristic values demonstrates the deviation from good joint in percentage over the inspected region of interest. For the defected samples namely debonding and weak bond, increase in bonding characteristic values express larger deviation from good joint. On the other hand $\boldsymbol{C}_{time}$, $\boldsymbol{C}_{frequency}$, and $\boldsymbol{P}_{frequency}$matrices represented for perfect bond with low bonding characteristic value illustrate high performance because the joint is good.

In Fig. 11, the bar graph represents the bonding characteristic values for different bonding quality composite-adhesive bonds for three different novel post-processing results. For frequency-amplitude based interface visualization $\boldsymbol{C}_{frequency}$, compared to traditional interface visualization technique $\boldsymbol{C}_{time}$, while the results for weak bond less contamination seems to be improved, they show slightly worse performance for other bonding quality samples. On the other hand, a significant increase in the performance has been observed for the phase-frequency based

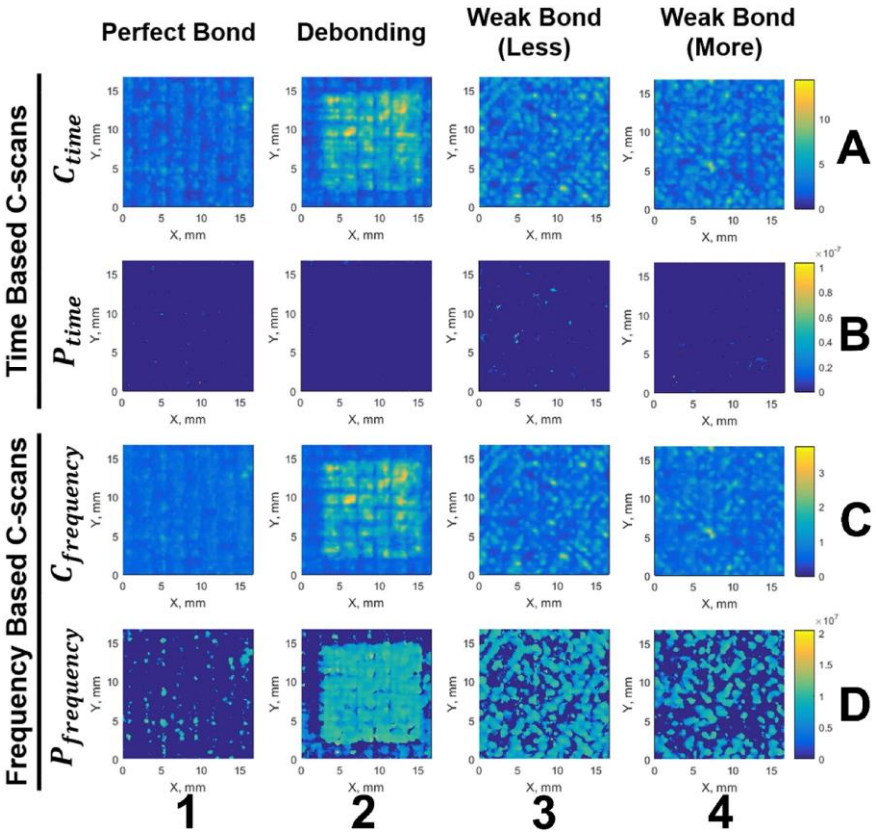

Fig. 10. Interface visualizations after multi-level post-processing algorithm (amplitude-time based (A), phase-time based (B), amplitude-frequency based (C), phase-frequency based (D)) for four different bonding quality (perfect bond (1), debonding with release film contamination (2), weak bond with less release agent contamination (3), weak bond with more release agent contamination (4)).

Table 1
Bonding characteristic values in percentile for the post-processed results.

Interface visualization		Bonding Quality:			
		Perfect Bond	Debonding (release film)	Weak bond (more contamination)	Weak bond (less contamination)
Time domain	C_{time}	3.68%	20.69%	8.23%	9.26%
	P_{time}	0.030%	0.008%	0.026%	0.134%
Frequency domain	$C_{frequency}$	4.27%	19.93%	7.14%	8.21%
	$P_{frequency}$	1.59%	23.89%	10.83%	19.52%

interface visualization $\boldsymbol{P}_{frequency}$ (Fig. 11). Specifically, weak bond less-contamination results with $\boldsymbol{P}_{frequency}$ shows high defect detection bonding characteristic values compared to weak-bond more contamination results with the same visualization technique.

$$BCV = \frac{\sum_{i=1}^{N}\sum_{j=1}^{M}\left(C^{ij}\right)^2}{\sum_{i=1}^{N}\sum_{j=1}^{M}\left(\max\left(C^{ij}\right) - C^{ij}\right)^2}\ x100 \tag{12}$$

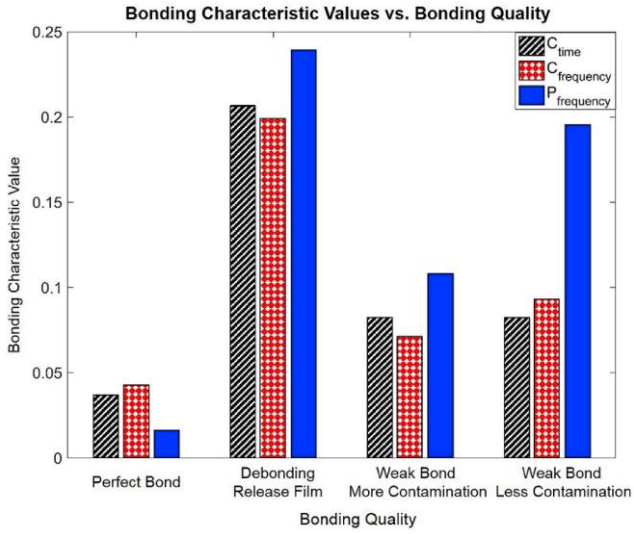

Fig. 11. Bonding characteristic values for defect detection along with different bonding quality samples and different post-processing results: time-amplitude based interface visualization performance (black-diagonal striped), frequency-amplitude based interface visualization performance (red-checked pattern), and frequency-phase based interface visualization performance (blue-plain pattern). (For interpretation of the references to colour in this figure legend, the reader is referred to the Web version of this article.)

7. Conclusions

The non-destructive evaluation of the quality of the composite-epoxy adhesive bond is challenging because the adhesion phenomenon occurs in a thin interface where the contamination that decreases the quality is also located. However, these contaminations must be detected because even small amounts may deteriorate the joint performance significantly. Characterization of small amounts of contamination is still challenging for conventional ultrasonic techniques due to similar acoustical impedance of contaminated interface and adhesives. It was determined that, developed novel post-processing algorithm with high frequency focused transducers used in acoustic microscopy is capable to visualize interface quality in composite-epoxy adhesive bonded structures. In addition, independent of the perfect bond inspection results, novel post-processing algorithm performs well to detect weak bond.

In this work, carbon-fibre reinforced epoxy-epoxy single-lap adhesive joints with three different bonding quality and pristine state have been investigated using acoustic microscopy. Advanced quantitative post-processing algorithm has been developed and applied to the experimental results. Investigations show that high frequency ultrasonic transducers can capture the interface quality in composite-epoxy adhesive joints and the developed post-processing algorithm enables the detection of weak bonds.

Using the developed post-processing algorithm, four different interface visualization images have been obtained for samples with different bonding quality. Comparing four different algorithms, time-phase based interface visualization P_{time} shows the goodness of the algorithm, therefore it is excluded from defect detection performance calculations. Time-amplitude based interface visualization C_{time} can be considered as conventional interface visualization, which mostly shows the maximum of the observed amplitude values in the time window of interest. Frequency-time based interface visualization $C_{frequency}$ is expected to show similar results to the conventional algorithm due to the amplitude dependence of the Fourier transform. However, frequency-phase based interface visualization $P_{frequency}$ demonstrates a novel technique to evaluate bonding quality. The qualitative results have also been compared with the quantitative bonding characteristic value calculations.

Analysing the frequency-phase based interface visualizations obtained using the developed algorithm, it is also observed that, the less contaminated regions show more defective zones than the more contaminated regions. It is expected that the diffusion of release agent into the adhesive film has been more dominant at more contaminated regions of the sample, on the other hand, the less contaminated regions had more release agent on the interface.

It was shown that the novel post-processing algorithm extracts more information on the evaluation of bonding quality. The presented results prove that the high-frequency acoustic microscopy with developed post-processing algorithm is a great candidate to evaluate bonding quality and detect weak bonds that occur due to bonding interface contamination. However, the limitations regarding structure dimensions and water immersion should be noted.

This study opens the discussion of possible post-processing algorithms that might help to detect weak bonds that occur due to contamination, yet, different bonding qualities such as kissing bond should be studied separately. The proposed novel post-processing algorithm could be utilized for the evaluation of the bonding quality in adhesive joints not only in aerospace structures but also in different industries such as automotive and marine, as adhesive joints are gaining their popularity and are used more and more.

Funding

This work was supported by NDTonAIR project from the European Union's Horizon 2020 research and innovation program under the Marie Sklodowska-Curie [grant number 722134].

References

[1] Scarselli G, Corcione C, Nicassio F, Maffezzoli A. Adhesive joints with improved mechanical properties for aerospace applications. Int J Adhesion Adhes 2017. https://doi.org/10.1016/j.ijadhadh.2017.03.012.

[2] Budhe S, Banea MD, de Barros S, da Silva LFM. An updated review of adhesively bonded joints in composite materials. Int J Adhesion Adhes 2017;72:30–42. https://doi.org/10.1016/j.ijadhadh.2016.10.010.

[3] Jasiūnienė E, Mažeika L, Samaitis V, Cicėnas V, Mattsson D. Ultrasonic non-destructive testing of complex titanium/carbon fibre composite joints. Ultrasonics 2019. https://doi.org/10.1016/j.ultras.2019.02.009.

[4] Tornow C, Schlag M, Lima LCM b, Stübing D, Hoffmann M, Noeske P-LM, et al. Quality assurance concepts for adhesive bonding of composite aircraft structures-characterisation of adherent surfaces by extended NDT. J Adhes Sci Technol 2015; 29:2281–94. https://doi.org/10.1080/01694243.2015.1055062.

[5] Adams RD, Drinkwater BW. Nondestructive testing of adhesively-bonded joints. NDT E Int 1997;30:93–8. https://doi.org/10.1016/S0963-8695(96)00050-3.

[6] Vine K, Cawley P, Kinloch AJ. The correlation of non-destructive measurements and toughness changes in adhesive joints during environmental attack. J Adhes 2001;77:125–61. https://doi.org/10.1080/00218460108030735.

[7] Adams RD, Cawley P. A review of defect types and nondestructive testing techniques for composites and bonded joints. NDT E Int 1991;24:105. https://doi.org/10.1016/0963-8695(91)90924-R.

[8] Nagy PB. Ultrasonic detection of kissing bonds at adhesive interfaces. J Adhes Sci Technol 1991;5:619–30. https://doi.org/10.1163/156856191X00521.

[9] Brotherhood CJ, Drinkwater BW, Guild FJ. The effect of compressive loading on the ultrasonic detectability of kissing bonds in adhesive joints. J Nondestr Eval 2002;21:95–104. https://doi.org/10.1023/A:1022584822730.

[10] Jeenjitkaew C, Guild FJ. The analysis of kissing bonds in adhesive joints. Int J Adhesion Adhes 2017;75:101–7. https://doi.org/10.1016/j.ijadhadh.2017.02.019.

[11] Dillingham G, Oakley B, Voast PJV, Shelley PH, Blakley RL, Smith CB. Quantitative detection of peel ply derived contaminants via wettability measurements. J Adhes Sci Technol 2012;26:1563–71. https://doi.org/10.1163/156856111X618416.

[12] Crane R, Dillingham G, Oakley B. Progress in the reliability of bonded composite structures. Appl Compos Mater 2017;24:221–33. https://doi.org/10.1007/s10443-016-9523-2.

[13] Markatos DN, Tserpes KI, Rau E, Markus S, Ehrhart B, Pantelakis S. The effects of manufacturing-induced and in-service related bonding quality reduction on the mode-I fracture toughness of composite bonded joints for aeronautical use. Compos B Eng 2013;45:556–64. https://doi.org/10.1016/j.compositesb.2012.05.052.

[14] Titov SA, Maev RG, Bogachenkov AN. Pulse-echo NDT of adhesively bonded joints in automotive assemblies. Ultrasonics 2008;48:537–46. https://doi.org/10.1016/j.ultras.2008.07.001.

[15] Wang XG, Wu WL, Huang ZC, Chang JJ, Wu NX. Research on the transmission characteristics of air-coupled ultrasound in double-layered bonded structures. Materials 2018;11. https://doi.org/10.3390/ma11020310.

[16] Wu W-L, Wang X-G, Huang Z-C, Wu N-X. Measurements of the weak bonding interfacial stiffness by using air-coupled ultrasound. AIP Adv 2017;7:125316. https://doi.org/10.1063/1.5001248.

[17] Gauthier C, Ech-Cherif El-Kettani M, Galy J, Predoi M, Leduc D. Structural adhesive bonding characterization using guided Lamb waves and the vertical modes. Int J Adhesion Adhes 2020. https://doi.org/10.1016/j.ijadhadh.2019.102467.

[18] Ren B, Lissenden CJ. Ultrasonic guided wave inspection of adhesive bonds between composite laminates. Int J Adhesion Adhes 2013;45:59–68. https://doi.org/10.1016/j.ijadhadh.2013.04.001.

[19] Yan D, Drinkwater BW, Neild SA. Measurement of the ultrasonic nonlinearity of kissing bonds in adhesive joints. NDT E Int 2009;42:459–66. https://doi.org/10.1016/j.ndteint.2009.02.002.

[20] Bossi R, Lahrman D, Sokol D, Walters C. Laser Bond Inspection for adhesive bond strength. Int. SAMPE Tech. Conf. 2011:11. SAMPE 2011, May.

[21] Ecault R, Boustie M, Touchard F, Pons F, Berthe L, Chocinski-Arnault L, et al. A study of composite material damage induced by laser shock waves. Compos Part A Appl Sci Manuf 2013. https://doi.org/10.1016/j.compositesa.2013.05.015.

[22] Ehrhart B, Ecault R, Touchard F, Boustie M, Berthe L, Bockenheimer C, et al. Development of a laser shock adhesion test for the assessment of weak adhesive bonded CFRP structures. Int J Adhesion Adhes 2014;52:57–65. https://doi.org/10.1016/j.ijadhadh.2014.04.002.

[23] Jasiūnienė E, Žukauskas E, Dragatogiannis DA, Koumoulos EP, Charitidis CA. Investigation of dissimilar metal joints with nanoparticle fillers. NDT E Int 2017. https://doi.org/10.1016/j.ndteint.2017.08.005.

[24] Twerdowski E, von Buttlar M, Grill W. Scanning acoustic defocused transmission microscopy with vector contrast combined with holography for weak bond imaging. Heal Monit Smart Nondestruct Eval Struct Biol Syst V 2006;6177:617718. https://doi.org/10.1117/12.657881.

[25] Lazaro JC. Noise reduction in ultrasonic NDT using discrete wavelet transform processing. 2002 IEEE Ultrason. Symp. 2002. Proceedings. 2002;1:777–80. https://doi.org/10.1109/ULTSYM.2002.1193514. IEEE.

Composites Part B 178 (2019) 107461

Contents lists available at ScienceDirect

Composites Part B

journal homepage: www.elsevier.com/locate/compositesb

Evaluation of debonding in CFRP-epoxy adhesive single-lap joints using eddy current pulse-compression thermography

Q. Yi [a,*], G.Y. Tian [a], B. Yilmaz [b], H. Malekmohammadi [c], S. Laureti [c], M. Ricci [d], E. Jasiuniene [b]

[a] Department of Electrical and Electronic Engineering, Newcastle University, Merz Court, NE1 7RU, Newcastle upon Tyne, UK
[b] Ultrasound Research Institute, Kaunas University of Technology, Kaunas, Lithuania
[c] Department of Engineering, University of Perugia, Polo Scientifico didattico di Terni, Strada di Pentima 4, 05100 Terni, Italy
[d] Department of Informatics, Modeling, Electronics and System Engineering, University of Calabria, Rende, 87036, Italy

ARTICLE INFO

Keywords:
Eddy current pulsed thermography (ECPT)
Pulse-compression
Adhesive joints
CFRP
Kernel principal component analysis
Debonding
Eddy current pulse-compression thermography (ECPuCT)

ABSTRACT

Contaminations arising during the manufacturing or usage of Carbon Fiber Reinforced Plastic (CFRP)-epoxy adhesive single-lap joints can drastically affect the mechanical performance of the structure and eventually lead to its catastrophic failure. Eddy current stimulated thermography has been recently proposed for detecting and characterizing defects in composite materials. The characterization of debonding in adhesive single-lap joints in composites by eddy current stimulated thermography can be challenging due to the anisotropic thermal diffusion caused by the anisotropic conductivity and multi-layer nature of the composites. This work tackles the challenge of detecting the interface contamination by combining eddy current pulse-compression thermography and image post-processing algorithms. The impulse responses from samples containing either brass, release film or release agent contaminations obtained through pulse-compression combined with Eddy Current Pulsed Thermography (ECPT). Non-uniform heating patterns are removed by partial least square technique. Then, the time instants containing meaningful information about the contaminated interface layer are inferred by comparing each norm of kernel principal component over suitable time windows. The evaluation of contamination depths and properties are conducted in selected time windows by principal component analysis and time-phase analysis. Results proved that release agent contamination plays the minor role in changing the electrical and thermal properties of the single-lap joints compared with brass and release film.

1. Introduction

CFRPs are extensively used in the aerospace industry owed to their extraordinary properties such as high strength to weight ratio, great thermal stability, and high resistance over impacts [1]. Adhesive bonding is one of the most advantageous joining technologies in composites material because the mechanical properties of such joints are significantly better than those achievable with other joint designs *e.g.* rivet. This can be attributed to their reduction of peel stress and interfacial shear stress [2]. Moreover, the adhesive joints are relatively simple to realize and cost-effective. The major advantages of the adhesive bonded joints include the reduction of local delamination, prevention of galvanic corrosion due to the fasteners, significant reduction in weights of the joints and a smooth external surface of the final component [3]. However, the risk of trapped air, dust, release film, release agent or other contaminations occurring during the manufacturing process can lead to the premature failure of the component, when they are not detected and repaired [4]. To cope with the high safety standards and regulations existing in highly developed industries such as aerospace, the quality of the bonded structures should be checked both after manufacturing and during usage. The lack of understanding in bonding quality with the current non-destructive testing (NDT) technologies limits adhesive bonding applications. However, it has been proved that some NDT methods can be used to detect the presence of contaminations [5–8], thus they show promises for detecting improper bonding between two items. Nevertheless, it must be noted that failures of multi-layer bonded materials can be challenging to be detected by NDT methods due to the presence of local heterogeneities along with bonded layer.

Active Thermography (AT) is one of the most promising NDT techniques for the evaluation of the bonding quality and for determining the presence of contaminations [9,10]. Being a non-contact method with the capability of inspecting a large area of the Sample Under Test (SUT), AT

* Corresponding author.
E-mail address: qiuji.yi@newcastle.ac.uk (Q. Yi).

https://doi.org/10.1016/j.compositesb.2019.107461
Received 12 July 2019; Received in revised form 2 September 2019; Accepted 16 September 2019
Available online 19 September 2019
1359-8368/

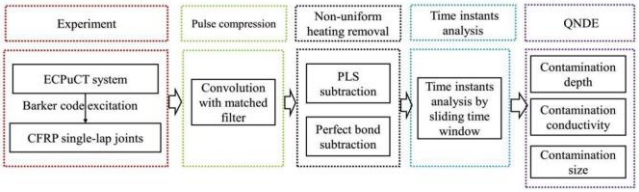

Fig. 1. System diagram.

has been extensively used for the detection of fabrication defects in bonded joints [11,12]. The detection and sizing of defects in adhesively bonded joints can be done by thermographic imaging, as the defect plane is typically perpendicular to the thermal wave propagation direction [13]. Surface roughness, artificial defects and grooves could be detected in adhesively bonded metallic joints using lock-in thermography [14]. The defect detection capability of traditional light-based AT techniques is highly influenced by the thermal diffusion length of the SUT. In light-based AT, the thermal waves are generated on the surface of the SUT and they need to diffuse to the required depth, being reflected by the buried defect and then back-propagate to the inspection surface to be detected by monitoring the surface temperature. To overcome this limitation, Eddy Current Pulsed Thermography (ECPT) has been recently proposed for composite evaluation. When ECPT is applied to CFRP, the stimulation can be considered volumetric since the electrical conductivity is relatively low. Depending on the excitation frequency of the Eddy Current (EC) and the sample thickness, the typical achieved skin depths are greater than the sample thickness itself, or at least comparable to it [15]. In addition, due to the multi-physics nature of the ECPT, the electrical and thermal properties can be evaluated simultaneously in one experiment. ECPT is also less influenced by the surface conditions of the SUT such as emissivity and roughness with respect to optically-stimulated thermography. In the case of ECPT the heat generation is volumetric, therefore the influence of the mentioned parameters on the absorbed energy by the SUT can be ignored [16]. Moreover, ECPT can be exploited to evaluate the barely visible impact damage on composites [15,17,18] and the presence of delamination [19–21].

However, the evaluation of the interface quality in bonded structures is still a challenging task. This is because the faithful evaluation of bonded areas is hindered by various factors: (i) their complex shape, (ii) the heterogeneous nature of the multilayer adherend, (iii) the non-uniform heating pattern combined with significant lateral thermal diffusion. All the mentioned factors contribute to the recorded thermograms and cause poor Signal-to-Noise Ratio (SNR), therefore being difficult to be interpret the results.

To tackle these challenges, a Barker Code (BC) modulated eddy current excitation combined with Pulse-compression (PuC), hereinafter called Eddy Current Pulse-compression Thermography (ECPuCT) is used. This approach was exploited to enhance the SNR and faithfully evaluate CFRP adhesive joints containing different contaminations in the form of release agent, brass film, and release film inclusion. The system diagram is shown in Fig. 1. For each investigated sample, a series of thermograms were collected during both the heating and cooling stage shown in the first block, and the impulse response of the SUT has been derived pixelwise by using PuC algorithm presented in the second block. To find contamination layer at certain depth and conduct the characterization of different contaminations, as illustrated in the Fig. 1, three processing steps of impulse response images are undertaken: (1) non-uniform heating pattern removal by Partial Least Square (PLS) technique, as shown in the third block; (2) time analysis carried out to select optimal time windows for Kernel Principal Component Analysis (K-PCA), shown in the third block; (3) contamination properties comparison by proposed feature including norm of principle component, derivates of impulse response and quantification of the inclusion size by spatial kurtosis over the selected time windows.

The main findings of this work are: (i) PLS aids in removing the non-uniform heating pattern and to solve the possible problem of misalignment of spatial coordinates resulting from different experiments; (ii) the use of sliding K-PCA features can be applied for detection of contamination layer in heating and cooling stages; (iii) the contamination properties can be classified using the derivatives of the retrieved impulse response at specific time. In particular, the release agent contamination has the minimum influence on the electrical and thermal properties of the adhesive layer compared with brass film and release film, though it still affects the thermal properties in a measurable amount.

The paper layout is as follows: Chapter II introduces the principle of ECPuCT and the mathematical description of PuC and PLS techniques. Chapter III presents the samples' manufacturing process and the experimental setup. Chapter IV gives insight about non-uniform heating removal by PLS and perfect bond subtraction, as well as the investigation of the electromagnetic behavior of contaminated bonds. Chapter V summarizes the work and explains possible future works.

2. Methodology of ECPuCT and feature extraction techniques

2.1. Principle of eddy current stimulated thermography for CFRP

The theory of ECPT on metallic materials has been addressed in previous researches [22–24]. Even if it relies on the same physical principle, *i.e.* the Joule effect due to the presence of eddy current in the sample, ECPT applied to CFRP is quite different in practice for both the heating mode and the thermal wave diffusion. Indeed, the spatial distribution of eddy current into a conductive sample is regulated by the skin depth δ that decreases monotonically as the frequency increases:

$$\delta = \frac{1}{\sqrt{\pi \mu \sigma f_{carrier}}}, \tag{1}$$

where $f_{carrier}$ is the frequency of the excitation current [Hz], σ is electrical conductivity [S·m^{-1}], and μ is magnetic permeability [H·m^{-1}]. In general, for CFRP the bulk conductivity σ value is in the order of 15000 S m^{-1} and it is non-magnetic [25]. Considering an $f_{carrier} = 300$ kHz, the corresponding penetration depth is 7.50 mm while for the same value of $f_{carrier}$, the penetration depth in steel ($\sigma = 9.93 \times 10^6$S·m^{-1}, $\mu = 3.77 \times 10^{-4}$ H·m^{-1}) is equal to 29.08 μm, which is significantly smaller than the one obtained for CFRP. Thus, if the thickness of the CFRP sample is lower than the corresponding value of δ, as in the present case, the heating can be assumed volumetric, while in the case of steel the heating occurs in a small surface layer. It must be stressed out that the induced eddy currents are regulated by the skin effect (Eq. (1)), which has been retrieved from the solution of the conduction current density in a semi-infinite conductive material in z direction. Although, Eq. (1) is defined for a perfect isotropic and homogenous conductor but can be used in our case for CFRP material since the conductivity in depth direction can be considered as a bulk value and δ is bigger than the

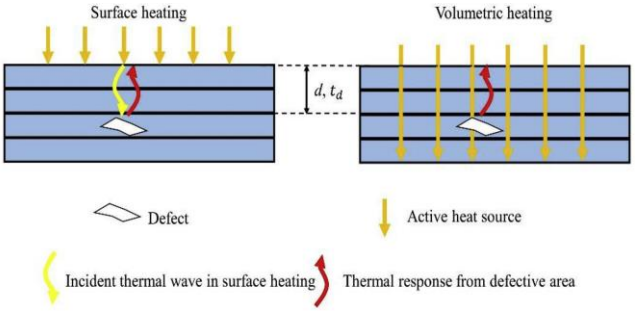

Fig. 2. Schematic comparison of surface and volumetric heating and their effect on the defect detection time. The defect response time with surface heating is larger than the volumetric heating defect one. This is due to the additional traveling time taken by the incident thermal wave for traveling from the surface to the defect and coming back. This is indicated by a light-yellow arrow on the left image. (For interpretation of the references to colour in this figure legend, the reader is referred to the Web version of this article.)

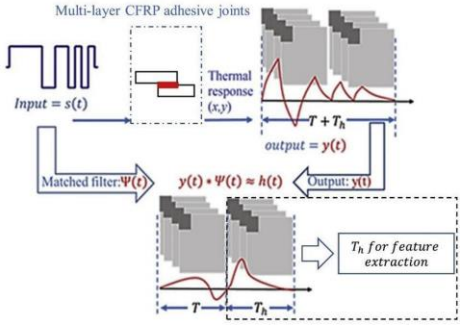

Fig. 3. Eddy current pulse compression thermography principle.

thickness [26,27].

In the case of volumetric heating, the ECPT characterization can be either in transmission or reflection mode. If the thermal diffusion length μ is greater than the depth d at which the delamination/defect is possibly buried, the response from the defect can be observed through the acquired surface temperature field. The unique advantage of the volumetric heating compared to the surface heating scenarios (*e.g.* as in the case of light-stimulated thermography) comes from the direct interaction between the buried defect and the induced EC field. In surface heating mode, the generated thermal wave must be reflected by the defect, taking twice the time with respect to the volumetric heating mode before being recorded by the infrared (IR) camera. In addition, the thermal waves travel double the distance, which implies doubling also the attenuation in a logarithmic scale [9]. The volumetric heating by the EC excitation is depicted in Fig. 2. The whole specimen's thickness is heated-up by the induced EC and Joule's effect [18].

The information needed for characterizing the defects comes from the thermal waves traveling from the defected area at a depth d (see Fig. 2, right), which will have a different amplitude than those generated in the surrounding sound area. Instead in surface heating, the defect signal comes from the thermal waves originated at the surface and reflected by the defect. The diffusion time in this case is more than twice for the same defect depth since due to the longer distance the higher frequency components are more attenuated and the resulting mean diffusion velocity is lower.

2.2. Pulse-compression techniques

PuC is used to improve the range resolution and SNR of the signals *e.g.* in RADAR and ultrasonic applications. Coded signals together with PuC have been also applied on ECPT, leading to ECPuCT [28,30], or without exploiting coded signals and just correlation technique *i.e.* thermal wave radar [29]. In ECPuCT, the sample is excited with a coded excitation, a Barker code (BC) in the present case, of duration T and thermograms are collected for an overall time duration of $T + T_h$. An estimated impulse response $\tilde{h}(t)$ of duration T_h is retrieved after performing the PuC algorithm, as shown schematically in Fig. 3. PuC relies on the existence of a pair of signals: an excitation signal $s(t)$ of duration T and bandwidth B, and a matched filter $\Psi(t)$, such that their convolution $s(t)*\Psi(t)$ approximates the Dirac's Delta function $\delta(t)$:

$$s(t) * \Psi(t) = \tilde{\delta}(t) \approx \delta(t). \tag{2}$$

If Eq. (2) is satisfied, and $s(t)$ excites a SUT that is characterized by the ideal impulse response $h(t)$, then an estimation of the $h(t)$, *i.e.* $\tilde{h}(t)$, can be obtained by convolving the output signal $y(t)$with $\Psi(t)$. Eq. (3) shows the mathematical formulation for a single pixel of the acquired thermograms, in presence of an Additive-White-Gaussian-Noise $e(t)$, which is considered uncorrelated with $\Psi(t)$. The estimated impulse response can be obtained as:

$$\tilde{h}(t) = y(t)*\Psi(t) \xrightarrow{y(t)=h(t)*s(t)+e(t)} h(t)*s(t)*\Psi(t) + e(t)*\Psi(t) = \\ = h(t)*\tilde{\delta}(t) + \tilde{e}(t) \approx h(t) + \tilde{e}(t). \tag{3}$$

The main advantage of ECPuCT compared with ECPT is that the impulse response can be estimated by delivering energy to the system in a significantly longer time. This flexibility can be exploited, as in the present case, either to increase the SNR by providing more energy than in the ECPT scheme or to use lower power heating sources while maintaining the same SNR level. In this paper, $s(t)$ is a BC of order equal to 13 and the matched filter $\Psi(t)$ is the time-reversed sequence of the input coded signal, *i.e.* $s(-t)$ [31].

2.3. Non-uniform heating removal by partial least square

As shown in the block 3 of Fig. 1, to remove the non-uniform heating pattern, the PLS technique was applied to reconstruct the non-uniform heating pattern generated by the coil shape and the anisotropy of the material properties. As for the implementation, the PLS can reconstruct the whole three-dimensional data (x, y, t) to characterize the non-uniform heating pattern at each time. Thus, by subtracting the original data by the PLS reconstructed data, the surface condition and anisotropic conductivity influences are mitigated. The algorithm is depicted in Fig. 4 and mathematical formulation is shown below.

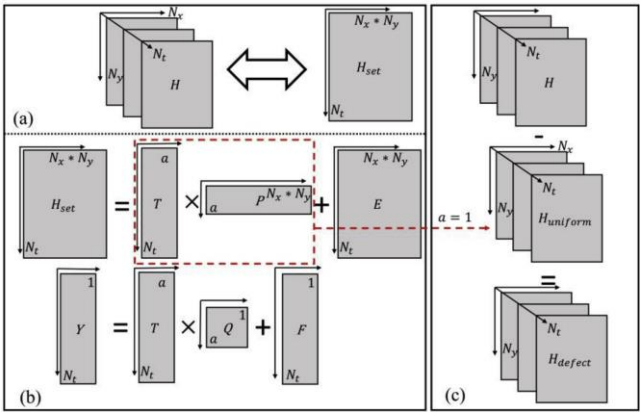

Fig. 4. Implementation process for PLS subtraction: (a) Data reshape process, (b) PLS component calculation, (c) Subtraction on the first PLS component.

The set of impulse responses $H_{N_x \times N_y \times N_t}$ retrieved after PuC is reshaped from 3D to 2D as $H_{N_t \times (N_x * N_y)}$, which can be shortened as H_{set}. The PLS mathematical modelling of H_{set} is conducted as:

$$H_{set} = TP^T + E \quad , \quad Y = TQ^T + F, \tag{4}$$

where $Y_{N_t \times 1}$ is corresponding to each frame number vector $[1, \ldots, N_t]$ and $T_{N_t \times a}$ is the score matrix. The scores are interpreted as latent variables of each frame provoking systematic variation in H_{set}. $P_{N_t \times a}$ and $Q_{a \times 1}$ are the loadings matrices, which describe the way of projecting $T_{N_t \times a}$ to H_{set} and Y respectively. H_{set} and Y are assumed to be partly modelled by same latent variables $T_{N_t \times a}$. The score matrix $T_{N_t \times a}$ columns are orthogonal to each other and H_{set}can be estimated as linear combination of $T_{N_t \times a}$ with coefficient weights $W_{(N_x * N_y) \times a}$. Thus, scores T can be expressed as:

$$T = H_{set} W. \tag{5}$$

After the calculation of scores, loadings P and Q are estimated through the regression of H_{set} and Y. Then, residual matrices are computed by subtracting the estimated TP^T and $TQ^T$from H_{set} and Y, respectively. The regression coefficients B for the model are obtained using the following equations:

$$B = WQ^T, \tag{6}$$

that can be solved as:

$$Y = H_{set} B + F = H_{set} WQ^T + F. \tag{7}$$

The PLS problem is solved based on Iterative Partial Least Square

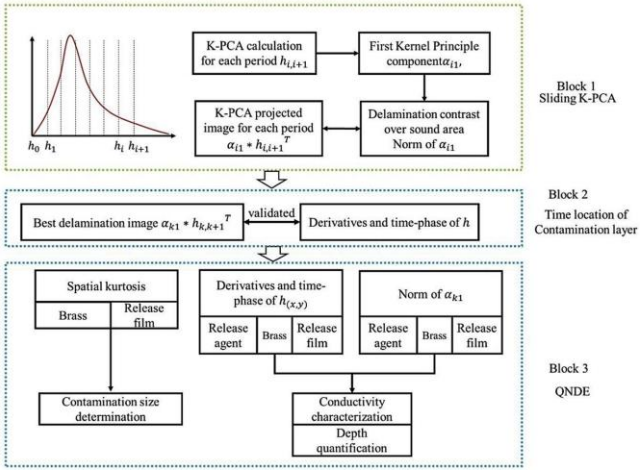

Fig. 5. Diagram depicting the proposed methodology for the characterization of contamination properties at the bonding interface.

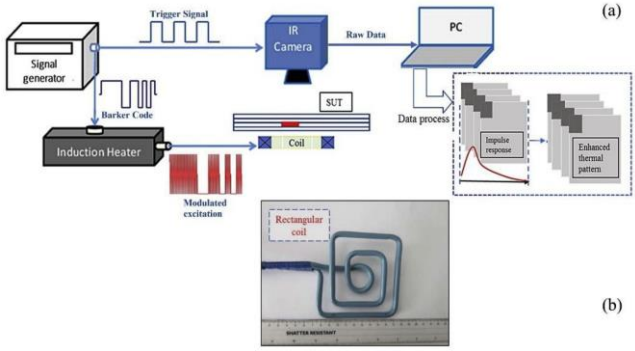

Fig. 6. Experimental setup: (a) system block diagram, (b) detail of the employed rectangular coil.

(IPALS) algorithm. After obtaining PLS components TP^T of the data H_{set}, the first PLS component is applied to reconstruct the non-uniform heating pattern and PLS subtraction is conducted on the first component reconstructed data.

2.4. Feature extraction techniques for impulse response

This section introduces the approach to locate the time when the information is maximum about the contamination layer. The evaluation of contamination properties is conducted based on optimal time window. The process to evaluate the electrical and thermal properties of the contamination is based on the selection of a proper time window within the pixelwise-retrieved $\tilde{h}(t)$ that provides the information about the contamination layer. The proposed procedure is schematically depicted in Fig. 5.

If $H_{N_x \times N_y \times N_t}$ is segmented evenly in time as $h_{i,i+1}$, where i denotes the time position of a chosen time window, then the projected image can be calculated as $\alpha_{i1} * {h_{i,i+1}}^T$ by using K-PCA for $h_{i,i+1}$ to obtain the first principal component. For each projected image $\alpha_{i1} * {h_{i,i+1}}^T$, the contrast of the delamination over sound area is considered as the norm of each corresponding α_{i1}, which is presented as the Sliding K-PCA part in Fig. 5. By selecting the best image with positive local maximum α_{k1}, the corresponding image is reconstructed as $\alpha_{k1} * {h_{k,k+1}}^T$.To understand if the period $\alpha_{k1} * {h_{k,k+1}}^T$ contains the maximum information, derivative and time-phase of the impulse responses are used, as shown in the middle part of Fig. 5. Then, the image $\alpha_{k1} * {h_{k,k+1}}^T$ is used to locate the contamination response $h_{k,k+1}$ for brass film, release film, and release agent, as it is shown in Fig. 5 (QNDE labelled part). The contamination properties are characterized by the norm distance of α_{k1}, and the size of brass film and release film is determined by spatial kurtosis on the image. $\alpha_{k1} * {h_{k,k+1}}^T$.

3. Experimental setup and the sample under test

ECPuCT system setup is introduced in the Section 3.1 and CFRP single lap joints with different contaminations including highly electrically conductive brass, release film and release agent with low electrical conductivity are introduced in Section 3.2.

3.1. ECPuCT system

The ECPuCT system diagram is depicted in Fig. 6(a). An Agilent 33500B single output signal generator was used to send both the BC modulating signal to the induction heating unit and a reference clock trigger to the IR camera to acquire thermograms at 50 Frames Per Second (FPS). A Cheltenham EasyHeat 224 induction heating unit was employed for exciting the coil with a maximum excitation power and current values of 2.40 kW and 400 A respectively, with tunable $f_{carrier}$ within 150–400 kHz. For the reported experimental results, values of excitation current I equal to 40 A and $f_{carrier}$ of 240 kHz were selected to prevent damaging the CFRP sample due to the long excitation time using BC signal.

Fig. 6(b) shows a picture of the employed rectangular coil made from

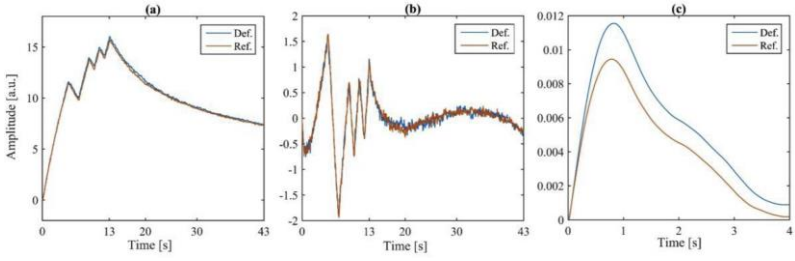

Fig. 7. An example of signals for one reference point on sound area and on contaminated area (brass), (a) Acquired raw signal, (b) raw signal after removal of step heating contribution, (c) impulse response after PuC process.

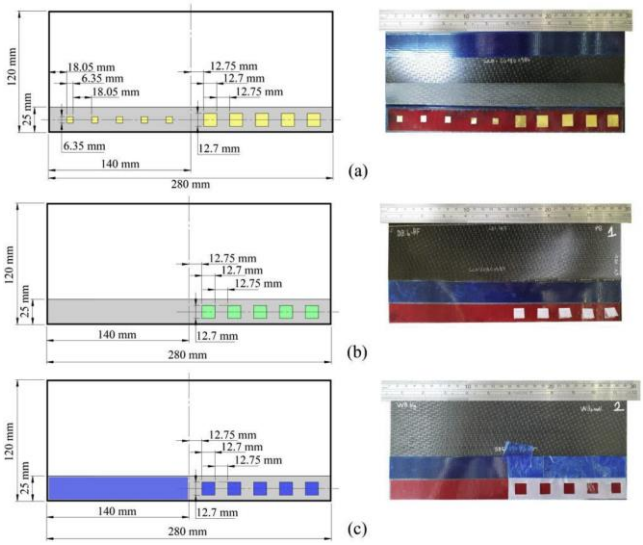

Fig. 8. CFRP-epoxy adhesive single-lap joints plan sketch: (a) Perfect bond and release film inclusion, (b) Brass film inclusion, (c) Release agent inclusion.

high conductivity hollow copper tube with the outer and inner diameters of 6.35 mm and 4.00 mm respectively. Water cooling was implemented to the coil to avoid over-heating and the lift-off maintained at 3.00 mm from the SUT's surface to ensure the volumetric heating of the sample. Only one side of the coil is selected as a linear coil to induce parallel eddy currents in the direction of maximum conductivity within the sample, the length of this side was 9.30 mm. The IR camera was the FLIR SC655, equipped with an un-cooled microbolometer detector array having a resolution of 640 × 480 pixels, spectral range of 7.5–14.0 μm and NETD <30 mK. The IR camera recorded the SUT's surface temperature distribution during the whole 13 s BC modulated stimulus, as well as for an additional 30 s of cooling period [32] with a frame rate of 50 Hz, *i.e.* 50 FPS. Please note that the 13 s of BC and the additional 30 s of acquisition correspond to $T + T_h$ described in Section 2.2. Fig. 7 depicts the acquired raw signal, the raw signal ready for the PuC algorithm to be applied and the impulse response after applying PuC process. It

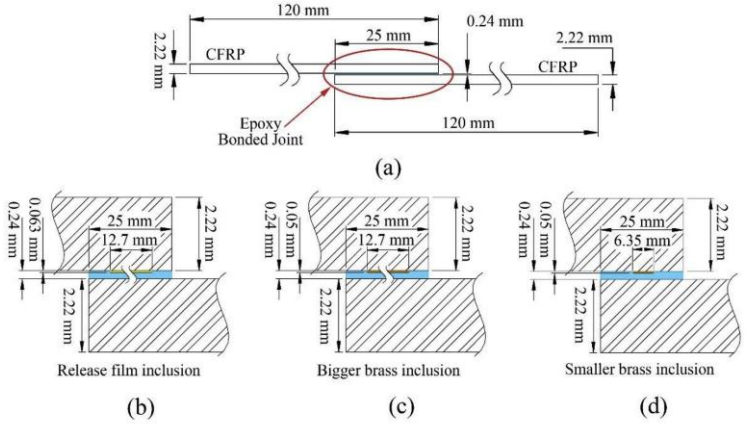

Fig. 9. CFRP-epoxy adhesive joints cross section sketch: (a) Perfect bond, (b) Debonding with release film, (c) Debonding with bigger brass film, (d) Debonding with smaller brass film.

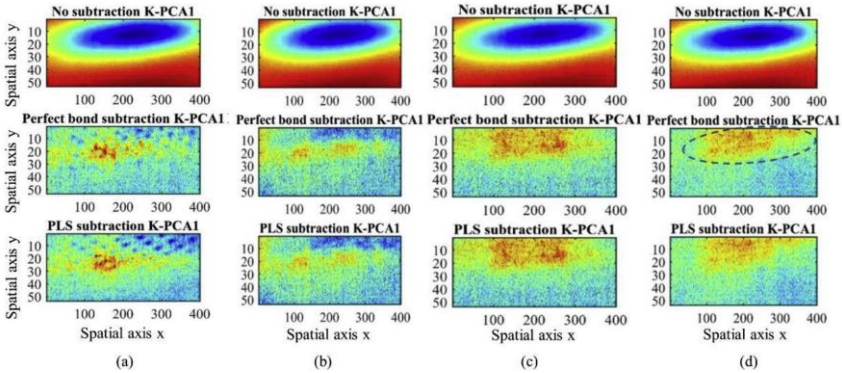

Fig. 10. Results obtained without subtraction and with subtraction of PLS and perfect bond for: (a) Brass film, (b) Release film, (c) More release agent contamination, (d) Less release agent contamination.

must be noted that the problem of passing from a raw signal containing a step heating contribution provoked from the use of monopolar heating source as in the present case (Fig. 7(a)) to the signal ready for PuC (Fig. 7 (b)) has been thoroughly reviewed and explained in previous papers from the authors [28,30,32]. The interested reader is suggested to refer to the mentioned works to gain more insight on the technique.

Finally, the captured thermogram sequences were transmitted to a PC for visualization and post-processing, including signal pre-process, PuC, thermal pattern enhancement and feature extraction.

3.2. Investigated samples description

As explained in Section 1, three types of contaminated debonding of brass, release film and release agent were manufactured. The composite plates were manufactured using six plies of HexPly M21 - 5H Satin woven prepreg. Due to woven structure and the number of lay-up, residual stress can occur in specimens. The thickness of the specimens may vary through the structure. However, the mentioned variation is here negligible as it is in the range of 10^{-6} m. The interfacial contaminations were realized by using brass film, Wrightlon 4600 release film and Marbocote 45 release agent. As it is shown in Fig. 9(a), two CFRP plates were overlapped to create a single lap joint, such that the bonded area was 280 mm × 25 mm while the total area of each composite plate was. 280 mm × 120 mm

In the bonding area, two-fold brass film and release film inserts were added to simulate debonding at the interface; release agent was sprayed over the epoxy film sheet prior to second adherend placement in order to weaken the epoxy quality. As shown in Fig. 8(b) and Fig. 9(b), five square release films were placed at the upper interface, having a nominal thickness of 0.076 mm and size of 12.70 mm × 12.70 mm. Ten square-shape brass inclusions all having thickness equal to 0.05 mm were embedded into the sample as depicted in Figs. 8(a), Fig. 9(c). Please note that these brass inclusions had different sizes: bigger ones are 12.70 mm × 12.70 mm, and smaller ones 6.35 mm × 6.35 mm. As for the weak bond sample, the part with less contamination was made by spraying the release agent on a mask above the uncured adhesive epoxy, as shown in Fig. 8(c). On the other hand, the part with more contamination was made by spraying the release agent uniformly on the whole bonding area, as shown by a blue area in Fig. 8(c). It should be noted that in latter case, the release agent has been diffused into the uncured epoxy, which may result in untraceable amounts at the interface between epoxy adhesive and composite adherend.

4. Results and discussion

In this section, the PuC thermal data are pre-processed to remove non-uniform heating by PLS, time window sliding for depth detection of contamination and quantitative evaluation of contamination layers including classification and sizing of contamination as illustrated in Fig. 1, QNDE part.

4.1. Non-uniform heating pattern removal

The non-uniform heating pattern usually generated by coil in induction heating can hinder the ability to detect and locate the defect. Thus, as it is shown in third block of Fig. 1, this section focusses on the implementation of non-uniform heating pattern removal. The non-uniform heating pattern generated by the anisotropy of the material, geometry and coil shape should be removed to obtain a more uniform image. This would help achieving a better feature extraction. Two different methods have been used to remove non-uniform heating pattern: PLS and perfect bond subtraction using a reference.

In this work, PLS reconstructed thermal data is subtracted from the PuC thermal data. As shown in Fig. 4, only the first PLS component is used to reconstruct the non-uniform heating because according to Ref. [33], the first component contains the heating pattern, while second or third components might carry defect information. Besides the PLS approach, repeatable experiment on the perfect bonding sample is also conducted to obtain data without defect but containing non-uniform heating pattern. The results of both approaches are illustrated in Fig. 10. In Fig. 10(a), the 12.70 mm × 12.70 mm brass film is identified by three heated fibers shown in K-PCA1 using perfect bond and PLS subtraction methods respectively. It is of utmost importance to note that the PLS subtraction method does not require to gather data from the sound sample, thus the misalignment of spatial coordinates caused by different experiments is avoided. Instead, further efforts are needed to subtract perfect bonding in a proper way. Therefore, in the case of K-PCA1 with PLS subtraction, the brass pattern is more uniform and closer to the real square shape than the one obtained over the same sample using perfect bond subtraction (see third row of Fig. 10(a)). However, the pattern of the smaller brass film inclusion 6.35 mm × 6.35 mm is not clearly visible in Fig. 10(a) that can be due to the texture of the fibers above the brass. In the case of release films depicted in Fig. 10(b), the defects are more clearly visible. The difference in the SNR of the patterns from bigger brass and the release film is due to the fact

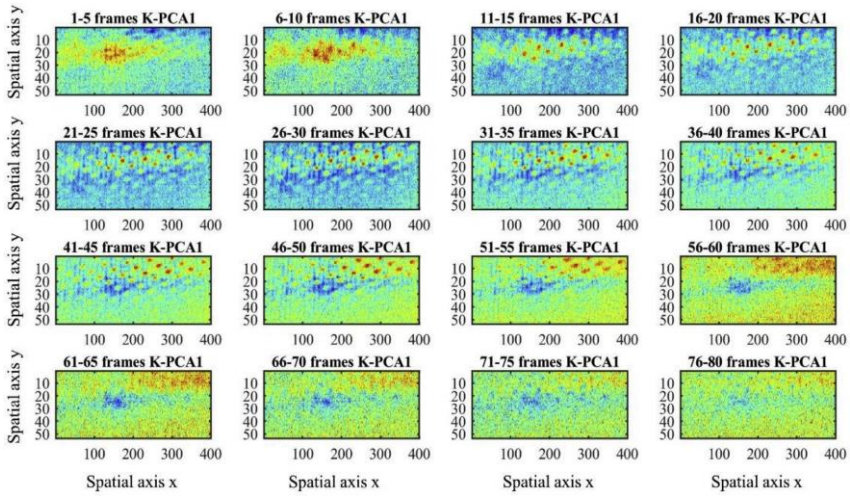

Fig. 11. Sliding K-PCA results for brass film inclusion.

that brass inserts have higher electrical conductivity than the sound sample, hence not only allowing eddy currents flowing but also heating up due to the Joule's effect. Release film defects are not electrically conductive, therefore completely interrupt and deviate the eddy current flux around them.

It can be observed in the first row of Fig. 10 that the K-PCA1 obtained from the raw acquired $h(t)$'s contains the elliptical thermal pattern generated by the excitation coil. On the other hand, by subtracting either the perfect bond or the PLS data from the various contaminated bonding data, the debonding area is further enhanced, as it is visible in second and third rows of Fig. 10. For the release agent inclusion, the detection capability is heavily reduced as shown in Fig. 10(c) and (d). The contrast between more release agent inclusion and sound area is observable in Fig. 10(c). The release agent might have been diffused into the epoxy resin or distributed uniformly along the bonded area. However, in Fig. 10(d), the defect pattern is similar to the non-uniform heating pattern, which shows that less release contamination agent is not detectable.

Based on the discussion above, the proposed non-uniform heating removal process using PLS techniques can remove the non-uniform

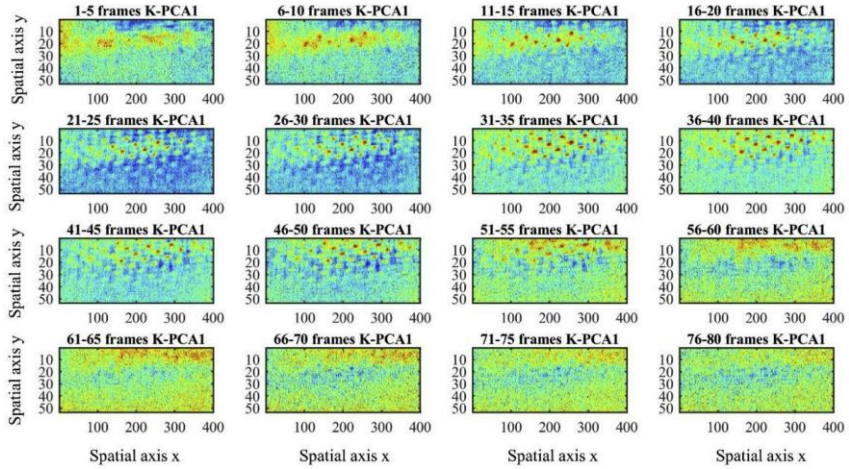

Fig. 12. Sliding K-PCA results for release film inclusion.

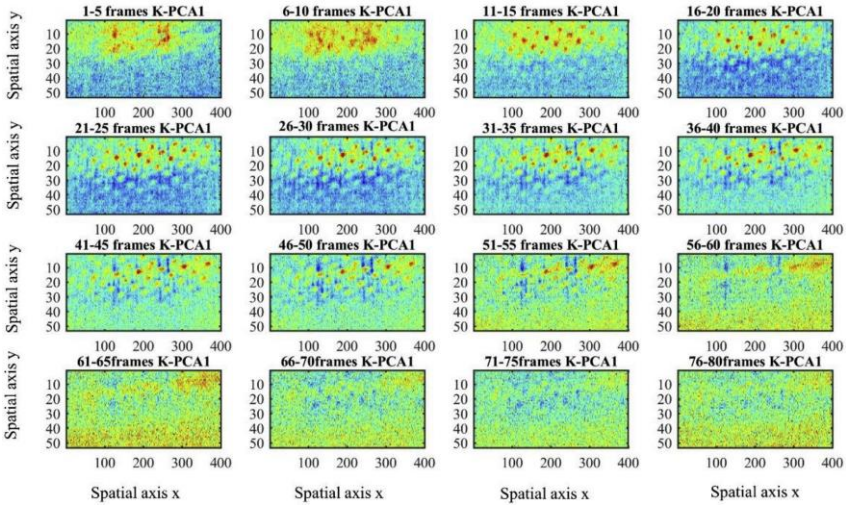

Fig. 13. Sliding K-PCA results for weak bond with more contamination.

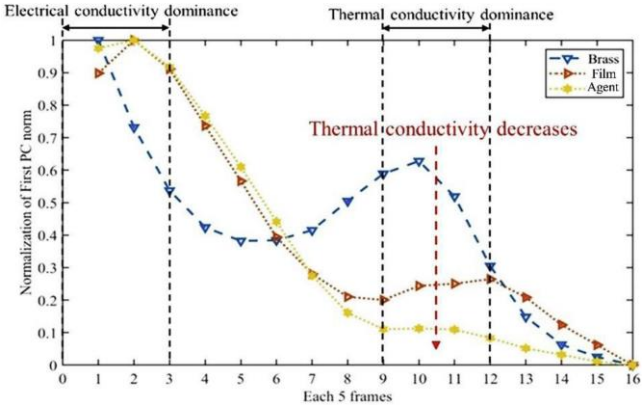

Fig. 14. First PC norm of different contaminations versus number of frames.

heating pattern for detection of contamination. Mismatch of spatial coordinates can be avoided through PLS subtraction.

4.2. Multi-physics analysis based on sliding window of K-PCA

In order to find the time instance carrying the maximum information about the contamination layer, physical analysis of the eddy current and thermal phenomena based on sliding K-PCA is conducted. The impulse response-based K-PCA calculation is presented in previous work [28]. The time series of the images is subdivided into non-overlapping time-windows each one having five frames. In K-PCA, the linear kernel is applied due to the limited number of data in five frames. The calculation is based on the first principal component, which can help compress major information. The physical meaning of K-PCA1 after PLS subtraction is to observe the variations of SUT's thermal response. The feature used as depth indicator is the norm of first principal component for every five frames within the first 80 frames of PLS subtracted data.

The Sliding K-PCA results of brass, release film and release agent inclusions are presented in Figs. 11–13 for every 5 frames. As shown in Fig. 11, a higher contrast between brass and sound area is achieved in the first ten frames. This can be explained by the higher electrical conductivity of brass, so that larger eddy current density is expected than that in the surrounding CFRP and bonding material. According to Ref. [34], in the first phase of the induction heating EC is the dominant

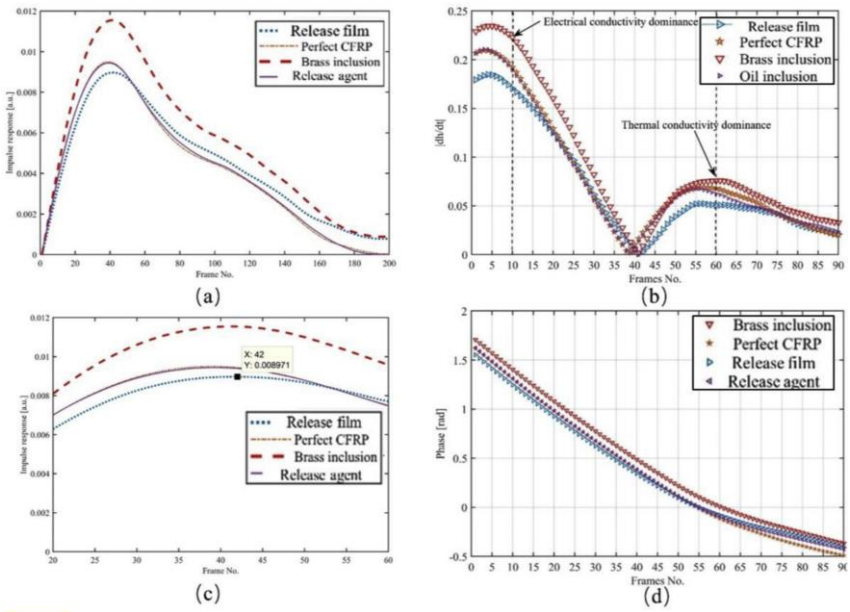

Fig. 15. Data of different material at selected position (a) Impulse responses, (b) Absolute value of impulse response derivatives, (c) Zoom of the peak value of impulse responses, (d) Time-phase variations of different inclusions.

effect, thus the higher the conductivity, the higher the EC density and the resulting heating due to the Joule's effect. As shown in Figs. 11 and 12, the highest contrast is also found at the beginning for release film and release agent samples. The difference between conductive contamination (brass) and non-conductive ones (release film and release agent) is the time to reach the peak contrast. It can be seen in Fig. 14 that it only takes 5 frames (100 ms) for the brass to reach its maximum contrast but for non-conductive contaminations it takes 10 frames (200 ms). In Figs. 11–13, from frame 11 to 25, the defect pattern is covered by the response from the texture of the CFRP layer over the debonding area. Heat diffusion between the layers plays a major role in the detection of debonding: for brass film, the heat diffuses from brass to the surrounding, for release agent contamination or release film, the heat from the surrounding CFRP diffuses into the contaminated area.

Within the 80 frames, shown in Fig. 14, first 15 frames indicate the maximum domination of the Joule's effect, while in the cooling stage, around frame number 60, thermal diffusion plays a significant role.

4.3. Classification of contamination and quantitative evaluation of size

In this Section, the impulse response and its derivatives are compared to classify thermal and electrical properties of contamination materials as well as the brass size. In Fig. 15(a), it can be observed that at the beginning of the heating stage, the impulse response of brass rises quicker than other two contaminations and CFRP due to its higher electrical conductivity. The release film shows the least significant response to the Joule's effect because it is not conductive. Impulse response of intact CFRP shows a slightly higher heating response than the release agent at its peak time.

It is observed that the peak value and its time instant for the brass is different from release film inclusion, which has a later peak time than the CFRP and release agent as shown in Fig. 15(c). After reaching the peak, the release film inclusion cools down slower than both intact CFRP and weak bond as it hampers the heat diffusion. This effect is visible in Fig. 15(a).

However, it is challenging to evaluate the thermal conductivity of the brass contamination only by the impulse response because the Joule heating is more significant in the brass with respect to the sound CFRP surrounding area. Therefore, the heat diffuses from the brass to the surrounding area even at the cooling stage. Thus, the derivative of the impulse response can be used to evaluate the thermal conductivity as shown Fig. 15(b). Figs. 14 and 15(b) show similar trends, *i.e.* electrical conductivity plays a dominant role at around 10th frame while thermal conductivity shows a prominent role at 60th frame. It can be seen in Fig. 15(b) that at 60th frame the absolute value of impulse response's derivative from brass has higher value than other contaminations, proving its higher thermal conductivity. Comparing the difference of release agent and CFRP in heating and cooling stages in Fig. 15(b), it is observed that the release agent has more influence on thermal conductivity of contaminated area than the electrical conductivity. In addition, by using the time-phase information of the impulse responses defined through Hilbert transform [31], it can be observed that the phase turning point also happens at 60th frame (see Fig. 15(d)). Please note that the turning point happens at the same value at which there is the transition in Figs. 14 and 15(b).

In order to determine the size of contaminations, spatial kurtosis is applied to the data. The sizing data was derived from five pixels lines of data in the best contrast image. Since the size of bigger brass is 12.70 mm × 12.70 mm and smaller one is has one fourth of the area, it is observed that the spatial kurtosis of smaller one over bigger one is 2.05/

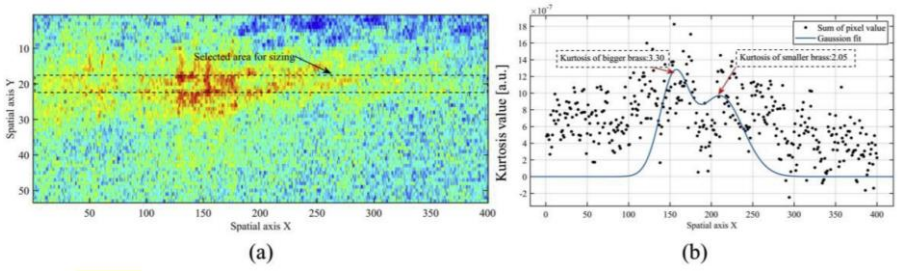

Fig. 16. Spatial kurtosis for sizing of bigger and smaller brass films: (a) Selected area for size quantification, (b) Results of spatial kurtosis.

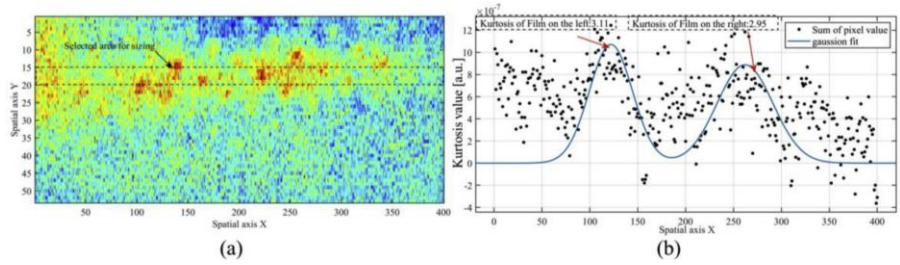

Fig. 17. Spatial kurtosis for sizing of the release films. (a) Selected area for size quantification, (b) Results of spatial kurtosis.

3.30 = 0.62, which is slightly bigger than 0.5 for the width ratio shown in Fig. 16. This can be caused by the texture influence, which has been explained in Section 4.1. For the release films, the kurtosis ratio of two same films with the same size is 3.11/2.95 = 1.05, which indicates their similar size as shown in Fig. 17.

It is proved that at first 15 and 60 frames the physical properties of inclusions can be classified and using the spatial kurtosis at 15th frame brass size can be quantified.

5. Conclusion and future work

This work focusses on detection and evaluation of the CFRP-epoxy adhesive single-lap joints with artificially embedded contaminations of different materials in separate samples using eddy current pulse-compression thermography. Three processing steps have been applied: (1) the removal of non-uniform heating through PLS; (2) sliding Kernel Principal Component Analysis for determination of the best time interval to reveal information about contamination layer; (3) classification of contamination properties at the specific time using proposed features. The conclusions are as follows:

1. PLS can remove the non-uniform heating pattern and achieve better results of perfect bond subtraction because it solves the possible problem of misalignment of spatial coordinates resulting from different experiments;
2. After removal of non-uniform heating pattern, sliding K-PCA features and norm of principal component can be applied for detection of contamination layer in heating and cooling stages. Since eddy current can generate volumetric Joule heating in CFRP, the first time instant of the high contrast happens at the very beginning of the retrieved impulse responses, *i.e.* first 15 frames (300 ms), indicating the difference in contamination's electrical properties on adhesive joints. It has also been verified that 60th frame contains the maximum information about the contaminations in the cooling stage;
3. The contamination proprieties can be classified using the derivatives of impulse response at specific time. The release agent contamination has the minimum influence on the electrical and thermal properties of the adhesive layer compared with brass film and release film. The release agent contamination affects the thermal properties of the adhesive epoxy layer more than the electrical properties.

This approach can address the non-uniform heating problem with complex geometry and improve SNR for the detection and characterization of contaminations. Future work will investigate the quantitative determination of electrical and thermal properties of the multilayer structures using eddy current thermography techniques.

Acknowledgments

This project is funded by the European Union's Horizon 2020 research and innovation programme under the Marie Skłodowska-Curie grant agreement No 722134 – NDTonAIR.

References

[1] Barile C, Casavola C, Pappalettera G, Vimalathithan PK. Characterization of adhesive bonded CFRP laminates using full-field digital image stereo-correlation and finite element analysis. Compos Sci Technol 2019;169:16–25.
[2] Lim AS, Melrose ZR, Thostenson ET, Chou T-W. Damage sensing of adhesively-bonded hybrid composite/steel joints using carbon nanotubes. Compos Sci Technol 2011;71:1183–9.
[3] Casavola C, Palano F, De Cillis F, Tati A, Terzi R, Luprano V. Analysis of CFRP joints by means of T-pull mechanical test and ultrasonic defects detection. Materials 2018;11:620.

[4] Heide-Jørgensen S, de Freitas ST, Budzik MK. On the fracture behaviour of CFRP bonded joints under mode I loading: effect of supporting carrier and interface contamination. Compos Sci Technol 2018;160:97–110.
[5] Muliana A, Nair A, Khan KA, Wagner S. Characterization of thermo-mechanical and long-term behaviors of multi-layered composite materials. Compos Sci Technol 2006;66:2907–24.
[6] Tornow C, Schlag M, Lima LCM, Stübing D, Hoffmann M, Noeske P-LM, et al. Quality assurance concepts for adhesive bonding of composite aircraft structures–characterisation of adherent surfaces by extended NDT. J Adhes Sci Technol 2015;29:2281–94.
[7] Palumbo D, Tamborrino R, Galietti U, Aversa P, Tatì A, Luprano V. Ultrasonic analysis and lock-in thermography for debonding evaluation of composite adhesive joints. NDT E Int 2016;78:1–9.
[8] Markatos D, Tserpes K, Rau E, Markus S, Ehrhart B, Pantelakis S. The effects of manufacturing-induced and in-service related bonding quality reduction on the mode-I fracture toughness of composite bonded joints for aeronautical use. Compos B Eng 2013;45:556–64.
[9] Yang R, He Y. Optically and non-optically excited thermography for composites: a review. Infrared Phys Technol 2016;75:26–50.
[10] Milovanović B, Banjad Pečur I. Review of active IR thermography for detection and characterization of defects in reinforced concrete. J Imaging 2016;2:11.
[11] Shin PH, Webb SC, Peters KJ. Pulsed phase thermography imaging of fatigue-loaded composite adhesively bonded joints. NDT E Int 2016;79:7–16.
[12] Waugh R, Dulieu-Barton JM, Quinn S. Pulse phase thermography and its application to kissing defects in adhesively bonded joints. Appl Mech Mater: Trans Tech Publ 2011:369–74.
[13] Grosso M, Lopez JE, Silva VM, Soares SD, Rebello JM, Pereira GR. Pulsed thermography inspection of adhesive composite joints: computational simulation model and experimental validation. Compos B Eng 2016;106:1–9.
[14] Waugh RC, Dulieu-Barton JM, Quinn S. Thermographic identification of defects in adhesively bonded joints. Advancement of optical methods in experimental mechanics, ume 3. Springer; 2014. p. 347–51.
[15] Ren W, Liu J, Tian GY, Gao B, Cheng L, Yang H. Quantitative non-destructive evaluation method for impact damage using eddy current pulsed thermography. Compos B Eng 2013;54:169–79.
[16] Bai L, Tian S, Cheng Y, Tian GY, Chen Y, Chen K. Reducing the effect of surface emissivity variation in eddy current pulsed thermography. IEEE Sens J 2013;14:1137–42.
[17] Cheng L, Gao B, Tian GY, Woo WL, Berthiau G. Impact damage detection and identification using eddy current pulsed thermography through integration of PCA and ICA. IEEE Sens J 2014;14:1655–63.
[18] Liang T, Ren W, Tian GY, Elradi M, Gao Y. Low energy impact damage detection in CFRP using eddy current pulsed thermography. Compos Struct 2016;143:352–61.
[19] Cheng L, Tian GY. Comparison of nondestructive testing methods on detection of delaminations in composites. J Sensors 2012;2012.
[20] Yang R, He Y. Eddy current pulsed phase thermography considering volumetric induction heating for delamination evaluation in carbon fiber reinforced polymers. Appl Phys Lett 2015;106:234103.
[21] He Y, Yang R. Eddy current volume heating thermography and phase analysis for imaging characterization of interface delamination in CFRP. IEEE Trans. Ind. Inf. 2015;11:1287–97.
[22] Zimnoch M, Oliferuk W, Maj M. Estimation of defect depth in steel plate using lock-in IR thermography. Acta Mech Automatica 2010;4:106–9.
[23] Tian GY, Gao Y, Li K, Wang Y, Gao B, He Y. Eddy current pulsed thermography with different excitation configurations for metallic material and defect characterization. Sensors 2016;16:843.
[24] Gao Y, Tian GY, Wang P, Wang H, Gao B, Woo WL, et al. Electromagnetic pulsed thermography for natural cracks inspection. Sci Rep 2017;7:42073.
[25] Li Z, Meng Z. A review of the radio frequency non-destructive testing for carbon-fibre composites. Meas Sci Rev 2016;16:68–76.
[26] Yang R, He Y. Polymer-matrix composites carbon fibre characterisation and damage inspection using selectively heating thermography (SeHT) through electromagnetic induction. Compos Struct 2016;140:590–601.
[27] He Y, Yang R, Zhang H, Zhou D, Wang G. Volume or inside heating thermography using electromagnetic excitation for advanced composite materials. Int J Therm Sci 2017;111:41–9.
[28] Yi Q, Tian G, Malekmohammadi H, Zhu J, Laureti S, Ricci M. New features for delamination depth evaluation in carbon fiber reinforced plastic materials using eddy current pulse-compression thermography. NDT E Int 2019;102:264–73.
[29] Yang R, He Y, Mandelis A, Wang N, Wu X, Huang S. Induction infrared thermography and thermal-wave-radar analysis for imaging inspection and diagnosis of blade composites. IEEE Trans. Ind. Inf. 2018;14:5637–47.
[30] Malekmohammadi H, Laureti S, Ricci M, Yi Q, Zhu J, Tian GY. An experimental comparison of LED and eddy current pulse-compression thermography on an impact damage CFRP benchmark sample. In: 2018 IEEE far east NDT new technology & application forum (FENDT). IEEE; 2018. p. 13–7.
[31] Xu C, Zhou N, Xie J, Gong X, Chen G, Song G. Investigation on eddy current pulsed thermography to detect hidden cracks on corroded metal surface. NDT E Int 2016;84:27–35.
[32] Silipigni G, Burrascano P, Hutchins DA, Laureti S, Petrucci R, Senni L, et al. Optimization of the pulse-compression technique applied to the infrared thermography nondestructive evaluation. NDT E Int 2017;87:100–10.
[33] Lopez F, Ibarra-Castanedo C, de Paulo Nicolau V, Maldague X. Optimization of pulsed thermography inspection by partial least-squares regression. NDT E Int 2014;66:128–38.
[34] Yin A, Gao B, Yun Tian G, Woo W, Li K. Physical interpretation and separation of eddy current pulsed thermography. J Appl Phys 2013;113:064101.

applied sciences

MDPI

Article

Air-Coupled, Contact, and Immersion Ultrasonic Non-Destructive Testing: Comparison for Bonding Quality Evaluation

Bengisu Yilmaz [1,*], Aadhik Asokkumar [1], Elena Jasiūnienė [1,2] and Rymantas Jonas Kažys [1]

[1] Prof. K. Baršauskas Ultrasound Research Institute, Kaunas University of Technology, K. Baršausko St. 59, LT, 51423 Kaunas, Lithuania; aadhik.asokkumar@ktu.lt (A.A.); elena.jasiuniene@ktu.lt (E.J.); rymantas.kazys@ktu.lt (R.J.K.)

[2] Department of Electronics Engineering, Kaunas University of Technology, Studentų St. 48, LT, 51367 Kaunas, Lithuania

* Correspondence: bengisu.yilmaz@ktu.lt

Received: 14 September 2020; Accepted: 25 September 2020; Published: 27 September 2020

Abstract: The objective of this study is to compare the performance of different ultrasonic non-destructive testing (NDT) techniques for bonding quality evaluation. Aluminium-epoxy-aluminium single lap joints containing debonding in the form of release film inclusions have been investigated using three types of ultrasonic NDT methods: contact testing, immersion testing, and air-coupled testing. Apart from the traditional bulk wave ultrasound, guided wave testing was also performed using air coupled and contact transducers for the excitation of guided waves. Guided wave propagation within adhesive bond was numerically simulated. A wide range of inspection frequencies causing different ultrasonic wavelengths has been investigated. Average errors in defect sizing per ultrasonic wavelength have been used as a feature to determine the performance of each ultrasonic NDT technique. The best performance is observed with bulk wave investigations. Particularly, the higher frequencies (10–50 MHz) in the immersion testing performed significantly better than air-coupled testing (300 kHz); however, air coupled investigations have other advantages as contactless inspection. Whereas guided wave inspections show relatively lower accuracy in defect sizing, they are good enough to detect the presence of the debonding and enable to inspect long range. Even though each technique has its advantages and limitations, guided wave techniques can be practical for the preliminary in-situ inspection of adhesively bonded specimens.

Keywords: adhesive bonding; contact testing; immersion ultrasonic; air-coupled testing; air-coupled simulation; guided waves; defect sizing

1. Introduction

Adhesive bonding is an attractive alternative to other joining technologies due to its high performance to weight ratio, ability to join dissimilar materials, and homogenous load distribution. Although the advantages of the adhesive bonding are very attractive to highly developed industries, such as aerospace, their usage is limited due to the lack of the knowledge in the non-destructive testing (NDT) of bonding quality [1]. Hence, research in non-destructive evaluation of bonding quality is of great interest for decades.

The ultrasonic NDT techniques have been one of the most commonly used NDT techniques to evaluate bonding quality [2]. The ultrasonic NDT methods have been used not only to evaluate adherend integrity, but also for interface quality determination, debonding detection, and weak bond investigations [3].

Through-transmission immersion, ultrasonic NDT is considered the reference method within all ultrasonic NDT methods. The experiment itself requires two-sided access to the structure and the inspected component needs to be immersed in water [4]. Immersion pulse-echo ultrasonic inspection, on the other hand, requires only single-side access to the structure; however, it still requires water immersion of the sample [5,6]. In particular, pulse-echo immersion ultrasonic NDT techniques have been utilized for bonding interface visualization [7], debonding detection [8], adhesive quality evaluation [9], kissing bond evaluation [10], and for the defect positioning in dissimilar joints [11].

Moreover, scanning acoustic microscopy (SAM) allows structures to be inspected with high frequency-high resolution. While SAM provides higher spatial clarity, the size of the structure is limited, the experimental set-up is bulky and investigations are performed in water. SAM has been employed for the evaluation of weak bonds in composite joints [12], weak bond imaging with holography [13], and porosity identification in dissimilar joints [14].

Nowadays, air-coupled ultrasonic NDT has also gained interest for in-situ applications because, as a rapid ultrasonic testing, it can be performed without any contact medium and it applies to the industrial test line [15]. Compared to immersion ultrasonic, the air-coupled ultrasonic NDT has several advantages. However, it still lacks the high spatial resolution and fast inspections that are achieved with the immersion ultrasonic NDT. In a recent study, the interfacial stiffness coefficients of weak bonds have been investigated with air-coupled ultrasound [16]. Moreover, interface visualization of the tri-layer bonded aluminium plate has been performed with the air-coupled through-transmission ultrasonic testing [15]. While air-coupled through-transmission needs two-sided access, it is possible to inspect structures with pitch and catch by the propagation of Lamb waves [17].

The guided wave (GW) ultrasonic NDT is another promising technique to evaluate bonding quality that allows large structures to be inspected in a short time. GW ultrasound can be employed with non-contact systems, such as air-coupled transducers and laser interferometer [18–20]. Moreover, it is possible to excite and receive guided waves in specific modes with contact transducers, electromagnetic acoustic transducer (EMATs) [21], and macro fibre composite transducers (MCF) [22]. However, it should be noted that the evaluation with GW inspections requires an understanding of the wave propagation within the sample, which, in most cases, is achieved only by highly complex numerical investigations [23]. Several studies used guided waves to investigate bonding quality. While some works focused on the debonding and delamination detection with Lamb waves and vibrometry systems [24,25]; others discussed the scattering of the guided waves as a result of the change in interface quality [26,27]. In addition, weak bonds had been investigated by using Lamb wave inspection [28].

The comparison of ultrasonic NDT techniques is provided in Table 1 considering the overall capabilities and limitations of different techniques used in this study. In general, the bulk wave technique is more accurate because the insonified area is usually right beneath the transducer; however, that requires a time-consuming measurement process to scan a large structure. On top of that, immersion testing requires preparation of the setup, which includes a big water tank for inspection. Bulk waves in general are highly sensitive to the alignment of the transducers in case of the through-transmission technique. This is where the guided wave technique can excel because it is possible to use long-range inspection in short time.

This study aims to compare contact, immersion, and air-coupled testing techniques with the case study on single lap joints containing different bonding quality. Hence in this work, metal-adhesive bonded structures specifically, aluminium-epoxy-aluminium single lap joints having release film inclusions at the bonding interface have been investigated with different ultrasonic non-destructive testing techniques. Particularly, immersion ultrasonic NDT with through-transmission and pulse-echo techniques, scanning acoustic microscopy (SAM), air-coupled through-transmission, guided wave inspections with air-coupled excitation and a contact receiver, and guided wave inspections with a contact transmitter and receiver have been employed. Guided wave inspections have been validated via numerical simulations.

Table 1. Comparison of different techniques.

Techniques	Capabilities	Limitations
Immersion testing	MHz range operating frequency, coupling uniformity, less wear for probes, focused beams.	Limited materials due to corrosion.
Air-coupled testing	50 kHz to 2 MHz operating frequency, contactless coupling, focused beams.	High attenuation loss at higher frequencies, lower signal to noise ratio due to acoustical mismatch.
Contact Guided Wave (GW) testing	Up to 5 MHz operating frequency, the ability for faster inspection than air-coupled, superior coupling over immersion, and air-coupled methods hence higher transmissibility.	Wear of transducers and the material due to contact. Requires a special setup for angle excitation.
Air coupled excitation and contact reception Guided Wave (GW) testing	Possibility of mode selection, directional wavefront, long-range inspection.	Lower the signal to noise ratio.

2. Materials and Methods

2.1. Sample Description

The aluminium-epoxy-aluminium single lap joint containing release films have been manufactured at COTESA GmBH, Mittweida, Germany. For adherend, 1.6 mm thick aluminium 2024-T3 alloy sheets have been cut. For adhesive, 3M Scotch-Weld AF163 k-red structural adhesive film epoxy with the theoretical cured thickness of 0.24 mm has been selected. Prior to bonding, five square inclusions have been placed on the film adhesive (Figure 1a). Double-sided, 0.063 mm thick Wrightlon 4600 release film inclusions have been prepared as 12.7 mm by 12.7 mm to represent debonding at the interface. Bondline has been kept as 25 mm. Schematics of the cross-section of the sample is shown in Figure 1b. The properties of the material used for adhesive and adherend in the study are given in Table 2.

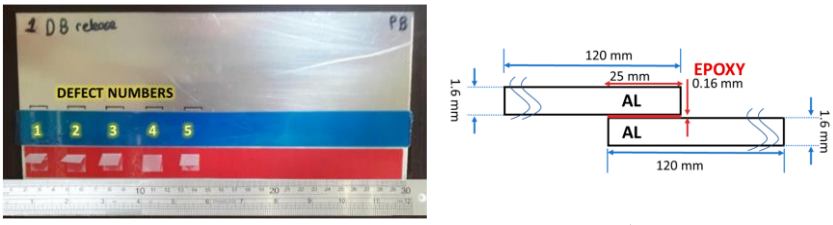

(**a**) (**b**)

Figure 1. Single lap joint containing double-sided release film debonding: (**a**) prior to bonding top view photo where the right side is perfectly bonded and the left side is with debonding; (**b**) side view schematics.

Table 2. Material properties for aluminium adherend and epoxy adhesive.

Material	Material Properties		
	Young's Module GPa	Density kg.m^{-3}	Poisson Ratio -
Aluminium 2024 T3	73.1	2780	0.33
Epoxy	4.27	1214	0.37

2.2. Techniques for Investigation

The aluminium-epoxy-aluminium bonded structure has been investigated by immersion, contact, and air-coupled ultrasonic methods. For bulk waves, classical immersion techniques, through-transmission and pulse-echo ultrasonic NDT techniques have been used. In addition, high-frequency high-resolution scanning acoustic microscopy was applied to evaluate bonding quality in the aluminium-adhesive bond. Moreover, NDT with air-coupled through-transmission method was performed. Additionally, two different guided wave inspections have been performed: using air-coupled excitation and a contact transducer as the receiver and a contact transducer excitation along with a contact transducer receiver. Figure 2 shows the inspection techniques as a classification tree.

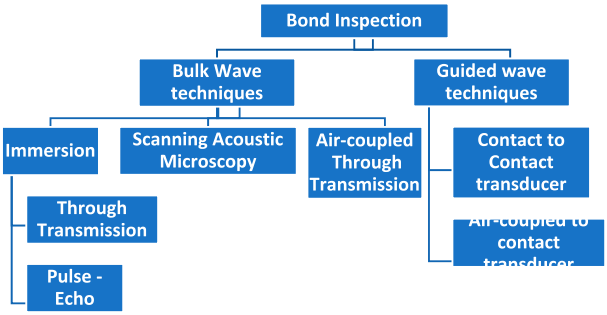

Figure 2. Ultrasonic non-destructive testing methods that were used for adhesive bond inspection.

2.3. Bulk Wave Techniques

2.3.1. Immersion Ultrasonic NDT

The adhesively bonded aluminium-epoxy-aluminium single lap joints containing different bonding quality have been investigated in an immersion tank by TecScan System (TecScan, Boucherville, QC, Canada). Single element focused transducers (Olympus V375-SU having 10 MHz central frequency, 9.525 mm diameter, and 50.8 mm focal distance) have been used in two different set-ups: through-transmission and pulse-echo. The sample has been placed in perpendicular to the transducer focal centre. To maintain the focus at the bonding interface, the distance between transducers and the sample has been kept at 43.29 mm. The schematic representation of through-transmission immersion testing is shown in Figure 3a.

2.3.2. Scanning Acoustic Microscopy (SAM)

Adhesively bonded aluminium-epoxy-aluminium single lap joints containing debonding have been investigated with the scanning acoustic microscope (KSI GmBH) located in Ultrasound Research Institute Kaunas University of Technology (KTU). The experimental set up shown in Figure 3b has been used to save images and A-scan data on small areas of the samples. 33.4 mm by 66.8 mm area has been selected as the region of interest and 250 points on each Cartesian axis (x and y) have been recorded for A-scan measurements. The samples have been investigated with the 50 MHz focused ultrasonic transducer PT-50-3-10 using the immersion pulse-echo technique. The ultrasonic transducer aperture is 3 mm, and the focal distance in water is 10 mm. During measurements, the sample has been placed perpendicular to the transducer. The distance between the transducer and the structure has been selected as 2.94 mm to focus the ultrasonic field on the bonding interface.

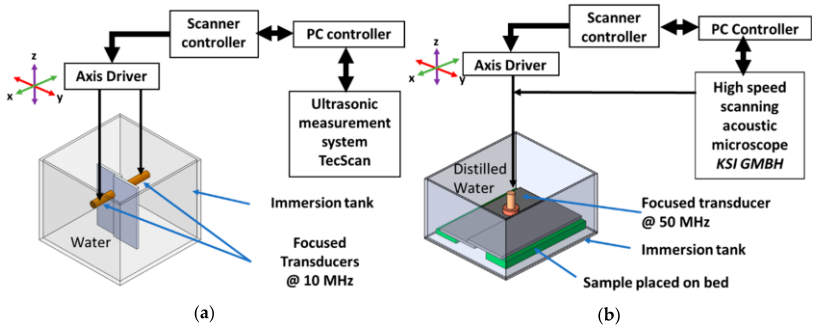

Figure 3. Experimental set-up: immersion ultrasonic non-destructive testing (NDT) with through-transmission (**a**) and scanning acoustic microscopy (**b**).

2.3.3. Air-Coupled through-Transmission

The 300 kHz single element flat air-coupled transducers (produced at Ultrasound Research Institute, KTU, Kaunas, Lithuania) were used for the investigation of the bonding quality in the case of air coupled through-transmission investigations. The active diameter of the air-coupled transducers is 14 mm. The nearfield distance for this transducer is calculated to be 43 mm. The distance between two transducers is kept at twice the near field distance (86 mm) and the plate is placed in the middle at the bonded region. The through-transmission setup is shown in Figure 4. Moreover, 10 periods rectangular burst signal with 750 V amplitude is used as the excitation signal. The received signal is pre-amplified by 50 dB static gain and 40 dB dynamic gain. The received signal is then averaged 64 times for each scanning point for noise reduction. The scanner is moved with a step of 0.5 mm and scanned along the bonded region with the defect.

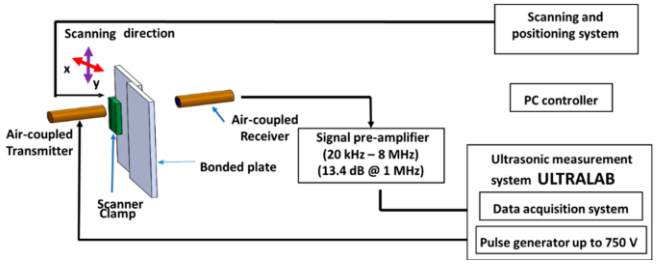

Figure 4. Air coupled through-transmission experimental setup.

2.4. Guided Wave Ultrasonic NDT Techniques

2.4.1. Analytical and Numerical Investigation

For bulk wave through-transmission method, it is straightforward that the loss of amplitude will indicate where there is a defect. However, in the case of guided waves, it can be beneficial to understand the physical phenomenon by using numerical simulation investigations to visualize the interaction of ultrasonic guided waves with the different characteristics of the guided medium. It is preferred to build a numerical model, then select experimental setup parameters according to the numerical results and validate. Thus, based on the investigation from the simulation, it would be easy to perform the experiment and to validate the numerical model with regards to the theory.

Therefore, a numerical model of air-coupled excitation and contact reception of guided waves was created, as shown in Figure 5.

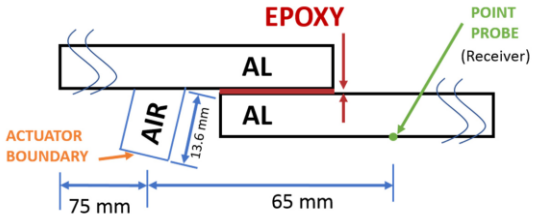

Figure 5. Schema of the simulation model for the air-coupled transducer to contact transducer guided wave.

To generate the guided waves in the bonded plate, it is essential to obtain the parameters from the dispersion curves so that the specific modes can be generated. The phase velocity dispersion curves for 1.6 mm thick aluminium 2024 plate were obtained by a semi-analytical finite element (SAFE) method developed in Ultrasound Institute, Kaunas, is shown in Figure 6. To reduce the complexity of the investigation, fundamental modes are preferred. Specifically, A0 mode was selected because it has high out-of-plane displacement when compared to the symmetric S0 mode. Since air is the coupling medium, the incidence angle of 10.84° to generate A0 mode at 300 kHz was calculated using Snell's law assuming the velocity of sound in air is 343.21 m/s and the phase velocity of A0 mode at 300 kHz is 1824 m/s.

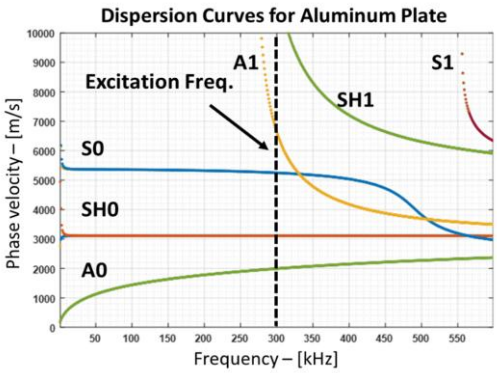

Figure 6. Phase velocity dispersion curves for aluminium 2024 plate with 1.6 mm thickness.

The symmetrical three-dimensional (3D) model as shown in Figure 7 was created in COMSOL Multiphysics. The air is assigned as a pressure-acoustics domain, where aluminium and epoxy are assigned as a solid domain. To reduce the complexity of the numerical model, the actual geometry of the transducers was not considered, but instead, only the air domain for the medium of propagation was considered. The acoustic domain and the solid domain are coupled using the COMSOL Multi-physics node called acoustic-solid interaction, where the necessary equations are loaded automatically.

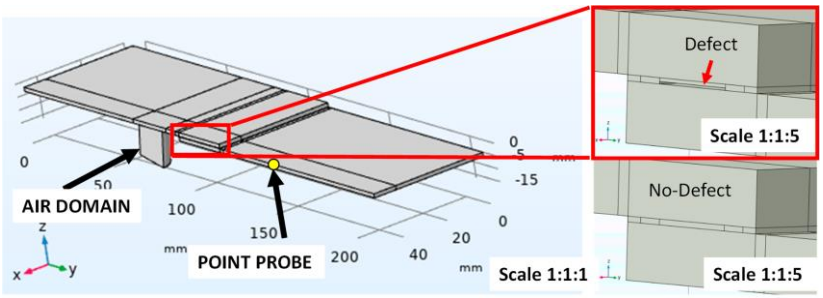

Figure 7. One-half of the symmetric model with two cases: one with the defect, and one without defect.

For the actuator, a cylindrical air domain with a diameter of 14 mm was considered, and the bottom flat surface was considered for excitation with a 10 period Hanning windowed sinusoidal burst at 300 kHz. For the reception, a point probe was considered to record the guided waves after passing through the bond. The normal displacement of the guided waves is recorded at 65 mm away from the transducer. Two simulations were performed, one case for a perfect bond condition and another case with a defect.

Here the defect is considered as a void where a rectangular portion of the epoxy is removed to simulate the artificial debonding within the structure. The size of the void is 12.7 mm × 0.063 mm. The change in amplitude of the ultrasonic signal will indicate the presence of debonding, and this effect will be compared with the results of the experiment. To avoid boundary reflection, the Rayleigh damping condition was applied to the edge surface of the plate and the radiating boundary condition was applied for the air domain to simulate an infinite acoustic medium.

The mesh size considered in each domain is according to the wavelength of each material at 300 kHz and the criteria of eight elements per wavelength was used. The second-order discretization (quadratic discretization) was used for elements. Hence, the following mesh sizes were considered: for air = 0.28601 mm, for Aluminium = 1.52 mm. The time step is calculated according to the Courant-Friedrichs-Lewy (CFL) criteria [29] for the slowest velocity in the simulation, which in this model is for air—343.21 m/s. Hence, the calculated time step is determined to be 8.33 nanoseconds. The total time of 170 µs was recorded. The computer used for the simulation has the configuration: Intel i7-3820 quad-core processor @ 3.60 GHz and 56 GB of RAM.

2.4.2. Air-Coupled to Contact Transducer Guided Wave Inspection

The aluminium-epoxy bonded structure was investigated using an air-coupled excitation and a point type contact reception technique. The air-coupled transducer is used as the transmitter placed at an angle of 10° to generate the A0 mode at 300 kHz. The guided waves in the plate are then received using the contact transducer placed normal to the surface of the plate to record the out of plane displacement. The schema of the setup is shown in Figure 8. For the reception, the contact transducer was spring loaded for a better contact, and glycerol was used as the coupling medium reducing the friction. The distance between the excitation air-coupled transducer centre and the contact transducer centre is kept at 65 mm (Figure 9).

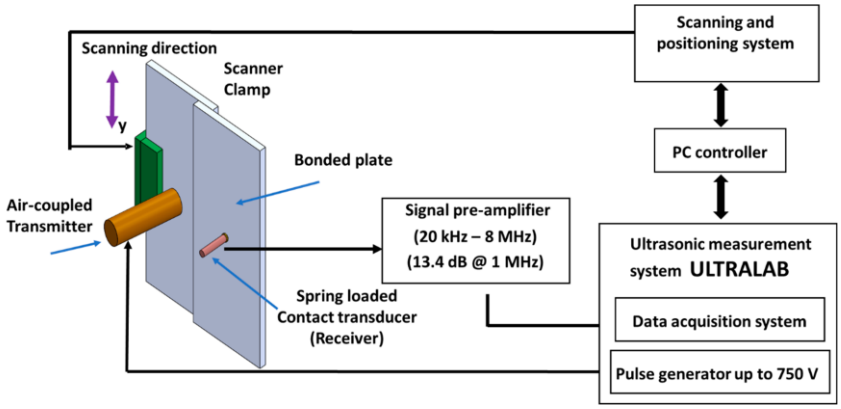

Figure 8. Guided wave inspection set-up with air-coupled to contact ultrasonic transducer.

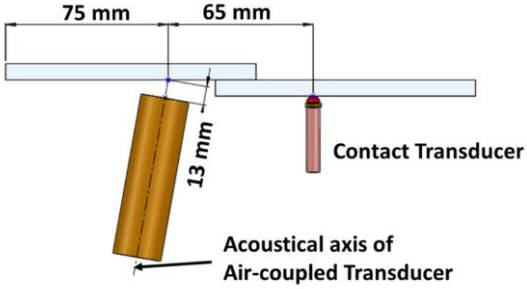

Figure 9. Side view of the air-coupled to contact guided wave (GW) inspection set-up.

2.4.3. Contact-to-Contact Transducer Guided Wave Inspection

For the contact-to-contact transducer guided wave technique, two spring-loaded point contact transducers at 300 kHz are placed normal to the surface of the plate as shown in Figure 10. The setup is similar to Figure 8, but instead of the air-coupled transducer, another contact transducer is placed normal to the plate. Those transducers are coupled to the plate with glycerol as the coupling medium. The distance between transducers is kept as 110 mm, while the bondline being at the centre.

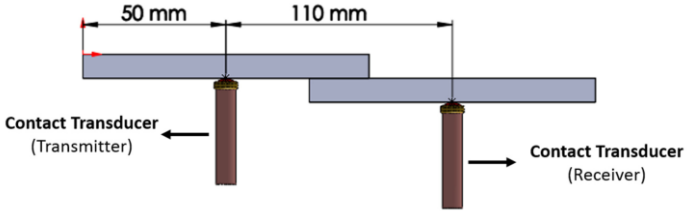

Figure 10. Guided wave arrangement with two contact ultrasonic transducers.

3. Results

3.1. Bulk Wave Technique Results

3.1.1. Immersion Techniques

Through-Transmission Immersion Ultrasonic Inspection

Through-transmission immersion ultrasonic testing with bulk wave results are shown in Figure 11. The A-scans indicate where there is debonding—the ultrasonic bulk wave transmission to the receiver is significantly reduced (Figure 11a). While C-scan results mostly agree with the A-scans, it can be observed that the defect at the far left (defect number 1) is not as consistent as the other defects (Figure 11b). The slice in the middle of the bondline shows normalized amplitude change where there is debonding and no debonding.

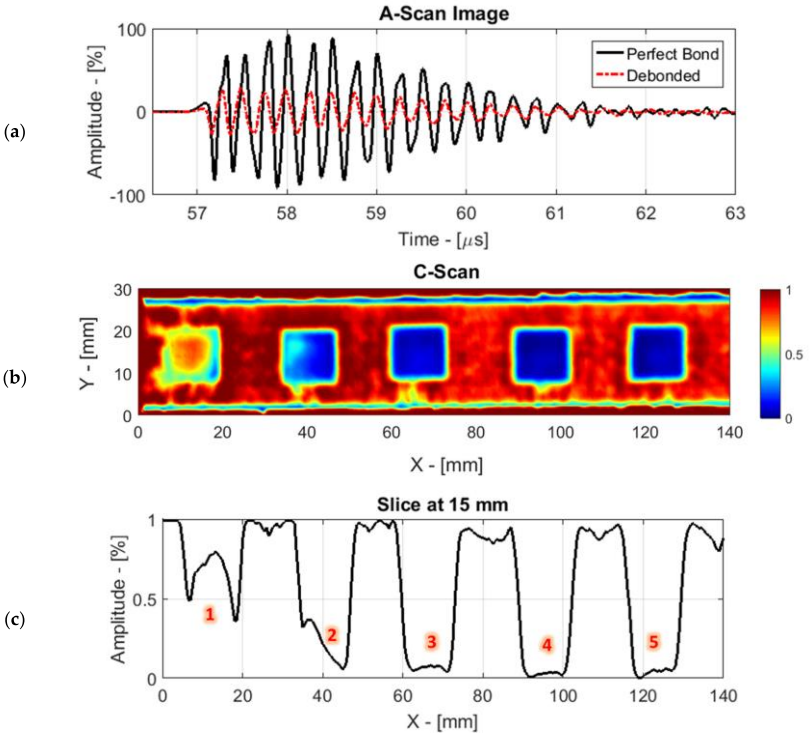

Figure 11. Immersion ultrasonic through-transmission results: (**a**) A-scan; (**b**) C-scan; (**c**) slice from the middle of the defects.

Pulse-Echo Immersion Ultrasonic Inspection Results

The results obtained by the pulse-echo immersion technique are shown in Figure 12. According to the A-scan results, the interface reflection is not easily separable from the multiple reflections (Figure 12a). The window in the time domain has been selected to create C-scans according to the time of flight calculations; however, multiple reflections needed to be considered. The C-scan results show

the defect position, however, the contrast between the defected zone and the sound area is not so clear (Figure 12b). The slice represents the normalized amplitude difference in the middle of the bondline. The higher values indicate the defect presence since the ultrasonic pulse-echo amplitude increases at the debonding due to impedance difference.

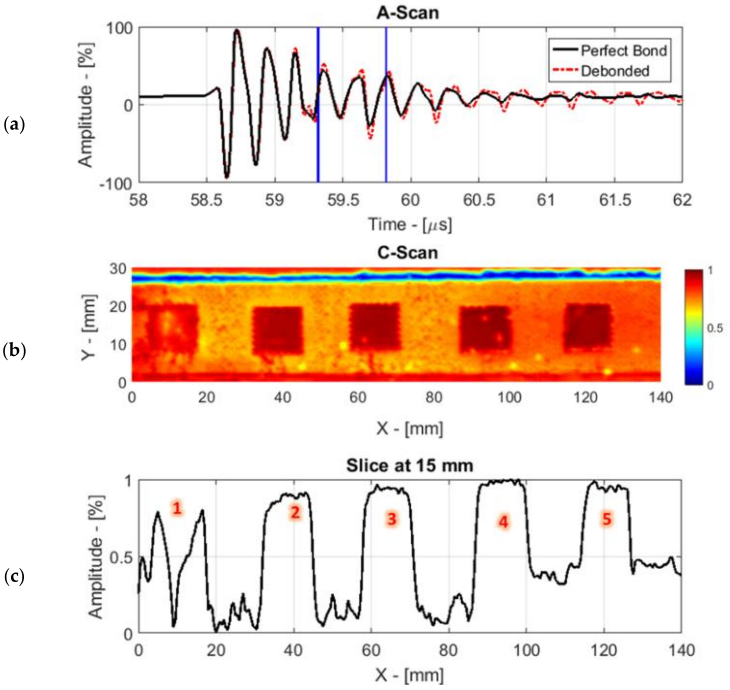

Figure 12. Immersion pulse-echo results: (**a**) A-scan; (**b**) C-scan with the gate at the bonding interface time of flight; (**c**) slice from the middle of the defects.

3.1.2. Scanning Acoustic Microscopy (SAM)

Experiments with the scanning acoustic microscope were performed and the results with A-scan, C-scan, and the slice in the middle of the bondline are shown in Figure 13. As seen in A-scan results, the amplitude in the debonded region is slightly increased, while the third wave packet which represents the reflection from the bottom interface has disappeared (Figure 13a). Due to the large size of the data, separate scans have been performed for each bond and then the resulting 5 C-scan images are stitched to form a single image in post-processing (Figure 13b).

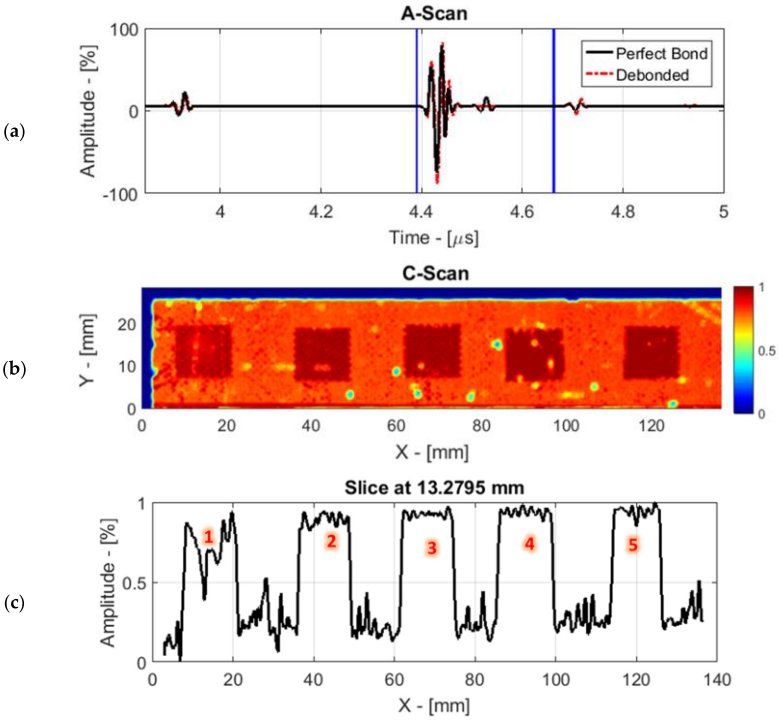

Figure 13. Scanning acoustic microscopy (SAM) results for debonded sample: (**a**) A-scan; (**b**) C-scan; (**c**) slice from the middle of the defects.

3.1.3. Air-Coupled Ultrasonic NDT through-Transmission Technique

The air-coupled through-transmission scan was performed in an area of 125 × 25 mm with a 0.5 mm step size, which resulted in 12,801 scanning points. To improve the signal to noise ratio, each scan point was averaged 64 times (Figure 14a). Each signal is band-pass filtered in the frequency range from 200 kHz to 500 kHz to reduce the noise level. The resulting normalized C-scan is shown in Figure 14b and a slice of the C-scan image at Y = 14 mm presented in Figure 14c shows the damage profile of the debonding present in the specimen.

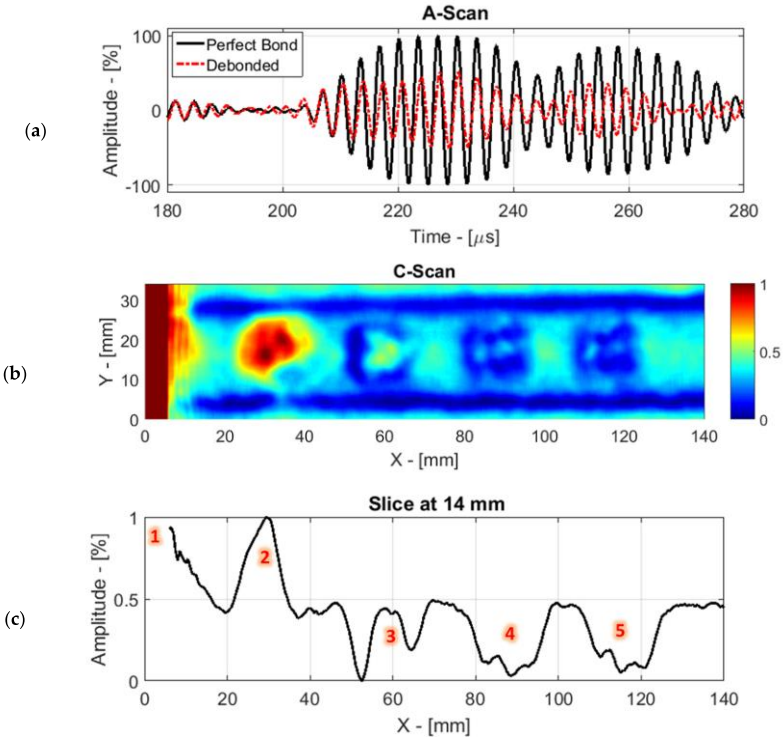

Figure 14. Results of the air-coupled through-transmission: (**a**) A-scan; (**b**) C-scan; (**c**) slice at Y = 14 mm.

3.2. Guided Wave Techniques Results

3.2.1. Simulation for Guided Waves

The simulation was performed to understand the constructive and destructive interference of the guided waves in the bonding region and to visualize the spatial distributions in the debonded region in order to understand what to expect in the experimental investigation. The snapshots of the normal distribution along the plane of symmetry at different time frames are shown in Figure 15 where propagation of only A0 mode is evident. In Figure 16a,b, the spatial distributions of the normal displacement for two cases are shown in the left and the middle at 75 μs where visually the two cases are almost indistinguishable. Thus, the differential image (Figure 16c) was obtained by taking a difference between the reference case without defect and the case with the defect at 75 μs. The differential image plot shows the area, which is most suitable to record the signals to obtain maximum information about the defect. The experimental parameters are selected based on these results. The A-scan results from the case with debonding and case with the perfect bond are shown in Figure 17. The results show that the guided waves in the debonded joint show a higher amplitude than the perfect bond. The results are likely to be caused by the splitting of guided waves in the debonded region, causing constructive interference after the waves have crossed the debonded region.

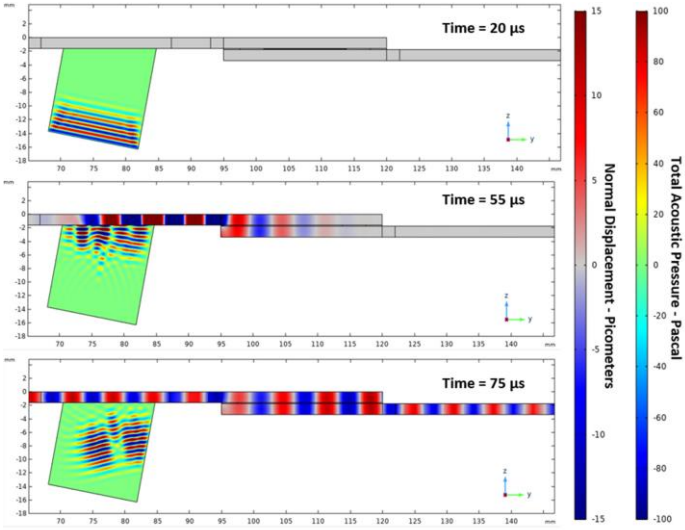

Figure 15. Snapshots of the normal displacements from COMSOL simulation (side view) of the no defect model at time instants 20 µs, 55 µs, and 75 µs showing propagation of A0 mode.

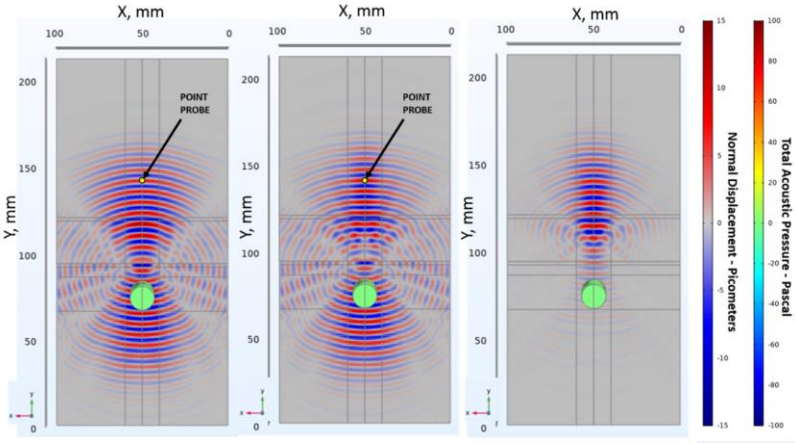

Figure 16. Snapshots from simulation (bottom view) of the mirrored model, which shows the normal distributions at the time instant 75 µs: (**a**) the case with no defect; (**b**) the case with the defect; (**c**) the differential image.

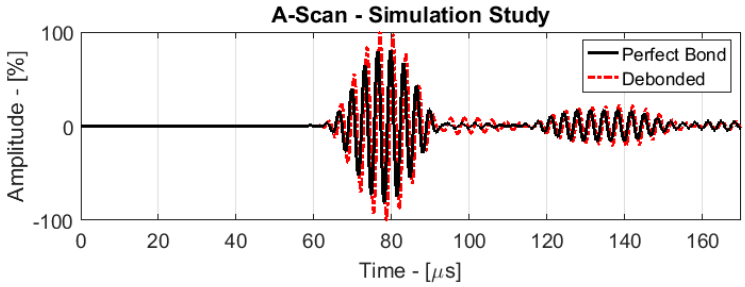

Figure 17. Guided wave A-scan—numerically simulated with probe point across the bond.

3.2.2. Air-Coupled to Contact Transducer Guided Wave

The air-coupled to contact guided wave B-scan is of length 170 mm with a step of 0.5 mm, which comprises of total 341 scans. The scan was made with 32 times averaging where each scan took 2 s. Since the contact transducer is used, there is not much signal pre-amplification necessary when compared to air-coupled through-transmission. In this case, the static gain and dynamic gain used were 50 dB and 10 dB, respectively.

The A-scan and B-scan of this experiment is shown in Figures 18a and 18b, respectively. In the B-scan, the normalized absolute values are shown where the increase in amplitude means that there is a presence of debonding while the lower values represent the place where there is no debonding (perfect bond). This kind of increase in amplitude when GW is passing through the bond is also observed in the simulation. This can be visualized from the A-scans as shown in Figure 18a. Along the B-scan, a slice at the time instant 62.84 µs is shown in Figure 18c, where it represents the damage profile along the scanning distance.

When using the air-coupled transducer as the actuator, the incidence angle can be changed. Since the incidence angle is not normal to the plate, the amplitude of the guided waves can be directionally controlled. This effect can be also visualized in the spatial distributions in the simulation. Thus, this way of excitation can be highly beneficial to focusing the amplitude of the guided wave in one direction and, thereby, avoiding the boundary reflection from the edges of the plate.

3.2.3. Contact-to-Contact Transducer Guided Wave Result

The scanning parameters were the same as that of the air-coupled to contact the GW method. However, in this case, since two contact transducers were used the transmission efficiency is higher in comparison to air-coupled transducers. Thus, the used static gain was 25 dB, and the dynamic gain was 10 dB. The A-scan and B-scan of the experiment with contact-to-contact transducers GW is shown in Figure 19a,b, respectively. The results in this method can be interpreted in a similar way to the results of the air-coupled to contact GW because the amplitude of the GW increases when it passes through the debonded region due to the constructive interference.

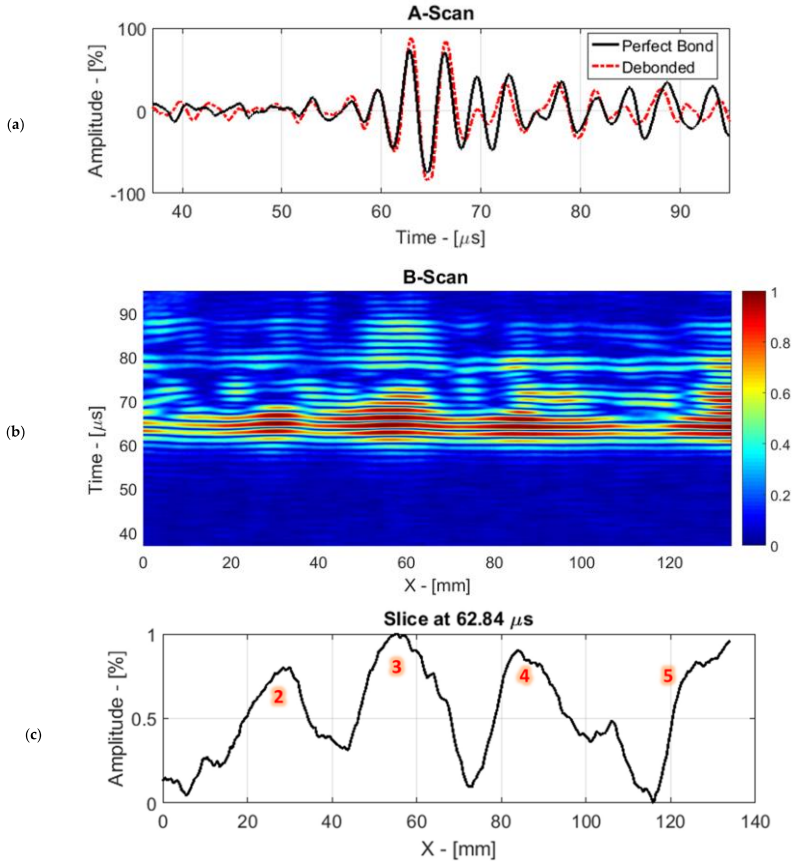

Figure 18. Air-coupled to contact guided waves results: (**a**) A-scan; (**b**) B-scan; (**c**) slice at time = 62.84 μs.

When compared to the air-coupled excitation method, where the incidence angle can be changed, here the angle of incidence is normal to the surface of the plate. Hence, the generated guided waves will have equal amplitudes in all directions. As a result, a strong boundary reflection was observed at the edge of the plate. This interference of the boundary reflection can hinder the possibility of detecting the defects near the edge of the plate boundary Figure 19b. The A-scans from the perfect bond path and the path with debonding is shown in Figure 19a.

The amplitude of the A-scan along the path with the debonding shows a higher amplitude than the amplitude of the A-scan along the perfect bond path. A similar effect can also be observed in the simulation and in air-coupled excitation and contact reception GW technique.

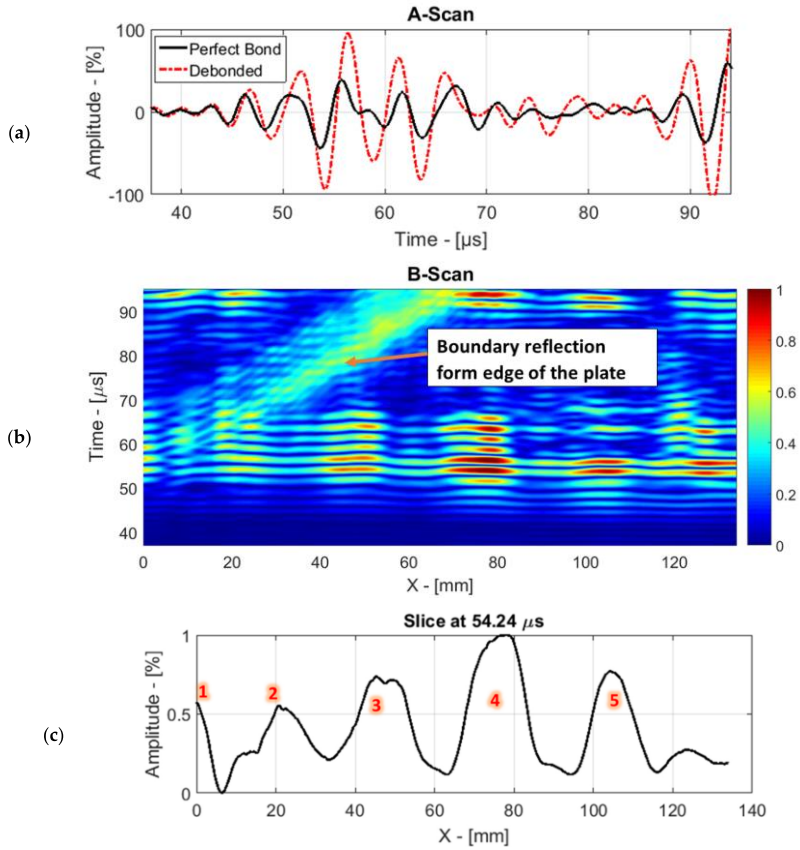

Figure 19. Contact-to-contact guided wave results: (**a**) A-scan; (**b**) B-scan; (**c**) slice at time = 54.24 µs.

4. Discussion on Comparison of NDT Techniques

Six different ultrasonic NDT techniques for the evaluation of adhesive bonding quality have been investigated. Aluminium-epoxy-aluminium bonded structures with interface debonding have been investigated with ultrasonic bulk waves as immersion through-transmission, immersion pulse-echo, scanning acoustic microscopy, and air-coupled ultrasonic through-transmission methods. Additionally, two guided wave inspections have been performed: air-coupled to contact transducer and two contact transducers.

According to different ultrasonic NDT results, the defect detection performance in immersion techniques is better than of the air-coupled methods. Specifically, immersion techniques—with through-transmission (Figure 11), pulse-echo (Figure 12), and scanning acoustic microscopy (SAM, Figure 13), identified five different defects successfully. Immersion through-transmission C-scan results suggest that the defect number 1 has different properties than other defects. The same abnormality is observed in immersion pulse-echo and SAM results; however, the level of contrast difference is less than using the through-transmission technique. This abnormality might be caused a physical phenomenon such as the lack of air within the double-sided release film. On the other hand, air-coupled

through-transmission ultrasonic NDT was successful to visualize four defects (2–5) as seen in Figure 14b. In this case, the defect number 1 was not identified because the active part of the transducer is exposed outside the plate boundary. Since there is no barrier between ultrasonic transducers, the ultrasonic wave is directly transmitted to the receiver causing significantly high amplitude values. Moreover, the second defect at left shows the higher transmission of the ultrasonic bulk wave than in the case of a perfect bond; therefore, the identification of this defect is questionable. Guided wave inspection with air-coupled to contact transducer has shown that three defects with defect numbers 2–4, which are at the centre of the investigation, have been identified as defects (Figure 18). With contact-to-contact transducer guided wave inspection, four areas are identified as defects (Figure 19). The defect number 1 is difficult to detect due to the wave packet reflected from the structure boundary.

Additionally, ultrasonic NDT techniques have been compared, according to defect sizing performances. For each NDT technique, the decibel drop method had been employed to determine the size of the defects (Figure 20) [30]. According to this technique, a slice with normalized amplitude from the observed C-scan or B-scan is crossed with a horizontal line at the desired decibel drop. For immersion ultrasonic NDT and scanning acoustic microscopy (SAM) results, the slice has been selected in the middle of the defects. The slice selections in air-coupled through-transmission C-scan and guided wave B-scans are performed according to the highest contrast observed. The defect size has been calculated with the −6 dB drop method except for air-coupled through-transmission NDT technique where the drop line is selected at −12 dB. The calculated defect sizes are reported in Table 3. Moreover, the relative errors have been estimated according to the known defect size (12.7 mm). It can be observed that the immersion techniques and SAM can size the defects with higher precision than the air-coupled and contact techniques. Compared to the guided wave inspections, the air-coupled through-transmission method shows higher accuracy of defect sizing. In-between guided wave techniques, the contact-to-contact method determines defect size better than the air-coupled to contact method. However, it is observed that the guided wave contact-to-contact method has high variation in defect sizing for different defects: while defect number 3 has been sized with less than 1% error, others show more than 20% relative error.

Table 3. The measured defect dimensions and relative errors for different ultrasonic NDT techniques over five debonding defects.

NDT Technique	Value	Defect #1	Defect #2	Defect #3	Defect #4	Defect #5
Immersion Through-Transmission	Size, mm	12.48	12.61	13.28	13.35	13.00
	Error, mm	0.22	0.09	0.58	0.65	0.30
	Error, %	1.70	0.66	4.60	5.17	2.38
Immersion Pulse-Echo	Size, mm	13.83	12.78	13.04	14.25	12.89
	Error, mm	1.13	0.08	0.34	1.55	0.19
	Error, %	8.92	0.62	2.65	12.21	1.46
Scanning Acoustic Microscopy (SAM)	Size, mm	13.19	12.91	13.23	13.85	12.32
	Error, mm	0.49	0.21	0.53	1.15	0.38
	Error, %	3.93	1.69	4.24	9.05	2.95
Air-Coupled Through-Transmission	Size, mm	-	-	13.18	16.03	15.29
	Error, mm	-	-	0.48	3.33	2.59
	Error, %	-	-	3.78	26.19	20.36
Guided Waves Air-Coupled to Contact	Size, mm	-	16.98	21.46	14.86	-
	Error, mm	-	4.28	8.26	2.16	-
	Error, %	-	33.70	69.01	17.00	-
Guided Waves Contact-to-Contact	Size, mm	-	4.82	12.65	15.48	9.61
	Error, mm	-	7.88	0.05	2.78	3.09
	Error, %	-	62.03	0.39	21.95	24.32

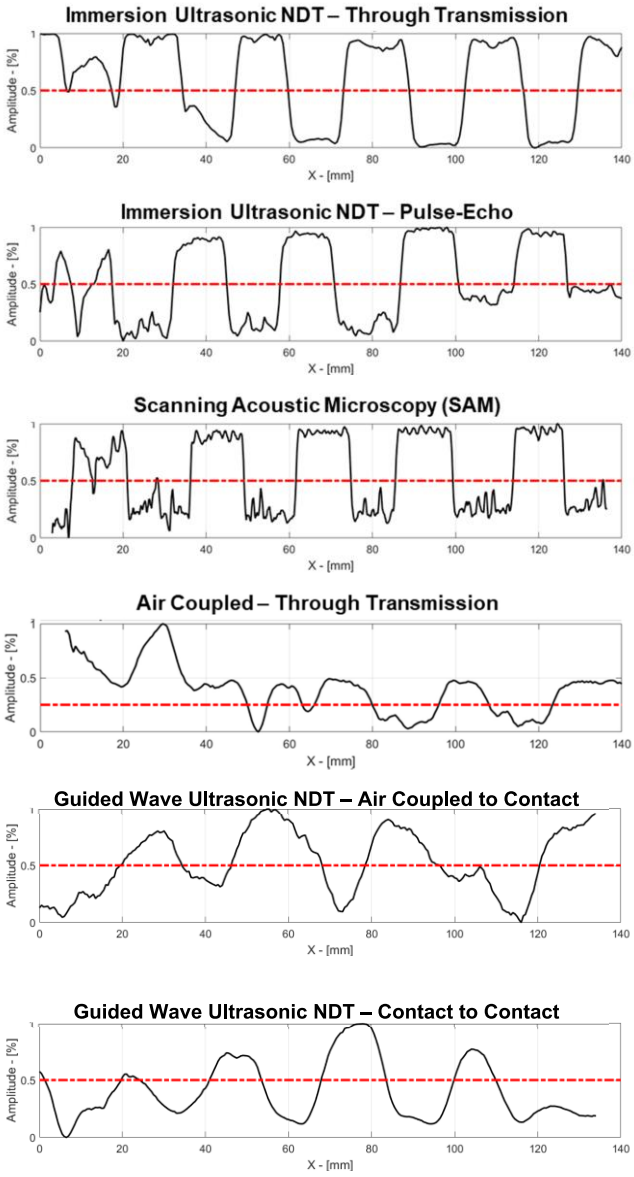

Figure 20. Decibel drop method (−6 dB and −12 dB) to measure the defect size for different ultrasonic NDT techniques: (**a**) immersion ultrasonic through-transmission; (**b**) immersion ultrasonic pulse-echo; (**c**) scanning acoustic microscopy; (**d**) air coupled ultrasonic testing through-transmission; (**e**) guided wave ultrasonic testing with air-coupled to contact; (**f**) guided wave ultrasonic testing with the contact-to-contact method.

While the performance in defect detection and defect sizing of the immersion ultrasonic techniques including SAM is significantly higher than of the air-coupled and contact NDT techniques; the applicability aspects should be discussed. Immersion ultrasonic NDT applications are limited because structures being under water makes them susceptible to corrosion. Additionally, open-wound defects, such as impact damages, are not recommended to undergo immersion testing. In the case of SAM, while the inspection time is shorter, any irregularity in structure geometry such as curved surfaces significantly affects the inspection performance. While air-coupled through-transmission system provides a clear visualization of the inner structure, the amplitude loss in the air makes the experimental set-up very sensitive to structure boundaries and environmental error. Hence, the experiments require higher averaging which leads to a time cost, nevertheless air-coupled experiments would be preferred in an industrial set-up. Furthermore, guided wave (GW) inspection gives us the possibility to inspect large bonded structures in a short time. GW air-coupled to contact transducer set up shows that only one side contact to the bonded structure might be enough to determine debonding defects. When compared to the air-coupled to contact transducer guided waves, two-contact transducers method can give results with significantly higher amplitude and lower transmission losses because of better coupling.

Considering the advantages and limitations that each ultrasonic NDT technique offers, we propose a relative comparison method where the average absolute errors have been normalized according to the ultrasonic wavelengths that have been transferred inside the adhesive bond. The wavelength is an important ultrasonic parameter that describes the relationship between the ultrasonic wave velocity and the inspection frequency. The half-wavelengths are used in the ultrasonic defect detection procedures as a limit to detect the smallest defect. The average absolute error values that are normalized with respect to the wavelengths are shown in Figure 21. For each ultrasonic NDT technique, the inspection frequency and the dominant ultrasonic wave velocity have been considered (the longitudinal velocity for bulk waves, the A0 velocity for GW). The graph presented allows one to evaluate the performance of the investigated NDT techniques. In between immersion techniques and SAM, the immersion through-transmission technique has the lowest error value. The air-coupled through-transmission indicate lower error values than the guided wave (GW) inspections. GW contact-to-contact method performs better than the GW air-coupled to contact method.

The investigated defects within adhesive joints might occur due to the foreign material inclusions at the manufacturing stage or the debonding caused by the fatigue in usage. Quality control of adhesive bonding must be performed both in the manufacturing line and in regular interval maintenance. Within all ultrasonic NDT techniques compared, the immersion through-transmission technique performs the best; however, in real life two-side access to the structures is very limited. On the other hand, although immersion ultrasonic techniques show a high performance, the experimental set-ups are bulky: difficult to change position and not applicable to in-situ testing. The scanning acoustic microscopy shows that the defect detection and sizing can be performed with a high precision, however, the detection systems are also bulky, and the structures inspected must be small. Moreover, where two-sided inspection is possible, air-coupled through-transmission techniques might achieve high efficiency. Finally, the guided wave inspection techniques are suitable for industrial set-ups in both manufacturing and maintenance scenarios, where the structures can be inspected in-situ. In order to evaluate bonding quality with high performance and low cost to the production/maintenance line, the structures can firstly be evaluated with guided wave inspections; then, if the anomalies are observed further, more accurate investigations might be performed using ultrasonic immersion techniques.

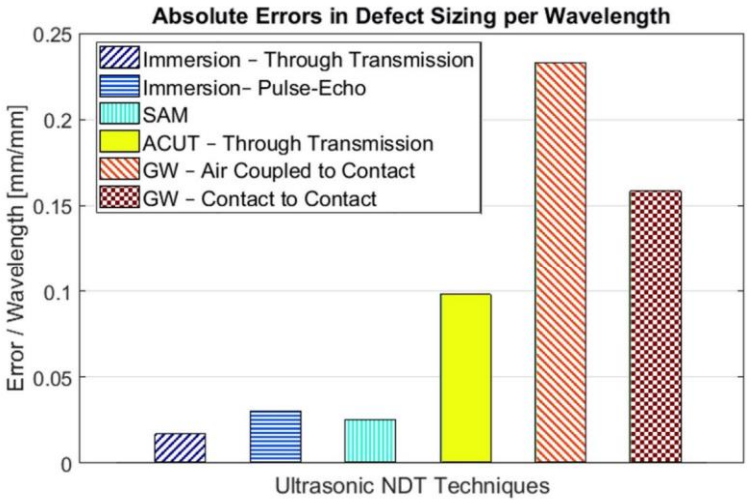

Figure 21. Defect sizing normalized absolute errors per wavelength for each defect and ultrasonic NDT techniques.

5. Conclusions

This paper compares the performance of immersion, air-coupled, and contact ultrasonic non-destructive testing techniques in bonding quality evaluation. The aluminium-epoxy-aluminium single lap adhesive joints containing debonding have been investigated with both bulk wave and guided wave inspections. According to the investigation results, the following conclusions have been made:

- For through-transmission techniques, the amplitude of the bulk wave decreases on the debonded area whereas in the case of guided waves and pulse-echo inspections, the amplitude increases when passing through the debonded area.
- The defect detectability and sizing performance of the immersion techniques and the scanning acoustic microscopy is higher than the performance of the air-coupled through-transmission and guided wave techniques.
- The relative comparison of ultrasonic NDT techniques in defect sizing has been performed by the ratio of average absolute defect sizing error to ultrasonic wavelength inside the adhesive bond. While the best performance is observed in the immersion through-transmission technique, the high performance for the air-coupled through-transmission technique cannot be disregarded.
- In this case study, ultrasonic techniques could be sorted from best to worst in defect sizing as: immersion through-transmission, SAM, immersion pulse-echo, air-coupled through-transmission, guided wave contact-to-contact, and guided wave air-coupled to contact.
- While immersion ultrasonic techniques and acoustic microscopy achieve high precision in defect detection and sizing, the structure under the test needs to be immersed in water. These NDT systems are bulky and expensive. Air coupled ultrasonic techniques reach lower precision than immersion techniques, but they allow non-contact inspection. Since the air-coupled through-transmission technique requires two-sided inspection, the guided wave inspections could be recommended for in-situ applications.
- In industrial applications, the structures can be inspected with less precise but more applicable techniques like guided wave ultrasonic methods, and if the abnormalities are detected, further

investigations with higher precision techniques, such as immersion and acoustic microscopy, could be used.

Author Contributions: Conceptualization, B.Y., A.A., E.J., and R.J.K.; methodology, B.Y., A.A., E.J., and R.J.K.; software, B.Y. and A.A.; validation, E.J., and R.J.K.; investigation, B.Y. and A.A.; formal analysis, B.Y. and A.A.; data curation, B.Y. and A.A.; writing—original draft preparation, B.Y., and A.A.; writing—review and editing, B.Y.; A.A.; E.J., and R.J.K.; visualization, B.Y. and A.A.; supervision, E.J., and R.J.K.; project administration, E.J.; funding acquisition, E.J. All authors have read and agreed to the published version of the manuscript.

Funding: This research was funded by the NDTonAIR project from the European Union's Horizon 2020 Research and Innovation program under the Marie Skłodowska-Curie, grant number 722134.

Acknowledgments: The authors would like to acknowledge the contributions of Reimondas Sliteris, Egidijus Zukauskas, Vaidotas Cicenas, Vykintas Samaitis, and Audrius Jankauskas on the experiments performed; and the contribution of Mastan Raja Papanaboina on the numerical investigations.

Conflicts of Interest: The authors declare no conflict of interest.

References

1. Tornow, C.; Schlag, M.; Lima, L.C.M.; Stübing, D.; Hoffmann, M.; Noeske, P.-L.M.; Brune, K.; Dieckhoff, S. Quality assurance concepts for adhesive bonding of composite aircraft structures–Characterisation of adherent surfaces by extended NDT. *J. Adhes. Sci. Technol.* **2015**, *29*, 2281–2294. [CrossRef]
2. Asif, M.; Khan, M.A.; Khan, S.Z.; Choudhry, R.S.; Khan, K.A. Identification of an effective nondestructive technique for bond defect determination in laminate composites—A technical review. *J. Compos. Mater.* **2018**, *52*, 3589–3599. [CrossRef]
3. Yilmaz, B.; Ba, A.; Jasiuniene, E.; Bui, H.K.; Berthiau, G. Comparison of different non-destructive testing techniques for bonding quality evaluation. In Proceedings of the 2019 IEEE 5th International Workshop on Metrology for AeroSpace (MetroAeroSpace), Torino, Italy, 19–21 June 2019; IEEE: Piscataway Township, NJ, USA, 2019; pp. 92–97. [CrossRef]
4. Ehrhart, B.; Valeske, B.; Muller, C.-E.; Bockenheimer, C. Methods for the Quality Assessment of Adhesive Bonded CFRP Structures—A Resumé. *Proc. Int.* **2010**, 1–9. [CrossRef]
5. Raišutis, R.; Kažys, R.; Mažeika, L. Application of the ultrasonic pulse-echo technique for quality control of the multi-layered plastic materials. *NDT E Int.* **2008**, *41*, 300–311. [CrossRef]
6. Titov, S.A.; Maev, R.G.; Bogachenkov, A.N. Pulse-echo NDT of adhesively bonded joints in automotive assemblies. *Ultrasonics* **2008**, *48*, 537–546. [CrossRef] [PubMed]
7. Tamborrino, R.; Palumbo, D.; Galietti, U.; Aversa, P.; Chiozzi, S.; Luprano, V.A.M. Assessment of the effect of defects on mechanical properties of adhesive bonded joints by using non destructive methods. *Compos. Part B Eng.* **2016**, *91*, 337–345. [CrossRef]
8. Scarselli, G.; Nicassio, F. Analysis of debonding in single lap joints based on employment of ultrasounds. *Health Monit. Struct. Biol. Syst.* **2017**, *1017020*, 1017020. [CrossRef]
9. Galy, J.; Moysan, J.; El Mahi, A.; Ylla, N.; Massacret, N. Controlled reduced-strength epoxy-aluminium joints validated by ultrasonic and mechanical measurements. *Int. J. Adhes. Adhes.* **2017**, *72*, 139–146. [CrossRef]
10. Wood, M.; Charlton, P.; Yan, D. Ultrasonic Evaluation of Artificial Kissing Bonds in CFRP Composites. *E-J. Nondestruct. Test.* **2014**, *19*, 1–10.
11. Jasiūnienė, E.; Mažeika, L.; Samaitis, V.; Cicėnas, V.; Mattsson, D. Ultrasonic non-destructive testing of complex titanium/carbon fibre composite joints. *Ultrasonics* **2019**. [CrossRef]
12. Yılmaz, B.; Jasiūnienė, E. Advanced ultrasonic NDT for weak bond detection in composite-adhesive bonded structures. *Int. J. Adhes. Adhes.* **2020**, *102*, 102675. [CrossRef]
13. Twerdowski, E.; von Buttlar, M.; Grill, W. Scanning acoustic defocused transmission microscopy with vector contrast combined with holography for weak bond imaging. *Health Monit. Smart Nondestruct. Eval. Struct. Biol. Syst. V* **2006**, *6177*, 617718. [CrossRef]
14. Jasiūnienė, E.; Žukauskas, E.; Dragatogiannis, D.A.; Koumoulos, E.P.; Charitidis, C.A. Investigation of dissimilar metal joints with nanoparticle fillers. *NDT E Int.* **2017**. [CrossRef]
15. Sunarsa, T.Y.; Aryan, P.; Jeon, I.; Park, B.; Liu, P.; Sohn, H. A reference-free and non-contact method for detecting and imaging damage in adhesive-bonded structures using air-coupled ultrasonic transducers. *Materials* **2017**, *10*, 1402. [CrossRef] [PubMed]

16. Wu, W.-L.; Wang, X.-G.; Huang, Z.-C.; Wu, N.-X. Measurements of the weak bonding interfacial stiffness by using air-coupled ultrasound. *AIP Adv.* **2017**, *7*, 125316. [CrossRef]
17. Kazys, R.; Demcenko, A.; Zukauskas, E.; Mazeika, L. Air-coupled ultrasonic investigation of multi-layered composite materials. *Ultrasonics* **2006**, *44*. [CrossRef]
18. Cerniglia, D.; Montinaro, N.; Nigrelli, V. Detection of disbonds in multi-layer structures by laser-based ultrasonic technique. *J. Adhes.* **2008**. [CrossRef]
19. Kazys, R.J.; Mazeika, L.; Sestoke, J. Development of ultrasonic techniques for measurement of spatially non-uniform elastic properties of thin plates by means of a guided sub-sonic A0 mode. *Appl. Sci.* **2020**, *10*, 3299. [CrossRef]
20. Zhang, K.; Zhou, Z. Quantitative characterization of disbonds in multilayered bonded composites using laser ultrasonic guided waves. *NDT E Int.* **2018**. [CrossRef]
21. Castaings, M. SH ultrasonic guided waves for the evaluation of interfacial adhesion. *Ultrasonics* **2014**, *54*, 1760–1775. [CrossRef]
22. Matt, H.; Bartoli, I.; Coccia, S.; Lanza di Scalea, F.; Oliver, J.; Kosmatka, J.; Gyuhae, P.; Farrar, C. Ultrasonic guided wave monitoring of composite bonded joints using macro fiber composite transducers. *Smart Struct. Mater.* **2006**. [CrossRef]
23. Siryabe, E.; Renier, M.; Meziane, A.; Castaings, M. The transmission of lamb waves across adhesively bonded lap joints to evaluate interfacial adhesive properties. *Phys. Procedia* **2015**, *70*, 541–544. [CrossRef]
24. Marks, R.; Clarke, A.; Featherston, C.; Paget, C.; Pullin, R. Lamb Wave Interaction with Adhesively Bonded Stiffeners and Disbonds Using 3D Vibrometry. *Appl. Sci.* **2016**, *6*, 12. [CrossRef]
25. Sherafat, M.H.; Guitel, R.; Quaegebeur, N.; Lessard, L.; Hubert, P.; Masson, P. Guided wave scattering behavior in composite bonded assemblies. *Compos. Struct.* **2016**, *136*, 696–705. [CrossRef]
26. Leiderman, R.; Figueroa, J.C.; Braga, A.M.B.; Rochinha, F.A. Scattering of ultrasonic guided waves by heterogeneous interfaces in elastic multi-layered structures. *Wave Motion* **2016**, *63*, 68–82. [CrossRef]
27. Leiderman, R.; Braga, A.M.B. Scattering of guided waves by defective adhesive bonds in multilayer anisotropic plates. *Wave Motion* **2017**, *74*, 93–104. [CrossRef]
28. Cho, H.; Hara, Y.; Matsuo, T. Evaluation of the thickness and bond quality of three-layered media using zero-group-velocity lamb waves. *J. Phys. Conf. Ser.* **2014**, *520*. [CrossRef]
29. Duczek, S.; Joulaian, M.; Düster, A.; Gabbert, U. Numerical analysis of Lamb waves using the finite and spectral cell methods. *Int. J. Numer. Methods Eng.* **2014**. [CrossRef]
30. Felice, M.V.; Fan, Z. Sizing of flaws using ultrasonic bulk wave testing: A review. *Ultrasonics* **2018**. [CrossRef]

sensors

MDPI

Article

Evaluation of Bonding Quality with Advanced Nondestructive Testing (NDT) and Data Fusion †

Bengisu Yilmaz [1,*], Abdoulaye Ba [2], Elena Jasiuniene [1,3], Huu-Kien Bui [2] and Gérard Berthiau [2]

[1] Ultrasound Research Institute, Kaunas University of Technology, K. Barsausko St. 59, LT-51423 Kaunas, Lithuania; elena.jasiuniene@ktu.lt

[2] Institute of Research in Electric Power of Nantes Atlantique (IREENA), University of Nantes, 37 Boulevard de l'Université BP-406, CEDEX, 44602 Saint-Nazaire, France; abdoulaye.ba@etu.univ-nantes.fr (A.B.); huu-kien.bui@univ-nantes.fr (H.-K.B.); gerard.berthiau@univ-nantes.fr (G.B.)

[3] Department of Electronics Engineering, Kaunas University of Technology, Studentu St. 48, LT-51367 Kaunas, Lithuania

* Correspondence: bengisu.yilmaz@ktu.lt; Tel.: +370-636-39-208

† Yilmaz, B.; Ba, A.; Jasiuniene, E.; Bui, H.K.; Berthiau, G. Comparison of different nondestructive testing techniques for bonding quality evaluation. In Proceedings of the 2019 IEEE 5th International Workshop on Metrology for AeroSpace (MetroAeroSpace), Torino, Italy, 19–21 June 2019; pp. 92–97, doi:10.1109/MetroAeroSpace.2019.8869692.

Received: 8 August 2020; Accepted: 4 September 2020; Published: 8 September 2020

Abstract: This work aims to compare quantitatively different nondestructive testing (NDT) techniques and data fusion features for the evaluation of adhesive bonding quality. Adhesively bonded composite-epoxy single-lap joints have been investigated with advanced ultrasonic nondestructive testing and induction thermography. Bonded structures with artificial debonding defects in three different case studies have been investigated: debonding with release film inclusion, debonding with brass film-large, debonding with brass film-small. After completing preprocessing of the data for data fusion, the feature matrices, depending on the interface reflection peak-to-peak amplitude and the principal component analysis, have been extracted from ultrasonic and thermography inspection results, respectively. The obtained feature matrices have been used as the source in basic (average, difference, weighted average, Hadamard product) and statistical (Dempster–Shafer rule of combination) data fusion algorithms. The defect detection performances of advanced nondestructive testing techniques, in addition to data fusion algorithms have been evaluated quantitatively by receiver operating characteristics. In conclusion, it is shown that data fusion can increase the detectability of artificial debonding in single-lap joints.

Keywords: nondestructive testing (NDT); ultrasonics; induction thermography; adhesive bond; data fusion

1. Introduction

Given the rise in the stage of composite materials, new joining technologies such as adhesive bonding have gained popularity in the aerospace industry. Adhesively bonded structures have a high strength-to-weight ratio and can join dissimilar materials and complex geometries. Additionally, adhesive joints preserve the structural integrity and smooth surface of composites compared to mechanical fasteners like rivets—i.e., composite structures—might be damaged via fiber breakage during riveting. However, not being able to determine the inclusions in the adhesive–composite interface may lead to significant strength reduction as well as unexpected catastrophic failures. In order to expand the application of adhesive joints, the geometry, size and position of these inclusions have to be identified via nondestructive

testing (NDT) techniques [1]. In our recent studies, interface defects in adhesive-bonded structures are inspected with ultrasonic and thermography nondestructive testing techniques [2,3].

Ultrasonic NDT had been used to investigate the adhesive bond quality with adherend integrity and interface quality evaluation, including disbond detection [4–9]. In addition, investigations to detect weak and kissing bonds have been performed in various studies [10–12]. Conventional longitudinal pulse-echo ultrasonic inspection as well as advanced measurement techniques, such as acoustic microscopy, air-coupled ultrasound, and guided waves, have been used to evaluate bonding quality [13–19]. Moreover, nonlinear behavior has been related to bonding quality with nonlinear ultrasonic NDT [20–22]. Ultrasonic NDT has advantages to detect and position defects since it is a directional technique. While the classical pulse-echo technique outperforms the through transmission technique by being a one-sided inspection, it requires structure to be coupled with specific substances such as water. Air-coupled ultrasonics overcome this limitation; however, the high impedance difference between air and structures causes a significant loss in signal amplitude [14]. On the other hand, guided wave inspections allow large specimens to be inspected in a short period of time; Lamb waves have been reported to be an effective technique to determine bonding quality [23,24]. However, the analysis of the results has a high level of complexity, and it is usually specimen-specific.

Additionally, active thermography is a promising NDT technique to investigate bonding quality [25–27]. Active thermography has advantages such as being very responsive, sensitive, noncontact, and suitable for automation; therefore, it is used to detect manufacturing defects within adhesive bonding [28]. Defect detection with traditional light-based active thermography is highly influenced by thermal diffusion and the anisotropy of the structures. In the case of conductive adherends such as CFRP, induction thermography can reduce this limitation [2,29]. Although induction thermography has many strengths and increased effectiveness by volumetric heating, the thickness of the structures and the complexity of the results limit its application [30].

Moreover, shearography can have a very high resolution and short response time; however, it is only effective in the case of surface and subsurface defects and requires high-stress solicitation [31]. It is reported that shearography is a suitable nondestructive testing technique to detect disbonding and subsurface defects in aluminum bonds [26]. Also, where possible, X-ray tomography can be used to investigate inner defects in bonded structures [27]. However, for composite-adhesive joints, similar diffraction coefficients and structures with a high level of aspect ratios might create limitations in this expensive NDT technique [32]. Recently, electromechanical impedance mismatching and an adhesion quality test with laser shock had been proposed to evaluate bonding quality [31,33,34]. While extended NDT for adhesive bonding is promising, these systems are expensive and costly to maintain.

The nondestructive evaluation of bonding quality is a challenging task because adhesive bonding is an interfacial phenomenon involving a thin layer of material, usually less than 10 microns [35]. Although adhesive bonding evaluations with different nondestructive testing techniques have been performed over the past decades, the challenges continue to rise to establish the ultimate reliable NDT technique [3]. Each NDT technique is limited to deliver a reliable evaluation of bonding quality due to its methodological and physical capabilities. Hence, we propose a combination of ultrasonic and induction thermography with feature-based data fusion.

Data fusion has been introduced to nondestructive testing and evaluation by Gros et al. and the research interest continues to rise [36,37]. While the detailed categorization of data fusion reveals the advantages for sensor applications [38], the survey on data fusion techniques for nondestructive evaluation also highlights numerous studies [39]. The application on concrete samples mostly used ground-penetrating radar (GPR), impact echo and ultrasonic testing as data fusion resources while deploying several data fusion algorithms such as fuzzy logic [40,41], artificial neural networks (ANN) [42], Hadamard, and the Dempster–Shafer rule of combination [43]. Considering the variety in nondestructive evaluation of composite structures, data fusion studies focused on several different combinations of NDT techniques. While Gusenbauer et al. [44] improved

porosity determination in composites with X-ray tomography and interferometer; Cuadra et al. [45] monitored the damage in composites with acoustic emission, digital image correlation (DIC), and thermography. Cao et al. [46] employed convolutional neural networks (CNN) in order to improve lock-in thermography imaging. Specifically, Daryabor and Safizadeh [1] worked on the image fusion for ultrasonic and thermography nondestructive evaluation of epoxy patches between composite and aluminum structures. They compared several basic and complex fusion algorithms, namely minimum, maximum, average, principal component analysis, wavelet transformation and pyramid.

This work focuses on the evaluation of bonding quality with the fusion of ultrasonic inspection and induction thermography data. Composite-adhesive single-lap joints containing three different artificial debonding defects were investigated by both ultrasonic NDT and induction thermography. Saved data had been preprocessed for data fusion. The feature matrices emphasizing the defect presence have been extracted from ultrasonic and thermography data. These feature matrices have been used as the source of data fusion algorithms. The data fusion algorithms have been evaluated with quantitative sensitivity analysis. In addition to the previous works that focused on data fusion with ultrasonic nondestructive testing techniques and thermography, this work investigates different types of defects in composite-adhesive bonds and utilizes information theory-based data fusion algorithms. Also, this work contributes to the quantitative bonding quality evaluation efforts with receiver operating characteristic curves and area-under-curve calculations.

2. Materials and Methods

2.1. Sample Description

Single-lap joints with carbon fiber-reinforced epoxy (CFRP) adherend and epoxy film adhesive were manufactured at COTESA, GmBH, Mittweida, Germany. Six layers of HexPly M21-5H satin woven prepreg, 2.22 mm thick, was used as an adherend. 3M Scotch-Weld AF163 k-red structural adhesive film epoxy with 0.24 mm theoretical thickness was used as adhesive. The epoxy film was placed on top of the cured CFRP adherends after required surface preparation. Single lap joints containing four different bonding quality were designed: three of them with interface inclusions, and one without any inclusion at pristine state as reference sample. Reference sample is called 'perfect bond' (Figure 1a(A) and Figure 1b(A)).

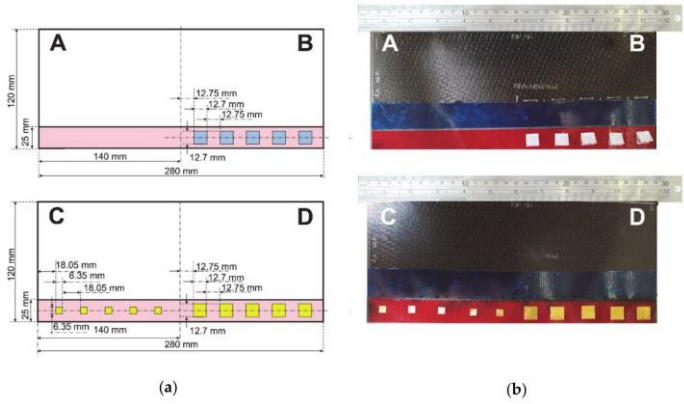

Figure 1. CFRP-epoxy single-lap joints with different bonding quality. (**a**) schematics and (**b**) pictures prior to bonding. (**A**: perfect bond, **B**: debonding with release film inclusion, **C**: Debonding with brass inclusion - small, **D**: Debonding with brass inclusion - large.).

As seen in Figure 1B five two-fold Wrigtlon 4600 (AirTech Europe, The City of Differdange, Luxemburg) release film inclusions with 12.7 mm edge length and 0.063 mm thickness were put on the bonding interface to demonstrate 'debonding with release film'. Additionally, 'debonding' at the interface were represented with brass film inclusions. On the one part of the sample, five two-fold square brass films with 12.7 mm edge length and 0.05 mm thickness were inserted onto the interface (Figure 1D). On the other side of the sample, smaller square brass film inclusions with 6.35 mm edge length and 0.05 mm thickness were inserted (Figure 1C). Both defects might occur at the manufacturing stage of bonding structures due to foreign object inclusions, such as glove parts, cutting blade, etc.

2.2. Nondestructive Testing

Single-lap joint adhesive bonds with four different bonding quality have been investigated with two different nondestructive testing techniques: pulse-echo immersion ultrasonic NDT and transmission induction thermography.

2.2.1. Ultrasonic Inspection

Ultrasonic inspection was performed in water immersion tank with the pulse-echo technique. A single-element-focused transducer Olympus V375-SU (Olympus Scientific Solutions Americas Inc., Waltham, MA, USA) having 10 MHz central frequency, 9.525 mm diameter, and 50.8 mm focal distance was used. The single-lap joints were placed perpendicular to the transducer and the distance between the transducer and the sample was kept at 46.3 mm to place the focal point at the bonding interface. The inspections have been performed in whole bonding area for each single-lap joint (covering all five defects at the interface), and the step-size was 0.5 mm. For each measurement point, A-scans have been saved. Schematics of the experiment can be seen in Figure 2a.

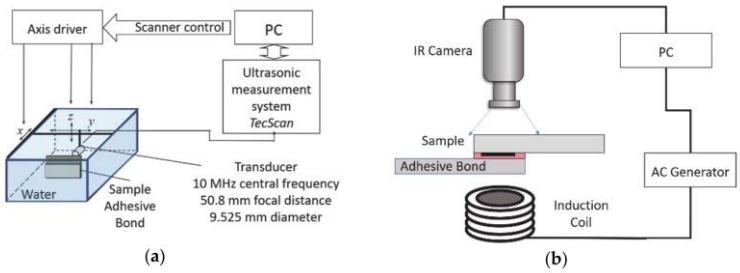

Figure 2. Experimental set-up schematics: (**a**) ultrasonic nondestructive testing (NDT) and (**b**) induction thermography.

2.2.2. Induction Thermography

The single-lap joints with different bonding qualities have been investigated with induction (eddy current stimulated active) thermography. As described in an earlier study [3], the induction coil frequency plays a significant role in the experiment performance. Hence the design of the coil is selected as a helical coil inductor (inner diameter 15 mm, outer diameter 25 mm, height 30 mm, five turns, manufactured at IREENA institute, Saint-Nazaire, France) to achieve 105 kHz frequency. During experiments, the coil is excited with 200 Ampere power for 1 s. Starting from the excitation time, an infrared camera recorded the surface temperature for 60 s with a sampling frequency of 25 frames per second. The experiments have been performed in transmission mode, where the sample is placed in between the camera and coil. Schematics of the experiment can be seen in Figure 2b.

2.3. Feature-Based Data Fusion

Data fusion is a post-processing technique that uses a synthesis of the data collected by multiple sources (sensors or systems) in order to provide more accurate information. The literature defines the different levels of fusion as data-level, feature-level and decision-level [39].

Before the application of fusion algorithms, it should be guaranteed that the collected data is comparable. In this work, raw data gathered from NDT investigations have been preprocessed. A multi-step preprocessing approach has been followed as shown in Figure 3.

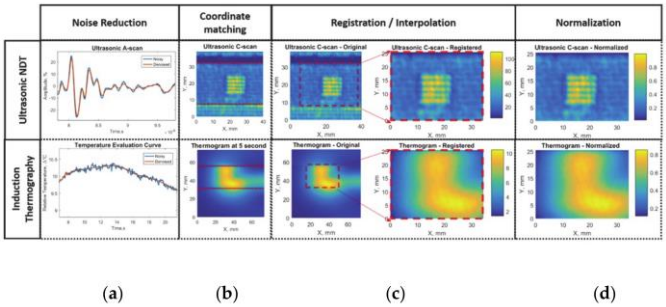

Figure 3. Data acquisition and preprocessing steps for feature-based data fusion: (**a**) noise reduction with digital filters, (**b**) coordinate matching according to bondline edge, (**c**) registration and interpolation of selected areas, (**d**) amplitude normalization.

First of all, in order to eliminate error multiplication due to *noise*, data collected during ultrasonic inspection and induction thermography experiments have been filtered separately (Figure 3a). Since the experiments took place in different conditions, recorded data had local coordinate systems. However, to apply data fusion, the coordinates of each experiment should match the other. Therefore, data have been aligned according to the position of bonding edges to *match coordinates* (Figure 3b). While the point-by-point match was achieved by this operation, scaling of the data was performed to have the same coordinate system in both sets of data. Hence, the ultrasonic inspection data has been interpolated to match the same coordinate values in the *registration* step (Figure 3c). The data was re-centered, keeping the center of the defect at the midline of horizontal coordinates with the parallel top and bottom edges to the edge of the bondline. No further registration step needed due to the perpendicular position of the IR camera and ultrasonic transducer to the specimen. Last but not least, both ultrasonic and thermography data amplitudes have been normalized (0 to 1) (Figure 3d).

After preprocessing, features were determined by the known physical relationship between each technique and the samples. For the ultrasonic pulse-echo inspection, maximum amplitudes recorded at time of the interface reflection have been extracted as features. In order to visualize bonding quality at the interface, C-scan images have been created by peak-to-peak amplitude values inside the selected time gate. This gate has been determined according to the interface reflection time-of-flight calculations by the knowledge of thickness and acoustic wave velocity of adherend and adhesive. (Figure 4a).

The inclusions causing debonding defects at the interface reflected higher amplitude ultrasonic echoes to the transducer due to high impedance mismatch, whereas no-defect/pristine state of bonding transmitted most of the ultrasonic wave further due to similar impedance values. The normalized feature values were separated into two conditions (Figure 4b): no defect below the average value and a defect above the average value.

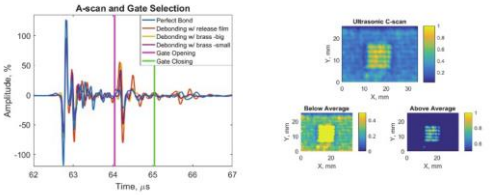

Figure 4. Ultrasonic response data with feature matrix image and decision procedures: (**a**) ultrasonic A-scan with gate at the interface reflection amplitude and (**b**) ultrasonic C-scan with below and above average for defect detection.

The induction thermography data have been evaluated with singular value decomposition-based principal component analysis (PCA). As described in the previous work [3], PCA allows to eliminate the nonuniform heating patterns and increase the defect contrast in thermography results. Since PCA calculates the eigenvectors within data and sorts them in ascending order; the first few principal components carry the most information [30]. To maximize defect detection, each recorded defected sample thermography data and perfect bonding sample thermography data was differentiated after alignment according to the bondline. As described in the previous study, the recorded surface temperature data was separated for heating part and cooling part with the novel separation algorithm, which depends on the constant rate of change (derivative) of the sample temperature to be reached (Figure 5a) [3].

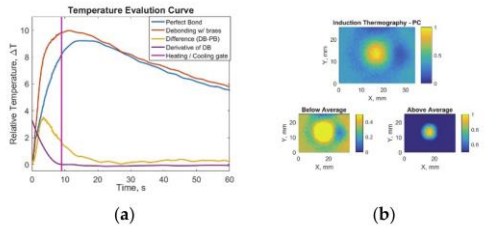

Figure 5. Induction thermography results with feature matrix image and decision procedures: (**a**) temperature evaluation curve with heating/cooling separation gate and (**b**) induction thermography -heating principal component analysis results with below and above average.

Only for the heating part, PCA algorithm was applied with MATLAB software. While the first principal components have been neglected due to the nonuniform heating pattern, the second principal components were saved as features emphasizing the defect (Figure 5b). Due to the nature of defects (metal- and polyester-based) some would have higher values at the defected region and some would have lower values; therefore, the absolute values are considered before normalization. The defect is present at above-the average-values, whereas no defect is present on the below the average values (Figure 5b).

2.4. Data Fusion Algorithms

After preprocessing and feature extraction, six different fusion algorithms were applied to the compatible 2D feature matrices on the pixel level. The details of fusion algorithms are given in Table 1.

Table 1. Data fusion algorithms with description and mathematical formulas.

Fusion Algorithm	Description	Mathematical Formula	
average	on pixel level, the average from two sources: UT[1] and TH[2]	$(UT + TH)/2$	(1)
difference	on pixel level, differentiating one matrix (TH) from the other (UT)	$(UT - TH)$	(2)
Weighted average	on pixel level, weighted average when one matrix has four times higher weight than the other	$((5xUT) + TH)/6$ $(UT + (5xTH))/6$	(3)
Hadamard product	pixel-wise multiplication of same-size matrices	$(UT \circ TH)_{ij} = (UT)_{ij}(TH)_{ij}$	(4)
Dempster–Shafer rule of combination	evidence theory based on mass, belief, and plausibility functions	$(m_1 \oplus m_2)(A) = \frac{1}{K-1} \sum_{B \cap C = A \neq \varnothing} m_1(B) m_2(C)$ *where* $K = \sum_{B \cap C = \varnothing} m_1(B) m_2(C)$	(5)

[1] UT stands for feature matrix of ultrasonic NDT. [2] TH stands for feature matrix of induction thermography NDT.

There are numerous data fusion algorithms that can be applied for two-dimensional feature-based fusion, such as basic combinations, wavelet-based combinations, artificial neural networks, Bayesian theory, and the Dempster–Shafer rule of combination [39]. In this study, a combination of basic and information theory-based fusion algorithms have been selected: average to indicate the equal performance of the sources, difference to clarify contradiction between sources, weighted average to highlight the importance of one source over the other, Hadamard to increase the signal-to-noise ratio, and Dempster–Shafer theory-based combination to highlight the importance of information theory.

As one of the basic fusion algorithms, *average* has been implemented. The resulting matrix has the average of each feature matrices. Then, to understand if two techniques are inversely correlated, *difference* algorithm has been performed. Afterward, two different *weighted average* algorithms—where one dataset is having four times higher importance than the other—have been studied (5UT-1TH, Table 1, Formula (3a)) where the weighted average of ultrasonic inspection matrix is four times higher than the thermography feature, (1UT-5TH, Table 1, Formula (3b)) where the weighted average of thermography feature is four times higher than the ultrasonic inspection). Furthermore, the *Hadamard product*, which is a simple algebraic operation based on pixel-wise multiplication of same-size matrices, has been applied to feature matrices [47]. The resulting matrix is a product of the pixel values on the same positions from different sources [43].

Finally, the Dempster–Shafer (DS) rule of combination has been applied to the feature matrices. DS evidence theory is introduced by Shafer [48] as an expansion of Dempster's theory [49]. In DS theory, the information from each source is considered as evidence of multiple events. The Dempster–Shafer rule of combination allows us to calculate a unique evidence mass (m) for a hypothesis by combining the evidence masses (m_1, m_2); in other words, beliefs associated with this hypothesis by various sources or operators [36]. In our case, these hypotheses are defected (positive), not defected (negative) and unsure if it is defected or not (doubt). The combination $(m_1 \oplus m_2(A))$ has been calculated via the orthogonal sum of different hypotheses from different sources (Table 1, Formula (5)). The sources $(m_1(B), m_2(C))$ are the feature matrices obtained from each NDT inspection. Where K represents the contradiction in the belief systems of two sources. If the K value is calculated close to 1, the calculated rule of combination results in very low values, and the rule of combination should be modified. Three hypotheses—positive, doubt, and negative—have been chosen according to the cross-section of local amplitude distribution over global Gaussian in the feature matrix. The local distribution has been calculated with the pixels and its surrounding (8) pixels' values. In Figure 6, the Dempster–Shafer global distribution and belief percentage calculation for a random pixel and its local neighborhood on the no-defect region is presented.

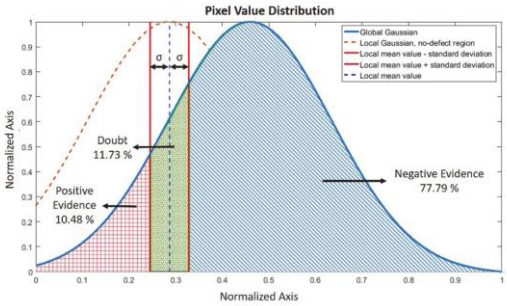

Figure 6. Dempster–Shafer belief percentage calculation for a random pixel and its local neighborhood on the no-defect region and global distribution for the induction thermography feature matrix.

According to the local distribution on the global Gaussian curve, the probability of three hypotheses have been calculated (Figure 6): positive evidence (DS-positive) where a defect is present corresponding to the left side of the Gaussian cross-section, negative evidence (DS-negative) where no defect is present, seen on the right side of the cross-section, and doubt (DS-doubt) where the plausibility is high, corresponding to the local amplitude variance crossing with the global Gaussian. For each pixel value, these three different belief probabilities have been calculated and then DS rule of combination algorithm has been applied. According to the graph in Figure 6, the selected point/pixel can be determined with a 77.79% probability that it is not in the defected region, with a 10.48% probability it is in the defected region and that it is a doubt with a 11.73% probability.

2.5. Evaluation of Different Techniques

The performance of each fusion algorithm and separate features have been evaluated quantitatively with Receiver Operating Characteristic (ROC) curves. In order to create ROC curves, each feature matrix and resulting fusion matrices have been analyzed for sensitivity and specificity.

Firstly, according to the known position of the defect, an artificial reference matrix where defects have been chosen as 1 and sound area is chosen as zeros have been created. In other words, the knowledge on the position of the defects according to the known model helped to create a numerical example of defect/no-defect matrix, which was used for comparison with the other techniques and named as *real defect*.

Every matrix has been binarized in order to evaluate it using ROC curves. For simplicity, histogram-based segmentation has been performed over a hundred (100) steps. According to the artificial reference matrix, each pixel segmented within the matrix has been classified with as true positive, false positive, true negative and false negative. –True Positive (TP) when there is defect in defect position, False Positive (FP) when there is defect in sound area, True Negative (TN) when there is no defect in sound area, False Negative (FN) when there is no defect in defect position-. According to sensitivity and specificity information [50] true positive rate (TPR) and false positive rate (FPR) have been calculated for each segmented matrix as follows, Equations (6) and (7):

$$TPR = TP / (TP + FN) \quad (6)$$

$$FPR = FP / (FP + TN) \quad (7)$$

Finally, the receiver operating characteristic curve has been obtained by plotting false positive rates against true positive rates. In order to quantitatively evaluate each fusion and feature result, area-under-curve (AUC) for each ROC curve has been calculated via trapezoids.

3. Results

The samples have been investigated with the above-described methodology. The results from perfect bond -no defect case- have been only used in order to eliminate environmental and system-based errors in induction thermography results. In this section, three different bonding quality investigations have been reported: debonding with release film inclusions (12.7 mm edge size), debonding with brass inclusion—Large (12.7 mm edge size), debonding with brass inclusion—Small (6.35 mm edge size) (Figure 1).

3.1. Case 1: Debonding with Release Film Inclusions (12.7 mm Edge Size)

The adhesive bond containing debonding with release film inclusion had been inspected using ultrasonic immersion NDT and induction thermography. Feature matrices have been obtained according to above-described post-processing methods (see Section 2.3). Data fusion algorithms (Section 2.4) have been applied to the feature matrices.

The feature matrices for ultrasonic inspection and induction thermography with data fusion results are presented in Figure 7.

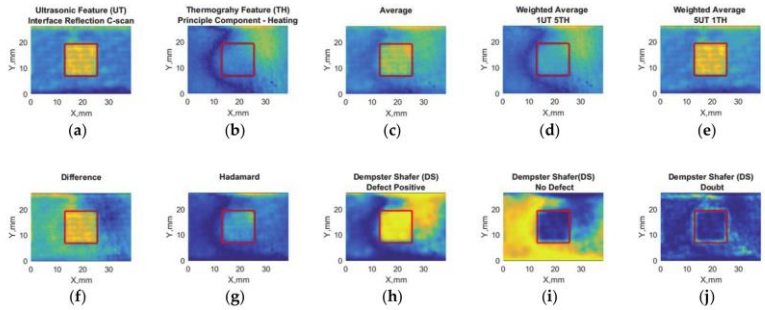

Figure 7. Debonding with release film (12.7 mm edge size) feature-based data fusion algorithm results: (**a**) ultrasonic feature (UT) with maximum values at interface reflection C-scan, (**b**) thermography feature (TH) principal component analysis response, (**c**) average of UT and TH, (**d**) weighted average where TH is five times more than UT, (**e**) weighted average where UT is 5 times more than TH, (**f**) absolute difference, (**g**) Hadamard fusion, (**h**) Dempster–Shafer fusion for defect placement, (**i**) Dempster–Shafer fusion for no defect positions, and (**j**) Dempster–Shafer fusion where doubt is high. The real position of the defect has been indicated with red squares.

The real defect position has been shown with a red square. The ultrasonic feature indicates the defect region with a higher amplitude response than the sound area (Figure 7a). In the induction thermography feature matrix, the defect position does not have a high contrast compared to the sound area (Figure 7b). On the other hand, averaging data fusion results show smoothen feature (Figure 7c), while the defect contrast is much higher in weighted average 5UT-1TH (Figure 7e) than the others. The difference fusion matrix shows relatively high performance on defect detection (Figure 7f). On the other hand, Hadamard fusion indicates very low performance in defect detection (Figure 7g) while DS performs well in the defected region (Figure 7h) but not well in the sound area (Figure 7i).

The receiver operating characteristic curves for adhesive bonds containing debonding with release film have been shown in Figure 8.

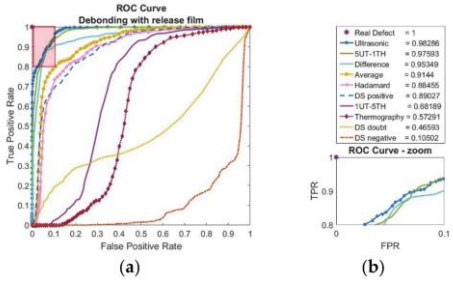

Figure 8. Debonding with release film (12.7 mm edge size) feature-based data fusion evaluation results with (**a**) receiver operating characteristic curve (ROC) and (**b**) area-under-curve (AUC) calculations with zoom image of ROC curve.

As seen in Figure 8b, the area under ROC curves have been calculated and indicated with the label. The best performance point is shown with 'star' at the position [0,1] where real defect is observed. According to Figure 8a, the ultrasonic feature and weighted average 5UT-1TH performs best. Furthermore, fusion results with difference, average, Hadamard, and DS-positive seem to perform reasonably well. The area-under-curve (AUC) calculations are in line with the ROC the results where the ultrasonic feature has the highest value with the follow-up of weighted average 5UT-1TH, difference, and average.

3.2. Case 2: Debonding with Brass Inclusion—Large (12.7 mm Edge Size)

The adhesive bond containing debonding with large-brass inclusion had been inspected via ultrasonic immersion NDT and induction thermography. Feature matrices have been obtained according to the above-described (Section 2.3) post-processing methods. Data fusion algorithms (Section 2.4) have been applied to the feature matrices.

The feature matrices for adhesive bond containing large-brass inclusion with ultrasonic inspection, induction thermography, and data fusion results are shown in Figure 9.

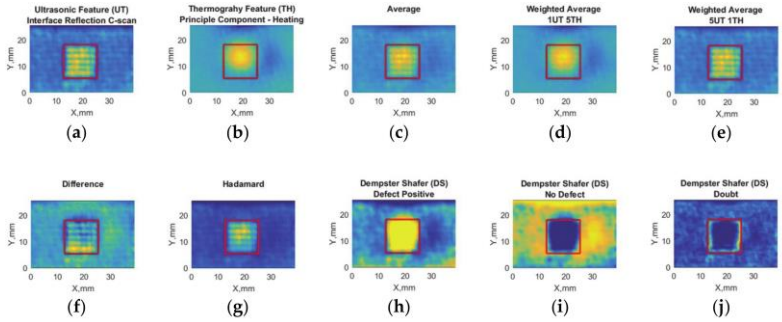

Figure 9. Debonding with brass inclusion (12.7 mm edge size) feature-based data fusion algorithm results: (**a**) ultrasonic feature (UT) with maximum values at interface reflection C-scan, (**b**) thermography feature (TH) principal component analysis response, (**c**) average of UT and TH, (**d**) weighted average where TH is five times more than UT, (**e**) weighted average where UT is five times more than TH, (**f**) absolute difference, (**g**) Hadamard fusion, (**h**) Dempster–Shafer fusion for defect placement, (**i**) Dempster–Shafer fusion for no defect positions, and (**j**) Dempster–Shafer fusion where doubt is high. The real position of the defect has been indicated with red squares.

While all feature matrices indicate a contrast between defect region and sound area, Dempster–Shafer-positive (Figure 9h) and negative (Figure 9i) fusion results seem to have the highest contrast in defect detection.

Quantitative evaluation results for debonding with large-brass film inclusion have been shown in Figure 10.

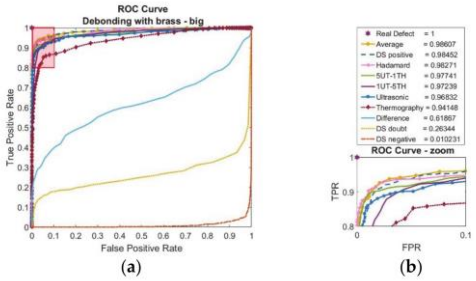

Figure 10. Debonding with brass inclusion (12.7 mm edge size) feature-based data fusion evaluation results with (**a**) receiver operating characteristic curve (ROC) and (**b**) area-under-curve (AUC) calculations with zoom image of ROC curve.

The performance of each technique is quite similar except the difference and DS-doubt, DS-negative. It shows that the doubt and contradiction between ultrasonic and induction thermography are very low. As seen in Figure 10b legend, the area-under-curve calculations agrees with ROC curves. While there is a small difference between each technique, basic averaging data fusion performs the best.

3.3. Case 3: Debonding with Brass Inclusion—Small (6.35 mm Edge Size)

The adhesive bond containing debonding with small-brass inclusion had been inspected via ultrasonic immersion NDT and induction thermography. Feature matrices have been obtained according to the above described (Section 2.3) post-processing methods. Data fusion algorithms (Section 2.4) have been applied to the feature matrices.

Feature-based data fusion results for adhesive bonds containing debonding with small-brass inclusions are shown in Figure 11.

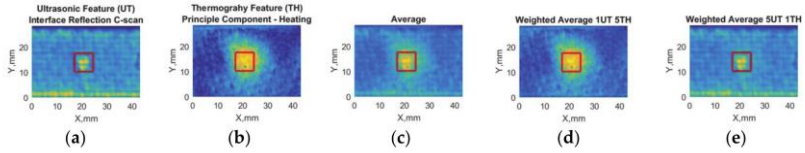

Figure 11. *Cont.*

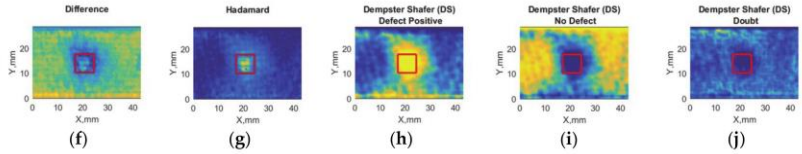

Figure 11. Debonding with brass inclusion (6.35 mm edge size) feature-based data fusion algorithm results: (**a**) ultrasonic feature (UT) with maximum values at interface reflection C-scan, (**b**) thermography feature (TH) principal component analysis response, (**c**) average of UT and TH, (**d**) weighted average where TH is five times more than UT, (**e**) weighted average where UT is five times more than TH, (**f**) absolute difference, (**g**) Hadamard fusion, (**h**) Dempster–Shafer fusion for defect placement, (**i**) Dempster–Shafer fusion for no defect positions, and (**j**) Dempster–Shafer fusion where doubt is high. The real position of the defect has been indicated with red squares.

The results suggest ultrasonic and induction thermography NDT features can detect the defect presence, while ultrasonic feature underestimates the defect size (Figure 11a); induction thermography overestimates it (Figure 11b). The difference data fusion suggests that there is no contradiction in between NDT techniques. DS-positive seems to have the highest contrast (Figure 11h).

According to receiver operating curve and area-under-curve calculations for the debonding with small-brass inclusion, the ultrasonic feature and weighted average with 5UT-1TH does not perform well compared to the others (Figure 12).

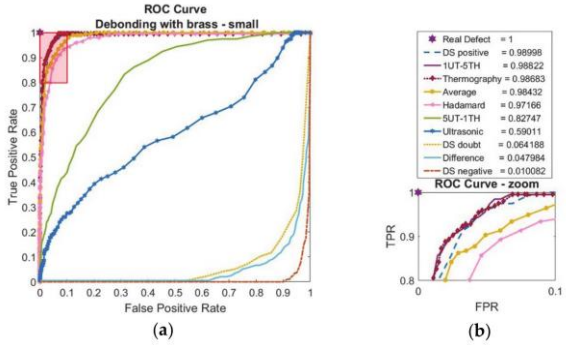

Figure 12. Debonding with release film brass inclusion (6.35 mm edge size) feature-based data fusion evaluation results with (**a**) receiver operating characteristic curve (ROC) and (**b**) area-under-curve (AUC) calculations with zoom image of ROC curve.

While the best performance is observed at DS-positive, the induction thermography feature also performs quite well. Low AUC values for difference, DS-doubt, and DS-negative suggest that the NDT techniques do not contradict each other.

4. Discussion

These results indicate that data fusion algorithms can improve the debonding type defect detection performance for bonding quality evaluation. In this work, three different cases of bonding quality have been investigated by ultrasonic immersion inspection and induction thermography. The obtained data had been preprocessed for data fusion with several steps. The feature matrices that have been

extracted from each nondestructive testing method results were used as the source for data fusion algorithms. The data fusion algorithms have been evaluated with quantitative sensitivity analysis.

In the case study one, a composite-adhesive single-lap joint with release film debonding artificial defect was investigated. Ultrasonic inspection with 10 MHz central frequency focused transducer detects the artificial defect fairly well (Figure 7a) due to high acoustic impedance difference between the air within the double-sided release film and single-lap joint interface. However, the induction thermography feature does not correlate well with the defect position (Figure 7b); because the electrical conductivity level of release film is quite similar to the epoxy adhesive. In this case, for induction thermography inspection, the thermal wave dominates over Joule's effect. Therefore, the fusion algorithms that are more focused on ultrasonics, such as weighted average 5UT-1TH (Figure 7e) has higher performance than thermography dominant fusion algorithms (Figure 8). As the difference fusion matrix shows defect presence in Figure 7f and is evaluated with high values in area-under-curve calculations (Figure 8), it can be said that two NDT techniques contradict each other in case study one.

In case study two, a composite-adhesive single-lap joint containing large brass film artificial debonding was investigated. Ultrasonic immersion investigation performs well with respect to qualitative and quantitative evaluation (Figures 9a and 10). However, it does not indicate clear results as good as case study one even though the defect dimensions are the same. On the other hand, compared to case study one, the high electrical conductivity of interfacial inclusion results with high temperature contrasts in thermography investigation (Figure 9b). Hence. The contradiction between two data fusion sources is much lower, as seen in the difference fusion algorithm (Figure 9e) and observed low-values for the difference in area-under curve calculations (Figure 10). While information theory-based fusion algorithms like DS perform quite well with detecting defects (Figure 9h), the basic algorithm average is evaluated better in receiver operating characteristic curve (Figure 10).

In case study three, the composite-adhesive single-lap joint with relatively small brass inclusions was investigated. Even though ultrasonic inspection results are improved by choosing a focused transducer rather than a flat transducer as in the previous work [3], the defect detection performance with ultrasonic NDT is still limited, as seen in Figure 11a and as evaluated by ROC curves (Figure 12). Since the brass inclusion has high electrical conductivity like in case two, induction thermography performed well in defect detection qualitatively, as seen in (Figure 11b) and quantitatively as calculated in the area-under-curve results (Figure 12). While the contradiction between ultrasonic NDT and thermography is low according to the difference fusion algorithm (Figures 11e and 12), both basic and information theory based fusion algorithms have increased the performance of separate techniques.

When considering ultrasonic inspection of adhesively bonded structures, transducer selection plays a significant role. The small defect detection performance is increased by changing from flat transducers to focused transducers. On the other hand, in order to obtain a clear ultrasonic response in the time domain -clear from the multiple reflections within the composite-adhesive bond, a high central frequency of the transducers is required. However, due to the high frequency, the highly attenuated composite adherend causes a drastic ultrasonic amplitude decrease, which makes the defect detection challenging.

The induction thermography results show that the brass inclusions have been detected with high performance. However, the release film inclusion at the interface is not detected with the same precision as the brass inclusions. This difference in the detection performance is caused by their electrical conductivity levels. While the brass is an electrically conductive material, which allows eddy current to form within, debonding with release film only affects the thermal diffusion. Therefore, induction thermography is a successful technique to detect inclusions that are electrically conductive, even for the small sizes.

It is important to mention that both ultrasonic inspection and induction thermography have advantages and limitations for bonding quality evaluation due to their physical and practical characteristics. Although ultrasonic inspection with the immersion technique is a successful method to detect debonding with release film inclusion, it requires the samples to be underwater, which may not

be applicable to every specimen. Induction thermography is, on the other hand, a noncontact NDT technique that does not require any contact medium. However, the nonconductive material inclusions and air-induced delamination may not be determined as successful as ultrasonic inspection. As these inclusions represent possible foreign object introduction to the bonding area during the manufacturing stage, both conductive and nonconductive inclusions are significant. However, at the maintenance scenario where air gap and porosity at the bondline causes debonding, only nonconductive inclusion results should be considered.

Considering three cases, it is observed that the data fusion of ultrasonic NDT with induction thermography can increase the detection performance of defect detection. While information theory-based fusion algorithms like DS perform well, the basic fusion algorithms such as Hadamard and averaging cannot be disregarded. In case study 1, ultrasonic testing performs the best; therefore, each data fusion algorithms that are favoring ultrasonic inspection, such as weighted average 5UT-1TH performs well. Also, it is seen that the area-under-curve values for the difference is close to 1, which indicated that the data fusion sources (induction thermography and ultrasonic inspection feature results) are in contradiction. In case study 2, it is observed that averaging, DS, and Hadamard improves the results from different NDT techniques. On the other hand, case 3 highlights the importance of information theory-based method DS: while averaging evaluated as lower performance than thermography, DS-positive performs very well on defect detection.

Composite-adhesive bonding nondestructive evaluation is considered one of the most challenging NDT applications. This application study only covers the detection of debonding and might not be applicable to weak and kissing bond predictions. Also, the proposed nondestructive evaluations might not suit perfectly for bonding structures with different material properties such as dissimilar joints and aluminum bonded structures. It is important to point out that the contradiction between sources and the preprocessing steps affects the performance of data fusion significantly. The limitations observed in this work might be overcome by deep learning algorithms to emphasize different features from different sources and evaluate the contradiction with statistical-based algorithms.

5. Conclusions

In this work, three different artificial debonding within composite-adhesive single-lap joints have been investigated with ultrasonic immersion pulse-echo technique and induction thermography. Data fusion has been used to increase the performance of different defect detection. The following points highlight the conclusions in this work.

- Ultrasonic immersion pulse-echo NDT technique is an advantageous method for debonding detection.
- Induction thermography NDT performs well with electrically conductive inclusion detection; however, it is not sensitive to nonconductive inclusions.
- While ultrasonic NDT performs better in release film inclusion, obvious fact that brass inclusion (or any inclusion with high electrical conductivity) is detected better with induction thermography.
- Data fusion performs well only if the sensors are not in contradiction.
- While the information theory-based fusion algorithm, the Dempster-Shafer rule of combination and Hadamard shows high performance, basic data fusion techniques such as averaging should not be disregarded.
- NDT of adhesive bonding is challenging, but as long as the sources do not contradict, data fusion increases the sensitivity and specificity of the inspection.

Author Contributions: Conceptualization, B.Y. and E.J.; methodology, B.Y., A.B., E.J. and H.-K.B.; software, B.Y. and A.B.; validation, E.J., H.-K.B. and G.B.; formal analysis, B.Y.; investigation, B.Y., A.B. and H.-K.B.; writing—original draft preparation, B.Y.; writing—review and editing, E.J., A.B. and H.-K.B.; visualization, B.Y.; supervision, E.J., H.-K.B. and G.B.; project administration, E.J. and G.B.; funding acquisition, E.J. and G.B. All authors have read and agreed to the published version of the manuscript.

Funding: This research was funded by NDTonAIR project from the European Union's Horizon 2020 Research and Innovation program under the Marie Sklodowska-Curie, grant number 722134.

Conflicts of Interest: The authors declare no conflict of interest.

References

1. Daryabor, P.; Safizadeh, M.S. Image fusion of ultrasonic and thermographic inspection of carbon/epoxy patches bonded to an aluminum plate. *NDT E Int.* **2017**, *90*, 1–10. [CrossRef]
2. Yi, Q.; Tian, G.Y.; Yilmaz, B.; Malekmohammadi, H.; Laureti, S.; Ricci, M.; Jasiuniene, E. Evaluation of debonding in CFRP-epoxy adhesive single-lap joints using eddy current pulse-compression thermography. *Compos. Part B Eng.* **2019**, *178*, 107461. [CrossRef]
3. Yilmaz, B.; Ba, A.; Jasiuniene, E.; Bui, H.K.; Berthiau, G. Comparison of different nondestructive testing techniques for bonding quality evaluation. In Proceedings of the 2019 IEEE 5th International Workshop on Metrology for AeroSpace (MetroAeroSpace), Torino, Italy, 19–21 June 2019; pp. 92–97. [CrossRef]
4. Galy, J.; Moysan, J.; El Mahi, A.; Ylla, N.; Massacret, N. Controlled reduced-strength epoxy-aluminium joints validated by ultrasonic and mechanical measurements. *Int. J. Adhes. Adhes.* **2017**, *72*, 139–146. [CrossRef]
5. Scarselli, G.; Nicassio, F. Analysis of debonding in single lap joints based on employment of ultrasounds. In Proceedings of the SPIE Smart Structures and Materials + Nondestructive Evaluation and Health Monitoring, Portland, OR, USA, 25–29 March 2017; p. 1017020. [CrossRef]
6. Tamborrino, R.; Palumbo, D.; Galietti, U.; Aversa, P.; Chiozzi, S.; Luprano, V.A.M. Assessment of the effect of defects on mechanical properties of adhesive bonded joints by using non destructive methods. *Compos. Part B Eng.* **2016**, *91*, 337–345. [CrossRef]
7. Katsiropoulos, C.V.; Pantelakis, S.G. Assessment of the imperfect bonding of adhesively bonded U-joints using ultrasonic inspection. *Plast. Rubber Compos.* **2014**, *43*, 316–321. [CrossRef]
8. Bhanushali, R.; Ayre, D.; Nezhad, H.Y. Tensile Response of Adhesively Bonded Composite-to-composite Single-lap Joints in the Presence of Bond Deficiency. *Procedia CIRP* **2017**, *59*, 139–143. [CrossRef]
9. Jasiūnienė, E.; Mažeika, L.; Samaitis, V.; Cicėnas, V.; Mattsson, D. Ultrasonic nondestructive testing of complex titanium/carbon fibre composite joints. *Ultrasonics* **2019**, *95*, 13–21. [CrossRef]
10. Jiao, D.; Rose, J.L. An ultrasonic interface layer model for bond evaluation. *J. Adhes. Sci. Technol.* **1991**, *5*, 631–646. [CrossRef]
11. Brotherhood, C.J.; Drinkwater, B.W.; Guild, F.J. The effect of compressive loading on the ultrasonic detectability of kissing bonds in adhesive joints. *J. Nondestruct. Eval.* **2002**, *21*, 95–104. [CrossRef]
12. Ding, J.; Wu, B.; He, C.-F. Longitudinal wave propagation in adhesive structure under different forms of interfaces. In Proceedings of the 2015 Symposium on Piezoelectricity, Acoustic Waves, and Device Applications (SPAWDA), Jinan, China, 30 October–2 November 2015.
13. Kazys, R.; Demcenko, A.; Zukauskas, E.; Mazeika, L. Air-coupled ultrasonic investigation of multi-layered composite materials. *Ultrasonics* **2006**, *44*, 819–822. [CrossRef] [PubMed]
14. Gaal, M.; Dohse, E.; Bartusch, J.; Köppe, E.; Kreutzbruck, M.; Hillger, W.; Amos, J. Ultrasonic Testing of Adhesively Bonded Joints Using Air-Coupled Cellular Polypropylene Transducers 1. Cellular polypropylene transducers for air-coupled ultrasonic testing. In Proceedings of the ECNDT 2014 - 11th European Conference on Non-Destructive Testing, Prague, Czech Republic, 6–10 October 2014.
15. Marks, R.; Clarke, A.; Featherston, C.; Paget, C.; Pullin, R. Lamb Wave Interaction with Adhesively Bonded Stiffeners and Disbonds Using 3D Vibrometry. *Appl. Sci.* **2016**, *6*, 12. [CrossRef]
16. Sherafat, M.H.; Guitel, R.; Quaegebeur, N.; Lessard, L.; Hubert, P.; Masson, P. Guided wave scattering behavior in composite bonded assemblies. *Compos. Struct.* **2016**, *136*, 696–705. [CrossRef]
17. Cho, H.; Hara, Y.; Matsuo, T. Evaluation of the thickness and bond quality of three-layered media using zero-group-velocity lamb waves. *J. Phys. Conf. Ser.* **2014**, *520*. [CrossRef]
18. Leiderman, R.; Braga, A.M.B. Scattering of guided waves by defective adhesive bonds in multilayer anisotropic plates. *Wave Motion* **2017**, *74*, 93–104. [CrossRef]
19. Nagy; Jeenjitkaew, C.; Stein, N.; Felger, J.; Becker, W.; Jeenjitkaew, C.; Luklinska, Z.; Guild, F.J.; Argust, G.; Hazimeh, R.; et al. Kissing bond detection in structural adhesive joints using nonlinear dynamic characteristics. *Int. J. Adhes. Adhes.* **2015**, *70*, 46–56. [CrossRef]

20. Yan, D.; Drinkwater, B.W.; Neild, S.A. Measurement of the ultrasonic nonlinearity of kissing bonds in adhesive joints. *NDT E Int.* **2009**, *42*, 459–466. [CrossRef]
21. Scarselli, G.; Ciampa, F.; Ginzburg, D.; Meo, M. Nondestructive testing techniques based on nonlinear methods for assessment of debonding in single lap joints. In Proceedings of the SPIE Smart Structures and Materials + Nondestructive Evaluation and Health Monitoring, San Diego, CA, USA, 8–12 March 2015. [CrossRef]
22. Solodov, I.; Kreutzbruck, M.; Ségur, D. Monitoring of bonding quality in CFRP composite laminates by measurements of local vibration nonlinearity. In Proceedings of the 12th International Workshop on Structural Health Monitoring: Enabling Intelligent Life-Cycle Health Management for Industry Internet of Things (IIOT), Stanford, CA, USA, 10–12 September 2019.
23. Asif, M.; Khan, M.A.; Khan, S.Z.; Choudhry, R.S.; Khan, K.A. Identification of an effective nondestructive technique for bond defect determination in laminate composites—A technical review. *J. Compos. Mater.* **2018**, *52*, 3589–3599. [CrossRef]
24. Gauthier, C.; Ech-Cherif El-Kettani, M.; Galy, J.; Predoi, M.; Leduc, D.; Izbicki, J.L. Lamb waves characterization of adhesion levels in aluminum/epoxy bi-layers with different cohesive and adhesive properties. *Int. J. Adhes. Adhes.* **2017**, *74*, 15–20. [CrossRef]
25. Grosso, M.; Marinho, C.A.; Nesteruk, D.A.; Rebello, J.M.A.; Soares, S.D.; Vavilov, V.P. Evaluating quality of adhesive joints in glass fiber plastic piping by using active thermal NDT. In Proceedings of the SPIE Defense, Security, and Sensing, Baltimore, MD, USA, 29 April–3 May 2013; Volume 8705, pp. 1–11. [CrossRef]
26. Hung, M.Y.Y. Review and comparison of shearography and pulsed thermography for adhesive bond evaluation. *Opt. Eng.* **2007**, *46*, 051007. [CrossRef]
27. Genest, M.; Martinez, M.; Mrad, N.; Renaud, G.; Fahr, A. Pulsed thermography for nondestructive evaluation and damage growth monitoring of bonded repairs. *Compos. Struct.* **2009**, *88*, 112–120. [CrossRef]
28. Shin, P.H.; Webb, S.C.; Peters, K.J. Pulsed phase thermography imaging of fatigue-loaded composite adhesively bonded joints. *NDT E Int.* **2016**, *79*, 7–16. [CrossRef]
29. Bui, H.K.; Wasselynck, G.; Trichet, D.; Ramdane, B.; Berthiau, G.; Fouladgar, J. 3-D modeling of thermo inductive non destructive testing method applied to multilayer composite. *IEEE Trans. Magn.* **2013**, *49*, 1949–1952. [CrossRef]
30. Cheng, L.; Gao, B.; Tian, G.Y.; Woo, W.L.; Berthiau, G. Impact damage detection and identification using eddy current pulsed thermography through integration of PCA and ICA. *IEEE Sens. J.* **2014**, *14*, 1655–1663. [CrossRef]
31. Ehrhart, B.; Valeske, B.; Bockenheimer, C. Nondestructive evaluation (NDE) of aerospace composites. In *Nondestructive Evaluation (NDE) of Polymer Matrix Composites: Techniques and Applications*; Woodhead Publishing: Cambridge, UK, 2013. [CrossRef]
32. Kiziltaş, G.; Papila, M.; Yilmaz, B.; Bilge, K. Challenges in Micro-CT Characterization of Composites. *Micro-Computed Tomogr. Med. Eng.* **2020**, 225–246. [CrossRef]
33. Bossi, R.; Lahrman, D.; Sokol, D.; Walters, C. Laser Bond Inspection for adhesive bond strength. In Proceedings of the International SAMPE Technical Conference, Paris, France, 28–29 March 2011.
34. Ecault, R.; Boustie, M.; Touchard, F.; Pons, F.; Berthe, L.; Chocinski-Arnault, L.; Ehrhart, B.; Bockenheimer, C. A study of composite material damage induced by laser shock waves. *Compos. Part A Appl. Sci. Manuf.* **2013**, *53*, 54–64. [CrossRef]
35. Marty, P.; Desai, N.; Andersson, J. NDT of kissing bond in aeronautical structures. In Proceedings of the 16th World Conference on NDT, Montreal, QC, Canada, 30 August–3 September 2004.
36. Gros, X.E.; Strachan, P.; Lowden, D.W. Theory and implementation of NDT data fusion. *Res. Nondestruct. Eval.* **1995**, *6*, 227–236. [CrossRef]
37. Jasiūnienė, E.; Žukauskas, E.; Dragatogiannis, D.A.; Koumoulos, E.P.; Charitidis, C.A. Investigation of dissimilar metal joints with nanoparticle fillers. *NDT E Int.* **2017**, *92*, 122–129. [CrossRef]
38. Dong, J.; Zhuang, D.; Huang, Y.; Fu, J. Advances in multi-sensor data fusion: Algorithms and applications. *Sensors* **2009**, *9*, 7771–7784. [CrossRef]
39. Liu, Z.; Forsyth, D.S.; Komorowski, J.P.; Hanasaki, K.; Kirubarajan, T. Survey: State of the art in NDE data fusion techniques. *IEEE Trans. Instrum. Meas.* **2007**, *56*, 2435–2451. [CrossRef]
40. Ploix, M.; Garnier, V.; Breysse, D.; Moysan, J. NDE data fusion to improve the evaluation of concrete structures. *NDT E Int.* **2011**, *44*, 442–448. [CrossRef]

41. Völker, C.; Shokouhi, P. Clustering Based Multi Sensor Data Fusion for Honeycomb Detection in Concrete. *J. Nondestruct. Eval.* **2015**, *34*, 1–10. [CrossRef]
42. Cotič, P.; Jagličić, Z.; Niederleithinger, E.; Stoppel, M.; Bosiljkov, V. Image Fusion for Improved Detection of Near-Surface Defects in NDT-CE Using Unsupervised Clustering Methods. *J. Nondestruct. Eval.* **2014**, *33*, 384–397. [CrossRef]
43. Völker, C.; Shokouhi, P. Multi sensor data fusion approach for automatic honeycomb detection in concrete. *NDT E Int.* **2015**, *71*, 54–60. [CrossRef]
44. Gusenbauer, C.; Reiter, M.; Plank, B.; Salaberger, D.; Senck, S.; Kastner, J. Porosity Determination of Carbon and Glass Fibre Reinforced Polymers Using Phase-Contrast Imaging. *J. Nondestruct. Eval.* **2019**, *38*, 1–10. [CrossRef]
45. Cuadra, J.; Vanniamparambil, P.A.; Hazeli, K.; Bartoli, I.; Kontsos, A. Damage quantification in polymer composites using a hybrid NDT approach. *Compos. Sci. Technol.* **2013**, *83*, 11–21. [CrossRef]
46. Cao, Y.; Dong, Y.; Cao, Y.; Yang, J.; Yang, M.Y. Two-stream convolutional neural network for nondestructive subsurface defect detection via similarity comparison of lock-in thermography signals. *NDT E Int.* **2020**, *112*, 102246. [CrossRef]
47. Horn, R.A.; Zhang, F. Basic Properties of the Schur Complement. In *The Schur Complement and Its Applications*; Springer-Verlag: Boston, MA, USA, 2005; pp. 17–46.
48. Smith, A.F.M.; Shafer, G. A Mathematical Theory of Evidence. *Biometrics* **1976**, *32*, 703–704. [CrossRef]
49. Dempster, A.P. Upper and Lower Probabilities Induced by a Multivalued Mapping. *Ann. Math. Stat.* **1967**, *38*, 325–339. [CrossRef]
50. Brierley, N.; Tippetts, T.; Cawley, P. Data fusion for automated nondestructive inspection. *Proc. R. Soc. A Math. Phys. Eng. Sci.* **2014**, *470*. [CrossRef]

This is an original manuscript of the article "Model assisted reliability assessment for adhesive bonding quality evaluation with advanced ultrasonic NDT" that is submitted to ELSEVIER in Journal of Nondestructive Testing and Evaluation (NDT&E) International on 27 April 2021, currently under review.

Model assisted reliability assessment for adhesive bonding quality evaluation with advanced ultrasonic NDT

Bengisu Yilmaz[1*], Damira Smagulova[1], Elena Jasiuniene[1,2]

1 Ultrasound Research Institute, Kaunas University of Technology, 51423, Kaunas, Lithuania

2 Department of Electronics Engineering, Kaunas University of Technology, 51367, Kaunas, Lithuania.

*corresponding author: bengisu.yilmaz@ktu.lt.

Abstract

This work proposes a novel cost-effective technique to evaluate the reliability of advanced ultrasonic non-destructive testing technique in bonding quality evaluation. Detectability of debonding defects and weak bonds in aluminum-epoxy single lap joints was estimated by model assisted probability of detection curves. For those adhesive joints containing three different bonding qualities –debonding at interface, weak bond with release agent contamination, and weak bond due to faulty curing– numerical models were built. Ultrasonic wave propagation is simulated by using semi-analytical finite element method via CIVA and validated with experimental investigations. In order to create a variation study, uncertain parameters and their distribution is determined based on experiments and expertise. Ultrasonic signal responses in time and frequency domain are analyzed as opposed to defect characteristic values. According to reliability analysis, it is shown that the detection probability of debonding is mostly based on the gate selection and ultrasonic echo amplitude, while weak bond detection requires a more delicate assessment. Frequency based calculations can improve the detection reliability of weak bond due to release agent contamination. Weak bonds caused by faulty curing are more sensitive to be detected via the attenuation of signal response.

Keywords: Model assisted probability of detection (PoD), adhesive bonds, ultrasonics, acoustic microscopy

1. Introduction

Adhesive bonding is an advantageous joining technology with the characteristics as homogenous load distribution, high strength to weight ratio, ability to join dissimilar materials and complex structures.

The durability of adhesively bonded structures might be affected during or after manufacturing by moisture, contamination or poor curing [1]. These variations might cause different type of defects [2], and even weak bonds – unreliable bonding quality hardly detectable by classical non-destructive testing (NDT) methods [3,4]. The lack of knowledge in NDT reliability is the key factor limiting adhesive bonding applications in regulated industries such as aerospace [5]. NDT reliability is usually quantified with Probability of Detection (PoD) curves [6], which relates the probability of detecting a defect with its characteristic value – usually considered to be the defect size [7,8]. While each nondestructive test is valid for the specific specimen, the detectability of defects is influenced by multiple uncontrollable factors like environmental conditions (temperature, radiation, moisture), inspection properties (experimental set-up and condition, control related uncertainties, digital and analog noise), human factors (personnel qualifications, experience, overwork) and variance occurring in specimens (material and dimensional properties) [9,10].

In practice, the reliability determination of NDT technique is a costly and time-consuming procedure that requires a large number of specimens and personnel. While experimental PoD curves are challenging to achieve, the need and acceptance of PoD curves for safety regulations are increasing. Therefore, the industries like aerospace are turning their face to simulation based reliability analysis, model assisted probability of detection (MAPOD) [11–13]. Use of simulation for PoD curve generation not only reduces the time and budget but also allows systematic work to be carried out. By using MAPOD large amount of data can be analyzed, even with configurations that are not possible to achieve experimentally [13,14].

MAPOD has been a research interest of many studies with applications on eddy current testing (for fatigue cracks in engine components [15], wing lap joints [15], in titanium plates [16]), induction thermography (for crack detection [17]) and ultrasonic NDT (defects in engine disk alloys [15], in railway axles [18]). A detailed review has been reported by Meyer et.al in 2014 [19]. Recently, Bato et.al compared experimental PoD with MAPOD estimations for eddy current testing of surface fatigue cracks [7]. Additionally, Baskaran et.al integrated two features as response signals with MAPOD for

the evaluation of flaw detectability with eddy current testing [20]. Jarvis et. al utilized MAPOD to estimate response operating characteristic curves on magnetic field measurements [21]. Rentala et.al highlighted the procedure and challenges to obtain MAPOD curves with a case study on flat bottom hole detection by ultrasonic NDT [22]. Also, Smagulova et al evaluated the reliability to detect debonding in dissimilar joints with ultrasonic testing by using MAPOD [23].

PoD curves can be obtained by two methods: hit-miss technique (binary method, defect is detected or not) and signal response analysis (where characteristic defect value (a) is compared with NDT response (â)). Most MAPOD analysis are based on signal response analysis (a vs. â) because numerical simulations allow recording signal response easily [19]. For ultrasonic testing, absolute maximum amplitudes (Amax) and time of flight difference (TOFD) methods are the most common signal responses in PoD curve calculations [24,25]. However, post-processing for the signal response selection plays an important role in the nondestructive evaluation of adhesive bonding quality since the probability of defect detection is low due to the structural noise caused by interface echoes for ultrasonic wave propagation [26] and thermal diffusion [27]. In general, ultrasonic defect characterization uncertainty might be reduced by using multiple features based on amplitude, phase, and frequency information [28]. In our previous work, it was demonstrated that the post-processing of ultrasonic interface echoes in frequency domain might increase the detectability of weak bonds that are weakened via release agent contamination [29].

This work aims to evaluate the reliability of debonding and weak bond detection with high frequency ultrasonic NDT by using MAPOD curves. In order to achieve this goal, three cases in aluminum-epoxy single lap joint were investigated with different bonding qualities: debonding, weak bond due to release agent contamination, and weak bond due to faulty curing. Nondestructive evaluation of the adhesive joints was performed by scanning acoustic microscopy in pulse-echo mode. Numerical models were built and ultrasonic wave propagation was simulated with semi-analytical finite element software CIVA [12]. After model validation, the metamodels are built by variances in uncertain parameters which are determined by design of experiments and expertise. For each bonding quality

case, different defect properties were selected as characteristic values: defect length in debonding, inclusion thickness in weak bond due to release agent, acoustic wave velocity of epoxy in weak bond due to faulty curing. Five different features are evaluated as signal response: peak to peak amplitude, time delay, frequency domain absolute maximum amplitude, frequency shift, attenuation. PoD curves are reported for all bonding quality cases with each feature in signal response.

2. Materials/Samples

Aluminum-epoxy single-lap adhesive joints with various bonding qualities have been manufactured in Cotesa GmBH, Germany. Two identical 1.6 mm thick aluminum 2024 sheets have been bonded together with 3M Scotch-Weld AF163 k-red structural adhesive film epoxy. For all samples, surface preparation is done by polishing with sandpaper and acetone cleaning. Bonding quality deviated with several different techniques. For reference, one sample has been produced with nominal settings, without any inclusion, and named as “perfect bond - PB” (Figure 1-a, right side II). The delamination at the bonding interface is demonstrated by adding square double-fold Wrigtlon 4600 release film (12.7 mm edge length, 0.063 mm thick) and named “debonding-DB” (Figure 1-a, left side I).

In addition, weak bonds scenario due to contamination of adhesive-adherend interface is replicated by adding Marbocote release agent prior to bonding and named as “weak bond due to release agent – WB-RA”. Different amounts of release agent were applied: 1ml/5500 mm^2 marked as thick inclusion, 0.2 ml/5500 mm^2 marked as thin inclusion. Lastly, in order to represent possible heating protocol deviations, the curing cycle for the bonding epoxy has been altered, and named “weak bond due to faulty curing – WB-FC”. While the standard cure temperature for AF163-K epoxy is 125°C, two poor curing specimens have been manufactured at 90°C and 75°C.

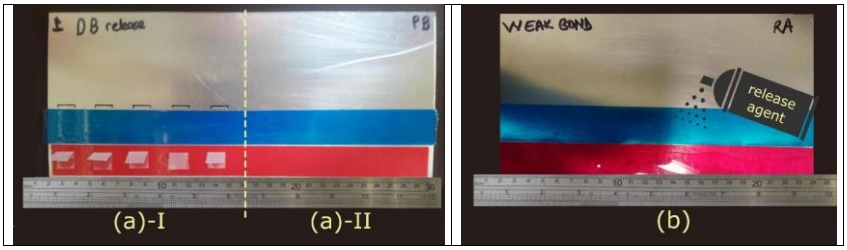

Figure 1 Sample pictures prior to bonding (a) Artificial debonding and perfect bond sample (b) weak bond release agent sample, epoxy covered with release agent.

3. Methodology

In order to evaluate the reliability of advanced ultrasonic nondestructive testing methods with model based probability of detection curves, a detailed study with multiple steps has been conducted (Figure 2). Firstly, the experimental analysis on samples has been performed and the ultrasonic echoes from the bonding region have been recorded. Then the numerical models were built to find the best match of the variable parameters to the experimental results. By careful consideration, separate experiments, and NDT experts' suggestions, uncertain parameters and their distribution were determined. Characteristic values for the metamodels were defined for each bonding quality. Numerical experiments were performed to obtain the characteristic value versus signal response curves. Statistical analysis was performed on the data to obtain the probability of detection curves. The threshold value was selected based on the separate calculations of background noise, which is considered to be adhesive bond without any defect (perfect bond-PB).

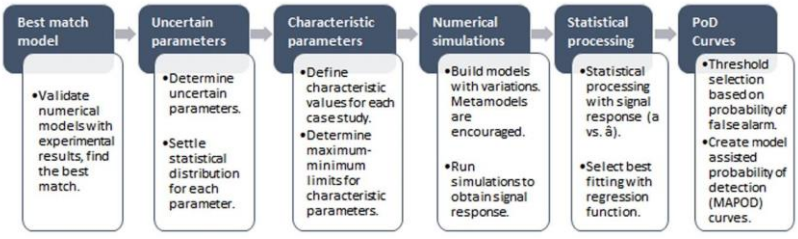

Figure 2 Methodological steps to obtain model based probability of detection curves.

3.1. Ultrasonic Non-destructive testing

Adhesively bonded aluminum-epoxy-aluminum single-lap joints with different bonding qualities have been investigated with scanning acoustic microscopy (KSI GmBH) at Ultrasound Research Institute, Kaunas University of Technology, Lithuania. The schematic of the inspection system is shown in Figure 3-a. Samples were investigated in a temperature controlled room (25°C) with immersion pulse-echo technique. Focused ultrasonic transducer which has 50 MHz central frequency, 3 mm aperture, and

10 mm focal distance in water (PT-50-3-10) is selected. In order to keep the transducer focus at the sample interface, the distance between the transducer and the sample is kept at 2.94 mm.

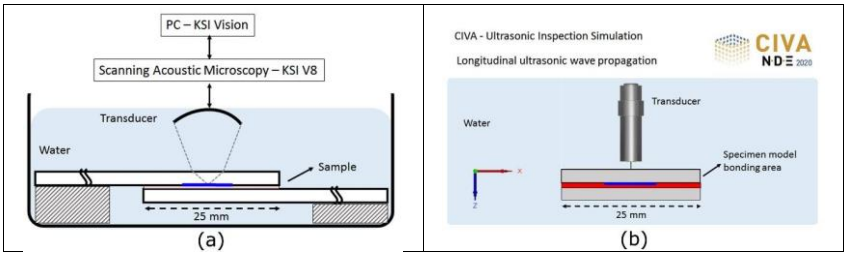

Figure 3 Sketch of scanning acoustic microscopy experimental set-up (a) and the numerical model for the ultrasonic wave propagation simulation with CIVA (b).

3.2. Numerical model and its validation

Numerical models of aluminum-epoxy single lap joints have been built and ultrasonic wave propagation was simulated with semi-analytical finite element method via CIVA software (CEA, Fr) (Figure 3-b). CIVA allows to define material parameters and inspection settings prior to simulation. Also, the excitation signal can be uploaded for ultrasonic wave propagation calculation. In this work excitation signal is recorded by scanning a standard reference thick aluminum block with acoustic microscopy with the same transducer. In order to reduce the computation time that is increased by multi-layer structure and high frequency, two dimensional calculations were performed. Each case of bonding quality has been studied carefully and the numerical models are validated by the experimental results.

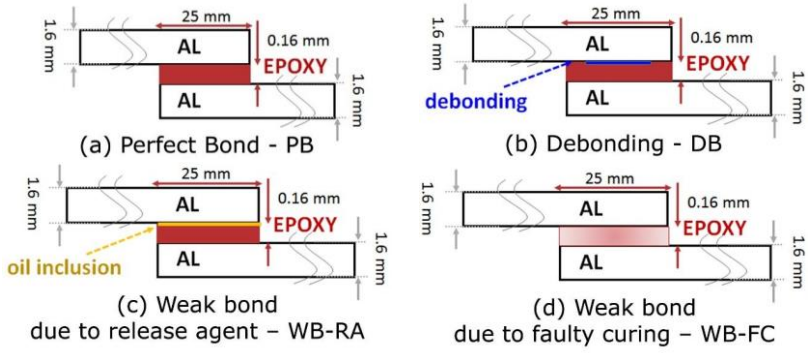

Figure 4 Schematics for aluminum-epoxy single-lap joints with different bonding quality: a) perfect bond-PB, b) debonding-DB, c) weak bond due to release agent (oil) inclusion – WB-RA, d) weak bond due to faulty curing – WB-FC.

Aluminum-epoxy-aluminum three-layer model has been built as the base for the ultrasonic wave propagation medium. The adhesive-adherend interfaces are modeled to be continuously in contact. For debonding defect, a rectangular defect has been placed at the top interface. An example of experimental A-scan response for perfect bond and debonding specimens are shown together with numerical results in Figure 5. It can be noticed that the ultrasonic echo signal shape and frequency of the experimental signal have been preserved in numerical calculations. While there is a small delay in numerical results, this might be related to the variations of the sample.

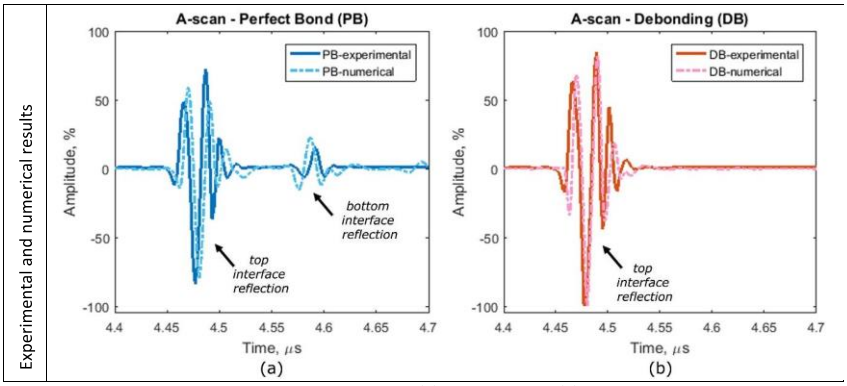

Figure 5 A-scan comparison for numerical model validations. (a) Perfect bond-PB, (b) Debonding-DB.

Numerical results show similar parameters as experimental results: debonding presence increases the top reflection amplitude, whereas bottom reflection is only observed in perfect bond (Figure 6). Also, it is observed that the presence of debonding at the top interface blocks the ultrasonic wave and no echo at the bottom interface, from 4.57 to 4.62 μs in time domain is visible.

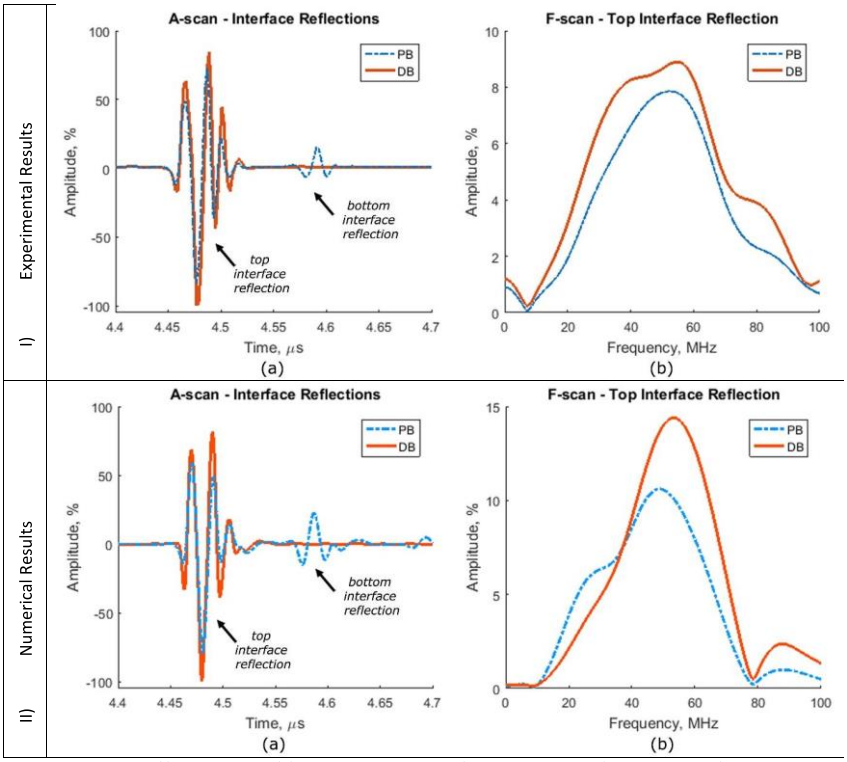

Figure 6 Experimental (I) and numerical (II) results for perfect bond (blue dashed line -PB) and debonding (red continuous line- DB) samples. Recorded and simulated ultrasonic A-scan results (a) and F-scan (frequency domain) with gate at top interface(b) is shown.

An extra oil layer has been added in between aluminum and epoxy interface to represent weak bond due to release agent inclusion (WB-RA). As seen in Figure 7, the addition of an oil layer as thin as 0.05 mm at the interface, affects the ultrasonic echo received at the transducer. Numerical results agree with the experimental ones that the bottom interface reflection amplitude decreases and the flight time of bottom reflection reception differ from the perfect bond. On the other hand, while numerical results show that there is a slight increase in amplitude in top interface reflection, this has not been observed in the experimental results. Therefore, time gate is considered to be at the bottom interface reflection flight time -from 4.57 to 4.62 μs- for WB-RA.

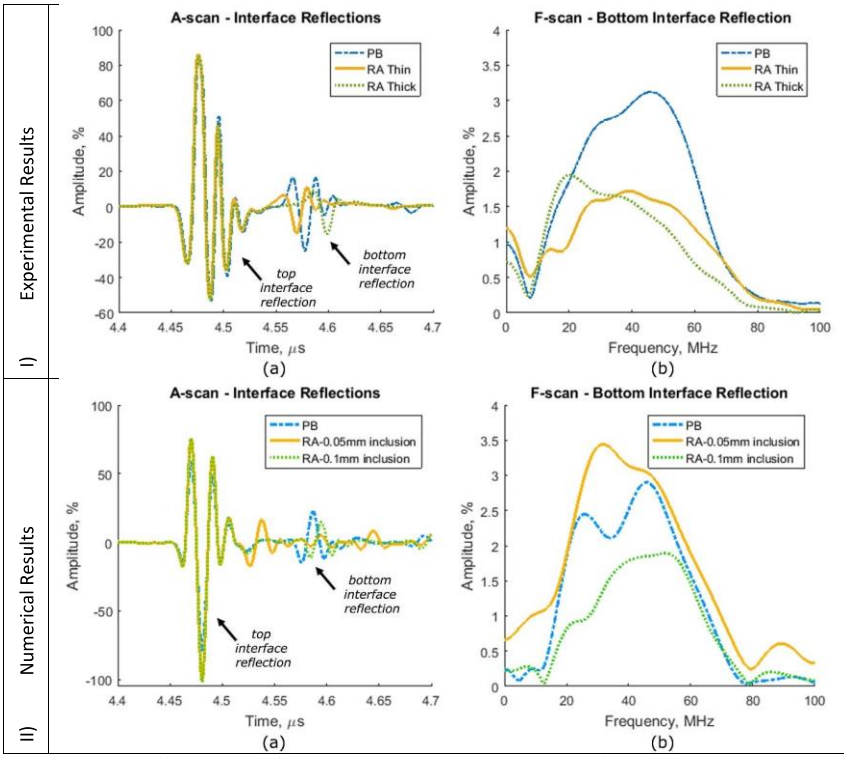

Figure 7 Experimental (I) and numerical (II) results for perfect bond (blue dashed line -PB), weak bond due to release agent thin inclusion (yellow continuous line- RA Thin), and weak bond due to release agent thick contamination (dotted green line- RA thick) samples. Recorded and simulated ultrasonic A-scan results (a) and F-scan (frequency domain) with gate at top interface(b) is shown.

Additionally, weak bond due to faulty curing is represented by the change in epoxy acoustic wave velocity – which is expected to be affected due to cure temperature dependence of material elasticity. As seen in Figure 8, in both experimental and numerical cases, top interface reflection has not changed due to the faulty curing. However, the bottom interface reflection amplitude is reduced slightly and the flight time of reception has been affected significantly. Hence, the second interface reflection observed –bottom reflection- has been considered to be of interest for this case.

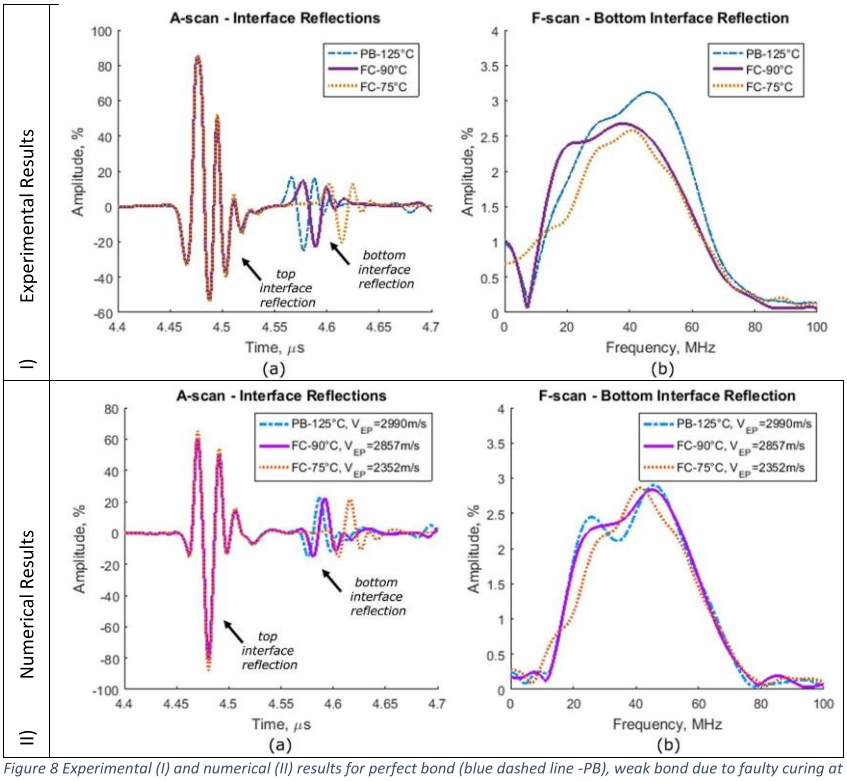

Figure 8 Experimental (I) and numerical (II) results for perfect bond (blue dashed line -PB), weak bond due to faulty curing at 90°C (purple continuous line- FC-90°C and at 75°C (orange dotted line - FC-75°C). Recorded and simulated ultrasonic A-scan results (a) and F-scan (frequency domain) with gate at top interface(b) is shown.

3.3. Determination of uncertain parameters & their statistical distribution

The uncertain parameters and their statistical distributions are one of the key factors to obtain reliable MAPOD curves. The uncertain parameters are the parameters that might be variant due to specimen based, experimental, environmental, or human factors. In order to determine uncertain parameters, design of experiments based on Morris design has been built with a large number of variables to determine the influential parameters. As listed in Table 1, eight influential parameters are marked as uncertain parameters to be used in the variation study. The statistical distribution for each uncertain parameter has been determined by using experimental investigations and expertise.

Table 1 Uncertain parameter limits and distribution characteristics.

Name	Definition	Mean Value	Standard deviation	Min Value	Max Value	Unit [SI]
Epoxy thickness	Epoxy thickness, thickness of the adhesive.	0.16	0.012	0.12	0.24	mm
Epoxy acoustic velocity	Longitudinal acoustic wave velocity of epoxy	2990	300	1186	4706	m/s
Aluminum thickness	Aluminum thickness (top adherend)	1.6	0.007	1.59	1.66	mm
Aluminum acoustic velocity	Longitudinal acoustic wave velocity of aluminum (top)	6300	50	6200	6600	m/s
Water path	The distance between transducer and specimen	2.94	0.004	2.92	2.96	mm
Water acoustic velocity	Longitudinal acoustic wave velocity of water	1480	10	1447	1506	m/s
Incidence angle	The tilt of the transducer	0	1	-3	3	degree (angle)
Defect position (in depth)	The defect position through the thickness from surface	1.6	0.012	1.6	1.72	mm

While thickness and acoustic velocity variances observed in adhesive and adherend are classified as specimen family uncertainties; the water path, water acoustic velocity, and incidence angle are considered to be operational uncertainties due to nondestructive inspection setup and human factor. On the other hand, defect position is considered to be defect related uncertainty.

Adhesive (epoxy) and top adherend (aluminum) thicknesses and acoustic wave velocity are taken into account as specimen related uncertain parameters. Epoxy and aluminum densities are also considered to be evaluated in the first design of experiments, however, they are not labeled as influential. Although the theoretical thickness of epoxy is given as 0.24 mm in the material datasheet, due to the applied pressure during the bonding manufacturing the epoxy thickness is suspected to decrease. For each sample, after bonding, the thickness of the bonded region has been measured several times with caliber. The mean value for epoxy thickness is determined as 0.16 mm whereas the standard deviation is 0.012 mm (Table 1). Theoretical epoxy acoustic velocity is calculated based on elastic properties given in the epoxy material data sheet as 1186 m/s. Time of flight (ToF) differences for epoxy layer (from top and bottom of epoxy) are obtained with pulse-echo scanning acoustic microscopy investigations. The acoustic wave velocity (v) is estimated based on the measured thickness (th) and calculated time of flight difference (ToF) by using equation (1). While minimal value is determined as

the theoretical estimation 1186 m/s, the mean value is determined as 2990 m/s along with 300 m/s standard deviation (Table 1).

$$\boldsymbol{ToF = 2 * \frac{th}{v}} \quad (1)$$

Aluminum thickness and acoustic wave velocity statistical distribution are determined by similar methodology. Top adherend thickness is measured by calipers and the acoustic wave velocity distribution is determined via scanning acoustic microscopy ultrasonic investigation. The mean value for aluminum thickness is assessed as 1.6 mm, while the deviation is 0.007 mm (Table 1). Acoustic velocity of aluminum has been estimated to change from 6200 to 6600 m/s within the sample with a standard thickness of 1.6 mm (Table 1).

Considering the surface reflection time of flights that have been recorded during experiments, the statistical distribution for water path has been determined as a mean value at 2.94 mm with 0.004 mm standard deviation (Table 1). On the other hand, the variance observed for water acoustic velocity is considered to be due to temperature changes in the experimental set-up or due to impurity content within the water (Table 1). Incidence angle, where the perpendicularity of the transducer is considered to be deviant, is set from 0$\pm$3 degrees; and it can be caused by the transducer alignment or sample placement (Table 1).

The defect position for the debonding case is considered to be changing. While the interface is more susceptible to debonding defects, multiple inclusions such as release films might get stuck within the adhesive during manufacturing. Therefore, the position of the defect is considered to be mostly at the adhesive-adherend interface, and distribution is affected by the thickness of the epoxy (Table 1). For the debonding case, the thickness of adherend (aluminum at top) has been considered to be constant at 1.6 mm in order to be able to simulate the defect always within adhesive with variance at the defect position.

3.4. Characteristic value determination & limits

The physical characteristics of the weakening indifferent bonding quality cases help to determine the characteristic value for reliability analysis. In the debonding numerical model, where debonding is

represented with zero-thickness rectangular defect, the defect size is considered as characteristic value. The thickness of oil addition has been selected as the characteristic value for weak bond due to release agent models (WB-RA). The epoxy acoustic velocity –which is significantly affected by poor curing caused by elasticity changes, is selected as the characteristic value for weak bond due to faulty curing (WB-FC). The limits for characteristic values are listed in Table 2.

Table 2 Characteristic values for each bonding quality and their limits; where DB is debonding, WB-RA is weak bond due to release agent, WB-FC is weak bond due to faulty curing.

Bonding Quality	Characteristic Value	Minimum Value	Maximum Value	Unit [SI]
DB	Defect size	0.01	5	mm
WB – RA	Oil inclusion thickness	0.005	0.1	mm
WB – FC	Epoxy acoustic velocity	1000	5000	m/s

With numerical beam computation by CIVA software, the characteristic of the transducer has been identified. The focal spot of the transducer (PT50-3-10) is determined as 0.2 mm, therefore the minimum and maximum limits for debonding defect characteristic are set to 0.01 mm - 5 mm, respectively.

The characteristic value for the weak bond due to release agent contamination is the thickness of the oil layer. Based on the correlation of the numerical validation with experimental results, the limits are set as 0.005 mm and 0.1 mm.

For the weak bond caused by faulty curing, the longitudinal acoustic velocity of epoxy is considered as the characteristic value. By changing the epoxy cure cycle, it is assumed that the elastic properties of epoxy are affected. The epoxy acoustic wave velocity is estimated based on the time of flight differences from top to bottom reflection observed in scanning acoustic microscopy investigations. According to experimental results, mean (μ) and standard deviation (σ) values for time of flight differences in samples are calculated for perfect bond (μ=107 , σ=13 nanosecond), faulty curing at 90°C (μ=112 , σ=7 nanosecond), and faulty curing at 75°C (μ=136 , σ=6 nanosecond). Theoretically, the relationship between epoxy acoustic velocity, epoxy thickness, and resulting time of flight differences from top to bottom epoxy reflection can be defined by equation (1). Figure 9 shows the epoxy thickness on X axis, epoxy acoustic velocity on Y axis and time of flight difference as the color

scale. The limits on the color axis have been determined according to $\mu \pm 3\sigma$ values calculated in the experimental data analysis. The assumption of elastic property change is supported by experimental results: when there is a reduction in curing temperature, measured acoustic wave velocity is decreased (Figure 9). While mean epoxy longitudinal acoustic velocity is 2990 m/s for perfectly cured adhesive; poor curing at 90°C resulted in 2857 m/s acoustic velocity. Faulty curing at 75°C is estimated to have 2352 m/s acoustic velocity in epoxy – that is the lowest value among all investigated samples.

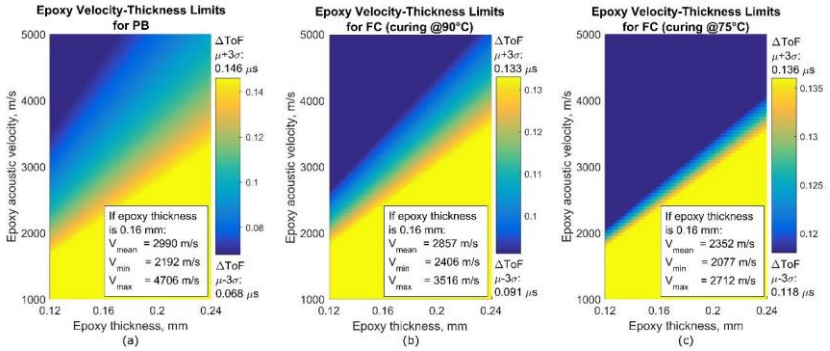

Figure 9 Epoxy acoustic velocity limitations for different bonding qualities (b: perfect bond, c:faulty curing at 90°C, d: faulty curing at 75°C) based on experimental calculations.

3.5. Numerical simulations and post-processing

Validated numerical models for each bonding quality have been used as reference models for the metamodel study. Metamodels, also known as response surfaces, are mathematical approximations that are used to reduce the computation time of high degrees of freedom numerical simulations [30]. The metamodels are built by implementing minimum and maximum values for each uncertain parameter as well as characteristic values. Each metamodel has more than 1000 calculation points and the Kriging method – Gaussian process regression- [30,31] has been used for interpolation.

Mostly, the metamodels are built with extracted parameters such as amplitude or flight time responses of numerical investigation. This work aims to evaluate the reliability of different features for the detection of debonding and weak bonds. Hence, for each of three bonding quality cases, metamodels have been built on five different features – which will be used as the signal response (â) in PoD curve data plots:

- peak to peak amplitude at the specified gate (Peak to Peak Amplitude)
- time delay of absolute maximum amplitude (Time Delay)
- maximum amplitude in frequency domain (Frequency Amax)
- frequency shift of absolute maximum amplitude (Frequency Shift)
- attenuation at the adhesive layer (Attenuation)

Response values for each feature are reported in Table 3 for the numerical example A-scan and F-scan in Figure 6Figure 7Figure 8(II).

Table 3 Feature response values for the example A-scan F-scans shown in numerical results – Figure 5-6-7-(II), for each bonding quality: PB stands for perfect bond, top for top reflection, bottom for bottom reflection, DB is debonding, WB-RA is weak bond due to release agent, WB-FC is weak bond due to faulty curing.

Bonding Quality / **Features**	**PB**	**PB**	**DB** defect size: 5mm	**WB – RA** inclusion: 0.05 mm	**WB – FC** V_{EP}: 2352 m/s
	top interface reflection	bottom interface reflection	top interface reflection	bottom interface reflection	bottom interface reflection
Peak to peak amplitude, %	138.3506	37.3949	181.7098	34.3194	36.5022
Time delay, μs	0	0	0.001	0.059	0.030
Frequency Amax, %	10.6116	2.8994	14.3958	3.4427	2.8608
Frequency shift, MHz	0	0	4.5	14	4.5
Attenuation, %	71.730	71.730	99.645	82.644	75.651

Since bonding quality information mostly lies in the interface reflection echoes, the interested time of flight is selected at the first top and first bottom interface reflections. In debonding case, the first interface reflection – which mostly represents the defect reflection is evaluated as the first option (DB-OPTION1). In order to decrease the false-positive rates in the DB case, a special gate selection algorithm is proposed and applied (DB-OPTION2). Normally, the gate starts before the first interface reflection. If the absolute maximum amplitude of the signal response is less than 100 percent and the second reflection observed, then the gate is placed at the second interface reflection. For weak bond due to release agent WB-RA and weak bond due to faulty curing WB-FC, second reflection (the wave packet observed after the top interface reflection) is of interest.

3.6. Statistical Processing: Signal response (a vs. â) analysis

In order to obtain PoD curves, the data plots have been created via CIVA software. Based on each metamodel – representing five features for three bonding quality cases, statistical settings have been set to satisfy both normality and variance rules based on Beren's hypothesis validity [13]. In this procedure, best fit is selected by mapping the signal response data (a vs. â) in logarithmic, normal and boxcox settings. Some of the data has been set as "noise" and "saturation" in order to minimize the fitting errors and satisfy Beren's validity on linearity, homoscedasticity, normality, and variance.

3.7. PoD curves – threshold selection

In addition to noise and saturation, the selection of threshold plays a significant role in PoD curve results. In this study, threshold selection is done by performing a variation study where no defect is present (perfect bond-PB) and uncertain parameters are applied. The results have been extracted for each feature and plotted against defect present cases as histogram densities. The amount of data in the PB data set which is above the threshold is calculated as probability of false alarms. According to MH-1823, no probability of detection is considered to be sufficient if the probability of false alarm is not calculated [8]. While in most standard NDT PoD studies, noise is considered to be the noise due to environmental or instrumental issues, in the case of adhesive joint inspections the highest "noise" is due to the bonding interface reflections. In each case, the threshold value is selected by taking most of the signal response into account and minimizing the probability of false alarms (PFA). In Figure 10, numerically calculated perfect bond, debonding and weak bond signal responses are represented as distributions along with threshold selection and calculated PFA percentages.

4. Results

Reliability analysis based on the numerical models for aluminum-epoxy adhesive bonding has been performed by following steps described in Figure 2. Model based probability of detection curves are reported for three different bonding qualities and five different features in Figure 11. Results are categorized by bonding quality cases:

- Case 1: Debonding (DB).

- Option 1 – where the ultrasonic time gate is selected on top interface reflection.
- Option 2 – where “smart” gate selection algorithm is applied.

- Case 2: Weak bond due to release agent (WB-RA).
- Case 3: Weak bond due to faulty curing (WB-FC).

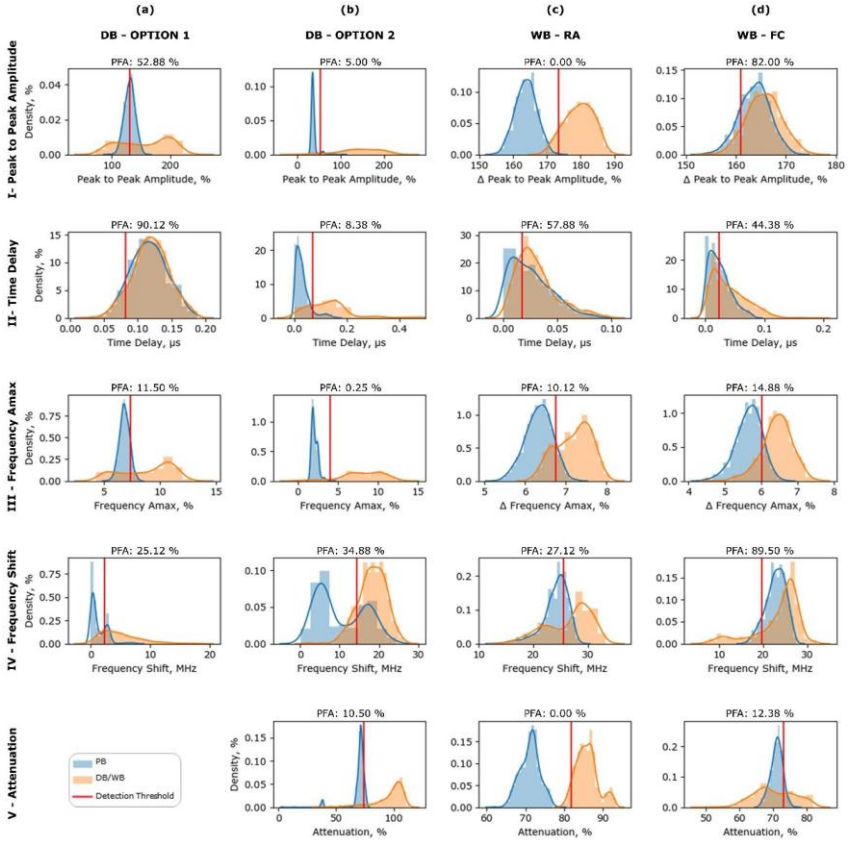

Figure 10 Perfect bond data distribution along with debonding and weak bond for each signal response, in order to determine threshold value and calculate probability of false alarms (PFA) for debonding DB option 1 (a), debonding DB option 2 (b), weak bond due to release agent WB-RA (c), weak bond due to faulty curing WB-FC (d); for five different signal response features I-peak to peak amplitude, II- time delay, III- frequency Amax, IV-frequency shift, V-Attenuation

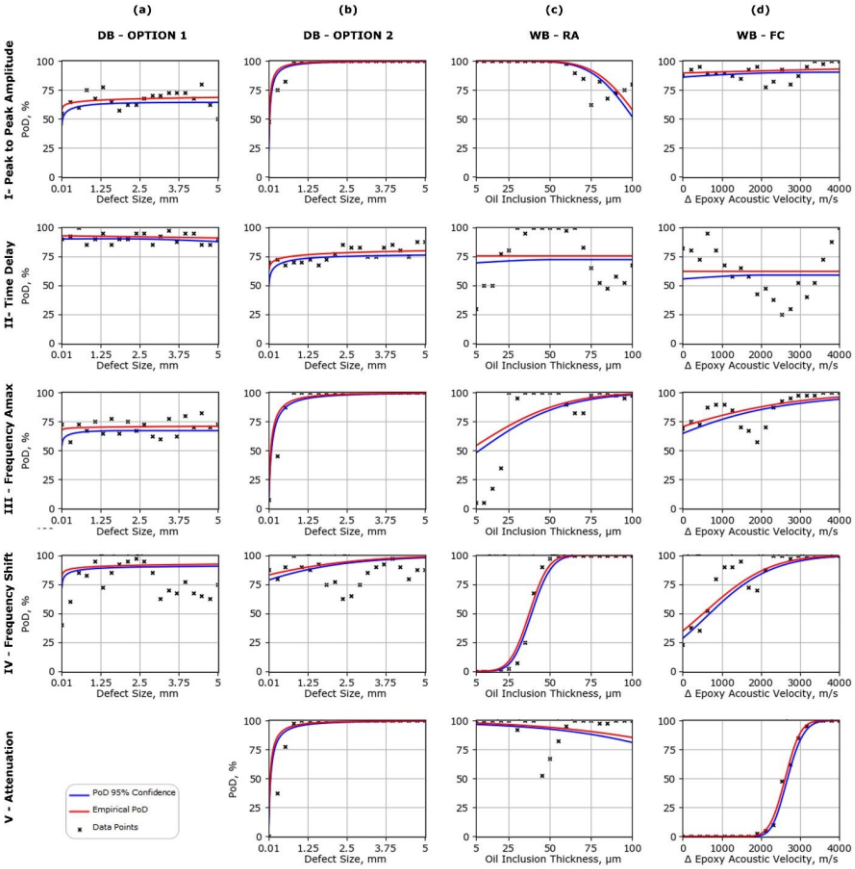

Figure 11 Estimated MAPOD curves for four different bonding quality cases (a) debonding DB – option 1 gate selection, (b) debonding DB – option 2 gate selection, (c) weak bond due to release agent WB – RA, (d) weak bond due to faulty curing WB – FC; considering five signal response features on the rows I- peak to peak amplitude, II- time delay, III- frequency Amax, IV-frequency shift, V- attenuation.

4.1. Case 1: Debonding (DB)

Reliability of detecting debonding defects placed at the interface of aluminum-epoxy single-lap joints is estimated based on numerical simulations. In order to create the variance in signal response, seven uncertain parameters were defined with distributions listed in Table 1, except aluminum thickness due to the counter interaction with defect depth. The defect size changing from 0.01 mm to 5 mm is used as characteristic value (a). Five response signals (â) are estimated by post-processing during

metamodel creation: peak to peak amplitude, time delay, frequency domain maximum amplitude, frequency shift, and attenuation.

Firstly, the defect detection has been done with gate position at the maximum amplitude observed; first peak of the interface reflection – named as DB- OPTION 1. MAPOD curves are shown in Figure 11-(a) for response signals as peak-to-peak amplitude (I), time delay (II), frequency domain amplitude (III), and frequency shift (IV). The results indicate that none of the PoD curves have reached the critical stage where $a_{90/95}$ values are observed. The false calls for peak-to-peak amplitude is as high as 53 %, while time delay is almost 90 %. This behavior is associated with false-positive rates within the calculation, where the response values are high however no defect is present.

In order to improve the reliability of the inspection, we propose a "smart" gate selection algorithm: the time gate is at the first peak observed (after surface reflection) unless the maximum amplitude is less than 100 % and there is no second peak observed in short interval. This algorithm allows to search for the bottom reflection echo, while not interfering with the small amplitude reflections due to small or disoriented defect sizes. The results are marked as DB-OPTION 2 for peak-to-peak amplitude (I), time delay (II), frequency Amax (III), frequency shift (IV), and attenuation (V) (Figure 11-(b)). By comparing standard gate selection, the reliability of detecting debonding defects in bonding has increased significantly. Except for time delay feature, in all other signal responses, it is calculated that 5mm defect size can be detected with 100 percent probability. In addition, probability of false alarms is drastically lower (< 10%) than in the previous case - except for the frequency shift response signal.

4.2. Case 2: Weak bond due to release agent contamination

Interface contamination of aluminum-epoxy adhesive joints is simulated with numerical models containing a small inclusion layer of oil with seven uncertain parameters as variants (Table 1, except defect position). The oil thickness, in other words, the thickness of the inclusion, from 5 μm to 100 μm has been used as the characteristic value. Five different features are extracted as the signal response during metamodel calculation: peak to peak amplitude change, time delay, frequency domain

maximum amplitude change, frequency shift, and attenuation. The gate was selected at the second signal wave packet, the one observed after top interface reflection.

Model based probability of detection curves and transformed data plots, along with the probability of false calls can be seen in Figure 11-(c). Results show that the detection probability of a small layer of inclusion is higher in the case of peak-to-peak amplitude change (I) or attenuation (V) signal responses. On the other hand, frequency Amax change (III) and frequency shift (IV) suggest that the probability of detecting thick oil inclusion is higher than the probability of detecting thin layers of oil.

4.3. Case 3: Weak bond due to faulty curing

In order to evaluate the detection probability of weak bonds due to faulty curing, the aluminum-epoxy single lap joints are modeled by considering six uncertain parameters (Table 1, except defect position and epoxy acoustic velocity); whereas epoxy acoustic velocity is a characteristic value. Five different signal responses are considered to be of interest: peak-to-peak amplitude change, time delay, frequency domain Amax, frequency shift and attenuation. The probability of detection curves and transformed data plots are shown in Figure 11-(d) side by side.

While the probability of detecting weak bonds due to faulty curing is quite insignificant with peak-to-peak amplitude (I) and time delay (II) response signals, frequency domain based responses (III-IV) show better performance. It should be noted that the probability of false alarm for frequency shift (IV) signal response is 90 %. On the contrary, by attenuation (V) percentage the weak bond due to faulty curing can be detected with a small probability of false calls, and high performance.

5. Discussion

Model assisted PoD curves are obtained for debonding (DB), weak bond due to release agent (WB-RA), and weak bond due to faulty curing detection with scanning acoustic microscopy. For each bonding quality, five different signal responses are calculated with post-processing during metamodel simulations. MAPOD curves are represented in the results section (Figure 11).

Firstly, the debonding defect detection reliability is estimated by analyzing first interface reflections through 0.01 mm to 5 mm defect sizes (DB- OPTION 1, Figure 11-(a)). It is observed that the detection

probability for debonding with this method is low, none of the signal response data has resulted with $a_{90/95}$ indicator. The false alarm rates are also observed to be high which is caused by the high signal responses observed without defect presence. As seen in Figure 6, both experimental and numerical A-scan and F-scan response differences between debonding defect (DB) and perfect bond (PB) are quite similar for the top interface reflection. Although the bottom interface reflection is only observed in the PB case. Hence, a new time gate is defined with “smart” algorithm: the wave packet of interest is the first interface reflection unless its absolute maximum amplitude is lower than 100 percent (when calibrated at 5 mm defect with nominal values) and the bottom reflection is present. The reliability results are updated with “smart” gate selection and reported as DB-OPTION 2 in (Figure 11-(b)). Compared to DB OPTION-1, the calculated reliability of the debonding detection has increased between 10% to 30 % for debonding detection probability. The signal responses- peak-to-peak amplitude, frequency Amax, and attenuation have reached 100 % PoD for DB-OPTION 2 with a relatively small probability of false alarms. Whereas features like time delay and frequency shift seem to be not prioritized for defect size characteristic value. However, it should be noted that time delay and frequency shift features might significantly impact the detection probability in the case defect position is more variant.

In case 2, weak bond due to release agent contamination detection is simulated with oil layer addition to the aluminum-epoxy interface. Time domain amplitude based features, namely peak-to-peak amplitude and attenuation, show that the detection probability will decrease with the increase in contamination thickness (Figure 11-(c)). On the contrary, the frequency domain based calculations (frequency Amax and frequency shift) indicate that detection of a high level contamination is increased by the signal response. The frequency shift feature is the most promising signal response observed in order to detect oil based contamination in adhesive bonding. These results support the previous work based on composite-epoxy experiments [29].

In case 3, a weak bond due to faulty curing is investigated by considering epoxy acoustic velocity as a characteristic value. The best reliability performance between different signal responses is observed

by attenuation for this case (Figure 11-(d)). If attenuation signal response is excluded, frequency domain based features perform better than time domain responses; however, the frequency shift signal response shows quite a high false-positive alarm rate.

For convenience, the PoD indicator $a_{90/95}$ and probability of false alarms for each bonding quality and each signal response feature are given in Table 4, as rows and columns, respectively. In the debonding case, $a_{90/95}$ indicator is not observed with DB-OPTION1. By implementing "smart" gate the debonding defect detection as small as 0.312 mm can be achieved with 90 percent probability and 95 percent confidence interval with a peak-to-peak signal response. While attenuation $a_{90/95}$ value is the second best, frequency Amax is third and the frequency shift is the last. Time delay response signal cannot achieve $a_{90/95}$ reliability even with smart gate. The PoD indicator $a_{90/95}$ suggests that the best signal response algorithm to detect weak bond due to release agent (WB-RA) is frequency shift, where 51.38 μm thick oil contamination can be detected. However, the probability of false alarm results suggest that by 10 μm thickness trade-off the frequency amplitude might be a good choice for WB-RA detection. In case of weak bond due to faulty curing (WB-FC), $a_{90/95}$ values suggest that the best detection would be with frequency shift with 2419 m/s change. However, the false-positive call percentages show that the attenuation and frequency Amax are the best candidates to detect WB-FC with high reliability.

Table 4 Estimated POD indicator a-90/95 values and probability of false alarms for each bonding quality deviation and each feature.

Bonding Quality / **Features**	DB – OPTION 1		DB –OPTION 2		WB-RA		WB-FC	
	$a_{90/95}$ [mm]	PFA [%]	$a_{90/95}$ [mm]	PFA [%]	$a_{90/95}$ [μm]	PFA [%]	$a_{90/95}$ [m/s]	PFA [%]
Peak to peak amplitude	--	0.53	0.312	0.10	74.912	0.00	2618	0.82
Time delay	--	0.90	--	0.35	--	0.58	--	0.44
Frequency Amax	--	0.12	0.687	0.00	61.537	0.10	2828	0.15
Frequency Shift	--	0.25	1.685	0.08	51.386	0.27	2419	0.90
Attenuation	NA	NA	0.506	0.05	66.134	0.00	3118	0.12

The detectability of weak bonds is reported to be more challenging in comparison to debonding defects for adhesive bonds. Generally, MAPOD calculations agree with the literature and suggest that

the defect detection in debonding can be performed with a higher probability than the defect detection in weak bond cases.

The application of these results can be implemented into a quality control inspection system, where the debonding defect can be detected with peak-to-peak amplitudes and weak bonds with attenuation and frequency shift. This type of application may allow the automatic inspection for the adhesive bonding parts with high reliability, therefore expanding their usage and application areas. On the other hand, overall the most sensitive response signal feature in all cases is observed as attenuation, which depends on the ratio change from top reflection of adhesive to the bottom reflection. It is sensitive to the changes in bonding quality no matter the reason for weakening. However, it should be noted that in order to obtain such a response signal, one should differentiate from top ultrasonic reflection from the bottom reflection –which requires high frequency investigations. Although scanning acoustic microscopy offers high frequency-high resolution imaging with a quite fast inspection, the choice of high frequency transducers might limit the application to relatively thin samples, since the transducer focal length is usually small for high frequency models.

The investigations are performed and modeled with high frequency (50 MHz) scanning acoustic microscopy in laboratory conditions. It must be noted that the change in frequency of the investigation and environment might affect the reliability curves significantly. High frequency selection is crucially important because when frequency is reduced thin adherend and adhesive causes interface echoes to be overlapped.

6. Conclusion

Model assisted probability detection curves for three different bonding quality cases (debonding, weak bond due to release agent, weak bond due to faulty curing) were estimated with five different signal response features (peak to peak amplitude, time delay, frequency Amax, frequency shift, attenuation). It is concluded that:

- The detection probability of debonding mostly depends on the gate selection algorithm and ultrasonic echo amplitude.

- For similar reliability, weak bond detection requires more delicate evaluation than debonding detection - frequency based calculations can improve detection reliability of the weak bond due to release agent contamination.
- Probability of the detection of weak bonds caused by faulty curing is highest using the attenuation feature.
- While the quantitative comparison is difficult due to different characteristic defect properties, MAPOD results show that the probability of detection for small sized debonding defect is higher than weak bond detection probability.
- Among all signal response features investigated, the best performed is attenuation while time delay is evaluated as the worst one.

Acknowledgement: This work was partly supported by NDTonAIR project from the European Union's Horizon 2020 research and innovation program under the Marie Sklodowska-Curie [grant number 722134].

References

[1] Budhe S, Banea MD, de Barros S, da Silva LFM. An updated review of adhesively bonded joints in composite materials. Int J Adhes Adhes 2017;72:30–42. https://doi.org/10.1016/j.ijadhadh.2016.10.010.

[2] Adams RD, Cawley P. Defect types and non-destructive testing techniques for composites and bonded joints. Constr Build Mater 1989;3:170–83. https://doi.org/10.1016/0950-0618(89)90011-1.

[3] Yan D, Neild SA, Drinkwater BW. Modelling and measurement of the nonlinear behaviour of kissing bonds in adhesive joints. NDT E Int 2012;47:18–25. https://doi.org/10.1016/j.ndteint.2011.12.003.

[4] Koodalil D, Barnoncel D, Rajagopal P, Balasubramaniam K. Detection of interfacial weakness in a lap-shear joint using shear horizontal guided waves. NDT E Int 2020;112:102248. https://doi.org/10.1016/j.ndteint.2020.102248.

[5] Adams RD, Drinkwater BW. Nondestructive testing of adhesively-bonded joints. NDT E Int 1997;30:93–8. https://doi.org/10.1016/S0963-8695(96)00050-3.

[6] Schneider CRA, Rudlin JR. Review of statistical methods used in quantifying NDT reliability. Insight Non-Destructive Test Cond Monit 2004;46:77–9. https://doi.org/10.1784/insi.46.2.77.55549.

[7] Bato MR, Hor A, Rautureau A, Bes C. Experimental and numerical methodology to obtain the probability of detection in eddy current NDT method. NDT E Int 2020;114. https://doi.org/10.1016/j.ndteint.2020.102300.

[8] USA Department of Defense. Nondestructive Evaluation System Reliability Assessment.

Department of Defense Handbook. MIL-HDBK-1823. 2009.

[9] Holstein R, Bertovic M, Kanzler D, Müller C. NDT reliability in the organizational context of service inspection companies. Mater Test 2014;56:607–10. https://doi.org/10.3139/120.110601.

[10] Bato MR, Hor A, Rautureau A, Bes C. Impact of human and environmental factors on the probability of detection during NDT control by eddy currents. Meas J Int Meas Confed 2019;133:222–32. https://doi.org/10.1016/j.measurement.2018.10.008.

[11] Aldrin JC, Medina EA, Lindgren EA, Buynak C, Steffes G, Derriso M, et al. MODEL-ASSISTED PROBABILISTIC RELIABILITY ASSESSMENT FOR STRUCTURAL HEALTH MONITORING SYSTEMS, 2010, p. 1965–72. https://doi.org/10.1063/1.3362348.

[12] Foucher F, Fernandez R, Leberre S, Calmon P. New Tools in CIVA for Model Assisted Probability of Detection (MAPOD) to Support NDE Reliability Studies. NDE Aerosp Mater Struct 2018 2018:32–43.

[13] Chapuis B, Calmon P, Jenson F. Best Practices for the Use of Simulation in POD Curves Estimation. Cham: Springer International Publishing; 2018. https://doi.org/10.1007/978-3-319-62659-8.

[14] Calmon P, Chapuis B, Jenson F, Sjerve E. The Use of Simulation in POD Curves Estimation: An Overview of the IIW Best Practices Proposal. 19th World Conf Non-Destructive Test 2016 2016:7.

[15] Thompson RB, Brasche L, Forsyth D, Lindgren E, Swindell P, Winfree W. Recent Advances in Model-Assisted Probability of Detection. Proc 4th Eur Work Reliab NDE, Berlin, Ger 2009:23–26.

[16] Rosell A, Persson G. Model based capability assessment of an automated eddy current inspection procedure on flat surfaces. Res Nondestruct Eval 2013;24:154–76. https://doi.org/10.1080/09349847.2013.779401.

[17] Azzabi Zouraq B, Bui HK, Peterzol A, Wasselynck G, Berthiau G, Trichet D, et al. A Model-Assisted Probability of Detection Study on Induction Thermography Technique. IEEE Trans Magn 2019;55:2019–22. https://doi.org/10.1109/TMAG.2019.2898733.

[18] Carboni M, Cantini S. A " Model Assisted Probability of Detection " approach for ultrasonic inspection of railway axles. 18th World Conf Nondestruct Test 2012:16–20.

[19] Meyer RM, Crawford SL, Lareau JP, Anderson MT. Review of Literature for Model Assisted Probability of Detection - PNNL-23714 2014:1–20.

[20] Baskaran P, Pasadas DJ, Ramos HG, Ribeiro AL. Integration of multiple response signals into the probability of detection modelling in eddy current NDE of flaws. NDT E Int 2021;118:102401. https://doi.org/10.1016/j.ndteint.2020.102401.

[21] Jarvis R, Cawley P, Nagy PB. Performance evaluation of a magnetic field measurement NDE technique using a model assisted Probability of Detection framework. NDT E Int 2017;91:61–70. https://doi.org/10.1016/j.ndteint.2017.06.006.

[22] Rentala VK, Mylavarapu P, Gautam JP. Issues in estimating probability of detection of NDT techniques – A model assisted approach. Ultrasonics 2018;87:59–70. https://doi.org/10.1016/j.ultras.2018.02.012.

[23] Smagulova D, Mazeika L, Jasiuniene E. Novel Processing Algorithm to Improve Detectability of Disbonds in Adhesive Dissimilar Material Joints † 2021;21:475–9. https://doi.org/10.3390/s21093048.

[24] Ribay G, Artusi X, Jenson F, Reece C, Lhuillier PE. Model-based POD study of manual ultrasound inspection and sensitivity analysis using metamodel. AIP Conf Proc 2016;1706. https://doi.org/10.1063/1.4940650.

[25] Bilgunde PN, Bond LJ. Model-assisted approach for probability of detection (POD) in high-temperature ultrasonic NDE using low-temperature signals. Nucl Technol 2018;202:161–72. https://doi.org/10.1080/00295450.2017.1419782.

[26] Yilmaz B, Asokkumar A, Jasiūnienė E, Kažys RJ. Air-Coupled, Contact, and Immersion Ultrasonic Non-Destructive Testing: Comparison for Bonding Quality Evaluation. Appl Sci 2020;10:6757. https://doi.org/10.3390/app10196757.

[27] Yi Q, Tian GY, Yilmaz B, Malekmohammadi H, Laureti S, Ricci M, et al. Evaluation of debonding in CFRP-epoxy adhesive single-lap joints using eddy current pulse-compression thermography. Compos Part B Eng 2019;178:107461. https://doi.org/10.1016/j.compositesb.2019.107461.

[28] Bai L, Velichko A, Drinkwater BW. Ultrasonic defect characterisation—Use of amplitude, phase, and frequency information. J Acoust Soc Am 2018;143:349–60. https://doi.org/10.1121/1.5021246.

[29] Yılmaz B, Jasiūnienė E. Advanced Ultrasonic NDT for Weak Bond Detection in Composite-Adhesive Bonded Structures. Int J Adhes Adhes 2020:102675. https://doi.org/10.1016/j.ijadhadh.2020.102675.

[30] Le Gratiet L, Iooss B, Blatman G, Browne T, Cordeiro S, Goursaud B. Model Assisted Probability of Detection Curves: New Statistical Tools and Progressive Methodology. J Nondestruct Eval 2017;36:1–12. https://doi.org/10.1007/s10921-016-0387-z.

[31] Teixeira R, Nogal M, O'Connor A. Adaptive approaches in metamodel-based reliability analysis: A review. Struct Saf 2021;89:102019. https://doi.org/10.1016/j.strusafe.2020.102019.

CRediT Author Statements

Bengisu Yilmaz: Conceptualization; Data curation; Formal analysis; Funding acquisition; Investigation;

Methodology; Software; Visualization; Writing - original draft.

Damira Smagulova: Investigation; Methodology; Software; Writing - review & editing.

Elena Jasiuniene: Project administration; Supervision; Validation; Writing - review & editing.

ACKNOWLEDGEMENTS

Personally, I would like to express my special thanks and sincere gratitude to my thesis advisor Professor Elena Jasiūnienė who has always been a source of inspiration for me with her endless support, enthusiasm, and encouragement. Working and interacting with her has broadened my vision not only professionally, but also personally.

I would like to thank to the reviewers both in the department and the committee, Professor Arunas Lukosevicius, Professor Dangirutis Navikas, Professor Liudas Mazeika, and Dr. Vykintas Samaitis. I am grateful for both supporting me in my research activities and for enriching my PhD thesis with their valuable comments and reviews. Also, I would like to thank the members of my defense board: Professor Arunas Lukosevicius, Professor Dangirutis Navikas, Professor Liudas Mazeika, Professor Chiara Bisagni, and Professor Helge Pfeiffer. I appreciate their willingness to enrich my doctoral thesis.

I must express my gratitude to my former advisor, Professor Melih Papila, who helped me realize how much I enjoy doing research and encouraged me to continue.

I feel happy to thank my dearest colleagues both at Kaunas University of Technology Ultrasound Research Institute and at NDTonAIR. I would like to thank Professor Marco Ricci and Dr. Stefano Laureti for uniting a great research team, sharing their wisdom and friendship. It was a great chance to be part of a fantastic research team. The collaboration through NDTonAIR network put this work to the next level. Specifically, I would like to thank Prof. Gui Yun Tian at Newcastle University; Prof. Gerard Berthiau and Dr. Huu Kien Bui at University of Nantes; Dr. Jakob Schulz, David Lietze and Falk Stelzmann at Cotesa GmBH for hosting and advising me during secondments.

I owe a sincere thanks to the dear people who made Europe home: Hamed Malekmohammadi, Khalid Rizwan, Sevilla Sunetchiieva, Abdoulaye BA, Quiji Yi, Sergey Gartsev, Tommaso Seresini, Michael Stamm, Luca Pecoriello, Marius Zienius, Monika Stankeviciute, Damira Smagulova, Vykintas Samaitis, Gitana Svediene and all of the people with whom I have shared some enjoyable research environment.

Furthermore, I am grateful to the European Union, *Horizon 2020 Marie Skolodowska Actions* for the opportunity that provided my training network NDTonAIR and project funding during my PhD studies. I feel privileged to be part of Marie Curie Alumni Association (MSCA).

Finally, my deepest gratitude goes to my family, specifically my parents Nural and Muhsin Yılmaz. Also, I would like to thank my other family, my partner Arvydas Sepetys, and my dear half-siblings Umay Solak, Merve Yuce, Ezgi Yildiz, Sidika Tunc, Meltem Celik, Serra Diptas, Mert Toka, Mete Icenler, Anil Kahraman, Farzin Javanshour, Yelda Yorulmaz – who have always been there for me even though the rivers and roads tried to keep us apart.

UDK 620.179.4(043.3)

SL 344. 2021-*-*, * leidyb. apsk. l. Tiražas 16 egz. Užsakymas 279
Išleido Kauno technologijos universitetas, K. Donelaičio g. 73, 44249 Kaunas
Spausdino leidyklos „Technologija“ spaustuvė, Studentų g. 54, 51424 Kaunas